Synthesis and Investigation of MX_2 (M = Ti, V, Cr; X = S, Se) as Electrocatalysts for the Hydrogen Evolution Reaction

University of Glasgow

Liudvika Masaityte

Submitted in fulfilment of the requirements of the Degree of Doctor of Philosophy

School of Chemistry
College of Science and Engineering
September 2022

Abstract

Rising attention to the climate crisis has boosted the search for alternative and clean energy. One of the most promising technologies to achieve it is water electrolysis. However, the process is thermodynamically unfavourable, therefore, catalysts are needed to lower the costs. The best catalysts known to this day are noble metal based. More cost-efficient and abundant materials have been investigated recently, such as transition metal phosphides, nitrides and transition metal dichalcogenides. The latter group of materials is at the centre of attention of this thesis, more specifically, early transition metal (Ti, V, Cr) sulphides and selenides.

The investigation of TMDCs begins with the synthesis of VS_2. Conflicting literature reports called for a very careful synthesis to obtain a genuine highly crystalline layered morphology of this compound, as most reports focused on nanostructured VS_2. Two routes were investigated – through alkali metal intercalates and hydrothermal synthesis. The alkali metal intercalate route was key in synthesising highly crystalline and stoichiometric VS_2, while the hydrothermal synthesis resulted in a nanostructured product. Contrary to literature reports, neither crystalline, bulk, nor nanostructure VS_2 was found to be good electrocatalysts for the hydrogen evolution reaction due to poor electrochemical stability and a large overpotential value.

VS_2 became a steppingstone in the investigation of isostructural transition metal dichalcogenides. The attention was then turned to TiS_2 and CrS_2 – materials that adopt the same crystal structure as VS_2. By preserving the crystal structure and only changing transition metal, the effect of transition metal on hydrogen evolution reaction was investigated. It was not possible to isolate CrS_2 as a pure phase preventing further electrochemical testing. However, as a single-phase TiS_2 sample was isolated, it was compared electrochemically with VS_2. The results hinted at a trend toward improvement in catalytic activity as Ti was replaced with V. Therefore, the investigation was expanded to selenides.

Facing the difficulties with chromium disulphide, the attention was turned to selenides. $TiSe_2$, VSe_2 and $CrSe_2$ are all isostructural between themselves and their corresponding sulphides. A successful synthesis of all selenides provides us with an opportunity to get insights into the transition metal effect on the electrocatalytic activity of transition metal selenides. While the electrochemical performance of $TiSe_2$ and VSe_2 followed the same

trend as for sulphides, $CrSe_2$ broke the underlying trend by revealing extremely high overpotential.

Lastly, V – S system was revisited, and the thermodynamically stable phases of VS_4, V_5S_8 and VS were investigated. This allowed for understanding whether the unexpectedly poor catalytic performance of VS_2 was a characteristic behaviour of V-based sulphides or originated from the metastability of the VS_2 phase. Varying the S-content allowed for preliminary insight into the effect metal to sulphur ratio has on the electrocatalytic activity of this system. The stoichiometric VS showed the lowest overpotential, reasonable current densities and good stability. However, the observed overpotential of –640 mV vs NHE at –10 mA cm^{-2} still makes it unattractive for any applications.

Acknowledgements

First and foremost, I would like to thank Dr. Alexey Ganin for providing me with this opportunity and for the support and guidance along the way. I have learned a lot while working with you and become a much better researcher than I would be without you.

I would also like to thank my second supervisor Dr. Harry Miras for his help along the way and the collaborations. My placement in Tarragona, ICIQ was an incredible experience. I would like to thank Prof. Carles Bo for welcoming me to their group and Dr. Mireia Segado for all the help while trying to navigate the world of computational chemistry.

The staff at the school of chemistry: Karen and Finlay from the stores; John, the glassblower who kindly helped with all matters related to glassblowing – from fixing the Schlenk lines to making sure our stocks of tubes for ampoules never run out. Andy for the help with the Raman instrument when it was acting out and Claire, for the same, just with X-ray machines. Thank you all; you made my life and research easier.

I am extremely grateful to the members of the Ganin group, the ones that were here when I started and those that joined later and are still on their journey through the PhD. Jessica and James, thank you both for the help in the lab and the good times we had in the office. Zoey, Youyi, Yuanshen, and Santosh – thank you for the chats and laughs. I would also like to thank Sproules group members, whom we get to share the office with – Cailean and Jake for encouraging the 1st year me that things will get better, and Oddyseas for keeping the atmosphere in the office welcoming and fun. You all have made the life in the office incredibly enjoyable.

To the friends that I made on the first day of induction week – Catherine, Ignas and Leanne – thank you for being such wonderful companions. I am extremely lucky to have had you by my side during these 4 years. I do not know what I would have done without you, all those coffee breaks, lunches and dinner parties.

I would like to express my gratitude to my family. To my parents and sister for supporting me on this journey, thank you for believing in me and what I do. To my boyfriend, Evaldas, for his love, care and jokes that helped me get through the tough times and enjoy the good ones even more. Thank you for putting up with me when things got crazy and I was stressed, I know it was not easy on you.

Lastly, to the friends I made in Glasgow during my 4 years here and to my friends back at home – thank you all, you have helped me keep my sanity during these crazy times.

Abbreviations

CCUS	Carbon Capture, Utilisation and Storage
CV	Cyclic Voltammetry
CVD	Chemical Vapour Deposition
DFT	Density Functional Theory
ECSA	Electrochemically Active Surface Area
EDX	Energy Dispersive X-Ray Spectroscopy
HER	Hydrogen Evolution Reaction
j	Current Density
LSV	Linear Sweep Voltammetry
MWCNT	Multi-walled Carbon Nanotubes
NHE	Normal Hydrogen Electrode
NMP	*N*-Methyl-2-pyrrolidone
OER	Oxygen Evolution Reaction
PEM	Proton Exchange Membrane
PXRD	Powder X-ray Diffraction
rGO	Reduced Graphene Oxide
RHE	Reversible Hydrogen Electrode
SEM	Scanning Electron Microscopy
TMDC	Transition Metal Dichalcogenide
XPS	X-Ray Photoelectron Spectroscopy

Thesis Contributions

Some of the work undertaken in this thesis was performed in collaboration with others. The details of collaboration are listed below.

- SEM images and EDX spectra of all transition metal dichalcogenides were obtained by James Gallagher at the University of Glasgow.

Author's declaration

I declare that, except where explicit reference is made to the contribution of others, that this dissertation is the result of my own work and has not been submitted for any other degree at the University of Glasgow or any other institution.

Printed name: Liudvika Masaityte

Signature:

Publications and Conferences

The following manuscripts were published as a result of work undertaken over the course of this PhD:

- Fraser, J. P., **Masaityte, L.**, Zhang, J., Laing, S., Moreno-Lopez, J. C., McKenzie, A. F., McGlynn, J. C., Panchal, V., Graham, D., Kazakova, O., Pichler, T., MacLaren, D. A., Moran, D. A. J. & Ganin, A. Y. *Commun Mater.,* **1**, 48 (2020)

- Elliott, A., McAllister, J., **Masaityte, L**., Segado-Centellas, M., Long, L., Ganin., A.Y., Song, Y., Bo, C., Miras., M. N. *Chem. Commun.*, **58**, 6906-6909 (2022)

The following conferences were attended over the course of this PhD:

- RSC Solid State Chemistry Christmas Meeting 2019 (Liverpool, UK) – poster presentation

- RSC Solid State Chemistry Christmas Meeting 2021 (online) – Oral presentation

Table of Contents

1. Introduction

1.1. Hydrogen economy

In recent years, the climate crisis has been widely acknowledged. It is agreed that fossil fuel-based energy infrastructure is causing greenhouse gas emissions, which contributes to climate change. With the climate crisis becoming more acute, attention is turned towards 'clean' or 'green' energy. Renewable power sources such as solar, wind and hydropower have already been successfully used to harvest energy. However, these energy sources do not supply constant electricity, as it is dependent on weather conditions. With surges and downtime, the energy produced via renewable sources could be much better used if it was either stored or immediately converted into energy that can be stored in a different form.

Hydrogen appears to be the perfect solution. Even though it is not an energy source in itself, it complements the handling and storage of energy very well. Hydrogen is commonly referred to as an 'energy vector' as it allows us to store energy in the form of a chemical bond and release it on demand by using hydrogen in fuel cells. Hydrogen fuel cells are a clean energy source as the by-product of this fuel cell is water, which is a non-pollutant (Figure 1-1).[1] This makes hydrogen a desirable power source.

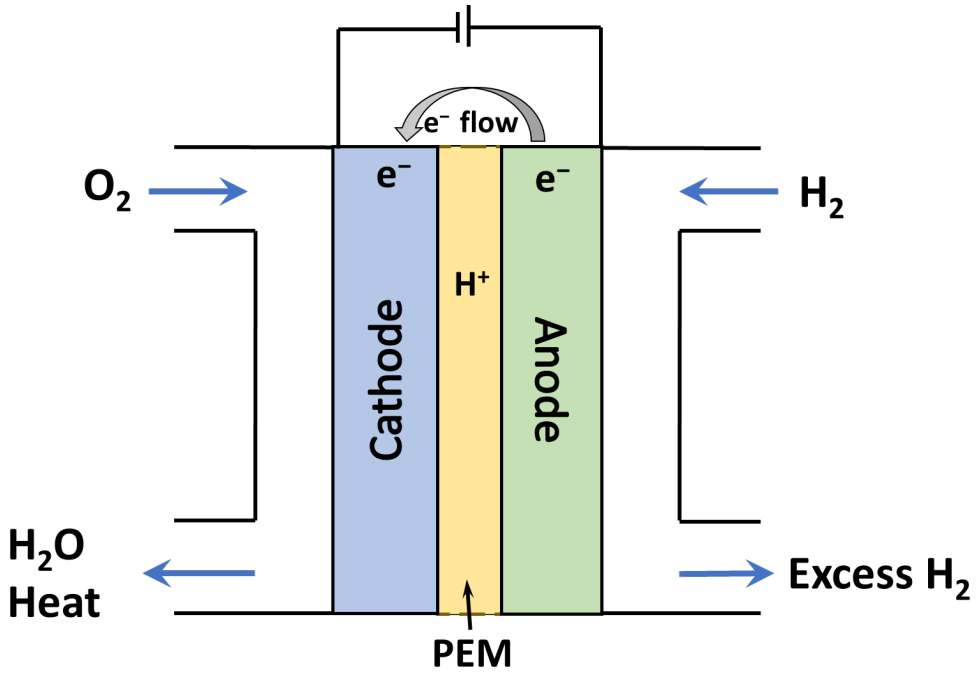

Figure 1-1. *Schematic representation of PEM hydrogen fuel cell.*

Multiple hydrogen production technologies, such as natural gas reforming, electrolysis, renewable liquid reforming, and fermentation, have been developing for decades. However, as of 2020, 80 % of the total hydrogen demand was met by hydrogen produced from fossil fuels.[2] This highly contributes to greenhouse gas emissions, defeating the purpose of hydrogen as a clean energy source.

Pairing hydrogen production via electrolysers with the use of clean, renewable energy sources produces genuinely 'green' hydrogen. However, only around 4 % of hydrogen is produced by electrolysers to this day. Electrolysers have another advantage as a technology for hydrogen production – considerably lower water consumption. Only 9 kg of water per kilogram of hydrogen is consumed in the electrolyser. For comparison, production from natural gas with Carbon Capture, Utilisation and Storage (CCUS) pushes water use to 13-18 kg H_2O per kg of H_2, while coal gasification jumps to 40-85 kg H_2O/kg H_2, depending on water consumption for coal mining.[2]

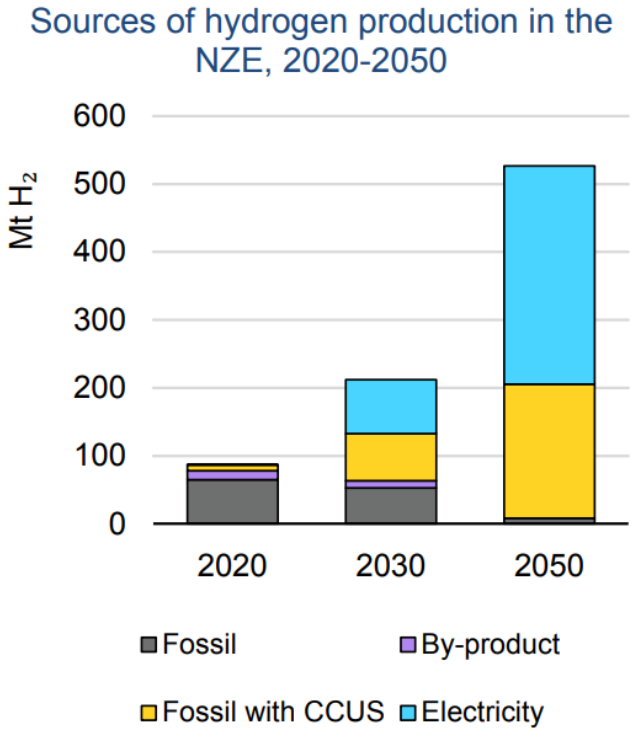

Figure 1-2. *Sources of hydrogen production in Net Zero Emission scenario. Source: IEA 2021 report.*[2]

In the net zero emission scenario, it is estimated that more than half of hydrogen demands will be satisfied by hydrogen from water electrolysers (Figure 1-2). Such a big emphasis is put on electrolysers as they are the key technology in reducing carbon footprint, hereby

placing the development and implementation of water electrolysers on an industrial scale in urgency.

1.2. Water electrolysis

Water electrolysis is a process of splitting water into its components – hydrogen and oxygen – using electric current. Hydrogen was first generated by water splitting using a direct current source as early as 1789 by van Troostwijk and Deiman.[3] Over 200 years later, water electrolysis has become a major research area. Water electrolysis can occur in alkaline and acidic environments; in each of them, it proceeds via slightly different routes. Nevertheless, the different methods presented here share the following overall reaction:

$$2\,H_2O\,(l) \rightarrow 2\,H_2\,(g) + O_2\,(g) \qquad (1)$$

It is also important to note that in recent years research efforts have been expanded to seawater electrolysis.[4,5] However, with that research field just picking up, we will focus on the two more established environments, acidic and alkaline, in the following sections.

1.2.1. Alkaline electrolysis

Alkaline electrolysers were the first water electrolysis systems to be scaled up to industrial levels. Large industrial-scale electrolysers were first installed in Norway in 1927. The schematics of a typical alkaline electrolyser are displayed in Figure 1-3. The cell consists of two electrodes, an anode and a cathode, separated by a diaphragm filled with alkaline solution (usually 30% KOH or 25% NaOH). In an alkaline medium, the overall reaction can be split into two half-reactions:

Cathode: $2\,H_2O\,(l) + 2\,e^- \rightarrow H_2\,(g) + 2\,OH^-\,(aq)$

Anode: $2\,OH^-\,(aq) \rightarrow H_2O\,(l) + 1/2\,O_2\,(g) + 2\,e^-$

When a sufficient electric current is applied to the electrodes, the water is split at the cathode, where it generates H_2 gas and releases OH^- ions. The hydroxide ions permeate through the diaphragm, release electrons at the anode, and combine to produce O_2. The separating diaphragm does not allow the gasses to pass through to the other side in high levels. The alkaline component of the electrolyte is not consumed during the process.

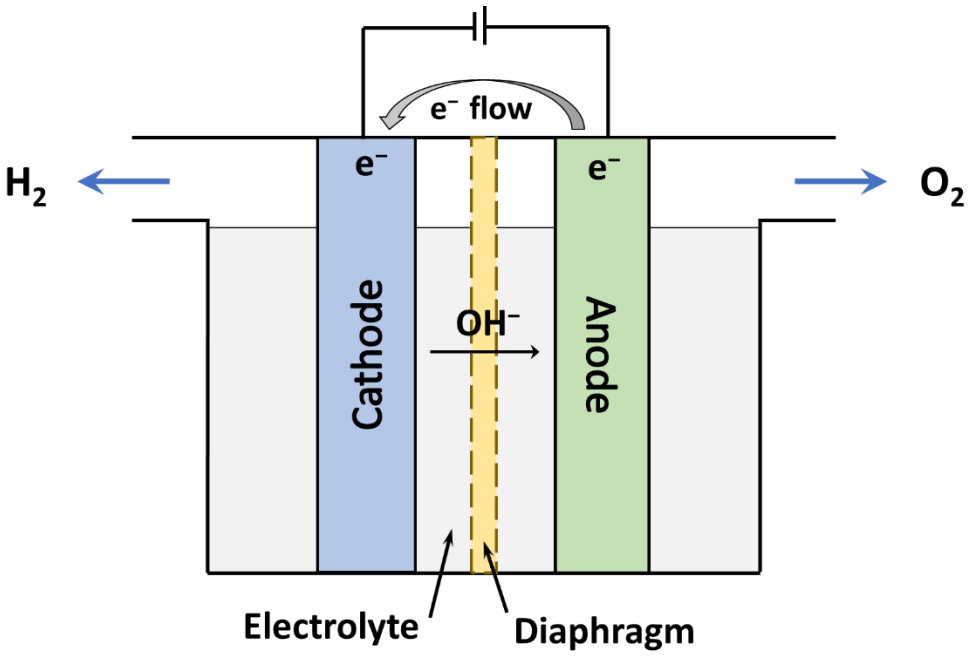

Figure 1-3. *Schematics of a conventional alkaline electrolyser.*

1.2.2. Acidic electrolysis

Research on acidic electrolysis picked up its pace after the introduction of the proton exchange membrane (PEM) and the development of the first PEM electrolysers. A typical PEM electrolyser is depicted in Figure 1-4. It consists of two electrodes, an anode, and a cathode, separated by a proton exchange membrane. Due to the no-gap design, PEM electrolysers are considerably smaller than conventional alkaline electrolysers. The cell is immersed in pure water, and the acidity comes from the PEM. In this type of electrolyser, the water is first split at the anode, where it forms O_2 and releases protons that then pass through the membrane and get reduced to H_2 at the cathode. This can be illustrated by two half-reactions:

Anode: $H_2O\,(l) \rightarrow 2\,H^+\,(aq) + 1/2\,O_2\,(g) + 2\,e^-$

Cathode: $2\,H^+\,(aq) + 2\,e^- \rightarrow H_2\,(g)$

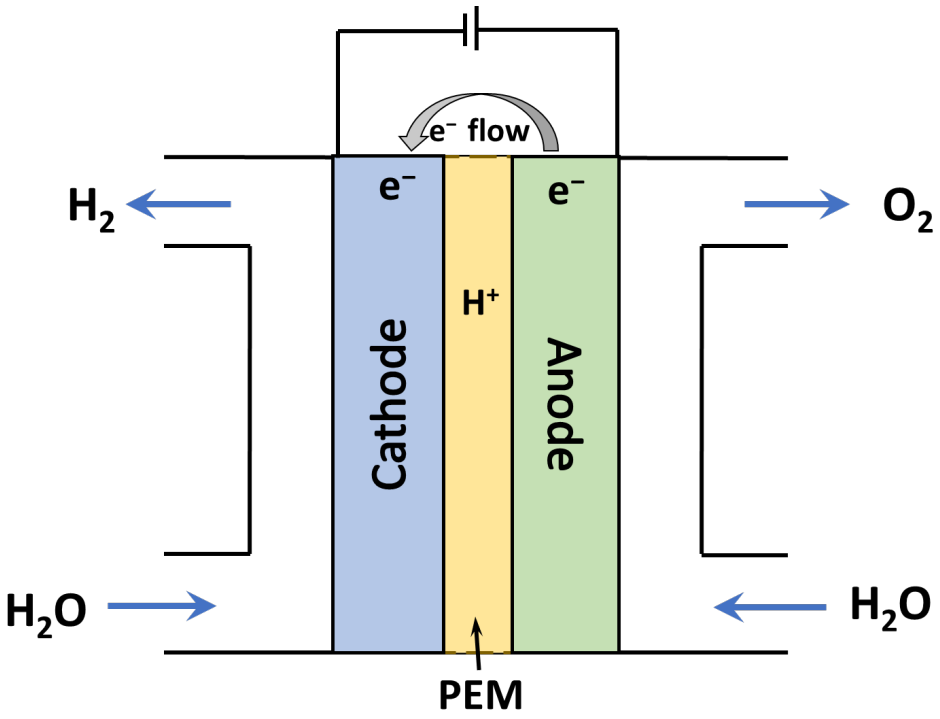

Figure 1-4. *Schematics of PEM electrolyser.*

The compact design of this system is not the only advantage. PEM electrolysers also operate at lower temperatures, are safer to operate (no handling of highly corrosive electrolytes is needed) and have lower power consumption.[6] However, PEM electrolysers are at a cost disadvantage compared to alkaline electrolysers. The success achieved with PEM electrolysers encouraged the search for the analogous membrane that would work in an alkaline setup. It is expected that with the discovery of a membrane that is as durable and reliable as PEM (i.e. Nafion), it would be possible to combine the alkaline and PEM electrolysis and reap the benefits of both systems, essentially lowering the overall costs of hydrogen production.

1.2.3. Thermodynamics of water electrolysis

The standard cell potential of water electrolysis is 1.23 V and is obtained by combining standard electrode potentials for the two half-reactions of water electrolysis. In acidic medium:

$$2\,H_2O \rightarrow O_2 + 4\,H^+ + 4e^- \qquad E^o_{anode} = -1.23\,V \quad (2)$$

$$4\,H^+ + 4\,e^- \rightarrow 2\,H_2 \qquad E^o_{cathode} = 0\,V \quad (3)$$

$$2\,H_2O \rightarrow 2\,H_2 + O_2 \qquad E^o_{cell} = -1.23\,V \quad (4)$$

In alkaline medium:

$$2\,OH^- \rightarrow H_2O + 1/2\,O_2 + 2\,e^- \qquad E^o_{anode} = -0.40\,V \quad (5)$$

$$2\,H_2O + 2\,e^- \rightarrow H_2 + 2\,OH^- \qquad E^o_{cathode} = -0.83\,V \quad (6)$$

$$2\,H_2O \rightarrow 2\,H_2 + O_2 \qquad E^o_{cell} = -1.23\,V \quad (7)$$

Standard potentials of the half-reactions are measured against the Normal Hydrogen Electrode (NHE). The theoretical potential for the NHE is defined as 0.00 V under standard temperature and pressure (298.15 K and 101.325 kPa). The identical E^o_{cell} value obtained in both acidic and alkaline medium is 1.23V. Even though pH impacts potential, in this case, the standard potentials of both half-cell reactions are affected equally. Therefore, the overall cell value remains constant. This can be easily illustrated via the Pourbaix diagram for water (Figure 1-5).

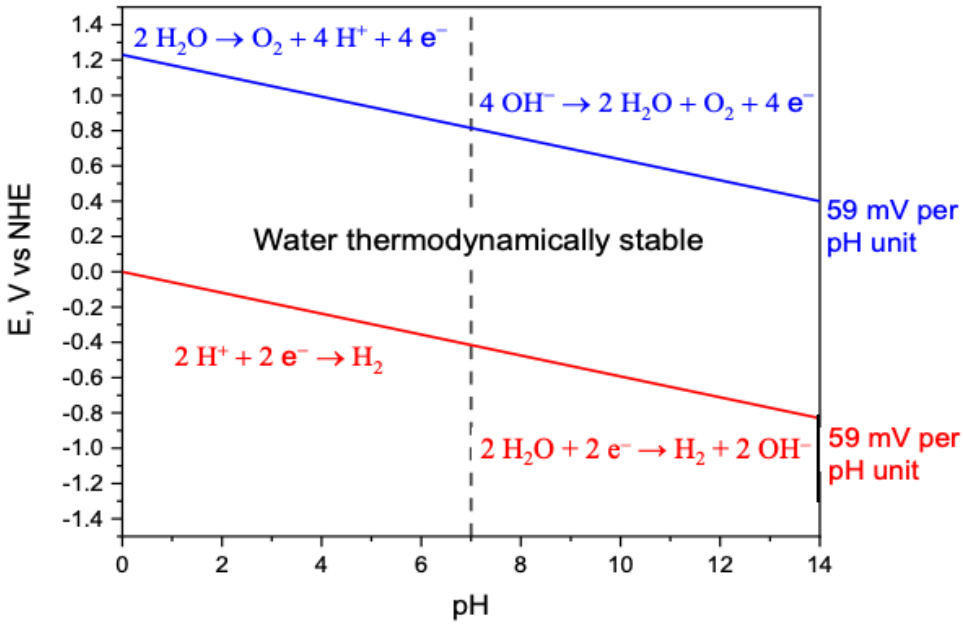

Figure 1-5. *Water Pourbaix diagram. Reproduced from K. Scott*[7].

The Gibbs free energy value of water electrolysis is related to the standard potential and can be calculated using the equation below:

$$\Delta G^o = \Delta H^o - T\Delta S^o = -nFE^o \qquad (8)$$

Where ΔG^o is the Gibbs energy; ΔH^o the standard enthalpy change (285.5 kJ mol^{-1}); ΔS^o is the standard entropy change (163 J K^{-1} mol^{-1}); n is the number of electrons in the half-reaction per mole of water split (n = 2); F is Faraday's constant (F = 96 500 C mol^{-1}); E^o is the standard potential in volts.

Gibbs energy value for water electrolysis is $\Delta G^o = +237\ kJ\ mol^{-1}$, meaning the process is nonspontaneous. This means that the cell needs external energy (in the form of heat) to keep the constant temperature. For an electrolyser cell to operate without losing any heat, it would require a potential of 1.48 V. This overpotential is called thermoneutral potential and can be calculated by rearranging equation (8).

The minimum potential of 1.23 V is not enough to drive a water electrolysis reaction in practice. Potentials higher than the minimum potential are needed. This additional potential is called an overpotential and will be discussed further in the following section.

1.2.4. Overpotential

The overpotential is a difference between the thermodynamically required potential and the experimentally observed potential and is composed of three components:

$$\eta = \eta_a + \eta_c + \eta_{ir} \qquad (9)$$

Where η_a is the activation overpotential caused by rate-limiting steps, η_c is the overpotential caused by concentration differences in the bulk and electrode surface due to mass transport limitations, and η_{ir} is the ohmic overpotential caused by resistance in electrolyte and electrode surface. The η_c component of the overpotential can be minimised by stirring or vibrating the electrode and the solution to promote better mixing and aid detachment of the bubbles from the electrode. The η_{ir} component of overpotential can be minimised by using an electrolyte with maximum conductivity. Finally, the $\eta_a$component can be minimised by using catalysts. The η_a contributes the most to the total value of overpotential. Therefore, a further look will be taken into electrocatalysts for hydrogen evolution reaction (HER).

The commonly used benchmark current density for hydrogen evolution reaction (HER) catalysts is −10 mA cm^{-2} which corresponds to a solar-to-fuel device operating at ∼10% efficiency.[8]

1.2.5. Volcano plot analysis

According to Sabatier's principle, the energy of reaction intermediates' adsorption to the catalyst should be neither too strong nor too weak. If the energy is high (interaction between the catalyst and intermediate species is strong), reaction products do not desorb from the surface of the catalyst. However, if the energy is low (interactions are weak), reaction intermediates do not adsorb to the catalyst surface. In both cases the overall reaction rate is limited.[9]

In hydrogen evolution reaction it is the adsorption of hydrogen to the surface of the catalyst that must be 'just right'. Parsons developed a volcano-type plot where exchange current density is correlated to the heat of adsorption of hydrogen. It was noticed that exchange current density was highest for the metals that adsorbed hydrogen moderately well and lower for those that adsorbed hydrogen weakly or strongly. [10] In his work, Parsons claimed that the maximum exchange current density would be achieved when the standard free energy of adsorption of hydrogen on the electrode surface is neutral (equals zero). Following the works of Parsons, Trasatti has identified a trend which led to the identification of possible electrocatalysts for HER.[11] In his work, the correlation of HER exchange current density of various metals with their chemisorption energy for hydrogen (evaluated by hydride formation energy) was made. In the resulting plot, platinum was found to be at the apex of the plot (Figure 1-6). Multiple different representations of volcano plots for HER have been composed since.[12]

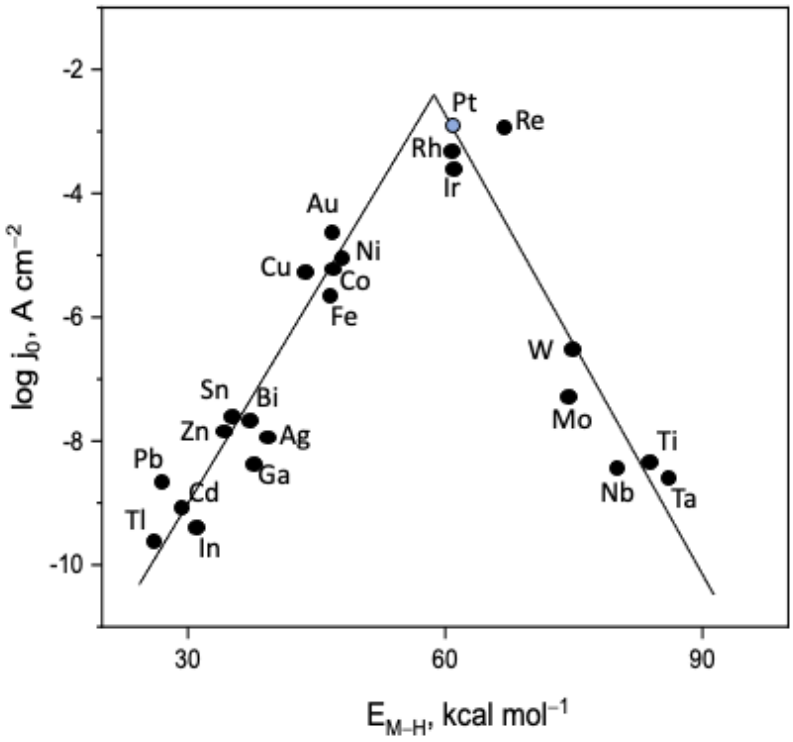

Figure 1-6. *Volcano plot proposed by Trasatti, where exchange current density is correlated with their chemisorption energy for hydrogen (evaluated by hydride formation energy). Figure reproduced from Trasatti*[11].

These days, the most common type of volcano plot for HER is one where exchange current density is correlated with calculated Gibbs free energies of the intermediates of the reaction. Hydronium adsorption and hydrogen gas desorption can be evaluated by calculating Gibbs free energy for hydrogen adsorption (ΔG_{H^*}).[13] For HER, the maximum reaction efficiency is achieved at the equilibrium potential when the free energy of hydrogen adsorption is close to zero.

1.2.6. Stability

Another important characteristic of a good electrocatalyst is its stability and durability. In acidic electrolysis, the catalyst must be capable of withstanding the corrosive environment of acid. Moreover, applied overpotential could further contribute to the decomposition of the catalyst material during the HER. While this may not be an issue for good electrocatalysts which require quite small overpotentials to drive hydrogen evolution reaction, electrocatalysts requiring high overpotentials might be placed in a further disadvantage as they would need to withstand higher reductive bias.

There are two common ways to determine the stability of an electrocatalyst - repetitive cyclic voltammetry (CV) and galvanostatic or potentiostatic electrolysis. In the cyclic voltammetry method, linear sweep curves before and after CV are compared, a number of CV cycles varies and can be as high as 5000 cycles. Little to no difference in these curves represent good stability of the catalyst. In galvanostatic or potentiostatic electrolysis a constant current or potential is applied for a period of time, usually more than 12 hours. Constant current or potential represents good stability.

1.2.7. Catalysts for hydrogen evolution reaction

As explained in previous sections, an overpotential is required to drive the water electrolysis reaction in practice. The majority of that overpotential can be reduced by using appropriate catalysts on both electrodes in the cell. This work focuses on one of the half-reactions – the hydrogen evolution reaction. Therefore, a brief look will be taken into the materials proposed as electrocatalysts for HER.

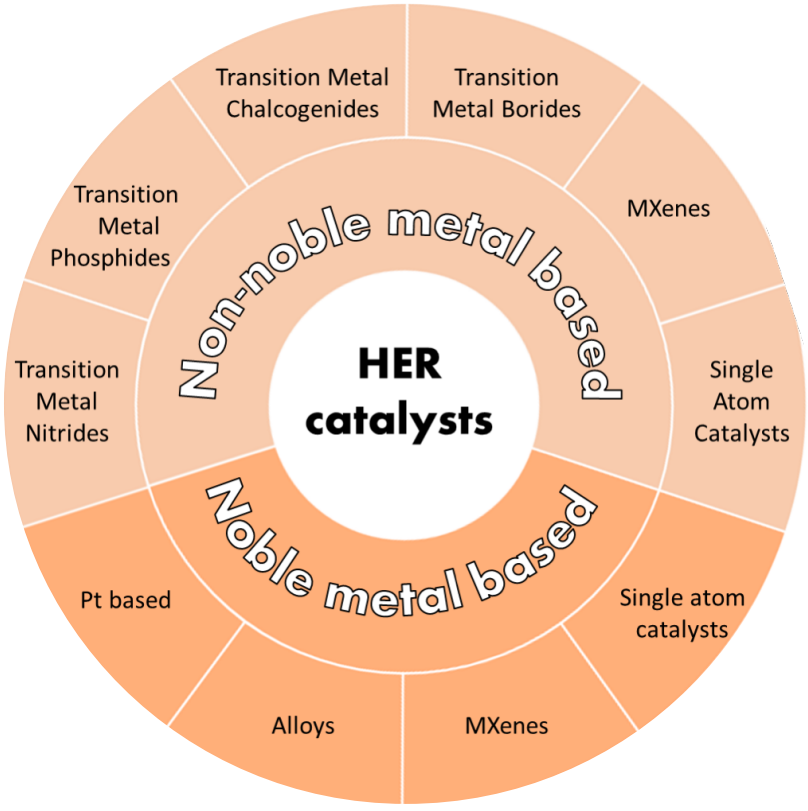

Figure 1-7. *A range of catalysts is being developed for use in electrolysers. The main groups and subgroups are displayed in this picture.*

As seen in Figure 1-7, there are two main groups of HER catalysts – noble metal based and non-noble metal based. The noble metal based catalysts, including Pt, are known as the best

electrocatalysts for HER. Developments on noble-metal catalysts focus on reducing the catalyst's loading while maximising efficiency in pursuit of cost reduction.[14]

The other group – non-noble metal based electrocatalysts consist of multiple subgroups such as transition metal phosphides, nitrides, and alloys, as well as MXenes and single-atom catalysts. In this group of catalysts, the research focus is on achieving efficiency and stability comparable to that of noble metal catalysts, as well as a reduction in the costs of production of the catalysts themselves. All subgroups are extensively researched, and promising results have been achieved.[15–22] In this work, we focus on transition metal dichalcogenides, a group of non-noble metal catalysts.

1.3. Transition metal dichalcogenides

Transition metal dichalcogenides (TMDCs) are layered compounds that attracted researchers' attention several decades ago (Figure 1-8). Since the rise of graphene, other 2D structures that were easier to manipulate to obtain desired properties have been investigated. TMDCs were one of the most attractive materials, as it was shown that their properties as single or multilayer compounds were dramatically different from their properties in a bulk state.[23–25] TMDCs, unlike graphene, are not inert; therefore, more strategies can be employed to tune the properties of these compounds, such as doping, defect and phase engineering.[26]

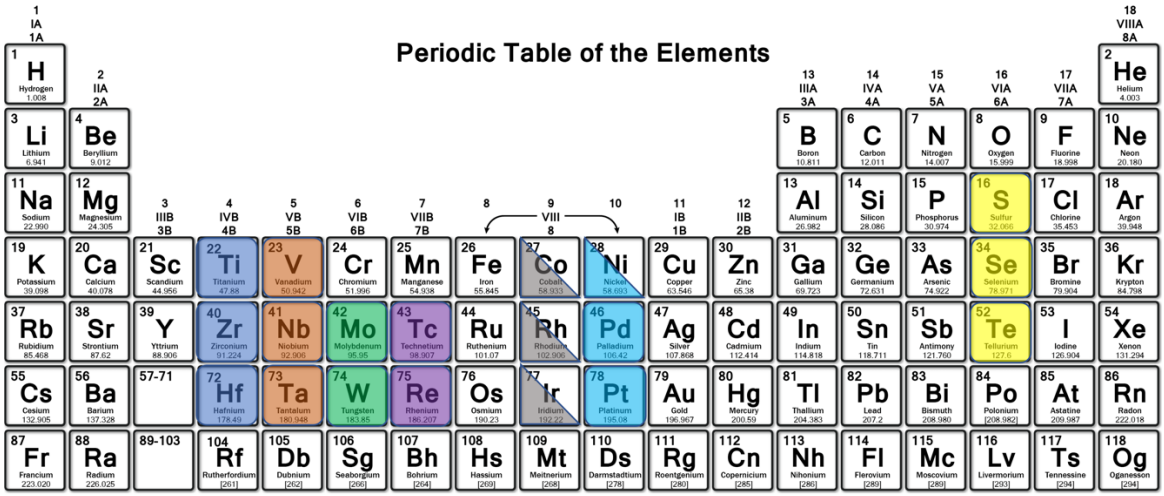

Figure 1-8. *The periodic table highlighting the transition metal atoms and chalcogens that predominantly form layered structures.*

Transition metal dichalcogenides are unlikely to complete with platinum in terms of catalytical activity and applications in conventional electrolysers at the present day. While transition metal dichalcogenides have been widely investigated as potential HER catalysts,

their performance rarely compares to that of noble metal catalysts. However, this does not discourage the research community, as TMDCs have found their place in HER catalysis for fundamental research instead of commercial applications.

1.3.1. Crystal and electronic structure of transition metal dichalcogenides

TMDCs are very interesting from a fundamental research perspective. The simple layered structure provides for easy surface determination. There are three main polymorphs in which TMDCs crystallise: 1T, 2H and 3R. The number indicates how many individual (non-repeating) layers are in a unit cell, and the letter indicates symmetry (T – trigonal, H – hexagonal, R – rhombohedral). The unit cell of these compounds is defined with the *c* axis perpendicular to the layers and *a* and *b* axes along the minimal chalcogen-chalcogen distance. Because of the hexagonal chalcogen packing and compact stacking of the layers, the interstitial sites can only be octahedral or tetrahedral in the Van der Waals gap. In 1T and 3R phases, the transition metal is in octahedral coordination within the layers and trigonal prismatic coordination in the 2H polymorph. Due to trigonal prismatic coordination in 2H polymorph, the chalcogen atoms within the layer are stacked in line with each other, wherein octahedral coordination, the chalcogen atoms from the same layer form a staggered structure, as illustrated in Figure 1-9.

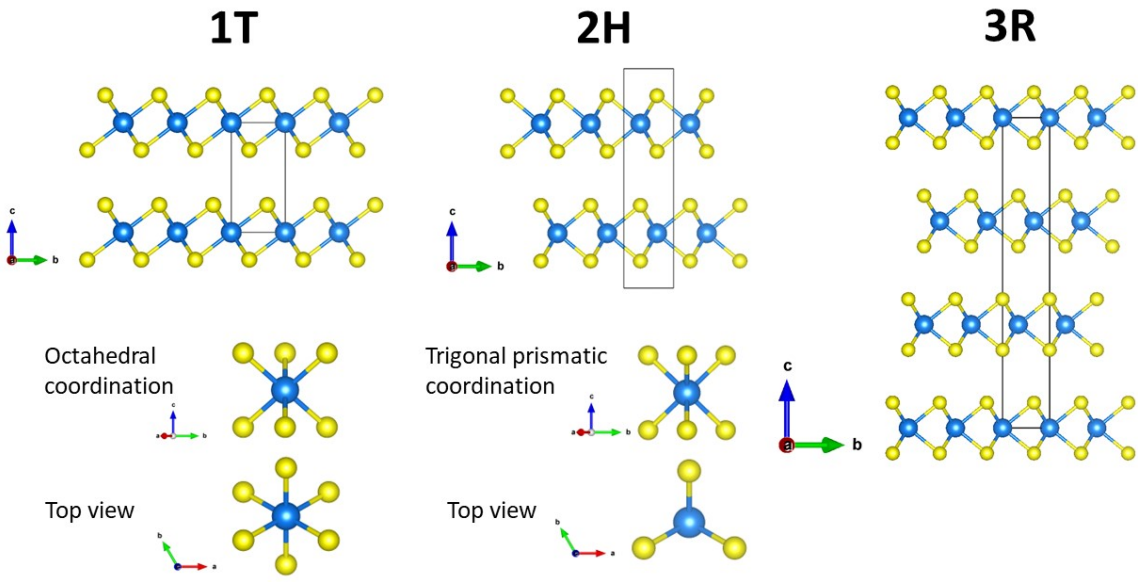

Figure 1-9. *Crystal structures of different polymorphs of TMDCs. The differences in transition metal coordination are shown with the side and top views displayed for clarity. Transition metal is represented in blue and chalcogen in yellow.*

In the 1T polymorph of TMDCs, the unit cell is composed of only one layer, as the layers in the bulk structure stack directly on top of each other, *i.e.* transition metal sits above the

transition metal in all layers, and all chalcogen atoms sit directly above the equivalent chalcogen atom in the layers. This stacking order can also be expressed as AbC AbC (upper case letters indicate the chalcogen, and lower-case letters indicate transition metal). When it comes to the 2H polymorph, there are three stacking sequences observed for this polymorph. The first one can be expressed as AbA CbC stacking. This means that the transition metals of neighbouring layers are in line with each other. Another stacking sequence observed in 2H polymorphs is CaC AcA, meaning that transition metal is aligned with two chalcogen atoms of the neighbouring layer. The last sequence reported for 2H polymorph is AbA CaC. Finally, the 3R structure has three layers in the unit cell. In the case of ordered structure, the stacking sequence is AbA BcB CaC, meaning that every layer is translated horizontally in reference to the neighbouring layer.

In some cases, for example, in group VI dichalcogenides, the 1T phase is distorted. Multiple distorted phases exist. The most common superstructures include zigzag chain formation (structure commonly called 1T'), tetramerization (also known as 1T''), and trimerization (also known as 1T'''). The 1T' phase is the most common, as it possesses the lowest formation energy for group VI dichalcogenides among other competing distorted structures.[27,28] The distortion of the 1T structure influences the electronic structure resulting in the 1T' phase displaying semi-metallic behaviour and 1T showing metallic behaviour. Due to the metastability of distorted phases, the structures are sometimes not carefully defined and frequently reported as 1T or metallic phases.[29–32]

The main difference between trigonal prismatic and octahedral polymorphs is their conductivity (except in group V materials, where both polymorphs express metallic behaviour). The differences arise from the coordination of the transition metal. In octahedral coordination, d orbitals split into two energy levels: lower level (orbitals d_{xy}, d_{yz} and d_{xz}) and higher level (orbitals d_{z^2} and $d_{x^2-y^2}$). In trigonal prismatic coordination d orbitals split into three different energy levels: lowest level (orbital d_{z^2}), middle (orbitals d_{xy} and $d_{x^2-y^2}$) and highest (orbitals d_{yz} and d_{xz}). The splitting of orbitals is illustrated in Figure 1-10. The Fermi level lies at the energy level of lower d orbitals in the octahedral polymorph. In trigonal prismatic coordination, it remains the same for group V dichalcogenides; however, group VI chalcogenides' Fermi level is higher than the lower d orbitals. Thus, making 1T phase of TMDCs semi-metallic and 2H phase semiconducting. Such generalisation should be taken with caution, as it is not uniformly accurate for all transition metal dichalcogenides, for example, group IV dichalcogenides TiS_2 and $TiSe_2$.

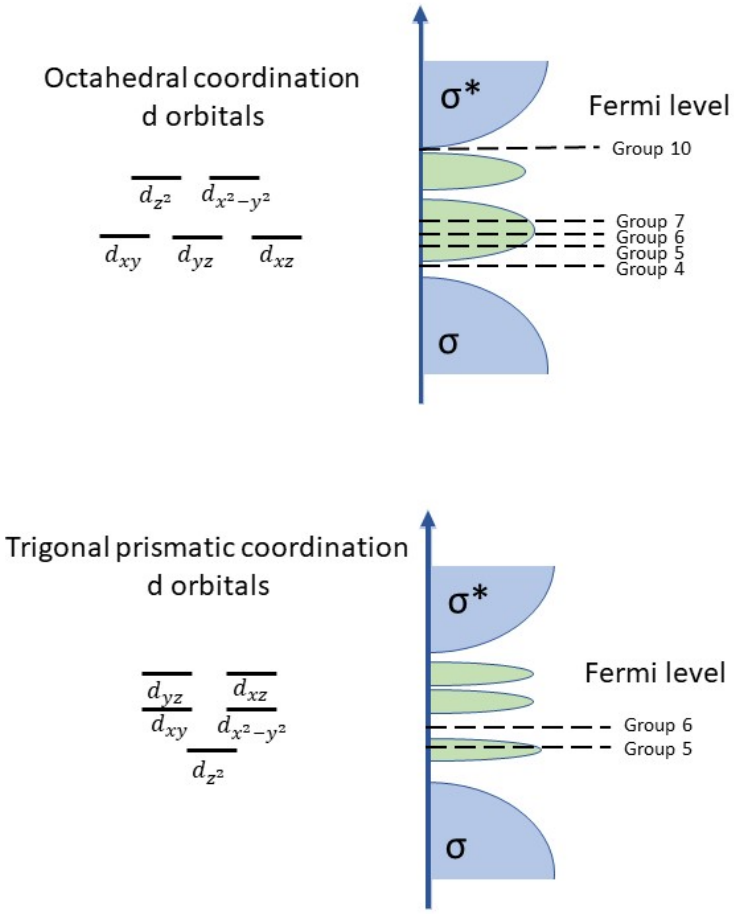

Figure 1-10. *The splitting of d orbitals in different coordination of transition metal. Corresponding energy levels and fermi levels are marked in a simplified electronic structure schematic.*

Interestingly, group IV dichalcogenide TiS_2 and its conductivity were disputed for decades as the experimental data, and computational studies pointed towards different answers. Experimentally, TiS_2 was thoroughly investigated, and many characteristics pointed toward TiS_2 being a semiconductor.[33] However, it was claimed that properties such as the Seebeck coefficient and resistivity were much easier to explain if TiS_2 was a metal.[34] DFT calculations backed the claim that TiS_2 was a semimetal in the early days of computational chemistry. However, in 2019 several computational studies came out, all independently claiming that TiS_2 is a small bandgap semiconductor and all experimental properties linked to semimetal behaviour arise from defects in this dichalcogenide.[35–37] Similar situation surrounds $TiSe_2$, which, despite all different claims, is considered a semiconductor.[38,39]

1.3.2. Morphology of TMDCs: basal planes and edge sites

Due to the layered nature of the structures, these compounds grow in platelet-like crystals, therefore providing a massive (with respect to the edges) flat surface area, which is also referred to as a basal plane and a much smaller area of edge sites (Figure 1-11).

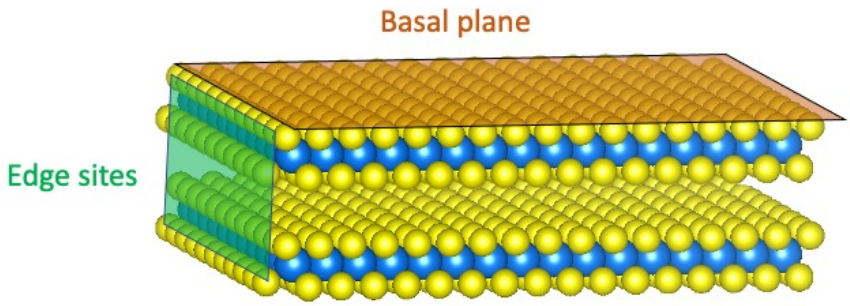

Figure 1-11. *Layered morphology of transition metal dichalcogenides with an indication of basal planes and edge sites. Transition metal is represented in blue and chalcogen in yellow. The plane in orange represents basal plane and the green plane represents edge sites.*

This renders layered compounds into perfect candidates for computational studies. They are easy to model as there are only two different surfaces. This is a huge advantage in the electrocatalysis field when trying to bridge the gap between computational models and catalyst performance in practice. The notorious platinum has a cubic structure, meaning it is hard to know which planes are exposed and contributing to electrocatalytic activity in practice. The same can be said for any cubic structured catalyst.

1.3.3. The catalytic activity of TMDCs: basal planes and edge sites

It has been theoretically predicted and later experimentally proved that in semiconducting polymorphs, the active sites of the transition metal dichalcogenides are in a relatively much smaller number of edge sites.[40] This led to research focused on edge site engineering and improving the catalytic activity of TMDCs through that. It was a challenging task, as the formation of basal planes is thermodynamically favourable due to the crystal structure.[41] However, multiple research groups have overcome the challenge. Kong *et al.* synthesised MoS_2 thin films with vertically aligned layers, maximising the exposure of edge sites of their thin films.[42] Kibsgaard *et al.* achieved a higher density of edge sites in their samples by synthesising double-gyroid MoS_2 by electrodeposition of Mo into a silica template followed by sulphuration with H_2S.[43] Another strategy to achieve a higher edge to basal plane ratio is nanostructuring of the material. In the case of MoS_2, this strategy has been reported to successfully increase the catalytic activity as early as 2013 by Xie *et al.*[44] Utilisation of a

hydrothermal synthesis route was proposed as a path to producing edge site rich materials on a bigger scale. The edge site engineering also meant increased surface area, which also contributed to the activity. Nevertheless, increased electrochemical activity was achieved via the utilisation of the techniques as mentioned above.

In recent years the focus has been shifted towards utilising the vast basal planes of TMDCs. The consensus has been reached that to unlock the full potential of TMDCs as electrocatalysts, basal planes should be utilised. To achieve that, multiple strategies have been developed in recent years. It can mainly be split into two categories: internal regulation and external regulation. The strategies include but are not limited to superlattice formation, doping, phase engineering, grain boundary formation and vacancy formation as means for internal regulation.[45–51] External regulation includes strain, electric field, heterostructures, and substrates.[52–56]

Whilst group VI dichalcogenides such as MoS_2 and WS_2 are thoroughly investigated, and most of the basal plane activation strategies are based on these compounds, literature on other transition metal dichalcogenides is lacking. With so much emphasis on the metallic 1T phase, one may find it surprising that systems naturally appearing in this structure have not been explored and widely reported. Group IV and V dichalcogenides can form a non-distorted 1T phase, which in some cases like TiS_2, $TiSe_2$ or VSe_2 is the thermodynamically stable structure. Thermodynamic stability should strongly benefit the research focused on the activity of basal planes of the metallic polymorphs.

1.3.4. Group IV TMDCs for HER

The first insights into group IV transition metal dichalcogenides as hydrogen evolution catalysts were reported by Toh *et al.* in their study of all nine compounds in this group.[57] In their study, the following trends in catalytic activity were observed and can be seen in Figure 1-12. For titanium dichalcogenides, the electrocatalytic activity was the same for TiS_2 and $TiTe_2$, whilst $TiSe_2$ showed slight improvement. Zirconium disulphide and diselenide had electrocatalytic performance with negligible differences, and ditelluride performed the worst. Hafnium dichalcogenides showed a clear trend of increasing overpotential as we go down the chalcogen group. All overpotentials needed to achieve benchmark current density of -10 mA cm^{-2} were close to or over -1 V vs RHE.

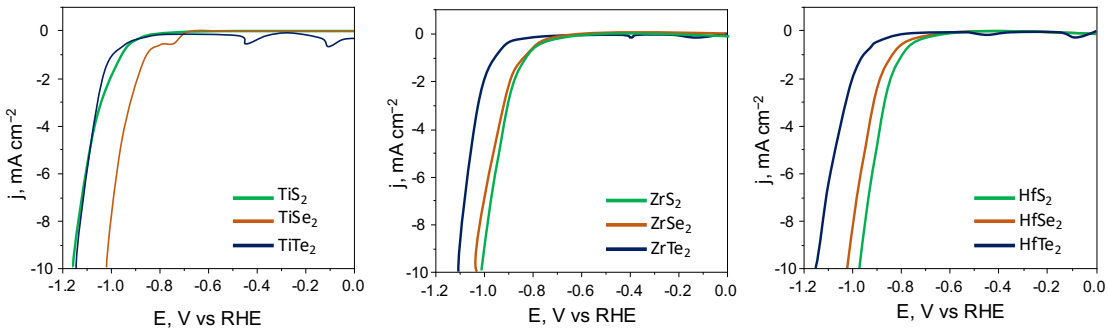

Figure 1-12. *Electrocatalytic activity of group IV dichalcogenides in an acidic environment. The effect of chalcogen is displayed for all three transition metals: titanium (a), zirconium (b), and hafnium (c). The figure reproduced from a study by Toh et al.*[57]

When the influence of transition metal is investigated, the following trends can be observed (Figure 1-13). Transition metal appears to impact the catalytic activity of sulphides, with the performance improving when going down the transition metal group. The transition metal did not affect the electrocatalytic activity of selenides. All of the samples showed the same overpotential. Lastly, similar to selenides, all tellurides showed similar activity towards HER.

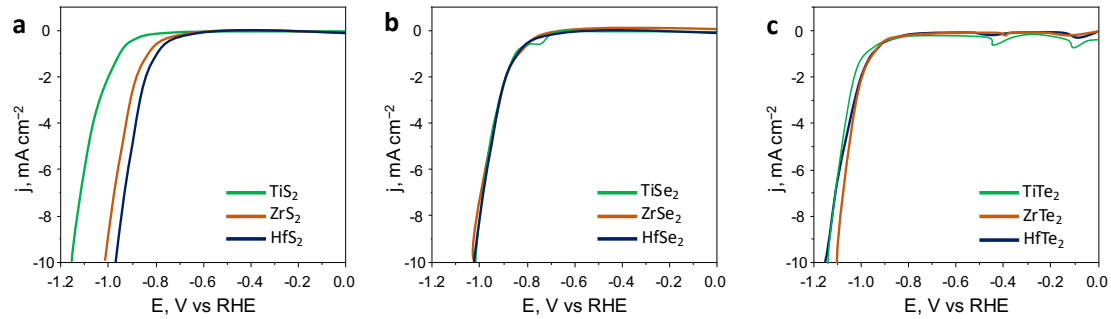

Figure 1-13. *Electrocatalytic activity of group IV dichalcogenides in an acidic environment. The effect of transition metal is displayed for all three chalcogens: sulphides (a), selenides (b), and tellurides (c). The figure reproduced from a study by Toh et al.*[57]

Powder X-ray diffraction (PXRD) indicated the compounds were all single phase, however, X-Ray photoelectron spectroscopy (XPS) analysis showed the presence of surface oxides in all sulphides, $TiSe_2$, and all tellurides. Sample composition determined by two methods in the study – energy dispersive X-ray spectroscopy (EDX) and XPS – reveals a high variation in metal to chalcogen ratio throughout the samples. Therefore, it is hard to tell if the catalytic activity is influenced by oxides, possible defects or whether it is genuine transition metal dichalcogenide activity. Nevertheless, the thorough study of all group IV chalcogenides is a valuable input to the topic and an excellent steppingstone for further investigations.

A highly contrasting report on the electrocatalytic activity of TiS_2 was published by Liu *et al.*[58] In their study, authors made TiS_2 with varying morphology – as nanosheets and quantum dots. Titanium disulphide nanosheets showed an overpotential of –350 mV vs RHE at a benchmark current density of −10 mA cm^{-2} and quantum dots needed only –245 mV vs RHE. Quantum dot samples were found to be partially oxidised from the XPS analysis of the samples, just as Toh *et al*. found their TiS_2 get oxidised as well. However, electrochemical activity reported by Liu *et al.* is much higher than it was shown in research conducted by Toh *et al.* XPS measurements carried out by Toh *et al.* on materials after electrochemical treatment revealed that oxide layer on TiS_2 persists even under reductive potentials.

$ZrSe_2$ was rendered into a plausible catalyst in a study conducted by Najafi *et al.*[59] In their work, bulk $ZrSe_2$ samples were exfoliated and further treated with microwaves. Exfoliated sheets reached benchmark current densities at an overpotential of –163 mV vs RHE. The presence of oxides in their sample was detected by XPS and XRD, indicating that the sample might be oxidised to a higher degree than just surface oxides. This overpotential could be highly impacted by oxides, as it was reported that bulk $ZrSe_2$ needs an overpotential of a little over –1V vs RHE to achieve benchmark current densities. No studies of the surface oxides were carried out on exfoliated $ZrSe_2$, therefore it is not known if surface oxides persist under reductive bias. While showing higher overpotentials towards HER, Toh *et al.* showed by XPS that their sample did not have any oxides before or after electrochemical treatments.

1.3.5. Group V TMDCs for HER

A study of a similar format as that of Toh *et al.* was carried out on group V dichalcogenides by Chia *et al*.[60] In their study, all nine group V dichalcogenides were synthesised, and their electrochemical properties were studied. The synthesised compounds were characterised by scanning electron microscopy (SEM), EDX and XPS. Electrochemical testing revealed high overpotentials needed to reach benchmark current densities for all compounds (approaching –1V vs RHE) apart from VTe_2. When the trends in electrocatalytic activity were investigated, the following trends emerged. Vanadium disulphide and diselenide showed very similar overpotential, whilst VTe_2 highly overperformed both with overpotentials close to –600 mV vs RHE. Amongst niobium compounds, $NbSe_2$ showed the best performance, however, the overpotentials of all niobium dichalcogenides were close to –1V vs RHE. Tantalum compounds expressed a trend of decreasing activity as we move down the chalcogen group. These trends are displayed in Figure 1-14.

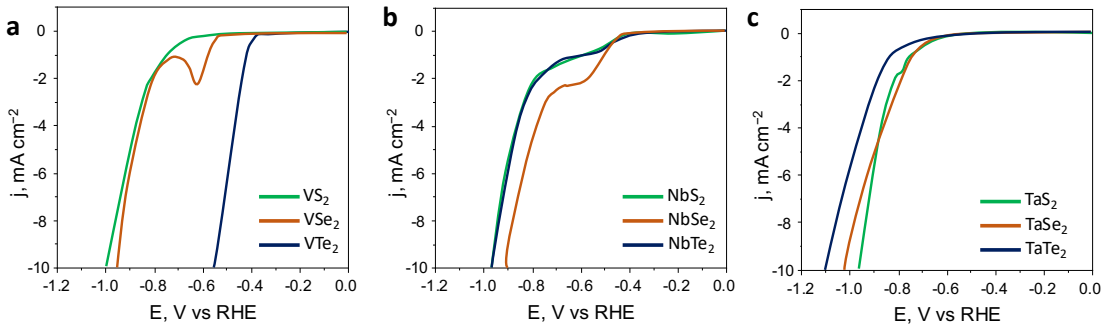

Figure 1-14. *Electrocatalytic activity of group V dichalcogenides in an acidic environment. The effect of chalcogen is displayed for all three transition metals: vanadium (a), niobium (b), and tantalum (c). The figure reproduced from a study by Chia et al.*[60]

Interestingly, when comparing all sulphide samples, they all show nearly identical electrocatalytic activity, with negligible differences in overpotential at benchmark current density. In selenide samples, $NbSe_2$ shows the best activity, closely followed by VSe_2 and $TaSe_2$. A clear trend of decreasing activity when going down the transition metal group can be seen in telluride samples. All these trends are displayed in Figure 1-15.

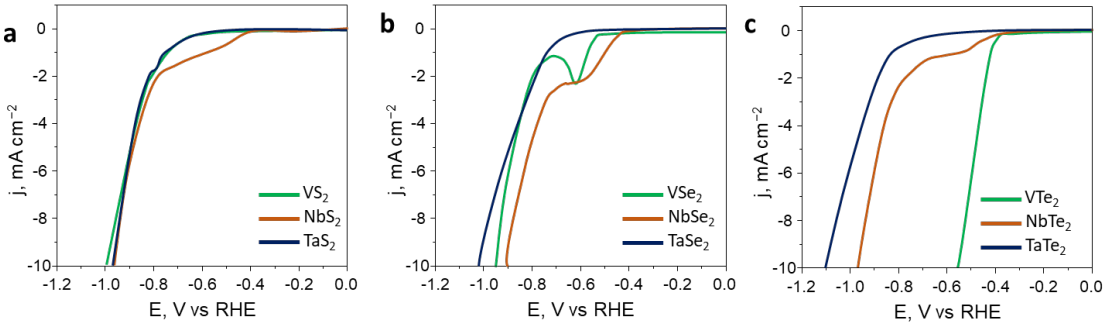

Figure 1-15. *Electrocatalytic activity of group V dichalcogenides in an acidic environment. The effect of transition metal is displayed for all three chalcogens: sulphides (a), selenides (b), and tellurides (c). The figure reproduced from a study by Chia et al.*[60]

No structural characterisation has been carried out on the samples in this study. SEM images showed that the majority of them displayed layered morphology, with VS_2, NbS_2 and $NbSe_2$ being exceptions. XPS analysis showed the presence of oxides in all dichalcogenide samples, and EDX analysis revealed a high distribution of stoichiometry. Stability tests on all catalysts in this work have been done by cycling the materials in an acidic environment for 100 cycles and comparing LSV curves before and after. Authors indicated that all compounds were found to be relatively stable, however, it is important to note that cycling was done in a smaller potential window where current densities reached only −0.1 mA cm^{-2}. Without phase

identification, the samples may have been composed of different polymorphs. In that case, a mixture of polymorphs may lead to inconclusive trends.

In a different study, Wang *et al.* synthesised and evaluated vanadium dichalcogenides and their lithium exfoliated counterparts for HER.[61] It was shown that electrocatalytic activity increased when going down the chalcogen group, with bulk VTe_2 samples having the lowest overpotential of just over –400 mV vs RHE (Figure 1-16 a). However, further investigation revealed that this overpotential dramatically increases in subsequent scans (Figure 1-16 b).

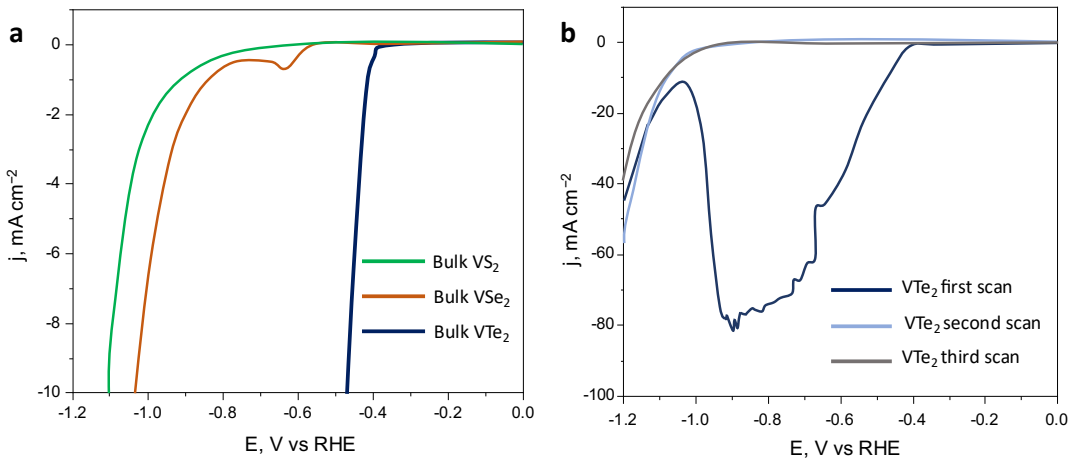

Figure 1-16. *Electrocatalytic activity of bulk vanadium dichalcogenides in acidic media (a). LSV scans of VTe_2 show an increase in overpotential in subsequent scans (b). Figure reproduced from a study by Wang et al.*[61]

The electrochemical activity of lithium exfoliated bulk chalcogenide counterparts showed reduced catalytic activity. The overpotentials were greater than those of bulk materials in the case of VSe_2 and VTe_2, with exfoliated VS_2 showing improvement in activity. The results contradict the usual trend of increased activity as material dimensions are lowered. However, the poorer performance could be explained by partial oxidation of samples during lithium exfoliation, as was proven by XPS and XRD. Moreover, the VS_2 did not follow this trend. Nevertheless, the bulk VS_2 could be identified as V_5S_8, which was further confirmed by EDX analysis of sample composition. The vanadium sulphide sample was also one that got destroyed the most during the exfoliation process, as not only oxides but also lithium vanadates could be detected by XRD. Stability studies on these materials have not been done.

Moreover, the overpotential of bulk VS_2 is dramatically higher than the overpotentials reported for nanostructured VS_2. Multiple researchers reported platinum-like activity for

nanostructures, and overpotentials in the range of –150 to –300 mV vs RHE was reported for hybrid materials.[62–65]

VS_2 is not the only one of vanadium sulphides that has dramatically varying overpotential values reported for HER. VSe_2 is another compound from this family with conflicting reports on its electrochemical activity. Bulk samples with varying compositions were prepared and investigated by Fu *et al.*[66] Their study showed that stoichiometric VSe_2 was the least active when compared to $VSe_{1.6}$ and $VSe_{1.8}$ (Figure 1-17). Interestingly, it still required only –247 mV vs RHE overpotential to drive HER. In contrast, the two previously discussed studies showed overpotentials of nearly –1000 mV vs RHE (at j = – 10 mA cm^{-2}) for this compound, also in the bulk form. An even lower overpotential was achieved for the non-stoichiometric vanadium diselenide with a composition of $VSe_{1.8}$; the sample reached benchmark current density at –160 mV vs RHE. The sample reached high current densities and demonstrated exceptional stability by maintaining a constant current density at applied overpotential for 48 hours.

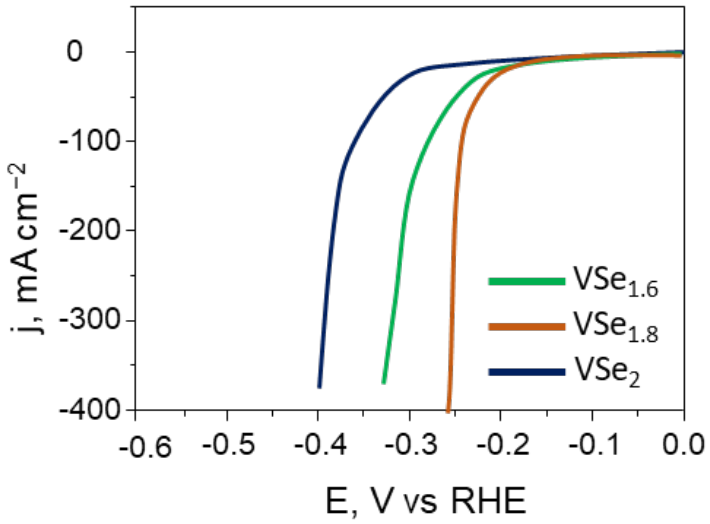

Figure 1-17. *Electrocatalytic activity of vanadium diselenide with a varying stoichiometry of the samples. Figure reproduced from a study by Fu et al.*

Wang *et al.* have successfully synthesised VSe_2 nanosheets and quantum dots.[67] The electrochemical activity of these morphologies of VSe_2 was investigated and revealed that the overpotential for nanosheets is –530 mV and –400 mV vs RHE for quantum dots. These overpotential values are in between the reported values for bulk materials. Moreover, quantum dots were found to be unstable, with overpotential increasing with each cycle.

A report on VTe_2 single crystals by Kwon *et al*. agrees with the initial values for benchmark overpotentials reported by Wang et al.[68] Single crystals produced by Kwon *et al*. needed an overpotential of just –441 mV vs RHE to drive HER. Since the study was carried out on single crystals, the majority of this activity was attributed to vast basal planes of the crystals. An improved overpotential (–216 mV vs RHE to drive HER) was demonstrated for VTe_2 nanosheets by Shi *et al.*[69] This reduction in overpotential when going from single crystal to nanosheet points towards the possibility to tune the electrochemical activity of this material by varying its thickness.

As we move down the group, the varying overpotentials reported for the same compound remain a characteristic. For example, NbS_2 flakes with a large lateral size have been reported to show an overpotential of –453 mV vs RHE by Kumar *et al.*[70] On the other hand, Yang *et al.* showed that their NbS_2 reached benchmark current density at an overpotential of –290 mV vs RHE.[71] Moreover, the researchers show that this performance can be further improved by Nb intercalation between the layers, with $Nb_{1.35}S_2$ showing lowered overpotential of –123 mV vs RHE. Incredibly high current densities can be achieved by this catalyst, as shown by the authors, to add, the catalyst shows exceptional stability by retaining its overpotential after 10 000 CV cycles. $NbSe_2$ was deemed an inefficient electrocatalyst in research by Toh *et al*., which we discussed at the beginning of this section. However, contrasting findings were reported by Zhao *et al*. and Wang *et al*., with the former reporting an overpotential of –450 mV vs RHE for hybrid nanobelts and the latter showing an overpotential of –22 mV vs RHE for porous nanosheets of $NbSe_2$.[72,73]

Tantalum dichalcogenides are no exception and, like other group V chalcogenides, have varying reports on their electrocatalytic activity toward HER. A study by Feng *et al*. explored all three polymorphs of TaS_2 and found that the 3R polymorph performed the best with an overpotential of only –196 mV vs RHE.[74] The other polymorphs required higher potentials to reach benchmark current densities: –475 mV vs RHE was needed for the 2H phase and –545 mV vs RHE for the 1T phase. In contrast, extremely low overpotential for 2H phase TaS_2 was reported by Shi *et al*.[75] Their TaS_2 flakes had overpotentials of –65 to –150 mV vs RHE depending on the thickness of the flakes. Moreover, the catalytic activity was found to increase with reductive cycling and was attributed to the reduction in flake size. Cycling has also been shown to improve the electrocatalytic performance of $TaSe_2$ in a study conducted by Wang *et al*.[76]

1.3.6. Group VI TMDCs for HER

Group VI is the group containing the most popular TMDC – MoS_2. The catalytic activity of molybdenum dichalcogenides and especially MoS_2 has been thoroughly studied. DFT calculations have shown that the activity of the edge sites of a semiconducting MoS_2 polymorph is much higher than that of the basal plane. This claim was based on the calculated values of the intermediate hydrogen adsorption to various active sites of MoS_2. Edge site values are close to thermoneutral, in contrast, basal planes were found almost inert as ΔG_{H*} values obtained were 10 times higher than those of edge sites. Exchange current density observed for MoS_2 edge sites in correlation with the aforementioned calculated ΔG_{H*} place it close to the upper part of the volcano plot as can be seen in Figure 1-18.[13]

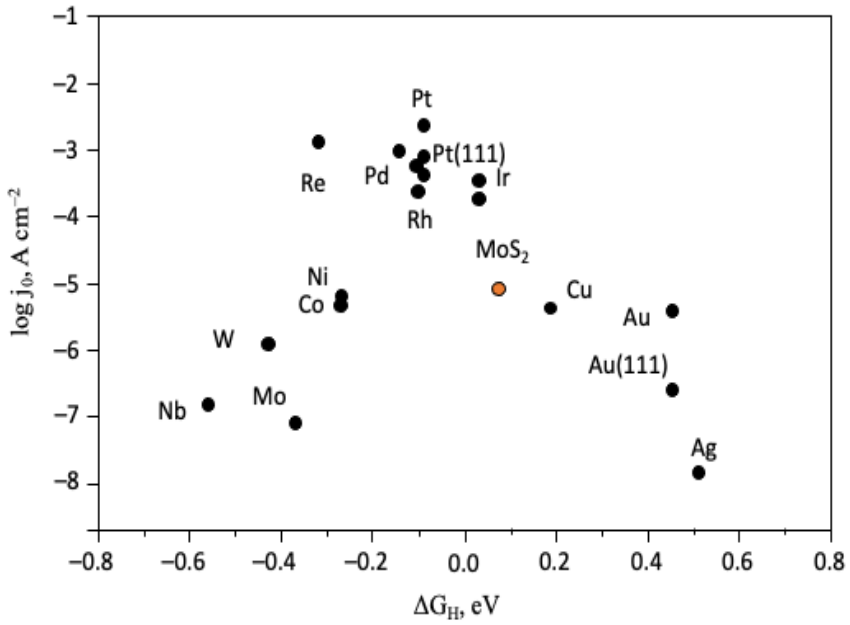

Figure 1-18. *Volcano plot of the exchange current density as a function of the DFT-calculated Gibbs free energy of adsorbed atomic hydrogen for nanoparticulate MoS_2 and the pure metals. Figure reproduced from Jaramillo et al.*[13]

Experimental data indicates that MoS_2 is a promising electrocatalyst, providing backing to the theoretical calculations (see Table 1-1). $MoTe_2$ is also one of the more popular electrocatalysts from the transition metal dichalcogenide group. Followed closely in popularity are tungsten dichalcogenides with 1T' WTe_2 showing promising performance toward HER.

Table 1-1. *Group VI transition metal dichalcogenides for HER.*

Sample	Overpotential at -10 mA cm^{-2}, mV vs RHE	Tafel slope, mV dec^{-1}	Ref
1T-MoS_2	352	72	[77]
1T-MoS_2	250	50	[71]
1T-WS_2	210	48	[71]
1T′-$MoTe_2$	340	78	[78]
1T′-$MoTe_2$	481	67	[79]
1T′-$MoTe_2$	480	N/A	[80]
1T′-$MoTe_2$	668	137	[68]
1T′-WTe_2	450	238	[81]
1T′-WTe_2	692	169	[68]

The less talked about and barely explored are chromium dichalcogenides. The main reason behind it is difficulties in synthesising layered structures of these compounds. Despite the challenges, CrS_2 flakes have been successfully synthesised by Su *et al*. via chemical vapour deposition (CVD).[82] A self-intercalated version of flakes was achieved by finely tuning the synthesis parameters, and the resulting flakes were investigated as electrocatalysts for HER. A decent overpotential of –260 mV vs RHE was achieved by CrS_2 flakes, and self-intercalated flakes showed an improved overpotential of only –151 mV vs RHE. The authors have also shown that this value can be further improved by engineering porous morphology.

The conflicting results across the literature urge comprehensive and careful studies that would answer the applicability of MX_2 (M = Ti, V, Cr; X = S, Se) as electrocatalysts for the hydrogen evolution reaction.

1.4. Aims

This thesis aims to evaluate the electrocatalytic activity of early transition metal dichalcogenides toward hydrogen evolution reaction. A strong emphasis in this study is put on crystal structures of compounds under investigation, as well as stoichiometry. Synthetic procedures are carefully tuned to achieve isostructural and stoichiometric samples of titanium, vanadium, chromium sulphides, and selenides. Achieved isostructural samples are then investigated to determine whether any trends in catalytic activity with the change of transition metal can be observed.

1.5. References

1. N. Sazali, W. N. W. Salleh, A. S. Jamaludin and M. N. M. Razali, New perspectives on fuel cell technology: A brief review, *Appl. Sci.*, 2020, **10**, 7708.

2. IAE, *Global Hydrogen Review 2021*, OECD, 2021.

3. S. Trasatti, Water electrolysis: Who first?, *J. Electroanal. Chem.*, 1999, **476**, 90–91.

4. J. Mohammed-Ibrahim and H. Moussab, Recent advances on hydrogen production through seawater electrolysis, *Mater. Sci. Energy Technol.*, 2020, **3**, 780–807.

5. M. A. Khan, T. Al-Attas, S. Roy, M. M. Rahman, N. Ghaffour, V. Thangadurai, S. Larter, J. Hu, P. M. Ajayan and M. G. Kibria, Seawater electrolysis for hydrogen production: A solution looking for a problem?, *Energy Environ. Sci.*, 2021, **14**, 4831–4839.

6. Y. Guo, G. Li, J. Zhou and Y. Liu, Comparison between hydrogen production by alkaline water electrolysis and hydrogen production by PEM electrolysis, *IOP Conf. Ser. Earth Environ. Sci.*, 2019, **371**, 042022.

7. K. Scott, *Introduction to Hydrogen, Electrolyzers and Fuel Cells Science and Technology*, Elsevier Ltd., 2022, vol. 4.

8. C. C. L. McCrory, S. Jung, I. M. Ferrer, S. M. Chatman, J. C. Peters and T. F. Jaramillo, Benchmarking Hydrogen Evolving Reaction and Oxygen Evolving Reaction Electrocatalysts for Solar Water Splitting Devices, *J. Am. Chem. Soc.*, 2015, **137**, 4347–4357.

9. G. Rothenberg, *Catalysis*, Wiley, 2008.

10. R. Parsons, The rate of electrolytic hydrogen evolution and the heat of adsorption of hydrogen, *Trans. Faraday Soc.*, 1958, **54**, 1053.

11. S. Trasatti, Work function, electronegativity, and electrochemical behaviour of metals: III. Electrolytic hydrogen evolution in acid solutions, *J. Electroanal. Chem. Interfacial Electrochem.*, 1972, **39**, 163–184.

12. J. K. Nørskov, T. Bligaard, A. Logadottir, J. R. Kitchin, J. G. Chen, S. Pandelov and U. Stimming, Trends in the Exchange Current for Hydrogen Evolution, *J. Electrochem. Soc.*, 2005, **152**, J23.

13. T. F. Jaramillo, K. P. Jørgensen, J. Bonde, J. H. Nielsen, S. Horch and I. Chorkendorff, Identification of Active Edge Sites for Electrochemical H_2 Evolution from MoS_2 Nanocatalysts, *Science*, 2007, **317**, 100–102.

14. D. Bhalothia, L. Krishnia, S.-S. Yang, C. Yan, W.-H. Hsiung, K.-W. Wang and T.-Y. Chen, Recent Advancements and Future Prospects of Noble Metal-Based Heterogeneous Nanocatalysts for Oxygen Reduction and Hydrogen Evolution Reactions, *Appl. Sci.*, 2020, **10**, 7708.

15. J. Cai, Y. Song, Y. Zang, S. Niu, Y. Wu, Y. Xie, X. Zheng, Y. Liu, Y. Lin, X. Liu, G. Wang and Y. Qian, N-induced lattice contraction generally boosts the hydrogen evolution catalysis of P-rich metal phosphides, *Sci. Adv.*, 2020, **6**, 1–9.

16. Z. Ge, B. Fu, J. Zhao, X. Li, B. Ma and Y. Chen, A review of the electrocatalysts on hydrogen evolution reaction with an emphasis on Fe, Co and Ni-based phosphides, *J. Mater. Sci.*, 2020, **55**, 14081–14104.

17. Y. Ren, Z. Li, B. Deng, C. Ye, L. Zhang, Y. Wang, T. Li, Q. Liu, G. Cui, A. M. Asiri, Y. Luo and X. Sun, Superior hydrogen evolution electrocatalysis enabled by CoP nanowire array on graphite felt, *Int. J. Hydrogen Energy*, 2022, **47**, 3580–3586.

18. B. Zhang, C. Xiao, S. Xie, J. Liang, X. Chen and Y. Tang, Iron-nickel nitride nanostructures in situ grown on surface-redox-etching nickel foam: Efficient and ultrasustainable electrocatalysts for overall water splitting, *Chem. Mater.*, 2016, **28**, 6934–6941.

19. Y. Sun, L. Wang, O. Guselnikova, O. Semyonov, J. Fraser, Y. Zhou, N. López and A. Y. Ganin, Revealing the activity of Co_3Mo_3N and $Co_3Mo_3N_{0.5}$ as electrocatalysts for the hydrogen evolution reaction, *J. Mater. Chem. A*, 2022, **10**, 855–861.

20. F. Song, W. Li, J. Yang, G. Han, P. Liao and Y. Sun, Interfacing nickel nitride and nickel boosts both electrocatalytic hydrogen evolution and oxidation reactions, *Nat. Commun.*, 2018, **9**, 4531.

21. Z. Ma, Z. Li, S. Li, P. Li and H. Zhang, Nanostructured Ni_2N thin films magnetron-sputtered on nickel foam as efficient electrocatalyst for hydrogen evolution reaction, *Mater. Lett.*, 2018, **229**, 148–151.

22. M. Jin, X. Zhang, R. Shi, Q. Lian, S. Niu, O. Peng, Q. Wang and C. Cheng, Hierarchical CoP@Ni_2P catalysts for pH-universal hydrogen evolution at high current density, *Appl. Catal. B Environ.*, 2021, **296**, 120350.

23. K. Synnatschke, P. A. Cieslik, A. Harvey, A. Castellanos-Gomez, T. Tian, C. J. Shih, A. Chernikov, E. J. G. Santos, J. N. Coleman and C. Backes, Length- And Thickness-Dependent Optical Response of Liquid-Exfoliated Transition Metal Dichalcogenides, *Chem. Mater.*, 2019, **31**, 10049–10062.

24. R.-S. Chen, C.-C. Tang, W.-C. Shen and Y.-S. Huang, Thickness-dependent electrical conductivities and ohmic contacts in transition metal dichalcogenides multilayers, *Nanotechnology*, 2014, **25**, 415706.

25. A. Ciarrocchi, A. Avsar, D. Ovchinnikov and A. Kis, Thickness-modulated metal-to-semiconductor transformation in a transition metal dichalcogenide, *Nat. Commun.*, 2018, **9**, 1–6.

26. A. Chaves, J. G. Azadani, H. Alsalman, D. R. da Costa, R. Frisenda, A. J. Chaves, S. H. Song, Y. D. Kim, D. He, J. Zhou, A. Castellanos-Gomez, F. M. Peeters, Z. Liu, C. L. Hinkle, S.-H. Oh, P. D. Ye, S. J. Koester, Y. H. Lee, P. Avouris, X. Wang and T. Low, Bandgap engineering of two-dimensional semiconductor materials, *npj 2D Mater. Appl.*, 2020, **4**, 29.

27. A. Singh, S. N. Shirodkar and U. V. Waghmare, 1H and 1T polymorphs, structural transitions and anomalous properties of (Mo,W)(S,Se)$_2$ monolayers: first-principles analysis, *2D Mater.*, 2015, **2**, 035013.

28. H. L. Zhuang, M. D. Johannes, A. K. Singh and R. G. Hennig, Doping-controlled phase transitions in single-layer MoS_2, *Phys. Rev. B*, 2017, **96**, 1–8.

29. D. Voiry, H. Yamaguchi, J. Li, R. Silva, D. C. B. Alves, T. Fujita, M. Chen, T. Asefa, V. B. Shenoy, G. Eda and M. Chhowalla, Enhanced catalytic activity in strained chemically exfoliated WS_2 nanosheets for hydrogen evolution, *Nat. Mater.*, 2013, **12**, 850–855.

30. Q. Liu, X. Li, Z. Xiao, Y. Zhou, H. Chen, A. Khalil, T. Xiang, J. Xu, W. Chu, X. Wu, J. Yang, C. Wang, Y. Xiong, C. Jin, P. M. Ajayan and L. Song, Stable Metallic 1T-WS_2 Nanoribbons Intercalated with Ammonia Ions: The Correlation between Structure and Electrical/Optical Properties, *Adv. Mater.*, 2015, **27**, 4837–4844.

31. Q. Liu, X. Li, Q. He, A. Khalil, D. Liu, T. Xiang, X. Wu and L. Song, Gram-Scale Aqueous Synthesis of Stable Few-Layered 1T-MoS_2: Applications for Visible-Light-Driven Photocatalytic Hydrogen Evolution, *Small*, 2015, **11**, 5556–5564.

32. B. Mahler, V. Hoepfner, K. Liao and G. A. Ozin, Colloidal synthesis of 1T-WS_2 and 2H-WS_2 nanosheets: Applications for photocatalytic hydrogen evolution, *J. Am. Chem. Soc.*, 2014, **136**, 14121–14127.

33. D. L. Greenaway and R. Nitsche, Preparation and optical properties of group IV–VI$_2$ chalcogenides having the CdI_2 structure, *Solid State Commun.*, 1965, **3**, 1445-1458.

34. A. H. Thompson, K. R. Pisharody and R. F. Koehler, Experimental Study Of Solid-Solutions $Ti_XTa_{1-x}S_2$, *Phys. Rev. Lett.*, 1972, **29**, 163+.

35. A. Stoliaroff, C. Latouche and S. Jobic, Versatile electrical behavior of 1T-TiS_2 elucidated from a theoretical study, *Phys. Rev. B*, 2019, **99**, 1–7.

36. A. Stoliaroff, S. Jobic and C. Latouche, Optoelectronic Properties of TiS_2: A Never Ended Story Tackled by Density Functional Theory and Many-Body Methods, *Inorg. Chem.*, 2019, **58**, 1949–1957.

37. H. Wang, Z. Qiu, W. Xia, C. Ming, Y. Han, L. Cao, J. Lu, P. Zhang, S. Zhang, H. Xu and Y. Y. Sun, Semimetal or Semiconductor: The Nature of High Intrinsic Electrical Conductivity in TiS_2, *J. Phys. Chem. Lett.*, 2019, **10**, 6996–7001.

38. J. C. E. Rasch, T. Stemmler, B. Müller, L. Dudy and R. Manzke, 1T-$TiSe_2$: Semimetal or semiconductor?, *Phys. Rev. Lett.*, 2008, **101**, 2–5.

39. M. M. May, C. Brabetz, C. Janowitz and R. Manzke, Charge-density-wave phase of 1T-$TiSe_2$: The influence of conduction band population, *Phys. Rev. Lett.*, 2011, **107**, 2–5.

40. G. Li, D. Zhang, Q. Qiao, Y. Yu, D. Peterson, A. Zafar, R. Kumar, S. Curtarolo, F. Hunte, S. Shannon, Y. Zhu, W. Yang and L. Cao, All the Catalytic Active Sites of MoS_2 for Hydrogen Evolution, *J. Am. Chem. Soc.*, 2016, **138**, 16632–16638.

41. A. Albu-Yaron, M. Levy, R. Tenne, R. Popovitz-Biro, M. Weidenbach, M. Bar-Sadan, L. Houben, A. N. Enyashin, G. Seifert, D. Feuermann, E. A. Katz and J. M. Gordon, MoS_2 Hybrid nanostructures: From octahedral to quasi-spherical shells within individual nanoparticles, *Angew. Chemie - Int. Ed.*, 2011, **50**, 1810–1814.

42. D. Kong, H. Wang, J. J. Cha, M. Pasta, K. J. Koski, J. Yao and Y. Cui, Synthesis of MoS_2 and $MoSe_2$ films with vertically aligned layers, *Nano Lett.*, 2013, **13**, 1341–1347.

43. J. Kibsgaard, Z. Chen, B. N. Reinecke and T. F. Jaramillo, Engineering the surface structure of MoS_2 to preferentially expose active edge sites for electrocatalysis, *Nat. Mater.*, 2012, **11**, 963–969.

44. J. Xie, H. Zhang, S. Li, R. Wang, X. Sun, M. Zhou, J. Zhou, X. W. Lou and Y. Xie, Defect-rich MoS_2 ultrathin nanosheets with additional active edge sites for enhanced electrocatalytic hydrogen evolution, *Adv. Mater.*, 2013, **25**, 5807–5813.

45. Z. Jiang, W. Zhou, A. Hong, M. Guo, X. Luo and C. Yuan, MoS_2 Moiré Superlattice for Hydrogen Evolution Reaction, *ACS Energy Lett.*, 2019, 2830–2835.

46. P. Liu, J. Zhu, J. Zhang, P. Xi, K. Tao, D. Gao and D. Xue, P Dopants Triggered New Basal Plane Active Sites and Enlarged Interlayer Spacing in MoS_2 Nanosheets toward Electrocatalytic Hydrogen Evolution, *ACS Energy Lett.*, 2017, **2**, 745–752.

47. D. Gao, B. Xia, C. Zhu, Y. Du, P. Xi, D. Xue, J. Ding and J. Wang, Activation of the $MoSe_2$ basal plane and Se-edge by B doping for enhanced hydrogen evolution, *J. Mater. Chem. A*, 2018, **6**, 510–515.

48. S. S. Chee, H. Jang, K. Lee and M. H. Ham, Substitutional Fluorine Doping of Large-Area Molybdenum Disulfide Monolayer Films for Flexible Inverter Device Arrays, *ACS Appl. Mater. Interfaces*, 2020, **12**, 31804–31809.

49. W. Xiao, P. Liu, J. Zhang, W. Song, Y. P. Feng, D. Gao and J. Ding, Dual-Functional N Dopants in Edges and Basal Plane of MoS_2 Nanosheets Toward Efficient and Durable Hydrogen Evolution, *Adv. Energy Mater.*, 2017, **7**, 1602086.

50. J. Pető, T. Ollár, P. Vancsó, Z. I. Popov, G. Z. Magda, G. Dobrik, C. Hwang, P. B. Sorokin and L. Tapasztó, Spontaneous doping of the basal plane of MoS_2 single layers through oxygen substitution under ambient conditions, *Nat. Chem.*, 2018, **10**, 1246–1251.

51. J. Xie, J. Zhang, S. Li, F. Grote, X. Zhang, H. Zhang, R. Wang, Y. Lei, B. Pan and Y. Xie, Controllable disorder engineering in oxygen-incorporated MoS_2 ultrathin nanosheets for efficient hydrogen evolution, *J. Am. Chem. Soc.*, 2013, **135**, 17881–17888.

52. Y. Zhou, J. V. Pondick, J. L. Silva, J. M. Woods, D. J. Hynek, G. Matthews, X. Shen, Q. Feng, W. Liu, Z. Lu, Z. Liang, B. Brena, Z. Cai, M. Wu, L. Jiao, S. Hu, H. Wang, C. M. Araujo and J. J. Cha, Unveiling the Interfacial Effects for Enhanced Hydrogen Evolution Reaction on MoS_2/WTe_2 Hybrid Structures, *Small*, 2019, **15**, 1–11.

53. M. S. Islam, M. Kim, X. Jin, S. M. Oh, N. S. Lee, H. Kim and S. J. Hwang, Bifunctional 2D Superlattice Electrocatalysts of Layered Double Hydroxide-Transition Metal Dichalcogenide Active for Overall Water Splitting, *ACS Energy Lett.*, 2018, **3**, 952–960.

54. F. L. Ling, T. W. Zhou, X. Q. Liu, W. Kang, W. Zeng, Y. X. Zhang, L. Fang, Y. Lu and M. Zhou, Electric field tuned MoS_2/metal interface for hydrogen evolution catalyst from first-principles investigations, *Nanotechnology*, 2018, **29**, 03LT01.

55. K. Jiang, M. Luo, Z. Liu, M. Peng, D. Chen, Y.-R. Lu, T.-S. Chan, F. M. F. de Groot and Y. Tan, Rational strain engineering of single-atom ruthenium on nanoporous MoS_2 for highly efficient hydrogen evolution, *Nat. Commun.*, 2021, **12**, 1687.

56. H. Li, C. Tsai, A. L. Koh, L. Cai, A. W. Contryman, A. H. Fragapane, J. Zhao, H. S. Han, H. C. Manoharan, F. Abild-Pedersen, J. K. Nørskov and X. Zheng, Erratum: Activating and optimizing MoS_2 basal planes for hydrogen evolution through the formation of strained sulphur vacancies, *Nat. Mater.*, 2016, **15**, 364.

57. R. J. Toh, Z. Sofer and M. Pumera, Catalytic properties of group 4 transition metal dichalcogenides (MX_2; M = Ti, Zr, Hf; X = S, Se, Te), *J. Mater. Chem. A*, 2016, **4**, 18322–18334.

58. Y. Liu, C. Liang, J. Wu, T. Sharifi, H. Xu, Y. Nakanishi, Y. Yang, C. F. Woellne, A. Aliyan, A. A. Martí, B. Xie, R. Vajtai, W. Yang and P. M. Ajayan, Atomic Layered Titanium Sulfide Quantum Dots as Electrocatalysts for Enhanced Hydrogen Evolution Reaction, *Adv. Mater. Interfaces*, 2018, **5**, 1700895.

59. L. Najafi, S. Bellani, M. I. Zappia, M. Serri, R. Oropesa-Nuñez, A. Bagheri, H. Beydaghi, R. Brescia, L. Pasquale, D. V. Shinde, Y. Zuo, F. Drago, K. Mosina, Z. Sofer, L. Manna and F. Bonaccorso, Transition metal dichalcogenides as catalysts for the hydrogen evolution reaction: The emblematic case of "inert" $ZrSe_2$ as catalyst for electrolyzers , *Nano Sel.*, 2022, **3**, 1069–1081.

60. X. Chia, A. Ambrosi, P. Lazar, Z. Sofer and M. Pumera, Electrocatalysis of layered Group 5 metallic transition metal dichalcogenides (MX_2, M = V, Nb, and Ta; X = S, Se, and Te), *J. Mater. Chem. A*, 2016, **4**, 14241–14253.

61. Y. Wang, Z. Sofer, J. Luxa and M. Pumera, Lithium Exfoliated Vanadium Dichalcogenides (VS_2, VSe_2, VTe_2) Exhibit Dramatically Different Properties from Their Bulk Counterparts, *Adv. Mater. Interfaces*, 2016, **3**, 1–8.

62. J. K. Das, A. K. Samantara, A. K. Nayak, D. Pradhan and J. N. Behera, VS_2 an efficient catalyst for an electrochemical hydrogen evolution reaction in an acidic medium, *Dalt. Trans.*, 2018, **47**, 13792–13799.

63. J. Chen, Z. Tang, Z. Pan, W. Shi, Y. Wang, Z. Q. Tian and P. K. Shen, Template-free growth of spherical vanadium disulfide nanoflowers as efficient anodes for sodium/potassium ion batteries, *Mater. Des.*, 2020, **192**, 108780.

64. P. Mohan, J. Yang, A. Jena and H. Suk Shin, VS_2/rGO hybrid nanosheets prepared by annealing of VS_4/rGO, *J. Solid State Chem.*, 2015, **224**, 82–87.

65. W. Zhang, X. Chen, J. Zhang, C. Tuo, L. Ji, H. Li, X. Zhang and F. Yang, Exposure of active edge structure for electrochemical H_2 evolution from VS_2/MWCNTs hybrid catalysts, *Int. J. Hydrogen Energy*, 2018, **43**, 22949–22954.

66. J. Fu, R. Ali, C. Mu, Y. Liu, N. Mahmood, W.-M. Lau and X. Jian, Large-scale preparation of 2D VSe_2 through a defect-engineering approach for efficient hydrogen evolution reaction, *Chem. Eng. J.*, 2021, **411**, 128494.

67. C. Wang, M. Jin, D. Liu, F. Liang, C. Luo, P. Li, C. Cai, H. Bi, X. Wu and Z. Di, VSe_2 quantum dots with high-density active edges for flexible efficient hydrogen evolution reaction, *J. Phys. D. Appl. Phys.*, 2021, **54**, 214006.

68. H. Kwon, D. Bae, H. Jun, B. Ji, D. Won, J.-H. Lee, Y.-W. Son, H. Yang and S. Cho, Basal-Plane Catalytic Activity of Layered Metallic Transition Metal Ditellurides for the Hydrogen Evolution Reaction, *Appl. Sci.*, 2020, **10**, 3087.

69. J. Shi, Y. Huan, X. Zhao, P. Yang, M. Hong, C. Xie, S. Pennycook and Y. Zhang, Two-Dimensional Metallic Vanadium Ditelluride as a High-Performance Electrode Material, *ACS Nano*, 2021, **15**, 1858–1868.

70. H. Kumar, K. Wang, F. Tang, X. Zeng, L. Gan and Y. Su, Unveiling active sites by structural tailoring of two-dimensional niobium disulfide for improved electrocatalytic hydrogen evolution reaction, *Int. J. Energy Res.*, 2020, **44**, 10551–10561.

71. J. Yang, A. R. Mohmad, Y. Wang, R. Fullon, X. Song, F. Zhao, I. Bozkurt, M. Augustin, E. J. G. Santos, H. S. Shin, W. Zhang, D. Voiry, H. Y. Jeong and M. Chhowalla, Ultrahigh-current-density niobium disulfide catalysts for hydrogen evolution, *Nat. Mater.*, 2019, **18**, 1309–1314.

72. B. Zhao, J. Huang, Q. Fu, L. Yang, J. Zhang and B. Xiang, MoS_2/$NbSe_2$ Hybrid Nanobelts for Enhanced Hydrogen Evolution, *J. Electrochem. Soc.*, 2016, **163**, H384–H387.

73. J. Wang, X. Liu, Y. Liu and G. Yang, Active Pore-Edge Engineering of Single-Layer Niobium Diselenide Porous Nanosheets Electrode for Hydrogen Evolution, *Nanomaterials*, 2019, **9**, 751.

74. Y. Feng, S. Gong, E. Du, X. Chen, R. Qi, K. Yu and Z. Zhu, 3R TaS 2 Surpasses the Corresponding 1T and 2H Phases for the Hydrogen Evolution Reaction, *J. Phys. Chem. C*, 2018, **122**, 2382–2390.

75. J. Shi, X. Wang, S. Zhang, L. Xiao, Y. Huan, Y. Gong, Z. Zhang, Y. Li, X. Zhou, M. Hong, Q. Fang, Q. Zhang, X. Liu, L. Gu, Z. Liu and Y. Zhang, Two-dimensional metallic tantalum disulfide as a hydrogen evolution catalyst, *Nat. Commun.*, 2017, **8**, 958.

76. M. Wang, L. Zhang, M. Huang, Y. Liu, Y. Zhong, J. Pan, Y. Wang and H. Zhu, Morphology-controlled Tantalum Diselenide Structures as Self-optimizing Hydrogen Evolution Catalysts, *ENERGY Environ. Mater.*, 2020, **3**, 12–18.

77. A. S. Goloveshkin, N. D. Lenenko, A. V. Naumkin, A. Y. Pereyaslavtsev, A. V. Grigorieva, A. V. Shapovalov, V. N. Talanova, A. V. Polezhaev, V. I. Zaikovskii, V. V. Novikov, A. A. Korlyukov and A. S. Golub, Enhancement of 1T-MoS_2 Superambient Temperature Stability and Hydrogen Evolution Performance by Intercalating a Phenanthroline Monolayer, *ChemNanoMat*, 2021, **7**, 447–456.

78. J. C. McGlynn, T. Dankwort, L. Kienle, N. A. G. Bandeira, J. P. Fraser, E. K. Gibson, I. Cascallana-Matías, K. Kamarás, M. D. Symes, H. N. Miras and A. Y. Ganin, The rapid electrochemical activation of $MoTe_2$ for the hydrogen evolution reaction, *Nat. Commun.*, 2019, **10**, 4916.

79. J. B. Mc Manus, G. Cunningham, N. McEvoy, C. P. Cullen, F. Gity, M. Schmidt, D. McAteer, D. Mullarkey, I. V. Shvets, P. K. Hurley, T. Hallam and G. S. Duesberg, Growth of 1T′ $MoTe_2$ by Thermally Assisted Conversion of Electrodeposited Tellurium Films, *ACS Appl. Energy Mater.*, 2019, **2**, 521–530.

80. R. J. Katz, Y. Zhu, Z. Mao and R. E. Schaak, Persistence and Evolution of Materials Features During Catalysis Using Topological and Trivial Polymorphs of $MoTe_2$, *ChemCatChem*, 2022, **14**, e2021017.

81. H. Yang, Y. Zhao, Q. Wen, R. Yang, Y. Liu, H. Li and T. Zhai, Single WTe_2 Sheet-Based Electrocatalytic Microdevice for Directly Detecting Enhanced Activity of Doped Electronegative Anions, *ACS Appl. Mater. Interfaces*, 2021, **13**, 14302–14311.

82. M. Su, W. Zhou, Z. Jiang, M. Chen, X. Luo, J. He and C. Yuan, Elimination of Interlayer Potential Barriers of Chromium Sulfide by Self-Intercalation for Enhanced Hydrogen Evolution Reaction, *ACS Appl. Mater. Interfaces*, 2021, **13**, 13055–13062.

2. Experimental methods

2.1. Synthesis

2.1.1. Degassed Na_2S

Sodium sulphide hydrate scales ($Na_2S \times xH_2O$, Sigma Aldrich) were loaded into a quartz tube. An open end of the tube was connected to the vacuum pump, and the other end was placed in the middle of the Carbolite tube furnace heating zone. The tube was slowly evacuated to 2×10^{-2} mbar before starting the heating programme. Whilst keeping the sample under dynamic vacuum, the furnace was heated to 700 °C (1 °C min^{-1} heating rate, 24 h dwell, natural cooling). It was made sure to always keep the sample under vacuum and only remove the product from the tube in an argon filled glove box. The resulting powders were light pink/grey in colour.

2.1.2. Synthesis of Na_xVS_2

$NaVS_2$ was always prepared in an argon-filled glove box (O_2 < 0.5 ppm) due to one of the precursors – Na_2S – being air and moisture sensitive. Stoichiometric amounts of sodium sulphide (prepared as mentioned above), elemental vanadium powder (Alfa Aesar, 99.5%, −325 mesh, metal basis) and elemental sulphur (May and Baker ltd, sublimed) were ground together using a mortar and pestle and loaded into a Pyrex tube. The tube was then evacuated to 1.6×10^{-3} mbar and sealed under vacuum using a propane/oxygen torch. The ampoule was gently shaken to homogenise the mixture further and placed upright in the furnace. The sample was then heated to 600 °C (1 °C min^{-1} heating, 72 h dwell, natural cooling) in a Lenton box furnace. To determine the single-phase regions, samples of the following stoichiometries were synthesised: $Na_{0.7}VS_2$, $Na_{0.8}VS_2$, $NaVS_2$, $Na_{1.1}VS_2$, $Na_{1.2}VS_2$, $Na_{1.5}VS_2$. Reannealing of the samples was done at 600 °C (5 °C min^{-1} heating, 24 h dwell, natural cooling) and later was deemed unnecessary. The nominal composition of $Na_{0.7}VS_2$ was routinely used in the synthesis of VS_2-Na samples. Synthesis was carried out on a 400-600 mg scale.

2.1.3. Synthesis of $LiVS_2$

$LiVS_2$ was always prepared in an argon-filled glove box due to lithium sulphide being air sensitive. Stoichiometric amounts of lithium sulphide (Alfa Aesar, 99.9%), elemental vanadium powder (Alfa Aesar, 99.5%, −325 mesh, metal basis) and elemental sulphur (May and Baker ltd, sublimed) were ground together using a mortar and pestle and loaded into a quartz tube. The tube was then evacuated to 1.6×10^{-3} mbar and sealed using a propane/oxygen torch. The ampoule was gently shaken to homogenise the mixture further

and placed upright in the furnace. The sample was then heated to 600 °C (1 °C min^{-1} heating, 72 h dwell, natural cooling). Synthesis was carried out on a 400-600 mg scale.

2.1.4. Synthesis of $LiTiS_2$

$LiTiS_2$ was always prepared in an argon-filled glove box due to lithium sulphide being air sensitive. Stoichiometric amounts of lithium sulphide (Alfa Aesar, 99.9%), elemental titanium powder (Alfa Aesar, 99.5%, –325 mesh, metal basis) and elemental sulphur (May and Baker ltd, sublimed) were ground together using a mortar and pestle and loaded into a quartz tube. The tube was then evacuated to 1.6×10^{-3} mbar and sealed using a propane/oxygen torch. The ampoule was gently shaken to homogenise the mixture further and placed upright in the furnace. The sample was then heated to 600 °C (1 °C min^{-1} heating, 72 h dwell, natural cooling). The product was then ground using mortar and pestle and reannealed at 600 °C (5 °C min^{-1} heating, 24 h dwell, natural cooling). Synthesis was carried out on a 400-600 mg scale.

2.1.5. Synthesis of $LiCrS_2$

$LiCrS_2$ was always prepared in an argon-filled glove box due to lithium sulphide being air sensitive. Stoichiometric amounts of lithium sulphide (Alfa Aesar, 99.9%), elemental chromium powder (Alfa Aesar, 99.5%, –200 mesh, metal basis) and elemental sulphur (May and Baker ltd, sublimed) were ground together using a mortar and pestle and loaded into a quartz tube. The tube was then evacuated to 1.6×10^{-3} mbar and sealed using a propane/oxygen torch. The ampoule was gently shaken to homogenise the mixture further and placed upright in the furnace. The sample was then heated to 600 °C (1 °C min^{-1} heating, 72 h dwell, natural cooling). The product was then ground using mortar and pestle and reannealed at 600 °C (5 °C min^{-1} heating, 24 h dwell, natural cooling). Synthesis was carried out on a 400-600 mg scale.

2.1.6. Synthesis of K_xCrSe_2

K_xCrSe_2 was always prepared and handled in an argon-filled glove box due to elemental K (Alfa Aesar, 99.9 %) being used in the synthesis and product of reaction being air sensitive. Stoichiometric amounts of K metal, Cr powder (Afa Aesar, 99.94 %, –200 mesh, metal basis) and Se shots (Alfa Aesar, 99.99 %, metal basis) were loaded into a Pyrex tube and sealed under vacuum using propane/oxygen torch. The ampoule was then placed upright in a Lenton box furnace. The sample was heated to 250 °C (1 °C min^{-1} heating) and pre-reacted at this temperature for 4 hours to avoid a violent reaction. Straight after this, the temperature was raised further to 600 °C (1 °C min^{-1} heating, 72 h dwell, natural cooling). Synthesis was carried out on a 400-600 mg scale and stoichiometry that was aimed for was K:Cr:Se = 1:1:2.

The sample was then taken out of the ampoule, ground using mortar and pestle and sealed under vacuum again for further reannealing at 600 °C (5 °C min^{-1} heating, 24 h dwell, natural cooling). Unlike vanadium alkali intercalates, re-annealing at 600 °C was necessary for K_xCrSe_2.

2.1.7. Alkali metal deintercalation

The same deintercalation procedure was applied for three compounds – $Na_{0.7}VS_2$, $LiVS_2$, $LiTiS_2$, $LiCrS_2$ and K_xCrSe_2. However, different iodine solution concentration had to be used for K_xCrSe_2. In a standard procedure for $Na_{0.7}VS_2$ and $LiVS_2$, ≈100 mg of powder was loaded into an air-tight vial with a septa lid in an argon-filled glove box. A magnetic stirrer bar was added to the vial and the septa lid was secured tight before taking the sample out of the glove box. The vial was then placed on a magnetic stirrer and ≈16 mL of 0.1M iodine solution in acetonitrile was introduced to the vial *via* syringe. The mixture was left to stir at room temperature for 48 hours.

The procedure was the same for K_xCrSe_2, however, a smaller scale was used and the routine deintercalation was carried out on ≈ 40 mg of powder using ≈ 18 mL 0.01M iodine solution. The product was then filtered and washed with acetonitrile first, then deionised water and ethanol and left to dry in a desiccator.

Iodine solution was prepared fresh before each deintercalation reaction and acetonitrile dried over molecular sieves was used to avoid sample exposure to moisture. The usual procedure involved dissolving 635 mg of Iodine lumps in 25 mL of dried acetonitrile. A lower concentration solution used for K_xCrSe_2 was prepared by dissolving 64 mg of Iodine lumps in 25 mL of dried acetonitrile.

2.1.8. Synthesis of TiS_2, $TiSe_2$, VSe_2

Stoichiometric amounts of metal powder – Ti (Alfa Aesar, 99.5 %, -325 mesh, metals basis) or V (Alfa Aesar, 99.5%, –325 mesh, metal basis) – and chalcogen (S or Se) were mixed together and sealed under vacuum in a Pyrex ampoule using a propane/oxygen torch. The samples were then heated to 600 °C (1 °C min^{-1} heating, 72 h dwell, natural cooling). After initial heating, the sample was taken out of the ampoule and ground using an agate mortar and pestle, then sealed in a Pyrex ampoule under vacuum again and reannealed at 600 °C (5 °C min^{-1} heating, 24 h dwell, natural cooling) Synthesis was carried out on a 400-600 mg scale.

2.1.9. Hydrothermal synthesis of VS_2

Firstly, the stock solution was prepared: Na_3VO_4 (Alfa Aesar, 99.9%, metals basis; 1.103 g, 6 mmol) and thioacetamide (Alfa Aesar, ACS, 99% min; 2.404 g, 32 mmol) were dissolved in deionised water (50 mL) and stirred for 1 h. The solution had no colour initially, however after some time, it turned very pale yellow and later transitioned into pale green colour. Secondly, 9 mL of stock solution was transferred into a stainless-steel autoclave with Teflon liner (20mL) and hydrothermally treated at 160 °C for 24 h. After cooling naturally to room temperature, the product was washed several times with deionized water and ethanol and dried in a desiccator overnight. The product was black in colour.

2.1.10. Synthesis of VS_4

Stoichiometric amounts of V (Alfa Aesar, 99.5%, –325 mesh, metal basis) and S were mixed and sealed under vacuum in a Pyrex ampoule using a propane/oxygen torch. The samples were then heated to 400 °C (1 °C min^{-1} heating, 48 h dwell, natural cooling). After initial heating, the sample was taken out of the ampoule and ground using an agate mortar and pestle. The sample was weighed before and after each heating step, and the loss of sulphur (sulphur could be seen on the inner walls of the reaction ampoule) was compensated for by adding the sulphur powder to the product before reannealing. Then, the mixture of product and sulphur powder was sealed in a Pyrex ampoule under vacuum again and reannealed at 400 °C (5 °C min^{-1} heating, 24 h dwell, natural cooling) two times with sample homogenisation and compensating for the loss of sulphur in between annealings. Synthesis was carried out on a 1g scale. To remove excess sulphur from the final product it was annealed under a dynamic vacuum at 200 °C for 30 minutes. The final product was homogenised using an agate mortar and pestle and was used for characterisation and measurements.

2.1.11. Synthesis of V_5S_8

Stoichiometric amounts of **V** (Alfa Aesar, 99.5%, –325 mesh, metal basis) and S were mixed together and sealed under vacuum in a Quartz ampoule using a propane/oxygen torch. The samples were then heated to 700 °C (1 °C min^{-1} heating, 24 h dwell, natural cooling). The synthesis temperature was raised to 800 °C (1 °C min^{-1} heating, 24 h dwell, natural cooling) to obtain a pure phase sample. The sample was homogenised using an agate mortar and pestle. This product was then used for characterisation and measurements.

2.1.12. Synthesis of VS

Stoichiometric amounts of **V** (Alfa Aesar, 99.5%, –325 mesh, metal basis) and S were mixed together and sealed under vacuum in a Quartz ampoule using a propane/oxygen torch. The

samples were then heated to 700 °C (1 °C min^{-1} heating, 24 h dwell, natural cooling). Afterwards, the ampoule was opened, sample homogenised using agate mortar and pestle. This product was then used for characterisation and measurements.

2.2. Characterisation

2.2.1. Powder X-ray diffraction

Diffraction techniques are ones of the most used to determine the crystal structure of inorganic compounds. Among them, Powder X-Ray Diffraction (PXRD) is one of the most readily available and commonly used for phase purity and crystal structure determination.

The technique relies on the scattering of X-rays by electrons in the atom. When atoms are arranged in an orderly manner and separated by distances similar to the wavelength of the incident X-ray beam diffraction can occur. The orderly placement of atoms in a crystalline solid creates an opportunity for constructive interference to happen. Hence, the amplified signal will be detected and sharp lines in a diffraction pattern will form.[1] An angle at which constructive interference occurs is described by Bragg's equation:

$$2d\ sin\theta = n\lambda$$

Where d is a spacing between two parallel planes of atoms, λ is a wavelength of X-rays, and n is an integer.

Powder X-Ray Diffraction (PXRD) of air-sensitive samples (in this work all alkali metal intercalated samples apart from $LiCrS_2$ were air sensitive) as well as of catalyst inks deposited on the electrode was performed on PANalytical X'Pert Pro diffractometer with Cu K_α (λ = 1.54178 Å) operating in Bragg-Brentano geometry. Air sensitive samples were measured using an airtight domed sample holder to prevent sample exposure to humidity and oxygen (Figure *2-1*). The powdered sample was packed into a holder using a glass microscope slide and closed in an Ar-filled glove box. The sample pattern was collected between 5° and 75° with a step size of 0.016° and time per step of 1.25° min^{-1}. The sample was rotated at a rate of 30 revolutions per minute.

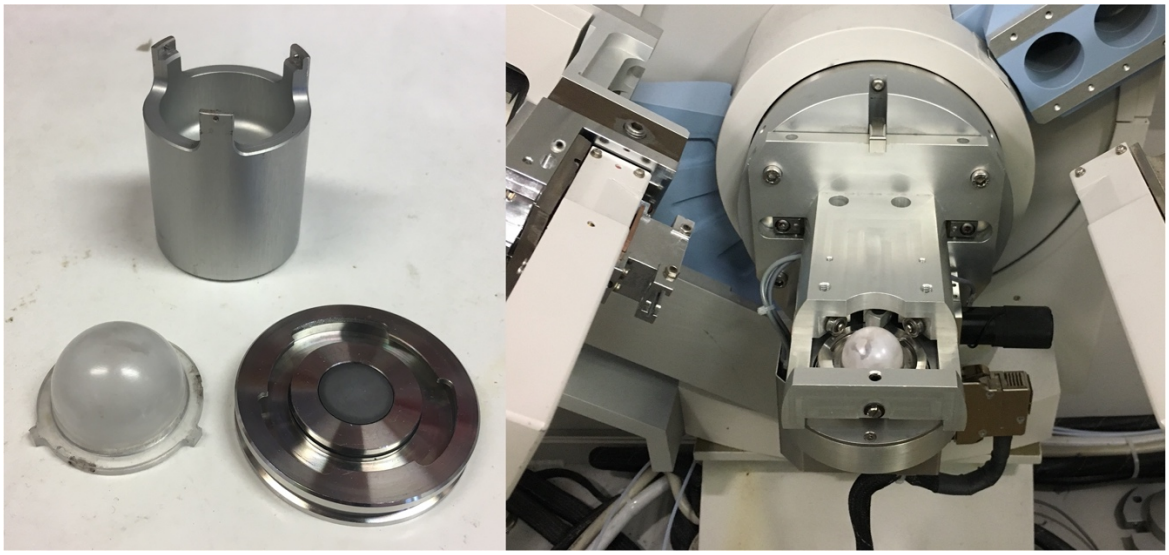

Figure 2-1. *Domed sample holder used for air sensitive sample measurement (left). Holder mounted on the 'spinner' attachment of PANalytical X'Pert Pro diffractometer (right)*

Catalyst ink diffraction patterns were collected by mounting an electrode on a specially made bracket covered in an aluminum foil (Figure 2-2). The electrode was then measured in a range of 5° and 75° with a step size of 0.016° and time per step of 2.5° min^{-1}.

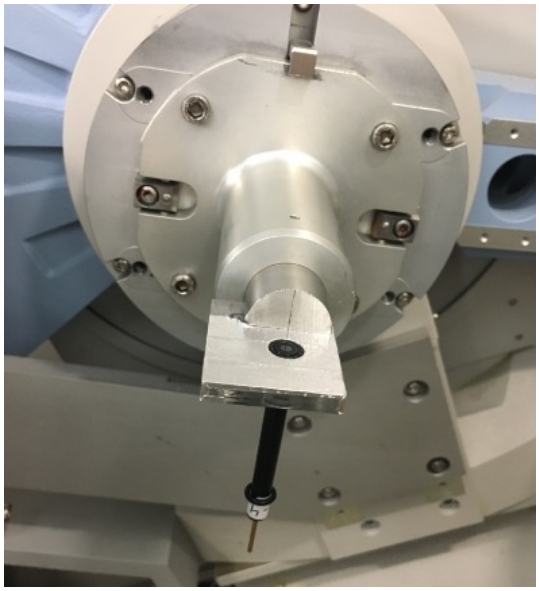

Figure 2-2. *Special bracket holder to mount electrode onto PANalytical X'Pert Pro diffractometer. The configuration was used to measure catalyst inks deposited on the electrode before and after measurements.*

PXRD of samples stable under ambient conditions (VS_2, VSe_2, TiS_2, $TiSe_2$, $CrSe_2$) were measured on a Rigaku MiniFlex 6G equipped with a D/teX Ultra detector, a 6-position (ASC-6) sample changer and Cu sealed tube ($K_{\alpha1}$ and $K_{\alpha2}$ wavelengths – 1.5406 and 1.5444 Å respectively) operating in the Bragg–Brentano geometry. Samples were carefully packed into zero background holders and levelled using a glass microscope slide. Diffraction

patterns were collected between 5° and 75° with a step size of 0.015° and time per step of 1.5° min^{-1}.

2.2.2. Le Bail and Rietveld refinement

Rietveld refinement is a technique based on fitting of calculated model to experimentally obtained pattern using non-linear least squares method. The structural model is being refined by changing various parameters that influence the experimental powder diffraction pattern (such as diffraction pattern background, unit cell, sample displacement, crystallite size and strain, atom displacement and so on) until a reasonable fit is achieved. It is important to note, that the method does not solve the crystal structure and requires a model of a crystal structure to be input manually. By considering multiple factors of the structure, Rietveld Refinement is a powerful tool to determine the precise crystal structure and atom positions in samples.[2]
Le Bail fitting is mostly used as an initial step in Rietveld Refinement as well as the technique of choice when the main reason behind refining structure is to obtain unit cell parameters. Different from Rietveld refinement, Le Bail fitting, also called full pattern decomposition, does not refine the peak intensities (they are not treated as least-squares parameters). Thus, the R-factors obtained in Le Bail fitting reveal the best possible values that could be obtained in a Rietveld refinement, helping to gauge the result of the consecutive Rietveld fit of the same pattern.[3]

While there are numerical indications of how good the fit is, it is argued, that the visual evaluation of the fit is the most important. Not only that, but also the model and parameters refined should be carefully chosen and reflect the real sample. It is still stated, that for the most part, $R_{wp} < 10\%$ and goodness of fit (GOF) between 1 and 2 are the desired results. In some cases, however, the numbers higher than these might still represent a good fit if the parameters that were refined are reasonable, and fit is visually confirmed to be good.

Le Bail and Rietveld fitting of PXRD data was performed using GSAS-II software.[4] In Le Bail refinements refined parameters included unit cell parameters, sample displacement, strain, and crystallite broadening. Background was fitted using shifted Chebyshev polynomic shape.

2.2.3. Raman spectroscopy

Raman spectroscopy is one of the techniques used to probe vibrations within the molecules. Along with infrared absorption techniques, it is quite a versatile tool allowing to investigate materials in various physical states: as solids or liquids, in hot or cold states, as bulk or microscopic particles and even thin layers. Raman spectroscopy is based on Raman

scattering. It occurs when the irradiating light interacts with the sample and distorts the cloud of electrons around the nuclei of the molecules in the sample. During this process, a 'virtual state' forms, however, it is short lived due to its instability and quickly re-radiates a phonon. Only scattering where nuclear motion is induced is regarded as Raman scattering. When nuclear motion is induced, the scattering is inelastic, the energy is transferred from the incident photon to the molecule photon or from the molecule to the scattered photon. Therefore, the energy of the scattered photon is different from that of the incident photon by one vibrational unit.[5]

Raman spectra of all samples were collected in a backscattering configuration on a Horiba JY HR800 spectrometer with a 532 nm laser excitation wavelength (laser power without any filters 100 mW) and a 600 g/mm grating. The spectra were acquired using a 50x objective. Accumulation times used were 1s, 5s, 10s, 30s and 60s; laser intensity was adjusted from 0.01% of full power to 10% of full power (10-fold increases in the filter applied). To prevent samples from oxidation in air, samples were loaded into capillaries (0.5 mm diameter, 0.1 mm wall thickness) in an Ar-filled glove box and sealed.

2.2.4. Scanning electron microscopy coupled with Energy dispersive X-ray Spectroscopy

Scanning electron microscopy (SEM) coupled with energy dispersive X-ray spectroscopy (EDX) provides information about the morphology of the sample as well as its elemental composition. During the measurement, the electron beam interacts with the sample causing it to scatter the beam. The scattered electrons are then collected by detector and an image of the sample can be produced. An electron beam interaction with the sample also causes an emission of characteristic X-rays. The number and energy of these X-rays can be measured by an energy dispersive X-ray (EDX) spectrometer and elemental composition of the sample can then be identified.[6]

Scanning Electron Microscopy (SEM) of all samples was carried out on Phillips XL30 ESEM instrument coupled with an Oxford Instruments X-act spectrometer for EDX measurements. The EDX was calibrated using INCA software with Cu as the calibration standard. The samples were immobilised on the holders using carbon stickers.

2.3. Electrochemical measurements

2.3.1. Electrochemical set up

All electrochemical measurements were carried out in a standard three-electrode cell. The electrolyte used was 1M H_2SO_4, carbon felt (Alfa Aesar) was used as a counter electrode, 3M Ag/AgCl electrode (IJ Cambria) was used as a reference electrode and glassy carbon electrode (0.071 cm^2 geometric surface area, IJ Cambria) was used as a working electrode. All measurements were carried out using Biologic SP-150 potentiostat. The electrode potentials were converted to NHE scale using the equation:

$$E(NHE) = E(Ag/AgCl) + 0.209\,V$$

In all measurements (unless stated otherwise) the internal resistance was compensated for using iR function of the potentiostat.

Peak analysis in EC-Lab software was used to integrate the area under the curve in order to obtain charge passed.

2.3.2. Electrode cleaning

Glassy carbon electrodes used as working electrodes were routinely cleaned before catalyst ink deposition. To do that, the electrode was polished using 1 μm diamond polish and polishing pad (IJ Cambria). After polishing, the electrode was cleaned electrochemically – 20 CV scans were run in a range from –1 V to +1 V *vs* NHE at a scan rate of 100 mV s^{-1}. In the cases where the electrode would display signs of contamination even after CV scans, the cleaning procedure would be repeated until clean CV scans were obtained. All scans were carried out using the general setup described in a section earlier.

2.3.3. Catalyst ink preparation

To determine the electrochemical behaviour of catalysts, catalyst ink was prepared and deposited on working GC electrode. The general protocol for ink preparation was as follows: 10 mg of catalyst, 1 mL of DMF and 50 μL of Nafion binder were mixed and sonicated in a closed vial for 30 minutes to achieve a uniform dispersion (Figure 2-3). Afterwards, 30 μL of dispersion was drop casted on freshly cleaned GC electrode and left to dry overnight. This resulted in working electrode with a catalyst loading of 4.22 mg cm^{-2}.

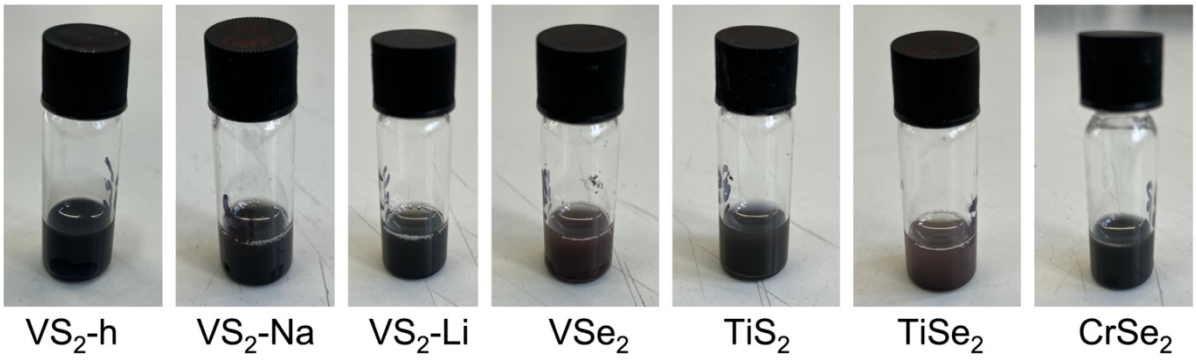

Figure 2-3. *Catalyst ink dispersions in DMF after 30 min sonication.*

2.3.4. Voltammetry

Voltammetry encompasses a variety of electrochemical techniques that are based on system response to the applied potential. Among the most common voltammetry techniques used in hydrogen evolution reaction investigation are cyclic voltammetry and linear sweep voltammetry.

In cyclic voltammetry (CV), the current is recorded over the pre-determined potential window. The potentials are swept in one direction first, and once the potential limit is reached, the potential is swept in the opposite direction. As a response to the change in potential, the current can increase when reductive/oxidative processes are driven by the applied potential.

Linear sweep voltammetry (LSV) is very similar to cyclic voltammetry, however, in this technique potential is swept in only one direction. The former technique (CV) is usually used to determine the stability and durability of catalyst. The potential is being swept between 0 V and negative potentials (usually the potentials at which catalyst reaches benchmark current density of −10 mA cm^{-2}) for a number of times (varies from study to study, anywhere between 100 and 5000). CV is also used in ECSA estimation and will be discussed later.

The latter technique (LSV) is used to record polarisation curves. Usually, a considerably slower scan rate is used (the most popular rates being 1, 2 and 5 mV s^{-1}). These polarisation curves can then be used for further analysis of hydrogen evolution reaction kinetics by using the data to obtain Tafel slopes.

Even though voltammetry can be carried out using two electrode configuration, 3-electrode arrangement is more commonly used. 3-electrode arrangement consists of a working electrode, a counter electrode, and a reference electrode. It has an advantage over the two

electrode arrangement as currents flowing between working and reference electrodes become negligible resulting in a more fixed reference electrode potential and prevents the reference electrode potential from 'floating'. When using a 3-electrode configuration it is also important to consider the counter electrode, more precisely, the surface area of a counter electrode. One should make sure that the surface area is large enough and that the electrode itself is not passivated during the measurements as otherwise a reaction happening at counter electrode might become a rate limiting process and affect the overall measurement results.[7]

Polarisation curves have been recorded using the 3-electrode cell described earlier (see section 2.3.1.) by scanning potentials from 0 V *vs* NHE to negative potentials at a scan rate of 5 mV s^{-1}. Where multiple polarisation curves were being collected, the working electrode was taken out of the electrolyte between each scan to ensure all bubbles from the surface were removed before the next scan. Moreover, the integrity of the catalyst film on the surface of the working electrode could be visually evaluated before running a following scan on the electrode. Cyclic voltammetry was carried out using the same apparatus configuration and sweeping potentials from 0 V to negative values (value varies for different catalysts) at a rate of 100 mV s^{-1}.

2.3.5. Electrical double layer measurements for ECSA

One of the methods to estimate electrochemically active surface area (ECSA) is by measuring a double layer capacitance. When measurements are carried out in a non-Faradaic region, the current recorded as the potential is swept arises purely due to charging of a double layer. The current is proportional to scan rate used:

$$i_C = \nu C_{DL}$$

In turn, when the current is plotted against a scan rate, the slope of this line yields double layer capacitance C_{DL}. Double layer capacitance is proportional to ECSA hence can be used to estimate it:[8]

$$ECSA = \frac{C_{DL}}{C_S}$$

Where C_s is specific capacitance of the sample. Double layer capacitance measurements were carried out in a non-Faradaic region of potentials (in this study the potential window used was – 0.05 V to 0.05 V vs Ag/AgCl (3M) reference electrode). The potentials were then swept between these values at varying scan rates (20, 40, 60, 80, 100, 120, 140, 160, 200 mV s^{-1}). 5 cycles of CV were recorded at each scan rate. The capacitive currents recorded

at 0 V (vs Ag/AgCl) were then plotted against scan rate and the gradient of the line represents the C_{DL}.

2.4. References

1. Pecharsky, V. K. & Zavalij, P. Y. *Fundamentals of Powder Diffraction and Structural Characterization of Materials*, Springer US, Boston, MA, 2009.

2. H. M. Rietveld, A profile refinement method for nuclear and magnetic structures, *J. Appl. Crystallogr.*, 1969, **2**, 65–71.

3. A. Le Bail, H. Duroy and J. L. Fourquet, Ab-initio structure determination of $LiSbWO_6$ by X-ray powder diffraction, *Mater. Res. Bull.*, 1988, **23**, 447–452.

4. B. H. Toby and R. B. Von Dreele, GSAS-II : the genesis of a modern open-source all purpose crystallography software package, *J. Appl. Crystallogr.*, 2013, **46**, 544–549.

5. Smith, E. and Dent, G. *Modern Raman spectroscopy—a practical approach*. John Wiley and Sons Ltd, Chichester, 2005.

6. J. I. Goldstein, D. E. Newbury, J. R. Michael, N. W. M. Ritchie, J. H. J. Scott and D. C. Joy, *Scanning Electron Microscopy and X-Ray Microanalysis*, Springer New York, New York, NY, 2018.

7. A. J. Bard and L. R. Faulkner, *Electrochemical Methods: Fundamentals and Applications*, Wiley, New York, 2nd edition, 2001.

8. S. Trasatti and O. A. Petrii, Real surface area measurements in electrochemistry, *Pure Appl. Chem.*, 1991, **63**, 711–734.

3. Vanadium disulphide for hydrogen evolution reaction

3.1. Introduction

Many transition metal dichalcogenides (TMDCs) (*i.e.* MoS_2, $MoTe_2$, WS_2) have been investigated and presented as viable catalysts for replacing platinum for the hydrogen evolution reaction from water.[1–6] The findings in these studies have pointed towards metallic phases of TMDCs being superior to the semiconducting ones. Hence, attention was turned toward TMDCs that would naturally appear in a metallic state. VS_2 was the TMDC that piqued interest, as computational studies revealed its stable polymorph in bulk to be a metallic 1T phase. However, up to this point, literature reports on the catalytic activity of this compound were primarily based on nanostructured or composite materials, masking insight into the intrinsic catalytic activity. Moreover, wide non-stoichiometry of vanadium sulphides proved to be a hurdle to accessing the layered and stoichiometric form of VS_2. Hence, a consistent investigation of phase pure, highly crystalline, and stoichiometric VS_2 is necessary to get an insight into its intrinsic catalytic properties towards the hydrogen evolution reaction from water.

3.1.1. Computational studies on VS_2 towards hydrogen evolution reaction

Considering environmental awareness, computational chemistry is being applied more often in research fields heavily reliant on experimental studies. For example, the hydrogen evolution reaction is one of the fields of interest in computational chemistry. By computationally evaluating various parameters (*i.e.,* phase stability, electronic structure, Gibbs free energy), experimental research can focus on the most promising candidates. Lately, computational methods have been developed to estimate the catalytic activity of various compounds. One of the most common groups of interest is the TMDs, likely due to their relatively simple structure, resulting in less computing resource-intensive research. They are also much easier to model due to the low number of possible active sites.

VS_2 got onto computational chemists' radar almost a decade ago with the first calculations being done on magnetic properties and structural stability of different polymorphs. In a study by Zhang *et al.*, it was found that the 2H polymorph of VS_2 is thermodynamically stable in monolayer form, and the 1T polymorph was found to be thermodynamically stable in bulk form.[7]

H. Pan has investigated group V chalcogenide monolayers in 2H configuration (due to this configuration being metallic/semi-metallic) for potential applications for water electrolysis.[8] It was found that VS_2 exhibits small calculated ΔG_{H^*} values (values close to zero) which makes it a promising electrocatalyst for water-splitting reactions. Unfortunately, ΔG_{H^*} value increases when the coverage of adsorbed hydrogen increases and eventually catalyst becomes passivated. The author noted that this behaviour is the opposite of that calculated for platinum. Further computational studies were carried out on this material by Tsai *et al.*[9] Authors have claimed that their calculations revealed the metallic character of VS_2 in both – 2H and 1T – polymorphs. Moreover, their calculations showed that VS_2 should display high activity on its basal planes as well as edge sites. This was illustrated by calculated reaction intermediate adsorption values of $\Delta G_{H^*} = 0.05$ eV for basal plane and $\Delta G_{H^*} = 0.01$ eV for edge site for 1T polymorph. However, it was also mentioned that despite expressing high activity towards HER, VS_2 was prone to stability problems. This was found to be true for most of TMDs studied in their research, as there was a trend of decreasing stability with increased activity.

He *et al.* have taken a different approach to that of his colleagues and did not rely on Gibbs free energy to evaluate the electrochemical performance of VS_2.[10] In their study, the authors investigated the hydrogen evolution reaction steps at the surface of 2H VS_2 and found that the reaction most likely takes place *via* Volmer – Heyrovsky route and overall reaction barrier was as high as 1 eV (which is much higher than those estimated for 1T phase) and was attributed to lower 2H phase activity towards HER. It was also discussed that while nanostructuring and getting to lower dimensions might increase activity towards HER, once the limit of phase transition is crossed, there should be a dramatic drop in electrocatalytic activity induced purely by phase transition. However, a recent study by Ran *et al.* presents perfect monolayer VS_2 (2H structure) as a possible candidate for platinum-like HER activity.[11] They present research where machine learning is employed to improve computational predictions for a catalyst for HER. The model consists of multiple steps (determining bandgap, formation energy, Gibbs energy for hydrogen adsorption) to screen the most likely candidates and introduce a new descriptor that considers the structure's valence electrons. Their study agrees well with a study by Zhang et al., as the stable monolayer of VS_2 adopts 2H structure. However, the calculated Gibbs energy $\Delta G_{H^*} = 0.08$ eV is much lower than that of previous reports.

3.1.2. VS_2 activity towards hydrogen evolution reaction in acidic media

Most literature reports on the activity of VS_2 towards the hydrogen evolution reaction in acidic media are on nanostructured or composite materials of VS_2 (see Table 3-1). Among these reports, some are reporting platinum-like HER activity with samples reaching benchmark current densities of −10 mA cm^{-2} at overpotentials as low as –41 mV vs RHE and Tafel slopes as low as 34 mV dec^{-1}. The electrochemical performance of composite materials is also impressive, and overpotentials ranging from –123 mV vs RHE to –350 mV vs RHE. Probably the more intriguing reports are those of bulk and lithium exfoliated samples. There is a stark difference between the overpotentials of bulk samples and nanostructured ones. Bulk samples are being reported less often. However, from the reports that are in the literature, it looks like the compound is not HER active at all; the benchmark current densities are only being achieved at > 900 mV vs RHE overpotentials. The bulk sample analysis is also quite complicated, as achieving a bulk sample in genuine layered and stoichiometric structure is a challenge. The reports on bulk and Li exfoliated samples note that the bulk sample displays a powder pattern similar to that of V_5S_8, and exfoliated sample shows lithium intercalated phase, as well as oxide phases forming.[12]

The stability of VS_2-based electrocatalysts have mostly been shown to be good – in studies where cycling was used to determine the stability LSV curves before and after cycling showed little to no change.[13–17] In some studies, an improvement in overpotential was noticed during stability studies (CV cycling, galvanostatic or potentiostatic methods).[17–19] These results indicate that the catalyst is stable in an acidic environment and under low reducing overpotentials. However, few studies suggest, that VS_2 is not a stable catalyst in acidic media. Qu et al. have observed no change in LSV curves before and after CV studies but an increase in potential needed to maintain −10 mA cm^{-2} current density was noticed during galvanostatic measurement.[20] Within the first 4 hours of the measurement, the potential needed to maintain current density went from around −50 mV vs RHE at the beginning of the measurement to almost −300 mV. Similar behaviour was noticed by Patil et al.[21] In their study, chronoamperometric measurements revealed that there is an almost 30% drop in current density achieved by the catalyst at a constant potential within 12 hours.

***Table 3-1**. Literature reports on HER activity in acidic media of VS_2 nano structures, bulk samples and composite materials.*

Mophology/composite	Structural characterisation	Overpotential at −10 mA cm^{-2}, mV vs RHE	Tafel slope, mV dec^{-1}	C_{DL}, mF cm^{-2}	Ref
VS_2 nanosheets	XRD, TEM	68	34	N/A	[18]
VS_2 nanosheets	XRD	450-500	210	N/A	[22]
VS_2/rGO	XRD, TEM	350	150		
VS_2 nano discs	XRD, TEM	42	36	93	[23]
Bulk VS_2	XRD (V_5S_8)	1100	N/A	N/A	[12]
Li exfoliated VS_2	XRD	950	N/A		
VS_2 nanoflowers	XRD, HRTEM	58	34	N/A	[20]
VS_2 nanoflowers	XRD, TEM	43	36	151	[13]
VS_2 nanoflowers	XRD	41	36	0.969	[24]
VS_2	XRD, TEM	400	170	1.8	[14]
VS_2/MWCNT		123	40	15.2	
VS_2/MWCNT 1:2		163	62	11.4	
VS_2/MWCNT 2:1		269	110	7.2	
VS_2, single crystals	N/A	561	136	N/A	[25]
V intercalated VS_2	XRD, TEM	59	38	25.2	[15]
VS_2 nanoflowers		67	50	11.8	
Annealed VS_2 nano discs	XRD, TEM	350	79	3.82	[16]
VS_2-Pd	XRD, TEM	157	75	N/A	[19]
VS_2		530	186	0.69	
VS_2 waffle structure	XRD TEM	82	61	0.34	[26]
Mo doped VS_2 nanostructures	XRD, TEM	243	53	6.20	[17]
VS_2 nanostructures		922	305	0.25	
VS_2 nanostructures	XRD, TEM	377	117	N/A	[27]
VS_2 on nickel foam	XRD, TEM	161	88	10	[21]

3.1.3. Synthesis of VS_2

Before the synthesis of VS_2 can be approached and discussed, a brief overview of the V-S phase diagram is needed. To this day, only a tentative phase diagram for this system exists, as literature reports are quite conflicting, especially in the region where the vanadium to sulphur molar ratio is close to that of 1:2 (Figure 3-1).

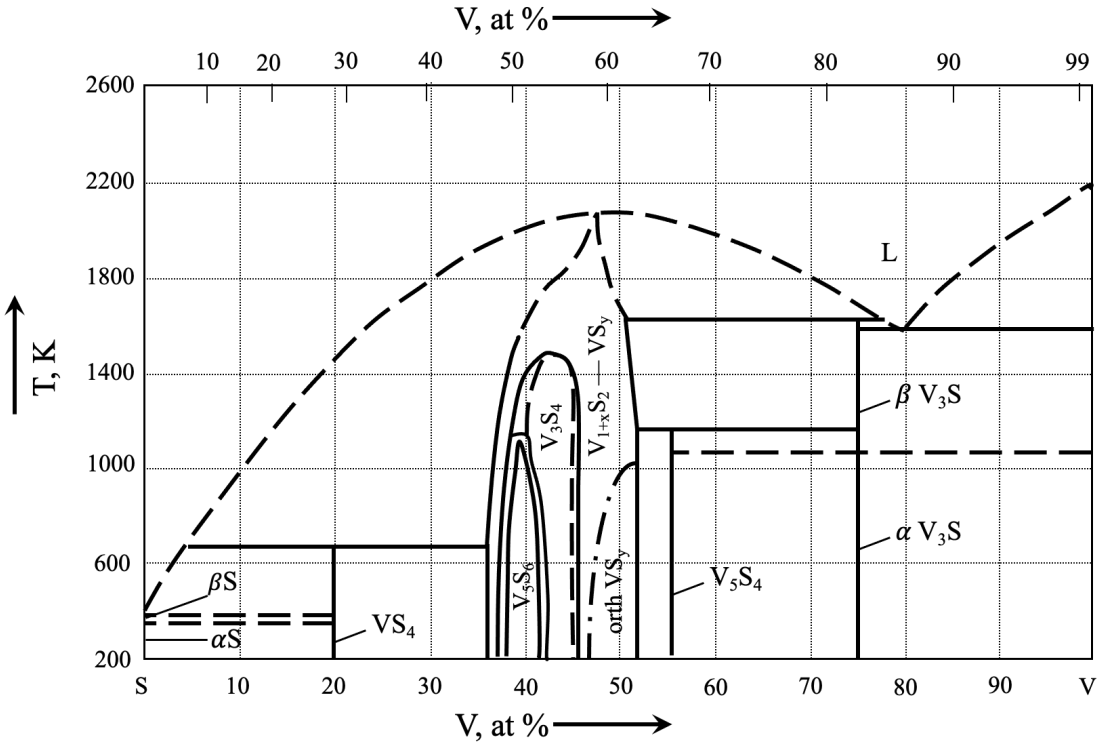

***Figure 3-1**. Tentative phase diagram of V – S system adapted from B. Predel*[28]

In an extensive study of solid-state synthesis of vanadium sulphides, Vries *et al.* briefly mention that vanadium sulphide with a structure of $Cd(OH)_2$ and nominal composition of $V_{0.6}S$ can be obtained by quenching the sample from 600 °C.[29] It was claimed by Tudo *et al.* that trigonal VS_2 could be formed by annealing VS_4 under vacuum. However, their claim was only supported by TGA curves and the phase was never isolated.[30] Jellinek later claimed to have isolated the phase using this method, however, the referenced work was never published.[31] Claims of the existence of VS_2 were largely disputed until *Murphy et al.* successfully isolated a stoichiometric trigonal VS_2 phase *via* deintercalation of Li from $LiVS_2$.[32]

Recently, the most popular synthesis method for VS_2 has been hydrothermal/solvothermal synthesis. There is a variation of precursors and solvents used. However, the most popular ones remain sodium orthovanadate or ammonia metavanadate as a vanadium source and thioacetamide as a sulphur source. This synthesis method has achieved a wide array of

morphologies, and a brief summary of conditions is displayed in Table 3-2. Reaction mechanism for hydrothermal and solvothermal processes has not been elucidated.

***Table 3-2**. Brief summary of reaction conditions reported in literature for VS_2 nanostructure and composite synthesis*

Vanadium source	Sulphur source	Solvent	Reaction temperature	Ref
Na_3VO_4	C_2H_5NS	Deionised water	160 °C	[22,23,33,34]
$VO(acac)_2$	$C_3H_7NO_2S$	NMP	200 °C	[35]
Na_3VO_4	C_2H_5NS	Diethylene glycol/deionised water	160 °C	[36,37]
NH_4VO_3	C_2H_5NS	Propylene glycol/ammonia	180 °C	[38,39]
$VO(acac)_2$	C_2H_5NS	Ethylene glycol	200 °C	[40]

Another popular synthesis method for VS_2 is chemical vapour deposition. A brief overview is in Table 3-3. This synthesis method is usually employed for nanosheet or nanoplate synthesis.

***Table 3-3**. Summary of parameters for CVD synthesis of VS_2*

Vanadium source	Sulphur source	Substrate	Carrier gas	Reaction temperature, °C	Ref
VCl_3	S	SiO_2/Si	10% H_2/N_2	700	[18]
VCl_3	S	SiO_2/Si	10% H_2/Ar	600	[41]
VCl_3	S	h-BN/SiO2/Si	10% H_2/Ar	650	[42]
VCl_3	S	Activated carbon	10% H_2/Ar	750	[43]
V_2O_5 /KCl	S	Al_2O_3	Ar	800	[44]

In general, it seems like the only method to synthesise stand-alone, crystalline VS_2 in bulk is via deintercalation reactions from alkali metal intercalates of VS_2; hence a further look into these compounds and their structures will be taken in the next section.

3.1.4. Intercalation compounds of VS_2

As a layered chalcogenide, VS_2 is a great host for alkali metals. Two of the intercalates – $LiVS_2$ and $NaVS_2$ – are at the centre of VS_2 synthesis in this work.

Regarding sodium intercalates of vanadium disulphide, Wiegers *et al.* reported three different phases the system could adopt.[45] The three phases differ in stacking of the vanadium disulphide layers and coordination of sodium atom by sulphur atoms. Authors claimed that the main phase formed in the experiments was the rhombohedral phase (Figure 3-2 b). In this phase, the unit cell consisted of three layers of VS_2 with sodium atoms in between them. The coordination of sodium atoms was that of trigonal prismatic. According to the authors, with prolonged storage at low temperatures, this phase would slowly turn into a hexagonal phase (Figure 3-2 c). In this phase, both metals – sodium and vanadium – are in octahedral coordination. It was noticed that the hexagonal phase would transition into rhombohedral upon heating. However, the opposite transition would be prolonged, taking months of storing a sample at room temperature. The third phase (Figure 3-2 a) reported by these authors was a phase that would often form as an impurity at higher sodium content samples. This form was again rhombohedral; however, different from the other rhombohedral form, as sodium atoms in this structure were in octahedral coordination. It was reported that this form would occasionally be obtained as a pure phase sample.

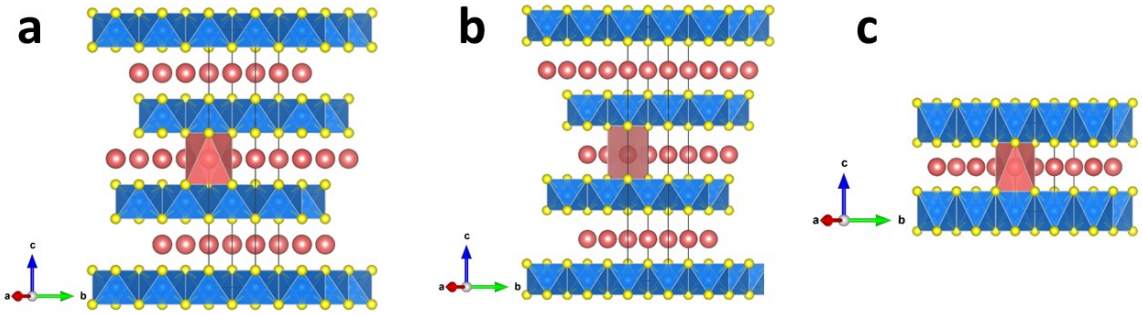

Figure 3-2. *Structures of VS_2 sodium intercalates. a) rhombohedral structure, space group R-3mH; b) rhombohedral structure, space group R3mH; c) hexagonal phase, space group P-3m1. Blue color represents vanadium atoms and its polyhedral, yellow color represents sulphur atoms and pink color represents sodium atoms and shape of polyhedral.*

Unlike sodium intercalates, only one crystal structure is observed and reported for lithium intercalates of VS_2.[32] The structure consists of layers of VS_2 where vanadium atoms are octahedrally coordinated by sulphur (Figure 3-3). Lithium atoms are sitting between the

layers and are also coordinated octahedrally. The space group *P-3m1* that the compound belongs to is the same as of VS_2. It is also isostructural to the hexagonal $NaVS_2$ structure.

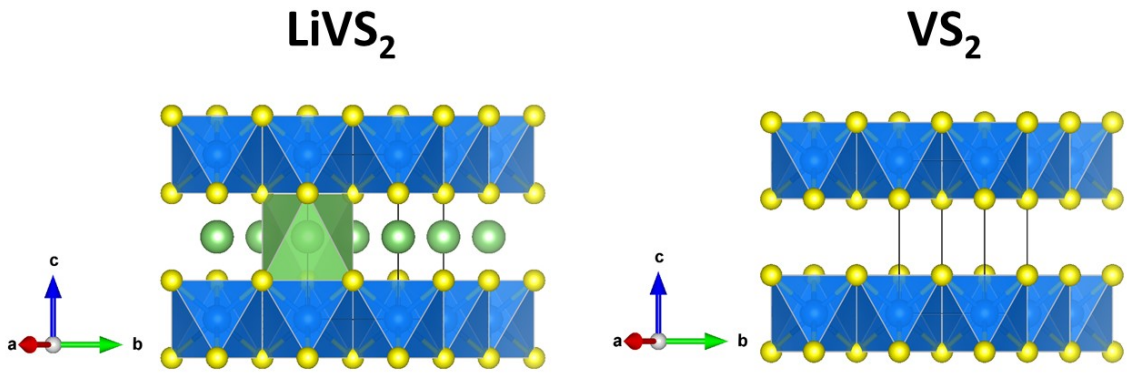

Figure 3-3. *Crystal structure of $LiVS_2$, space group P-3m1 (left) and VS_2, space group P-3m1 (right). Blue color represents vanadium atoms and its polyhedral, yellow color represents sulphur atoms and green color represents sodium atoms and shape of polyhedral.*

3.2. Aims

The main aim of this chapter is to apply an indirect reaction route via intercalation compounds to access highly crystalline, layered, and stoichiometric VS_2. Then, the electrochemical characterisation of bulk VS_2 will be carried out and compared to the electrochemical characteristics of nanostructured VS_2. It will provide an insight into the intrinsic catalytic properties of layered VS_2 as a standalone catalyst. Not only that, but the results may help bridge the gap between experiments and DFT methods, as the models can be adjusted based on the experimental results and further improve the quality of computational models.

3.3. Results and discussion

3.3.1. Synthesis and characterisation of VS_2 from $NaVS_2$

3.3.1.1. Synthesis of $NaVS_2$

A route through alkali intercalated compounds has been chosen as an indirect synthesis method to produce layered VS_2, with a sodium intercalated compound investigated first. Wiegers *et al*. claims that three different crystal structures of sodium intercalated vanadium disulphide exist.[45] These three structures are described in the chapter introduction (section 3.1.4.) and depicted in Figure 3-2. While authors claim that the product's structure depends on temperature and sodium content, we found that the transition between two rhombohedral structures could be controlled by sodium content within the Na_xVS_2 structure alone. When *x* is at or below 0.8, the product shows a rhombohedral structure where sodium atoms are in trigonal coordination (SG: *R 3 m H* (160)). Subsequently, at x = 1.2, the product adopts the rhombohedral structure where sodium atoms are coordinated octahedrally (SG: *R*–3*m*(166)). Attempts to synthesise $NaVS_2$ with the ideal Na:V:S= 1:1:2 stoichiometry led to a product that would often consist of a mixture of the two rhombohedral phases (see appendix Figure A 2, Figure A 3, Figure A 4).

As mentioned above, the single-phase range exists for Na-deficient compounds. Therefore, the product with a nominal composition $Na_{0.7}VS_2$ was synthesised. The synthesis procedure differed from that reported by Wiegers *et al.*, as sodium metal used by this group has been replaced by Na_2S in this work. The swap from Na metal to Na_2S in solid-state synthesis of Na_xVS_2 was previously reported by Lee *et al.*[46] The typical synthesis developed in this work was based on the synthetic procedures reported in those two reports was as follows. Stoichiometric amounts of Na_2S powder, V powder and S powder were mixed in an Ar-filled glovebox, loaded into a Pyrex glass ampoule, and sealed under vacuum (see the precise details in chapter 2). The sample was then slowly heated to 600 °C and left to react at this temperature for 72 hours. The sample was handled under an inert atmosphere as it is highly moisture sensitive. Powder X-ray diffraction was utilised for phase identification of the product of the reaction. When the pattern was compared to that calculated from the ICSD, it was confirmed that the product of the reaction was corresponding well with the previously reported $Na_{0.3}VS_2$ (Figure 3-4). While the pattern's resemblance was high, there was a slight shift in peak positions. This shift was expected as the sodium content in the sample was higher than that of the reference pattern. The shift in peak positions depending on sodium content was also discussed by Wiegers *et al.*

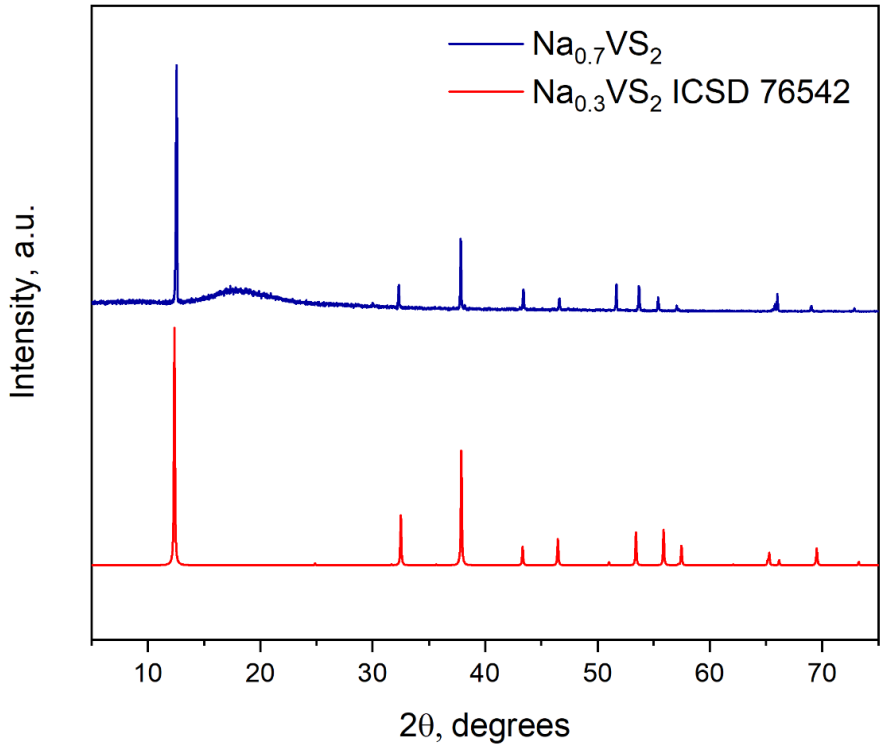

Figure 3-4. *PXRD pattern of the product of reaction between Na_2S, V and S powders sealed under vacuum and heated at 600 °C for 72 hours (top, dark blue). For comparison, calculated diffraction pattern of $Na_{0.3}VS_2$ from ICSD (card number 76542) is displayed at the bottom (red). Wide 'bump' at 15-20 degrees in the experimental pattern (top, blue) comes from an air sensitive holder used in the measurement.*

Remarkably, Lee *et al.* claimed that the second annealing was needed to fully homogenise the sample to achieve a single-phase product. However, the report by Wiegers claimed that only one heating cycle was sufficient; although the authors mentioned that sometimes their samples contained impurities or mixed phase. To test the impact of the second annealing, the PXRD patterns of the relevant products were compared. It was noticed that a second annealing of the sample had little to no impact (Figure 3-5). Therefore, all follow-up syntheses of $NaVS_2$ have been carried out as a single step-process.

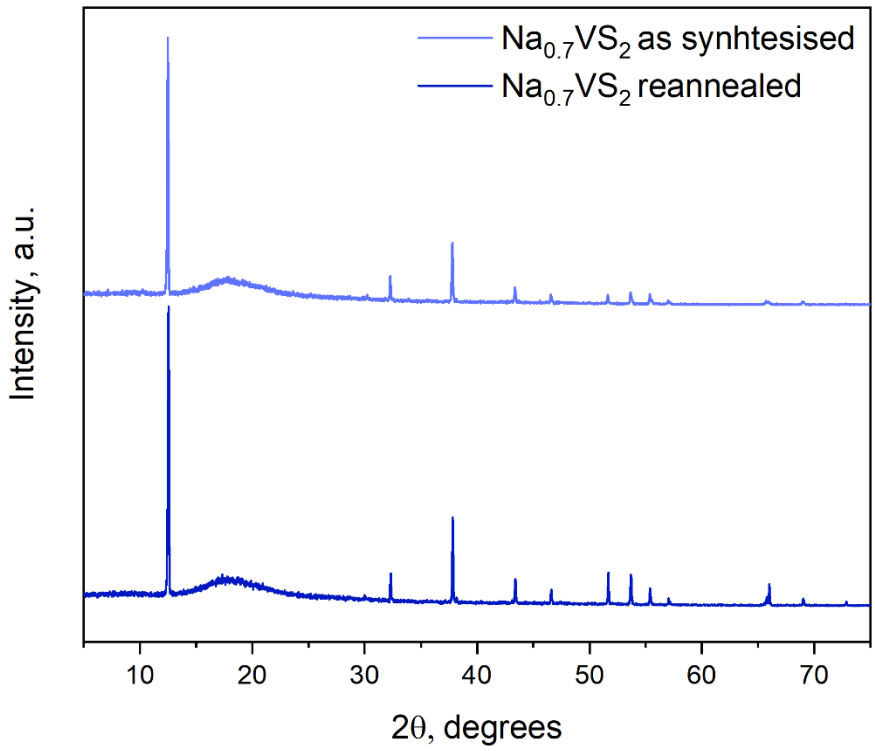

Figure 3-5. *PXRD pattern of the product of reaction between Na_2S, V and S powders sealed under vacuum and heated at 600 °C for 72 hours (top, light blue) in comparison with PXRD pattern of the same sample after annealing it at 600 °C for another 24 hours (bottom, dark blue). Wide 'bump' at 15-20 degrees in the experimental pattern (top, blue) comes from an air sensitive holder used in the measurement.*

3.3.1.2. Synthesis of VS_2-Na

After establishing a reproducible synthesis of $Na_{0.7}VS_2$, it was routinely used to synthesise VS_2 *via* deintercalation reaction. The method for alkali metal deintercalation has been reported by Murphy *et al.*[32] and was initially used for Li deintercalation from $LiVS_2$. The method required stirring alkali metal intercalated vanadium disulphide in I_2 solution in acetonitrile at room temperature (all details of the adaptation of this process can be found in chapter 2). It was crucial not to expose the initial compound to air. Therefore, the deintercalation reaction was carried out in a vial with a septa lid, where iodine solution could be introduced via syringe. The reaction takes place rapidly, as the colour of the solution introduced into the reaction vessel quickly changes from dark brown to colourless. Once no colour change is observed with the introduction of iodine solution, an excess of iodine solution is added to ensure full deintercalation. After 48 hours of continuous stirring, the

sample was filtered and washed with acetonitrile, followed by water and ethanol. Once the sample was dried, powder diffraction measurements were run to investigate the changes in the crystal structure.

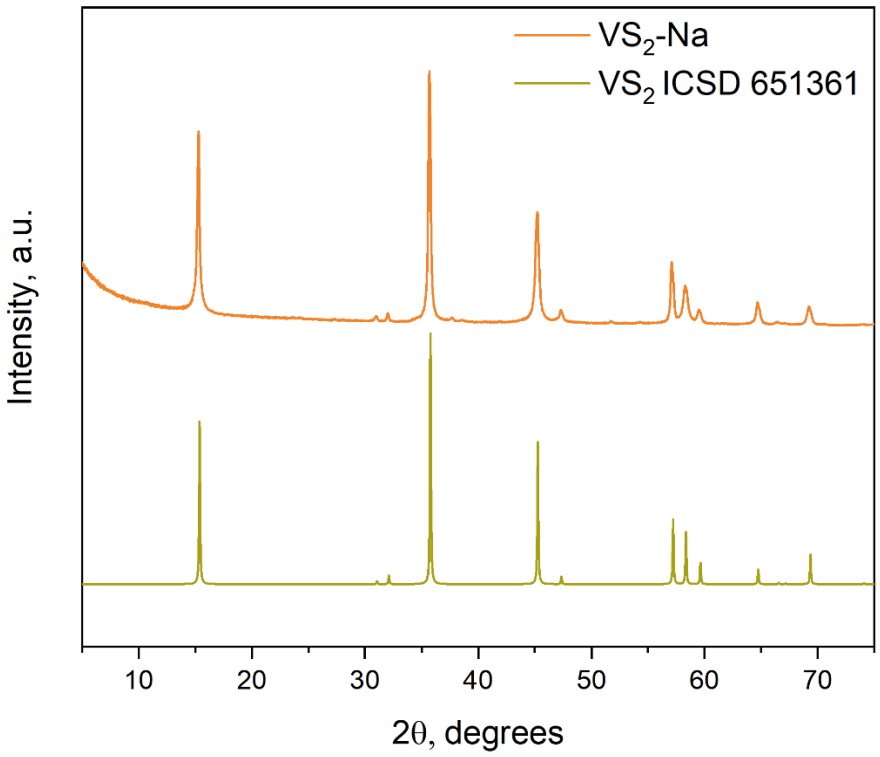

Figure 3-6. *PXRD pattern of the product of deintercalation reaction where $NaVS_2$ was reacted with I_2 solution in acetonitrile for 48 hours at room temperature under continuous stirring (top, orange). For comparison, calculated diffraction pattern of VS_2 from ICSD (card number 651361) is displayed at the bottom (mustard).*

No special precautions were taken to prevent the deintercalated sample from the exposure to the ambient conditions. As seen from the X-ray diffraction pattern (Figure 3-6), crystal structure change occurred during the sodium deintercalation process. The product of deintercalation – VS_2 – adopts a trigonal structure with space group *P–3m1* (164). The crystal structure is comprised of layers of VS_2 where metal atoms are sandwiched between sulphur atoms. Vanadium atoms are coordinated octahedrally by sulphur, with the octahedra sharing edges to form layers. This phase is commonly called the 1T phase. The sample prepared via deintercalation from $Na_{0.7}VS_2$ will be referred to as VS_2-Na from this point on. The change of crystal structure is indicative of the successful deintercalation of sodium atoms. A close match between the experimental and reference patterns shows the sample to be relatively stable in ambient conditions as no rapid degradation occurs upon exposure for at least several days. Unfortunately, the sample did not show good long-term stability at ambient conditions.

When the sample vial was opened after 6 months of storing it on the bench, the smell of sulphur was noticed. XRD diffraction run on the sample exposed to ambient conditions for 6 months can be found in Appendix (Figure A 1). It can be seen that sulphur peaks appear in the pattern, indicating sample decomposition or possible loss of sulphur due to oxidation. For this reason, the sample was always prepared fresh before electrochemical measurements. Le Bail refinement was employed to determine the cell parameters of the product, and the results are displayed in Table 3-4. The cell parameters of the sample agree with reported crystal structure data for this system. Overall reports of VS_2 include the samples where the stoichiometry drifts from that of perfect 1:2, in most cases it is claimed that the vanadium could be self-intercalated between the layers. However, from looking at available crystal structure data, the trend of very subtly shrinking *c* parameter with the increase of the vanadium content in the compound can be observed. This suggests that the samples prepared in this work are highly likely close to perfect stoichiometry.

Table 3-4. *Cell parameters of VS_2 produced via deintercalation reaction in comparison with values reported in literature.*

Sample	*a*, Å	*c*, Å	Ref
VS_2-Na	3.2167(8)	5.7503(6)	This work
VS_2	3.221	5.755	[47]
VS_2	3.217	5.755	[32]
$V_{1.1}S_2$	3.247	5.6949	[48]
$V_{1.11}S_2$	3.272	5.688	[49]
$V_{1.14}S_2$	3.265	5.6894	[48]
$V_{1.2}S_2$	3.281	5.668	[50]
$V_{1.2}S_2$	3.281	5.668	[29]

3.3.1.3. Composition and morphology of VS_2-Na

The elemental composition of the sample was investigated by EDX analysis. The analysis revealed that the sample has a nearly perfect metal to sulphur ratio (V:S = 1:2.04), and the results are displayed in Table 3-5. The results indicate that in the case of VS_2, the deintercalation route enables the synthesis of stoichiometric compounds.

Table 3-5. *EDX data of VS_2 prepared via deintercalation of Na from $Na_{0.7}VS_2$. The standard deviations are evaluated based on 12 independent points*

	VS_2-Na at. %	
Element	V	S
Experimental	32.9 (11)	67.1(11)
Theoretical	33.3	66.6

To analyse the morphology of the sample, SEM imaging has been done. As can be seen from the images (Figure 3-7), the sample consists of relatively large – the majority of them being approximately 20 μm in at least one dimension – crystallites. Crystals have a shape of thin platelets, some display larger pieces that consist of stacks of thin platelets. This morphology agrees well with the compound having a layered structure. There seems to be quite a high distribution in crystallite sizes. The crystals consisting of multiple stacked platelets display cracks in between the platelets, this cracking that seems to separate the platelets likely happens during the sodium deintercalation process.

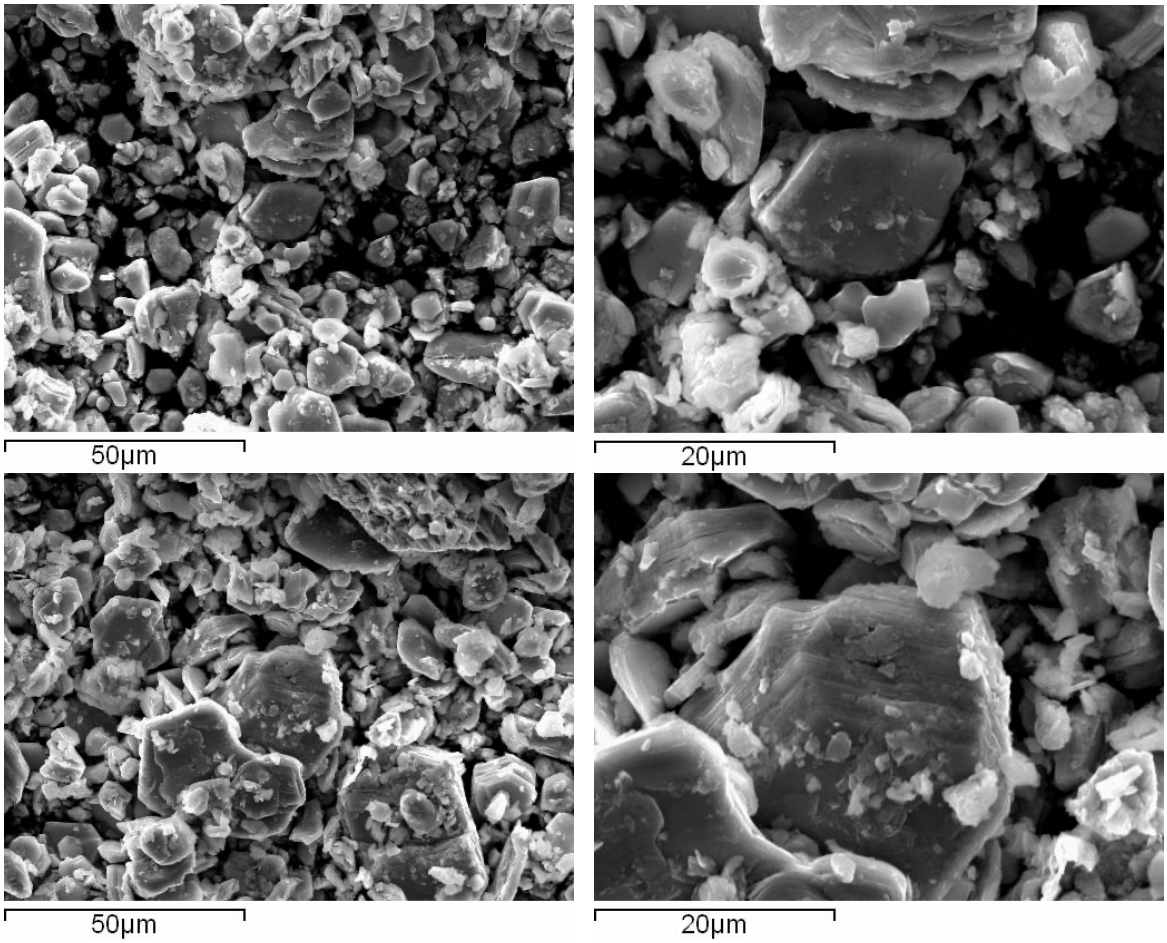

Figure 3-7. *SEM images of VS_2-Na. Two different magnifications of two different spots are displayed.*

3.3.1.4. VS_2-Na Raman spectroscopy

Raman spectroscopy was employed for further phase identification. Raman is a non-destructive technique, allowing for phase and possible impurity identification. In the case of vanadium disulphide, literature reports on Raman modes of layered VS_2 are conflicting to a certain degree. An example of a distribution of reported Raman peaks for this compound is in Table 3-6. There is quite a variation in Raman peaks reported, although two significant tendencies can be noticed. The Raman spectra that are reported within a smaller range (200-500 cm^{-1}) indicate only two peaks in the Raman spectrum of VS_2 positioned at 280 cm^{-1} and 403 cm^{-1}. Other reports that display wider range Raman measurements indicate that there are between three and six peaks present in the spectrum. It is important to note that peak positions reported within the smaller range Raman spectra match the peaks in the reports with a higher number of peaks. Another important note should be that computational studies on Raman modes of VS_2 (simulated for a crystal structure with a space group 164) indicated that Raman peaks should be observed at around 260 cm^{-1} and 380 cm^{-1}.[51] There is only one literature report claiming to have recorded this spectrum experimentally. The authors of the

study used a vacuum optical cryostat to minimise sample heating and oxidation under laser irradiation.

Table 3-6. *Raman peaks of VS_2 reported in literature*

Sample morphology	Synthesis method	Reported Raman peaks (position cm^{-1})	Ref
Sheets	CVD	300, 322	[52]
Nanosheets	CVD	260, 330, (and a 2-phonon mode at 150)	[18]
Micro flowers	hydrothermal	280, 404	[53]
Nanostructured films	CVD	280, 404	[54]
Ultrathin flakes	APCVD	263, 379	[51]
VS_2-SnS_2 hybrids	hydrothermal	287, 409	[55]
Nano flakes	CVD	63.1, 105.8, 157.2, 266.7, 298.4, 325.1	[42]
Nanosheets	hydrothermal	140.4, 192, 282, 406.6, 687.8 and 993.2	[56]
Microrods	hydrothermal	141, 281, 406, 993	[57]
Grass-like VS_2	sonication	279, 401	[58]
Nanoplates	wet synthesis	278, 403	[59]
Micro flowers	hydrothermal	141, 282	[60]
Nanosheets	hydrothermal	282, 389, 406	[39]
Nanowires	hydrothermal	286, 406, 693, 995	[61]
Nanoflowers	hydrothermal	140, 192, 282, 406, 687, 993	[34]
Nanosheets	Liquid exfoliation	275, 433	[62]
Nanoflowers	Hydrothermal	138, 200	[20]
Nanosheets	hydrothermal	138, 190, 278, 404, 686, 990	[63]

Considering all the above information, the question arises – why is literature so conflicted regarding the Raman spectrum of VS_2 and what are these reported peaks?

According to *Li et al.,* there are three reasons for the wide distribution of reported results.[64] First is the method of synthesis that was used, as different nucleation processes may result in different stacking of the layers or even self-intercalation of Vanadium. The second reason for discrepancies in Raman spectra was claimed to arise from different flake curvature and laser set-up. Last, and probably one of the more important reasons for the discrepancies in observed peaks, is the poor stability of VS_2 under laser irradiation. When measurements are

carried out in the ambient atmosphere, the burning and oxidation of the compound can be observed. This can be avoided by finely tuning the laser intensity and irradiation duration; however, a delicate and precise Raman spectrometer is needed to achieve that.

Based on the investigation of other vanadium sulphides (VS, V_5S_8 and VS_4), it has been found that all of them were very easily oxidised during the measurement and displayed Raman spectra are similar (this will be discussed in more detail in chapter 6). All those Raman spectra were also comparable to that of VS_2. As the first means to prevent the oxidation of the sample under laser irradiation, the power of the laser and measurement time were adjusted. However, using the available equipment in this work, this approach was unsuccessful as either no Raman peaks could be observed using lower laser power, or vanadium oxide peaks would appear once the power was increased (Figure 3-8).[65]

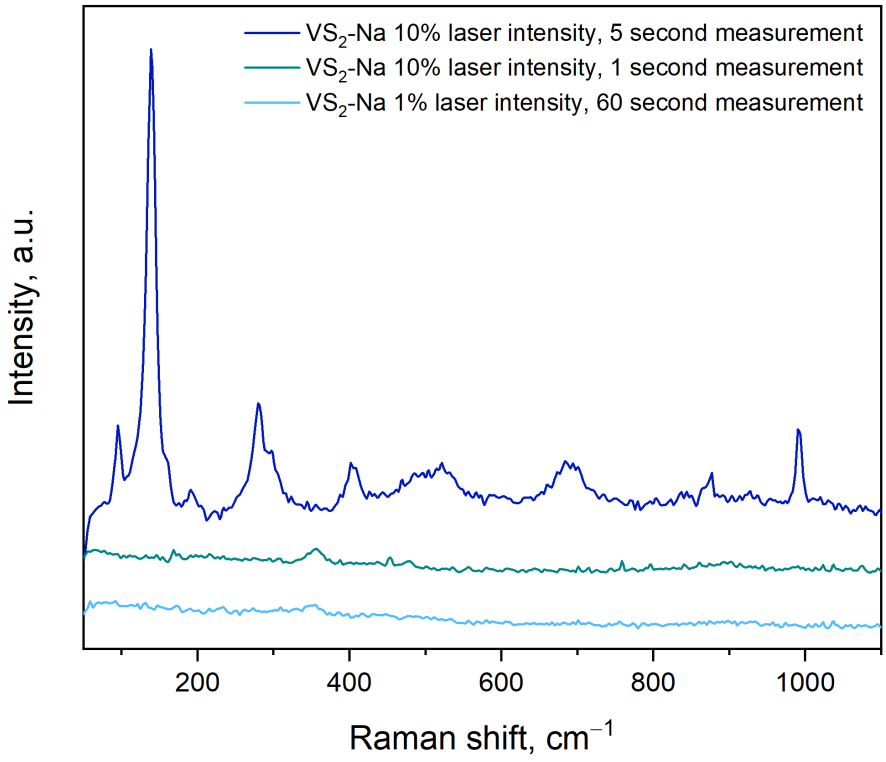

Figure 3-8. *Raman spectra of sample VS_2-Na. All spectra displayed in the figure have been collected in ambient conditions. The top spectrum is that of oxidized sample when higher laser intensities (10%) are used during the measurement. The middle spectrum is obtained when using the same 10% laser intensity but limiting the measurement time to 1s. The bottom spectrum is obtained when using a lower laser intensity (1%) and extending the measurement time to 60s.*

Lacking better control of the laser power, another strategy was employed. Raman measurements were carried out on samples sealed in capillaries under an inert (Ar) atmosphere to prevent them from oxidising. Whilst the lower laser power still had not provided any spectrum, when the laser intensity was raised to the power that was oxidising the sample, quite a different Raman spectrum could be observed. This time, peaks at 80 cm^{-1}, 148 cm^{-1}, 217 cm^{-1}, 473 cm^{-1} were observed (Figure 3-9). This spectrum did not match the computed or reported Raman spectra at all. Moreover, all the peaks matched the Raman spectrum of sulphur perfectly (Figure 3-10).[66] It is important to note that sulphur is highly Raman active; therefore, if it was present in the sample as an impurity or unreacted precursor, such high laser intensities would not be needed to observe sulphur peaks. Therefore, the appearance of sulphur peaks confirms the decomposition of the sample. To add, the images taken of the spot before and after the measurement could be compared, and it was visually confirmed that the sample has decomposed. (Figure 3-11)

All these results indicate that Raman spectroscopy should be used very carefully for vanadium disulphide phase identification.

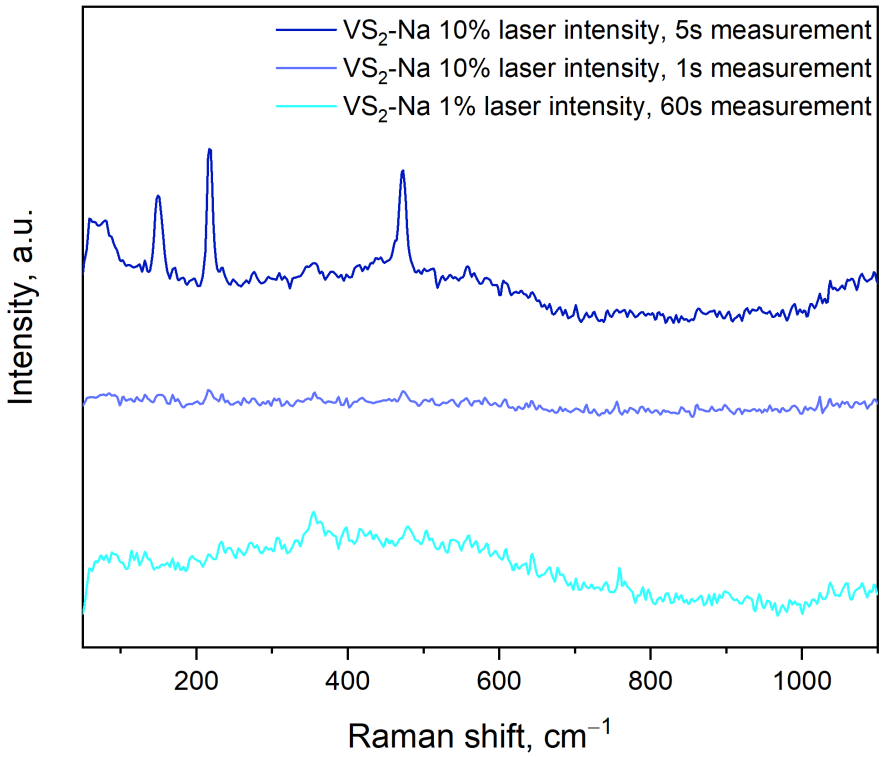

Figure 3-9. *Raman spectra of sample VS_2-Na. All spectra displayed in the figure have been collected on the sample sealed in a capillary prepared under an inert (Ar) atmosphere. The top spectrum is that of decomposed sample when higher laser intensities (10%) are used during the measurement. The middle spectrum is obtained when using the same 10% laser intensity but limiting the measurement time to 1s. The bottom spectrum is obtained when using a lower laser intensity (1%) and extending the measurement time to 60s.*

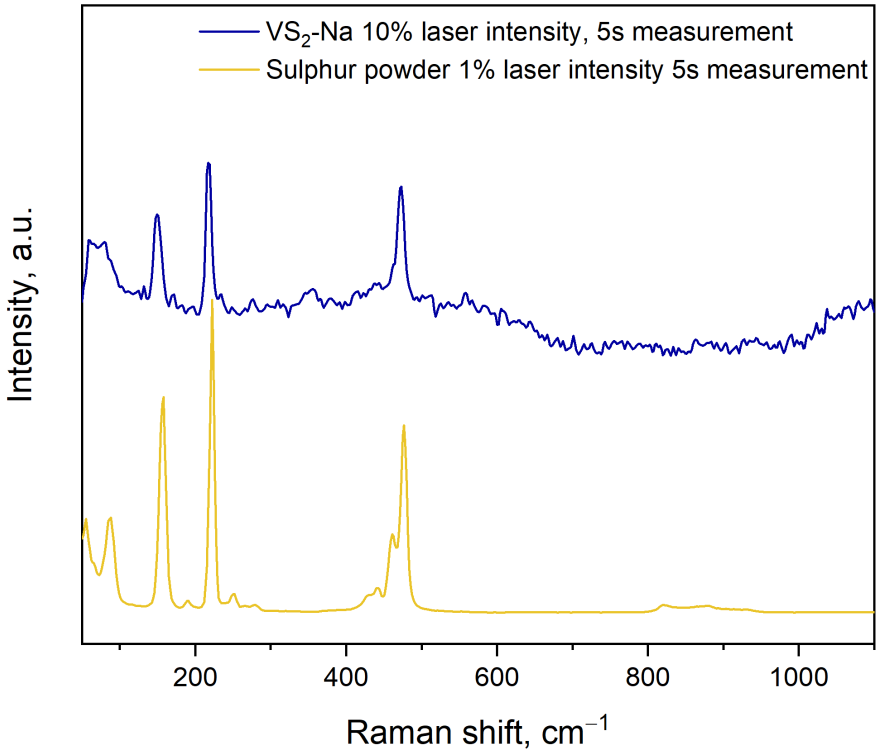

Figure 3-10. *Raman spectrum of sample VS_2-Na. Spectrum collected on a sample sealed in a capillary under an inert (Ar) atmosphere. The top spectrum is that of decomposed sample when higher laser intensities (10%) are used during the measurement. The bottom spectrum is obtained when measuring Sulphur powder at lower laser intensity (1%) and keeping the measurement time the same.*

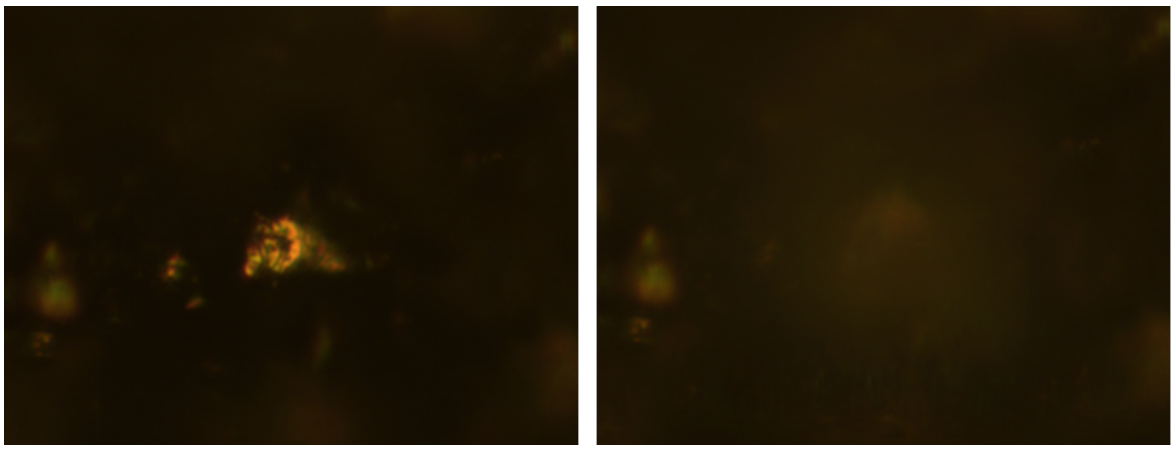

Figure 3-11. *Optical images of the spot of sample VS_2-Na (in a capillary sealed under Ar atmosphere) before Raman measurement using 10% laser intensity (left). Optical image of the same spot after measurement is on the right. The images illustrate clear sample decomposition under higher laser irradiation. Raman spectrum was recorded using 532 nm laser excitation and optical images were collected using 50x optical lens.*

3.3.1.5. Electrocatalytic activity of VS_2-Na toward HER

Electrocatalytic properties of VS_2-Na were investigated by preparing catalyst ink based on previous experience with other vanadium sulphides. DMF has been chosen as a solvent to obtain catalyst dispersion. The usual protocol was followed for the preparation of electrodes (the detailed procedure can be found in chapter 2). In short, the glassy carbon electrode was cleaned before depositing catalyst ink, and once the catalyst ink was deposited by drop casting method, the electrode was left undisturbed on the bench overnight so that the ink would dry and form a uniform catalyst film on the surface. This electrode would later be used as a working electrode. A three-electrode setup was used for electrochemical measurements, with carbon felt used as a counter electrode and Ag/AgCl (3M) electrode used as a reference electrode and 1M H_2SO_4 was the electrolyte of choice for testing in acidic media.

Polarisation curves were recorded at a scan rate of 5 mV s^{-1}. While there are several parameters suitable for determining electrocatalytic activity, one of the most widely used is the overpotential at which catalyst reaches a current density of –10 mA cm^{-2}. In this case, the catalyst reaches this current density at overpotentials of –557 mV (Figure 3-12). This overpotential is high, considering that 20% Pt/C commercial catalyst reaches the current density of 10 mA cm^{-2} at overpotentials as low as –37 mV vs NHE. While platinum is an exceptionally good catalyst for HER, other reports on VS_2 have been claiming that it can be comparable to platinum or has overpotentials close to those of platinum. The summary of the reported electrochemical activity of VS_2 can be found in the Table 3-1.

Moreover, the LSV curve of VS_2 is not as smooth as one would expect. There seems to be a slight reductive wave at around –200 mV vs NHE, which may come from surface oxides that many of TMDCs are prone to form on the surface. A simple way to deal with surface oxides is a pre-treatment cycle, where the catalyst is scanned once in the reductive region. The following polarisation curve then usually shows improvement, and the curve smooths out.

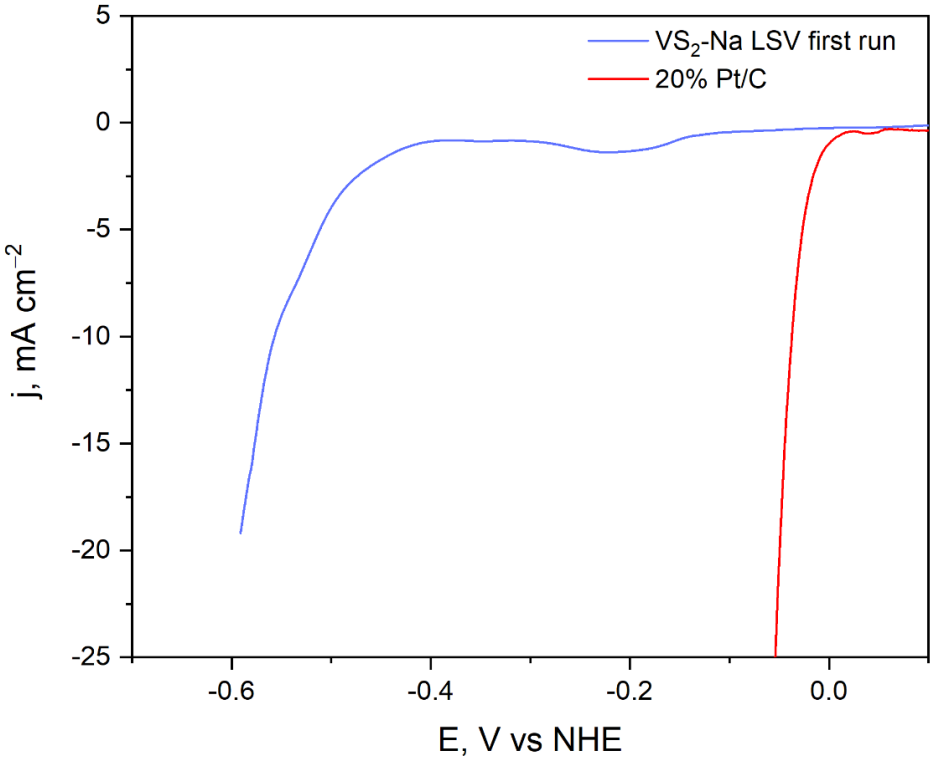

Figure 3-12. *Comparison of current densities achieved by VS_2-Na and commercial 20% Pt/C catalyst. Catalysts were prepared on a working glassy carbon electrode and detailed procedure can be found in chapter 2. Polarization curves were recorded using a sweep rate of 5 mV s^{-1}. 3 electrode setup in 1 M H_2SO_4 electrolyte where glassy carbon modified with catalyst was working electrode, carbon felt was used as a counter electrode and 3 M Ag/AgCl electrode as a reference electrode. Current density is calculated using geometric electrode area (0.071 cm^2).*

However, pre-treatment was ineffective in this case, as the reductive wave at around –200 mV was still present. Further cycling did not help improve the LSV curve's smoothness and eliminate the reductive wave. This can be seen in Figure 3-13, where polarization curves of the first and fifth runs are displayed. Not only is the reductive wave still present, but the current densities achieved by this catalyst drop quite dramatically, considering it was only cycled five times.

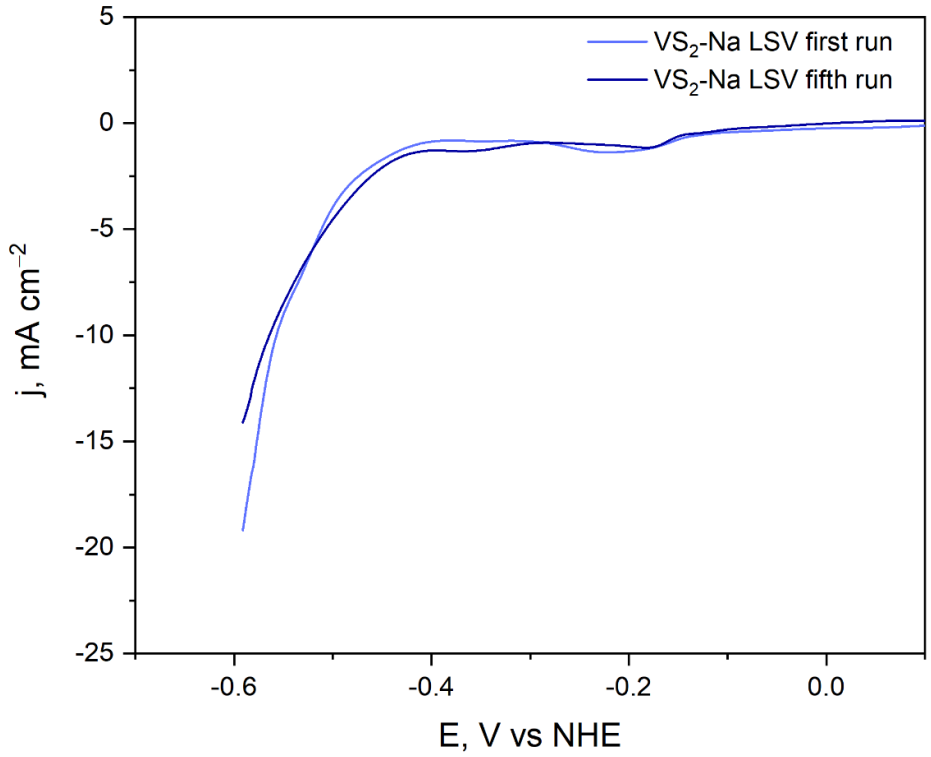

Figure 3-13. *Comparison of 1st and 5th LSV runs on VS_2-Na highlighting that reductive waves could not be removed via pre-treatment of the sample. Polarization curves were recorded using a sweep rate of 5 mV s^{-1}. 3 electrode setup in 1 M H_2SO_4 electrolyte where glassy carbon modified with catalyst was working electrode, carbon felt was used as a counter electrode and 3 M Ag/AgCl electrode as a reference electrode. Current density is calculated using geometric electrode area (0.071 cm^2).*

To further investigate the stability of the catalyst, it was subjected to 100 CV cycles (sweep rate of 100 mV s^{-1}). However, once the polarization curve was recorded after 100 CV cycles, it was revealed that the curve completely flattened, and the catalyst was no longer active toward hydrogen production (Figure 3-14). This result is quite concerning as the nanostructured and even single crystal counterparts of this material have been reported to display high durability. In some cases, overpotentials at which it reaches –10 mA cm^{-2} stay the same even after the catalyst has been subjected to 5000 CV cycles.[18]

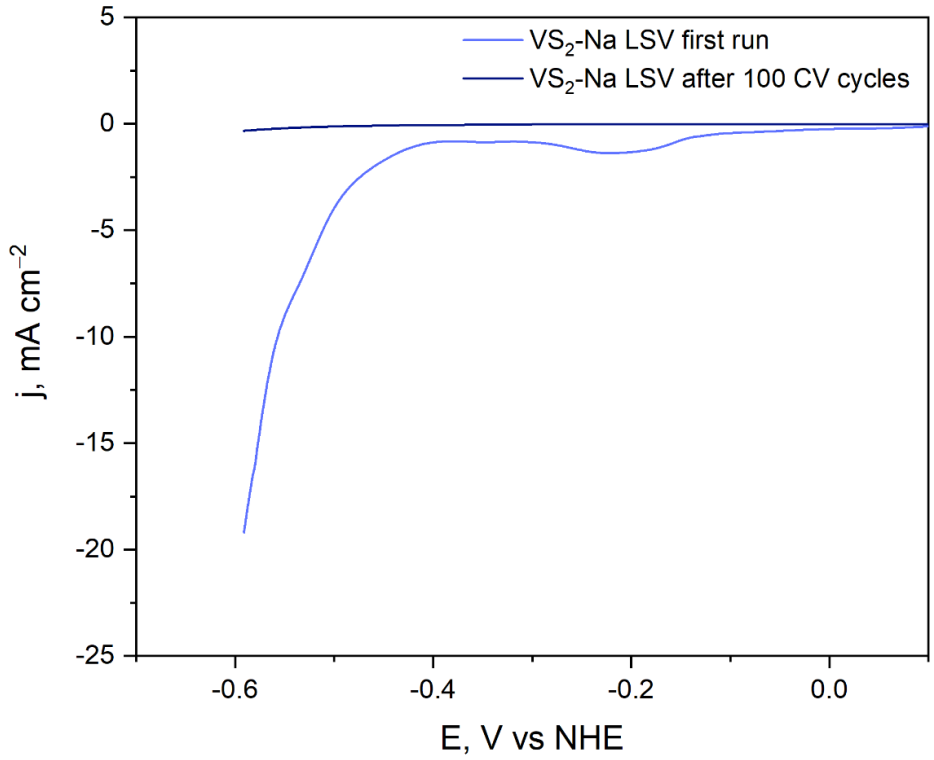

Figure 3-14. *Comparison of polarization curves recorded before and after CV cycling of VS_2-Na. Polarization curves were recorded using a sweep rate of 5 mV s^{-1}. 3 electrode setup in 1 M H_2SO_4 electrolyte where glassy carbon modified with catalyst was working electrode, carbon felt was used as a counter electrode and 3 M Ag/AgCl electrode as a reference electrode. Current density is calculated using geometric electrode area (0.071 cm^2).*

A question arose after electrochemical measurements of VS_2-Na. The reductive wave observed in the scans could potentially arise from defects of deintercalation (*i.e.,* not all sodium being completely removed from the sample). To investigate this, the VS_2 will be prepared from $LiVS_2$ as reports in the literature confirm the full deintercalation of Li.

3.3.2. Synthesis and characterisation of VS_2 from $LiVS_2$

3.3.2.1. Synthesis of $LiVS_2$

Unlike $NaVS_2$, $LiVS_2$ adapts only one crystal structure independently from Li content. $LiVS_2$ adopts the same crystal structure as that of VS_2 - trigonal structure with symmetry group *P-3m1* (164) and is comprised of layers of VS_2 where metal atoms are sandwiched between sulphur atoms. Li ions are positioned between the layers of VS_2. The synthesis of this compound was first reported back in 1971 by *Laar et al.*[67] The procedure involved heating vanadium oxides and lithium carbonate in an atmosphere of H_2S. Due to the lack of

access to H_2S source, the synthetic procedure which relied on the utilization of Li_2S was adopted instead.[68] The literature suggests that stoichiometric amounts of Li_2S, vanadium powder and sulphur powder (sealed in a quartz ampoule under vacuum) should be heated to 700-750 °C for 72 hours. However, we carried out the reaction at 600 °C to keep the synthetic conditions the same as was used for the synthesis of $NaVS_2$ samples. This was done to ensure that the morphology of the products stayed as similar as possible, which would allow for a reliable comparison of catalytic performance.

As displayed in Figure 3-15, PXRD pattern of synthesised $LiVS_2$ is comparable with the calculated pattern based on ICSD. Remarkably, multiple annealings and use of higher temperatures were deemed unnecessary, contrary to previous literature reports.

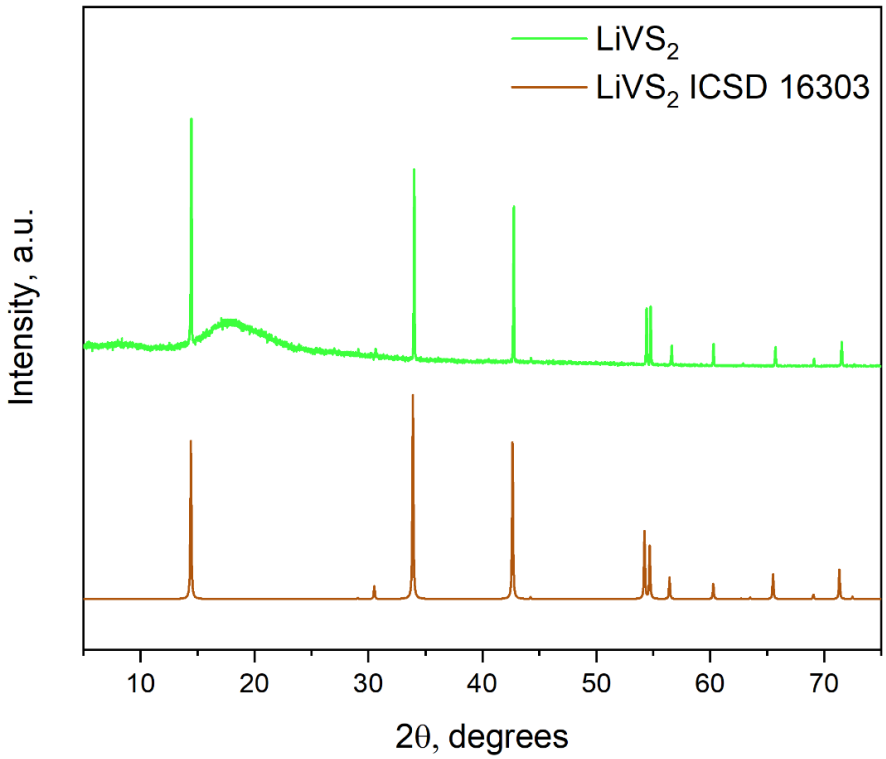

Figure 3-15. *PXRD pattern of the product of reaction between Li_2S, V and S powders sealed under vacuum and heated at 600 °C for 72 hours (top, green). For comparison, calculated diffraction pattern of $LiVS_2$ from ICSD (card number 16303) is displayed at the bottom (brown). Wide 'bump' at 15-20 degrees in the experimental pattern (top, green) comes from an air sensitive holder used in the measurement.*

3.3.2.2. Synthesis of VS_2-Li

As the sample was deemed phase pure $LiVS_2$ according to PXRD, it was then used in a deintercalation reaction. Exactly the same procedure was followed as with $NaVS_2$ to prepare VS_2. The sample prepared via deintercalation from $LiVS_2$ will be referred to as VS_2-Li from now on. The powder diffraction pattern of the product was then collected to identify the phase. As it can be seen from Figure 3-16, the PXRD pattern resembles that of VS_2, indicating no rapid degradation upon exposure to the ambient conditions as the sample was dried and PXRD recorded under ambient conditions. Even though no drastic structural change took place as in the case of $NaVS_2$, the cell parameters of the sample before and after deintercalation can be compared (Table 3-7). It is apparent that lithium deintercalation has taken place as *c* parameter of the unit cell has shrunk. Moreover, the *a* parameter is smaller in a deintercalated sample as well. Even though the VS_2 this time was obtained from $LiVS_2$, the cell parameters match perfectly with VS_2 from $NaVS_2$. This would support the claim that alkali metal can be fully deintercalated from the lattice despite it being Li or Na.

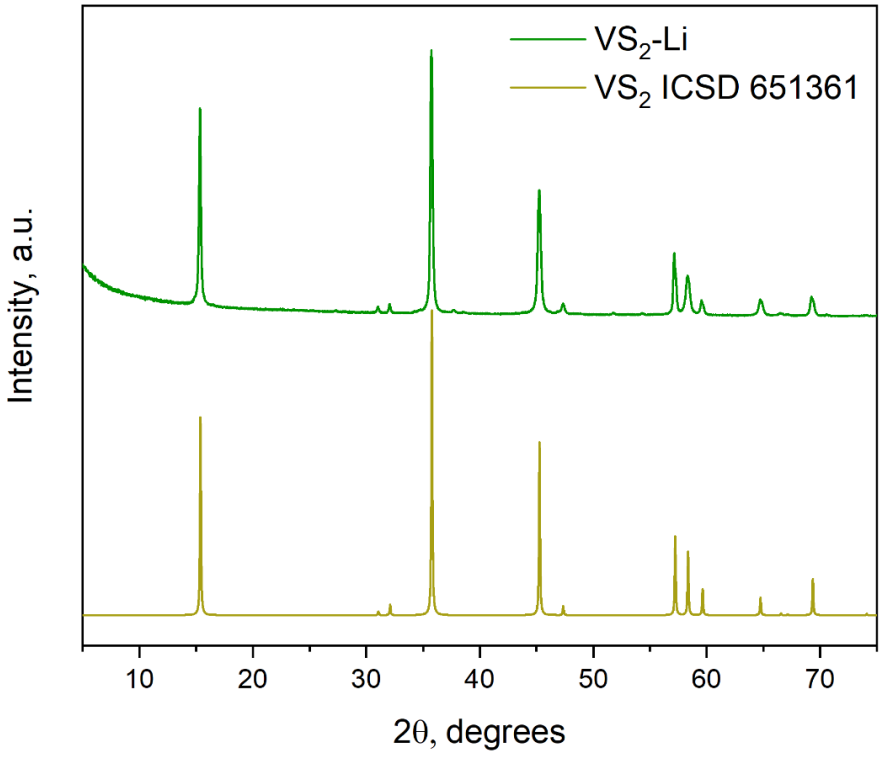

Figure 3-16. *PXRD pattern of the product of deintercalation reaction where $LiVS_2$ was reacted with I_2 solution in acetonitrile for 48 hours at room temperature under continuous stirring (top, green). For comparison, calculated diffraction pattern of VS_2 from ICSD (card number 651361) is displayed at the bottom (mustard).*

Table 3-7. *Unit cell parameters obtained from Le Bail refinement of $LiVS_2$ and VS_2-Li.*

Sample	*a*, Å	c, Å
$LiVS_2$	3.3715(1)	6.1393(1)
VS_2-Li	3.2180(9)	5.7554(8)

3.3.2.3. Composition and morphology of VS_2-Li

The elemental composition of the sample was investigated by EDX analysis. The analysis revealed that the sample, as well as the one made via $NaVS_2$ route, has a nearly perfect metal-to-sulphur ratio (V:S = 1:2.01). The results that are displayed in Table 3-8 indicate that for VS_2 deintercalation route enables the synthesis of highly stoichiometric compounds.

Table 3-8. *EDX data of VS_2-Li. Standard deviation is evaluated based on 12 different points.*

	VS_2-Li at. %	
Element	V	S
Experimental	33.2(14)	66.7(14)
Theoretical	33.3	66.6

To analyse the morphology of the sample, SEM imaging has been done. As it can be seen from the images (Figure 3-17), the sample consists of quite big – the majority of them being approximately 15 μm in at least one dimension – crystallites. The distribution of crystallite size is more uniform than that observed in a VS_2-Na sample. Crystallites have a shape of thicker platelets, and some display large pieces that consist of stacks of thin platelets. This morphology agrees well with the compound having a layered structure. The crystals consisting of multiple stacked platelets display delamination in between the platelets.

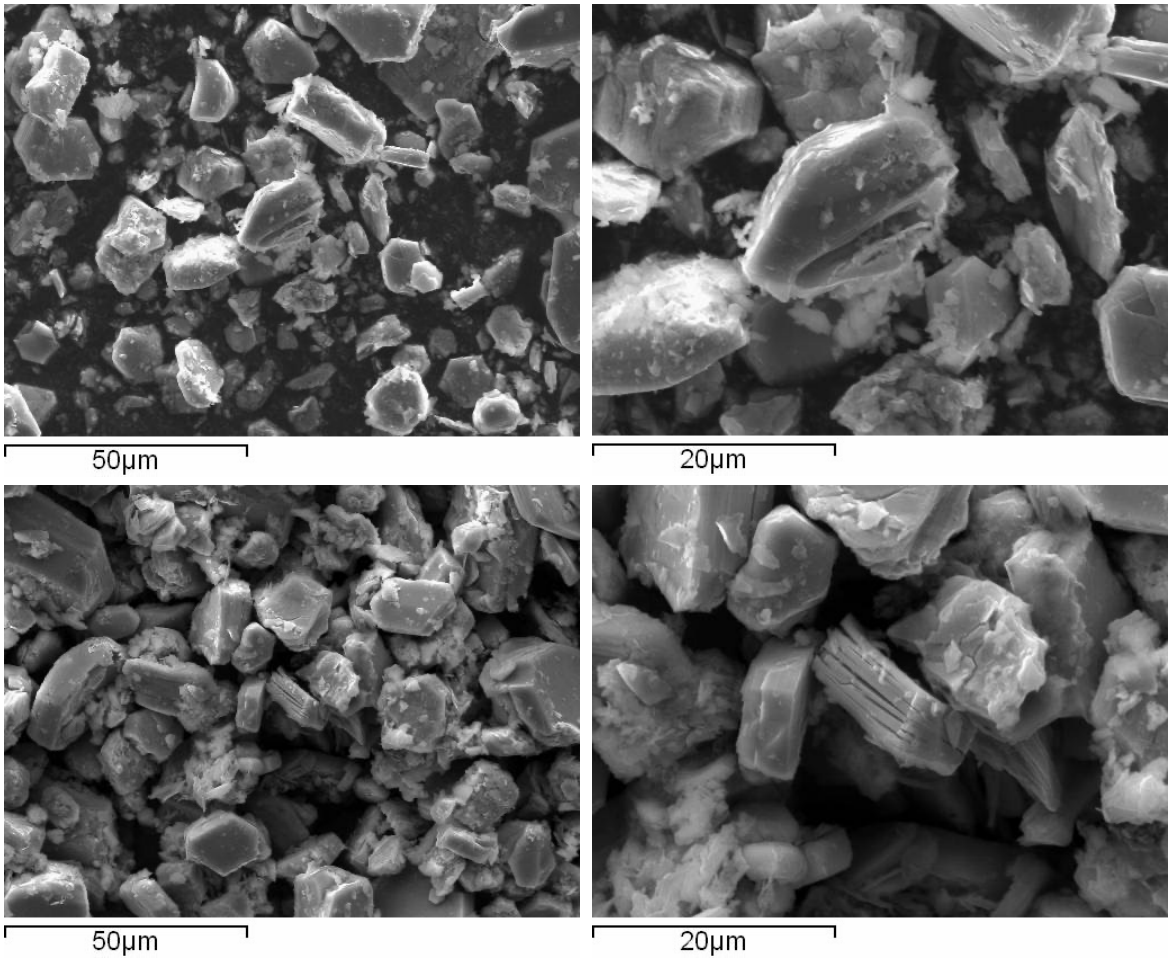

Figure 3-17. *SEM images of VS_2-Li. Two different magnifications of two different spots are displayed.*

3.3.2.4. VS_2-Li Raman spectroscopy

After an in-depth investigation of the Raman spectrum of VS_2-Na, subsequent VS_2 samples were only measured in capillaries. However, since this sample so far has been remarkably similar to that of VS_2-Na, it came as no surprise that no Raman spectrum could be recorded despite the sample being measured in a capillary. As it can be seen from Figure 3-18, just like VS_2-Na, this sample also decomposed at higher laser intensity (10% of full power). Despite not being able to get the Raman spectrum of VS_2-Li, measurements in capillary are highly beneficial, as they would allow seeing any other impurities or possible oxidation of the sample while handling it during/after deintercalation reactions. The fact that only decomposition of this sample can be observed in capillary measurements can be an indirect confirmation of sample being VS_2.

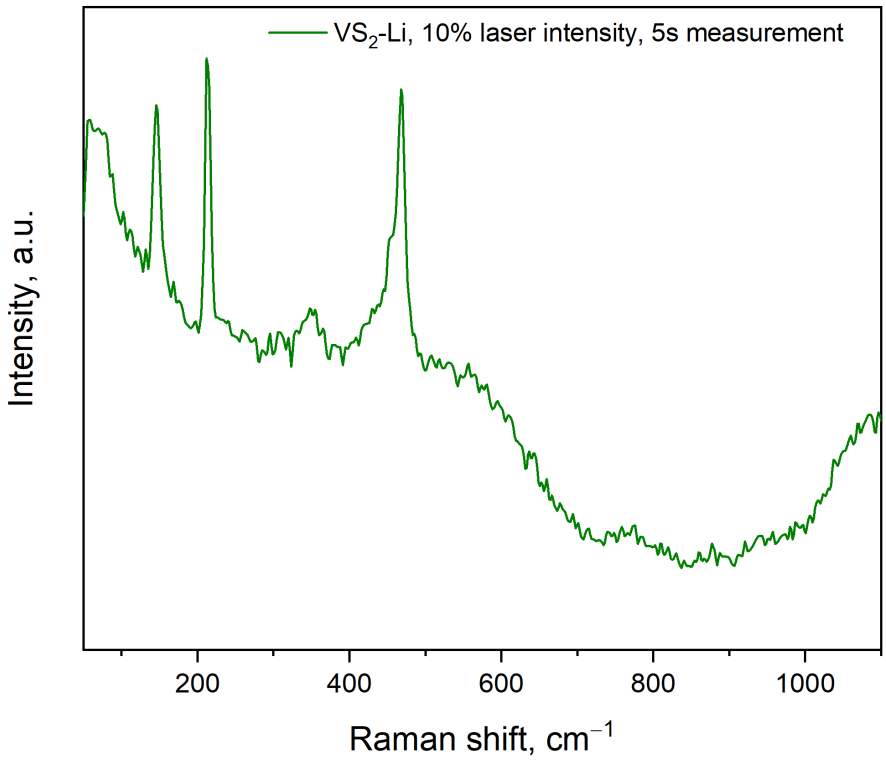

Figure 3-18. *Raman spectrum of sample VS_2-Li. Spectrum was collected on a sample sealed in a capillary under an inert (Ar) atmosphere.*

3.3.2.5. Electrocatalytic activity of VS_2-Li toward HER

Electrochemical testing revealed that VS_2-Li sample displays the same electrochemical behaviour as VS_2-Na sample (Figure 3-19). All the characteristics – reductive wave at around –200 mV vs NHE, high overpotentials needed to reach –10 mA cm^{-2} and poor stability under CV conditions – are identical between the two samples. Moreover, there is a more dramatic increase in the overpotentials at –10 mA cm^{-2} in VS_2-Li sample. The reductive wave does not show any improvement with cycling and only disappears together with the polarisation curve flattening completely.

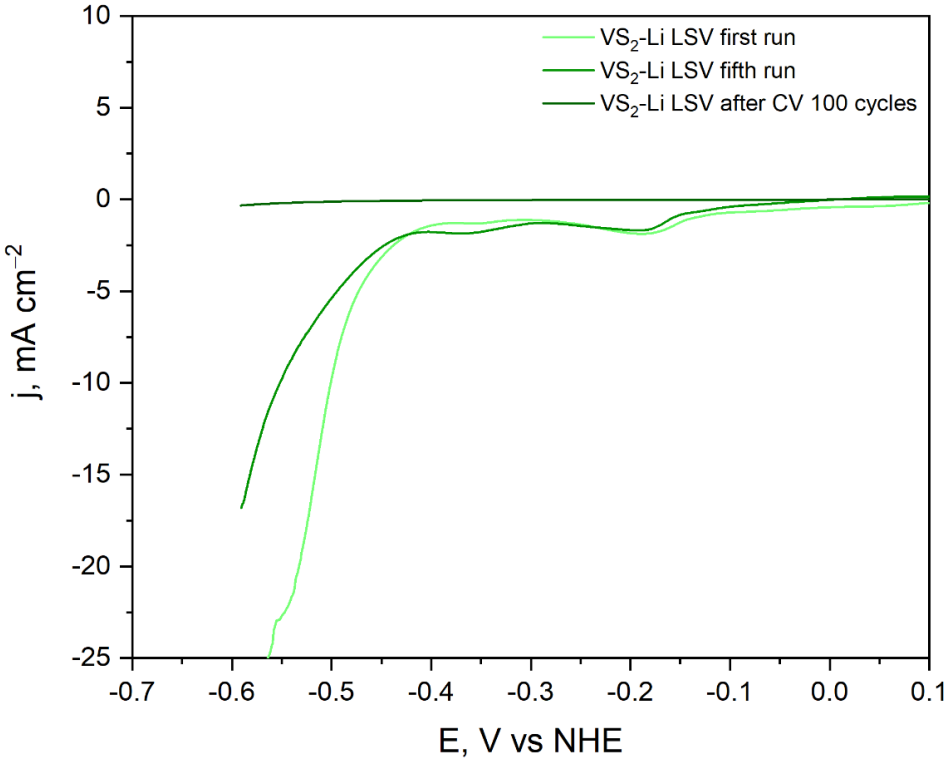

Figure 3-19. *Comparison of 1st and 5th LSV runs as well as LSV post CV cycling of VS_2-Li highlighting that reductive waves could not be removed via pre-treatment of the sample and diminishing catalytic activity. Polarization curves were recorded using a sweep rate of 5 mV s^{-1}. Three-electrode setup in 1 M H_2SO_4 electrolyte where glassy carbon modified with catalyst was working electrode, carbon felt was used as a counter electrode and 3 M Ag/AgCl electrode as a reference electrode. Current density is calculated using geometric electrode area (0.071 cm^2).*

While no distinct difference was noticed between the two samples – whether it was Na deintercalation or Li deintercalation – the electrochemical characteristics of the sample pointed out that the reduction of sample took place. However, to exclude the possibility that the reduction wave is due to impurities (undetectable by XRD) from the deintercalation reaction, a VS_2 sample was prepared following a commonly used literature procedure.

3.3.3. Synthesis and characterisation of VS_2-h

3.3.3.1. Synthesis of VS_2-h

The most popular synthesis method for VS_2 in the literature is a one-step hydrothermal synthesis. While there is some variation in vanadium and sulphur sources used as well as solvents, the most popular ones have been sodium orthovanadate, thioacetamide and water.

The detailed procedure can be found in chapter 2 of this thesis, but in short, the procedure adapted from a report by Qu *et al.* went as follows: Na_3VO_4 and thioacetamide (molar ratio 1:5) were dissolved in water. It was followed by heating at 160 °C in a Teflon-lined stainless-steel autoclave. The product was then washed with water and ethanol and dried in a desiccator overnight.

As it can be seen from Figure 3-20, the PXRD pattern collected on the sample is consistent with the simulated pattern. However, when compared to the VS_2 samples obtained via the deintercalation route, the crystallinity of this sample is low as the peaks have a broader shape. This should be expected for nanostructured samples, and the pattern points towards a successful synthesis of a nanostructured sample. VS_2 prepared via hydrothermal route will be referred to as VS_2-h from this point on.

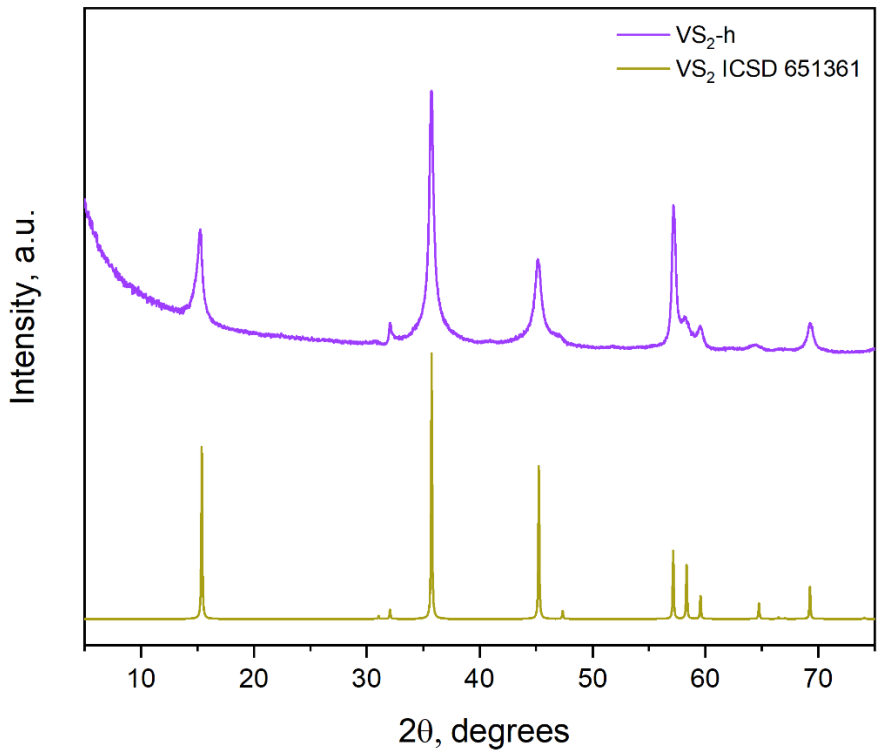

Figure 3-20. *PXRD pattern of VS_2-h (top, purple). For comparison, calculated diffraction pattern of VS_2 from ICSD (card number 651361) is displayed at the bottom (mustard).*

3.3.3.2. Composition and morphology of VS_2-h

Elemental analysis by EDX on this sample revealed that the sample has a metal-to-sulphur ratio of V:S = 1:1.95 (Table 3-9). The results of the EDX analysis are displayed in the table below. Given that all three samples discussed in this chapter have the same stoichiometry, it

is essential also to compare the morphology as it can influence the catalytic performance of the sample.

Table 3-9. *EDX data of VS_2-h. Standard deviation is evaluated based on 8 different points.*

	VS_2-h at. %	
Element	V	S
Experimental	33.9(14)	66.1(14)
Theoretical	33.3	66.6

SEM imaging has been carried out to determine the morphology. As could have been expected from broad peaks in diffraction pattern – the sample displays significantly different morphology compared with products prepared by the deintercalation method. The sample is comprised of flower-like particles (Figure 3-21). Each ‘blossom’ is approximately 10-20 μm in diameter, while the ‘petals’ are extremely thin. This way, a noticeably larger surface area is expected to be exposed to the electrolyte, which would greatly help in the catalytic application as more active sites would be accessible for hydrogen evolution.

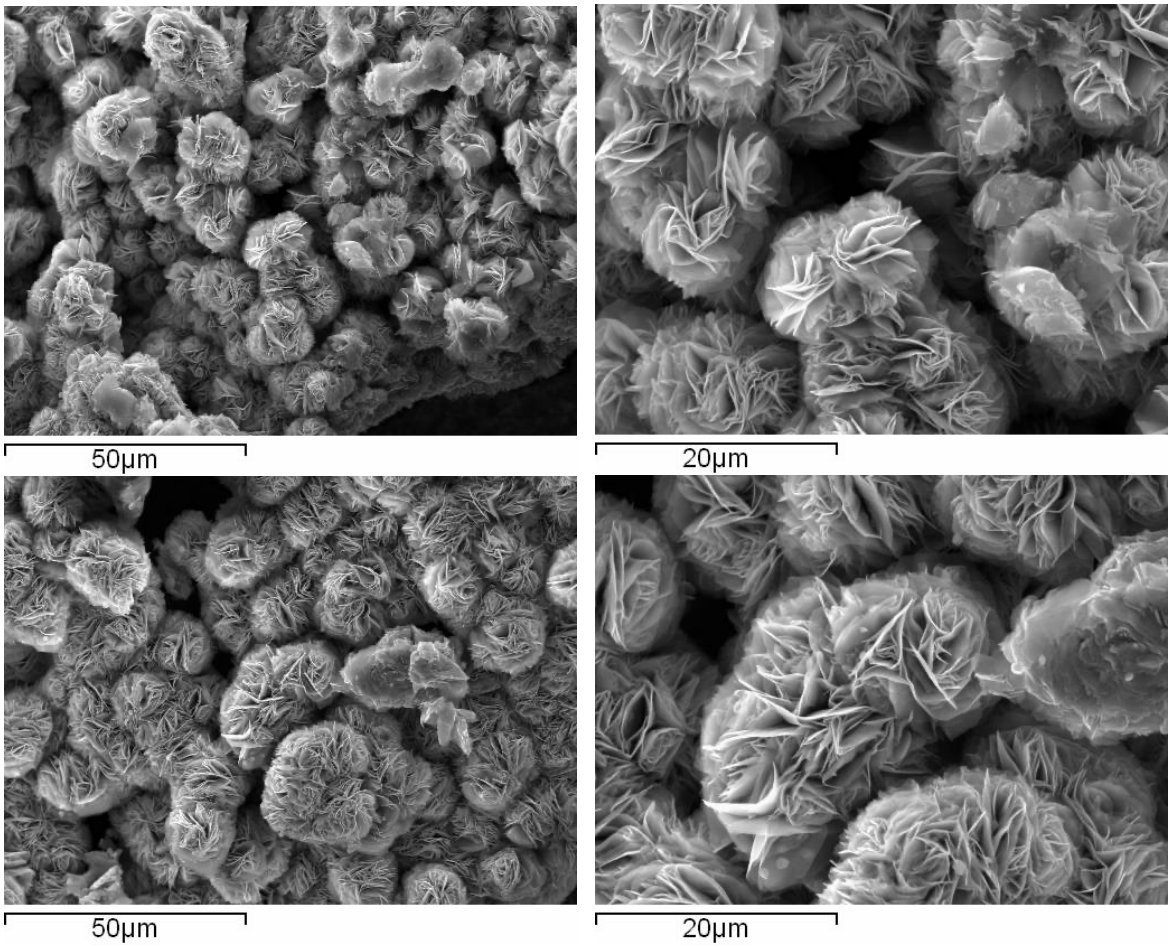

Figure 3-21. *SEM images of VS_2-h. Two different magnifications of the same spot are displayed.*

3.3.3.3. VS_2-h Raman spectroscopy

Having confirmed the morphology of the sample, Raman measurements have been carried out. It was expected that sample with the most common structure reported in the literature for VS_2 would improve the chances of observing the reported Raman spectrum. However, the usual caution of sample oxidation was considered; therefore, this sample, like the other two discussed above, was measured in a capillary sealed under an inert (Ar) atmosphere. Unfortunately, the spectrum that was observed (Figure 3-22) was again either lacking any peaks at low laser intensities or only had sulphur peaks show up at higher laser intensities.

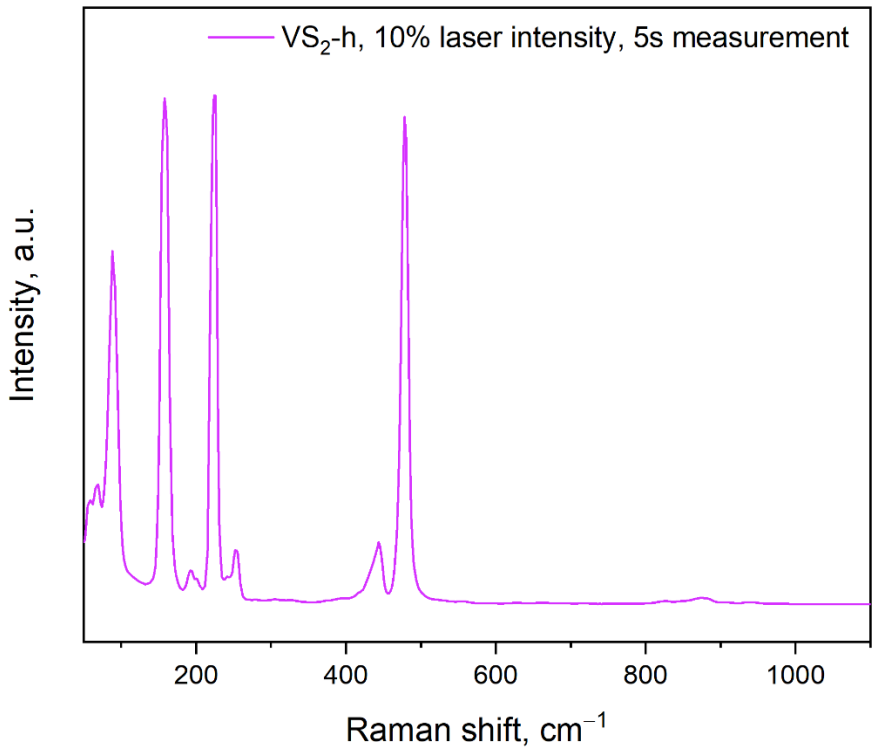

Figure 3-22. *Raman spectrum of sample VS_2-h. Spectrum collected on a sample sealed in a capillary under inert (Ar) atmosphere. All peaks are consistent with those expected from S suggesting decomposition of the sample in the beam.*

3.3.3.4. Electrocatalytic activity of VS_2-h toward HER

Following the characterisation of the sample, electrochemical measurements were carried out. Using the same setup as for the other two samples, polarization curves and CV measurements were done. Despite having different morphology, the VS_2-h sample showed similar characteristic to those prepared by the deintercalation method. This, however, ruled out the possibility that it was an oxidative deintercalation process (due to traces of Li or Na remaining within the structure) that was causing the reductive waves to appear at –200 mV *vs* NHE. The overpotential needed to reach current densities of –10 mA cm^{-2} was –580 mV. The value of the potential is extremely high, which contradicts literature values by a significant margin (Table 3-1). Although numerous studies carried out so far tended to prove that nanostructuring leads to dramatically improved catalytic activity, this seems not to be the case despite the relatively open morphology of hydrothermally synthesised VS_2 reported in our work. Furthermore, CV studies show that the LSV curve completely flattens out just after 100 scans (Figure 3-23).

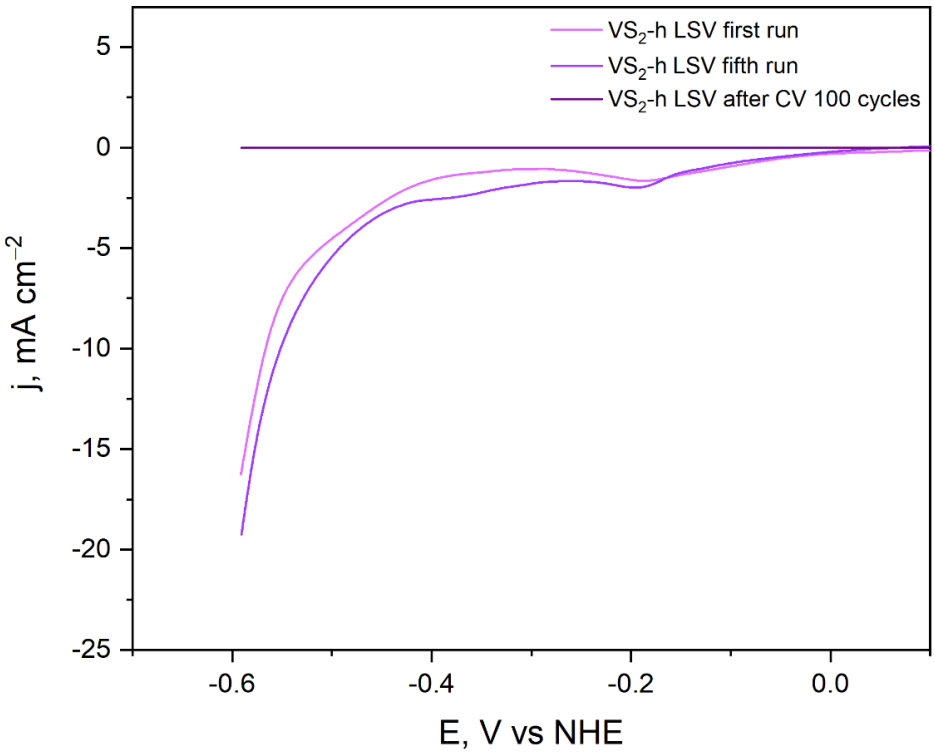

Figure 3-23. *Comparison of 1st and 5th LSV runs as well as LSV pre and post CV cycling of VS_2-h highlighting that reductive waves could not be removed via pre-treatment of the sample and diminishing catalytic activity. Polarization curves were recorded using a sweep rate of 5 mV s^{-1}. 3 electrode setup in 1 M H_2SO_4 electrolyte where glassy carbon modified with catalyst was working electrode, carbon felt was used as counter electrode and 3 M Ag/AgCl electrode as reference electrode. Current density is calculated using geometric electrode area (0.071 cm^2).*

Overall, independent of the synthetic method, VS_2 prepared in this work showed poor performance. Further investigation was carried out to get a deeper insight into the cause of poor electrochemical performance.

3.3.4. Further look into electrocatalytic performance of VS_2 samples

We carried out PXRD measurements to investigate the cause of poor electrochemical stability upon which VS_2 decomposes. The PXRD measurements were run *ex situ* on the VS_2 samples immobilized onto glassy carbon electrodes before and after electrochemical testing. All diffraction patterns were also compared to that of bare glassy carbon, as there are quite a few peaks appearing from the electrode itself, as well as the aluminium holder that is being used to mount the electrode to the diffractometer. Interestingly, in the case of

alkali metal deintercalated samples, a remarkably high preferred orientation can be observed in diffraction patterns (Figure 3-24 and Figure 3-25). Only the reflections of 00l planes are visible. Despite this, there seems to be no change in the pattern before and after cycling in acidic media. A hydrothermal sample is quite different from its alkali deintercalated counterparts. There are multiple sharp peaks in the pattern, that most likely arise from Nafion used in the inks (Figure 3-26). Moreover, only one peak that belongs to the sample itself can be observed in the pattern, making it hard to confidently identify the phase of the sample before and after the measurement. X-ray diffraction measurements confirm that phase decomposition does not proceed into the bulk of the sample during the electrochemical measurement. The decomposition at the surface, however, cannot be excluded entirely.

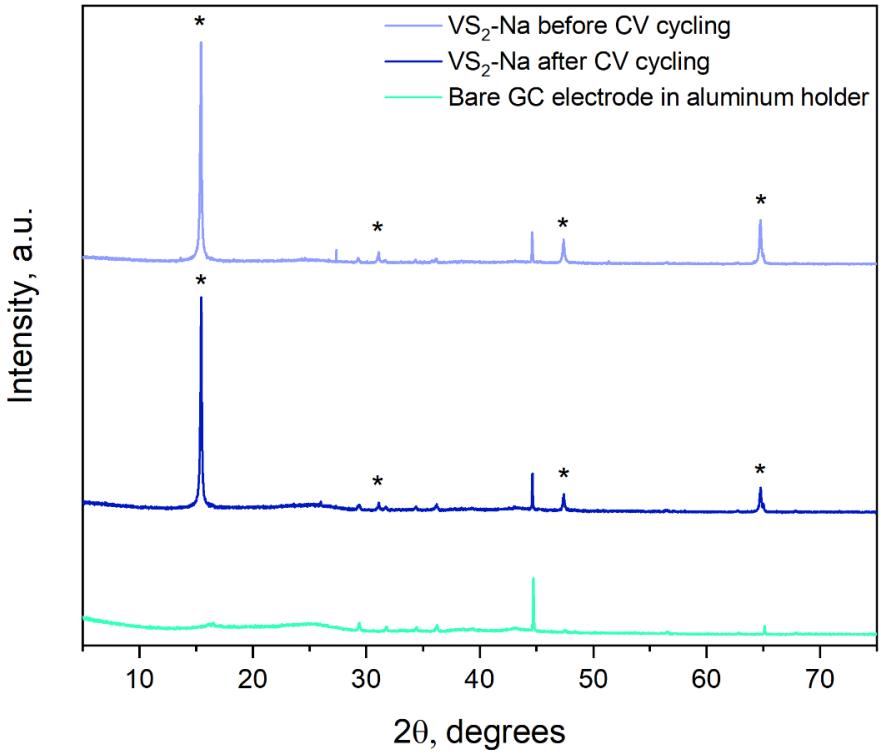

Figure 3-24. *PXRD patterns of VS_2-Na (top, light blue) and post (middle, dark blue) CV cycling. The patterns have been recorded directly on glassy carbon electrode. For comparison, PXRD pattern of bare glassy carbon electrode is displayed (bottom, green). VS_2 peaks are marked with an asterisk (*).*

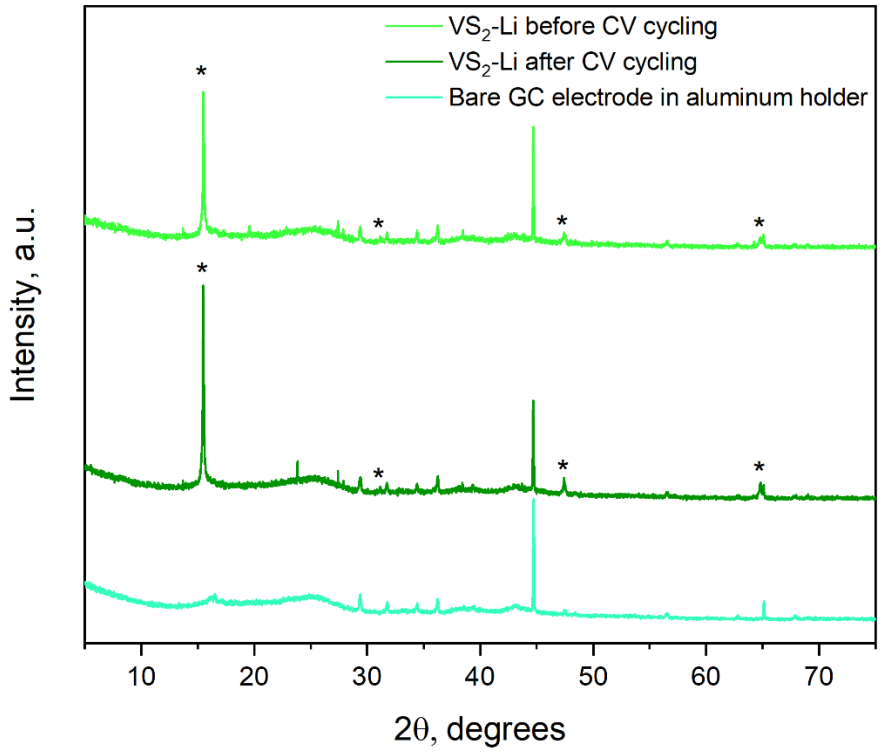

Figure 3-25. *PXRD patterns of VS_2-Li pre (top, light green) and post (middle, dark green) CV cycling. The patterns have been recorded directly on glassy carbon electrode. For comparison, PXRD pattern of bare glassy carbon electrode is displayed (bottom, green). VS_2 peaks are marked with an asterisk (*).*

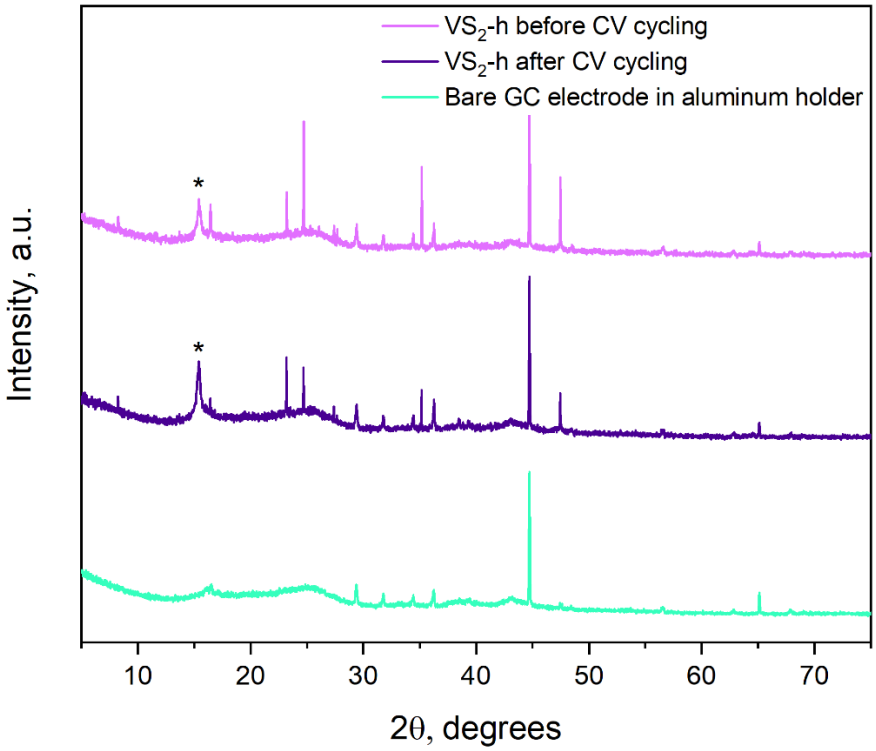

Figure 3-26. *PXRD patterns of VS_2-h catalyst pre (top, light purple) and post (middle, purple) CV cycling. The patterns have been recorded directly on glassy carbon electrode. For comparison, PXRD pattern of bare glassy carbon electrode is displayed (bottom, green). VS_2 peaks are marked with an asterisk (*).*

Another interesting result noticed during the comparison of electrochemical activity towards HER of samples with dramatically different morphologies was the exact same overpotential needed to achieve benchmark current densities. After learning that other small reductive waves present in scans of the sample only diminish when the current densities diminish at the same time, concern has arisen. Despite bubble production that is visible to the bare eye on the electrode when approaching benchmark current densities, it could be just another reduction wave. To investigate this scenario, the catalysts were tested again, this time recording the polarization curve over a much wider potential range. These measurements confirmed the theory, as the polarization curve would have a very intense reduction peak at potentials of –600 mV vs NHE. This was true for all three samples. However, the hydrothermal sample, while still having the same reduction wave, seems to have a narrower wave. Therefore, after getting over the reduction wave, the current densities would start increasing at lower potentials than those for alkali metal deintercalated samples. The second scan run on the same electrode would reveal that the reduction wave has been eliminated by

a single LSV scan in a reductive region (Figure 3-27 – Figure 3-29). This second scan is now believed to represent the genuine HER polarization curve for materials of interest.

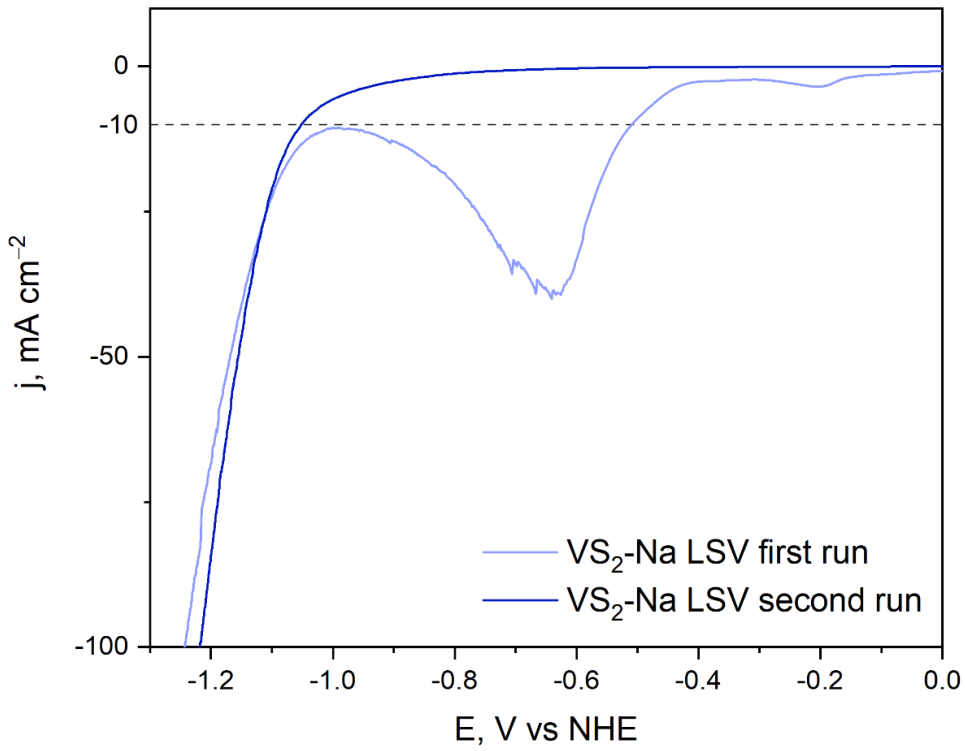

Figure 3-27. *Polarization curves recorded on sample VS_2-Na over wider potential window. The first scan reveals a reduction wave, whereas a second scan shows the actual HER overpotential. Polarization curves were recorded using a sweep rate of 5 mV s^{-1}. Three electrode setup in 1 M H_2SO_4 electrolyte where glassy carbon modified with catalyst was working electrode, carbon felt was used as a counter electrode and 3 M Ag/AgCl electrode as a reference electrode. Current density is calculated using geometric electrode area (0.071 cm^2).*

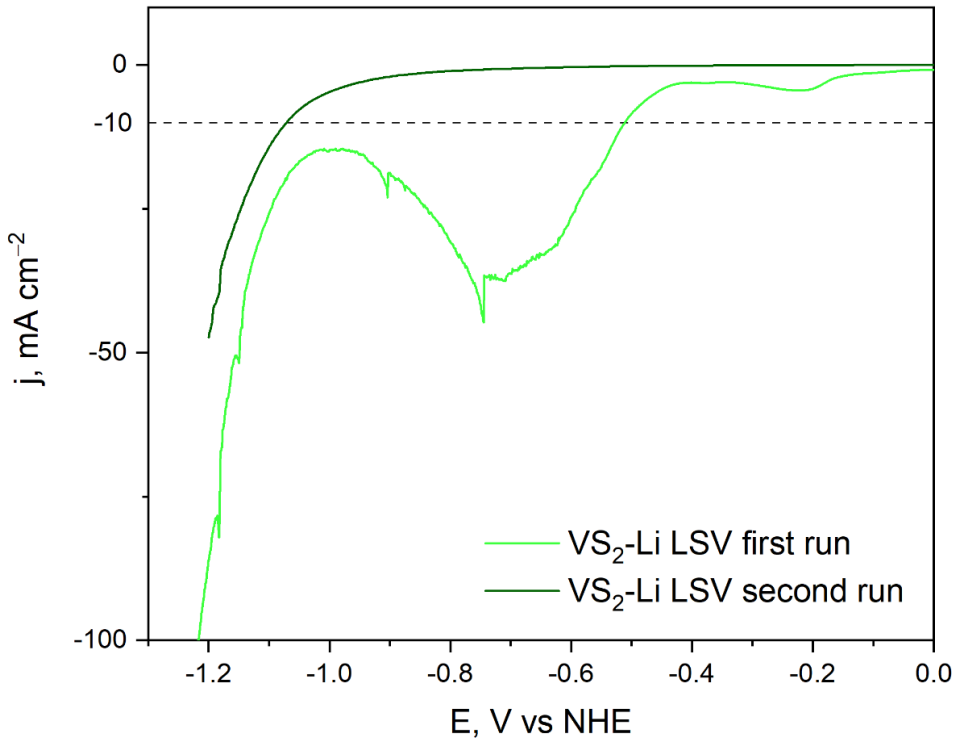

Figure 3-28. *Polarization curves recorded on sample VS_2-Li over wider potential window. The first scan reveals a reduction wave, whereas a second scan shows the actual HER overpotential. Polarization curves were recorded using a sweep rate of 5 mV s^{-1}. Three electrode setup in 1 M H_2SO_4 electrolyte where glassy carbon modified with catalyst was working electrode, carbon felt was used as a counter electrode and 3 M Ag/AgCl electrode as a reference electrode. Current density is calculated using geometric electrode area (0.071 cm^2).*

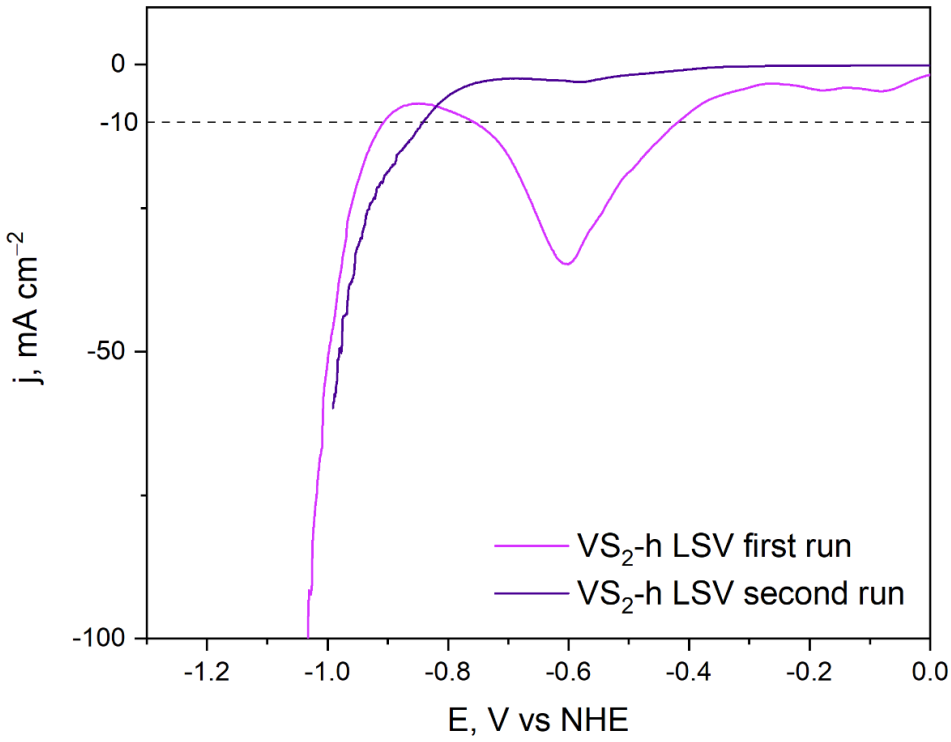

Figure 3-29. *Polarization curves recorded on sample VS_2-h over wider potential window. The first scan reveals a reduction wave, whereas a second scan shows the actual HER overpotential. Polarization curves were recorded using a sweep rate of 5 mV s^{-1}. Three electrode setup in 1 M H_2SO_4 electrolyte where glassy carbon modified with catalyst was working electrode, carbon felt was used as a counter electrode and 3 M Ag/AgCl electrode as a reference electrode. Current density is calculated using geometric electrode area (0.071 cm^2).*

The newly obtained overpotentials to achieve benchmark current densities are summarized in Table 3-10. These overpotentials are extremely high and deem VS_2 as an unsuitable catalyst for HER. Moreover, the stability measurements have not been conducted, as cycling glassy carbon electrode at such high potentials could damage it as well as influence the performance of catalyst. This is due to overpotentials needed to achieve benchmark current densities, especially in a case of alkali deintercalated samples, which are approaching the limit of inert region of glassy carbon in acidic media.[69]

Table 3-10. *Overpotentials needed to reach a benchmark current density of –10 mA cm^{-2} of VS_2 samples*

Sample	VS_2-Na	VS_2-Li	VS_2-h
Overpotential at –10 mA cm^{-2} vs NHE	−1051 mV	−1071 mV	−840 mV

When comparing the overpotentials, it can be noticed that the hydrothermal sample is now outperforming alkali metal deintercalated samples by a little more than 200 mV. Alkali metal deintercalated samples show similar overpotentials; however, they are still 20 mV apart. While it does not seem significant due to very high values, it is still worth further investigation as to where these shifts in overpotentials come from.

To do that, ECSA has been estimated for each catalyst. This has been done by measuring the double layer capacitance and figures from which values have been extracted are in Appendix (Figure A 6, Figure A 7, Figure A 8). As it can be seen from Figure 3-30, there seems to be a correlation between overpotential and double-layer capacitance of the samples. The biggest double layer capacitance is observed for the nanostructured VS_2-h sample, it is then followed by almost three times smaller values observed for VS_2-Na. VS_2-Li double-layer capacitance values were smallest of the three samples. In turn, the lowest overpotential was observed for VS_2-h sample, followed by VS_2-Na and VS_2-Li. There is high variation in double layer capacitance values reported for various VS_2 morphologies and are displayed in Table 3-1. When compared to the samples of similar morphology, C_{DL} of VS_2-h sample in this work is lower than its literature counterparts.

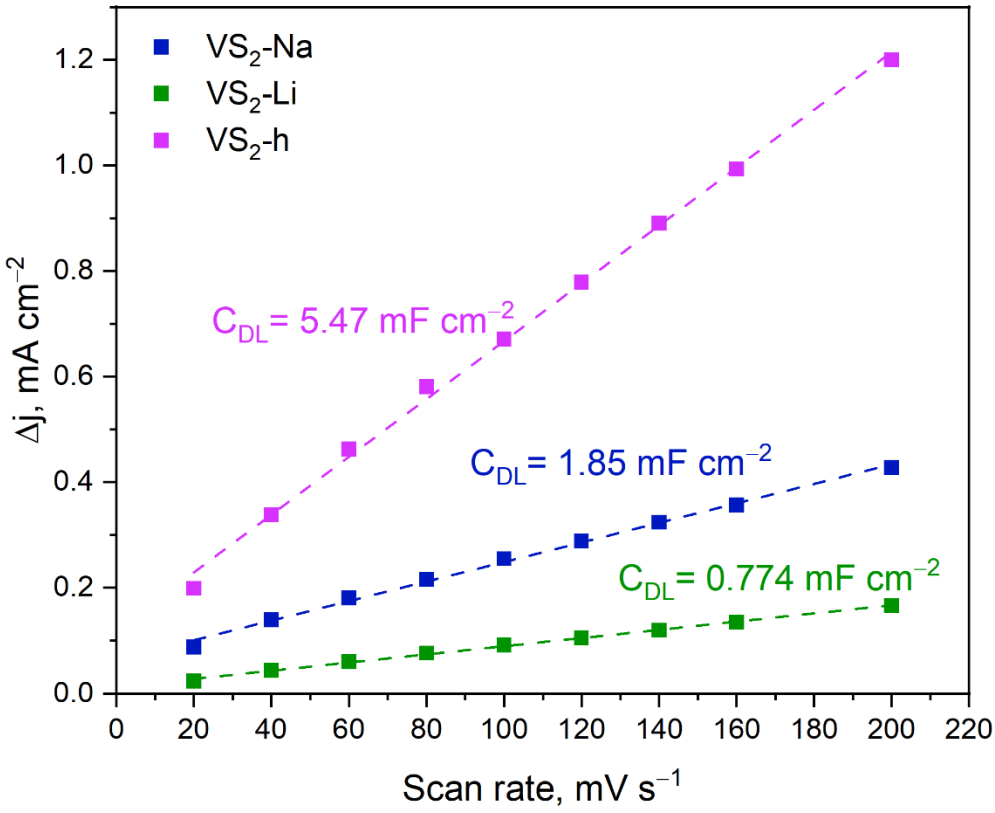

Figure 3-30. *Evaluation of double layer capacitance of three different VS_2 samples. Current density difference (reading taken at 209 mV vs NHE in 1 M H_2SO_4) is plotted against scan rate.*

3.4. Summary and comparison of all VS_2 samples

All three explored methods for synthesis of VS_2 were successful and resulted in pure phase samples. While alkali metal deintercalated samples exhibited very high crystallinity, the VS_2-h sample had much broader X-ray diffraction peaks. Broad peaks were hinting towards a different morphology of the sample which was confirmed by SEM. Despite that, the unit cell parameters and match with the model according to Le Bail refinement revealed that samples have an identical crystal structure. As it can be seen from Table 3-11, only the *c* parameter of the hydrothermally made VS_2 is of slightly lower values than the rest of the samples.

Table 3-11. *Unit cell comparison of all three VS_2 samples obtained from Le Bail refinement of PXRD data*

Sample	a, Å	c, Å
VS_2-Na	3.2167(8)	5.7503(6)
VS_2-Li	3.2180(9)	5.7554(8)
VS_2-h	3.209(6)	5.759(9)

As well as unit cell parameters, the sample stoichiometry determined by energy dispersive X-ray analysis revealed all samples to be close to the ideal V:S = 1:2 ratio (Table 3-12). While alkali metal deintercalated samples were slightly sulphur rich, the hydrothermal sample showed a minor sulphur deficiency. The main difference in the samples is their morphology.

Table 3-12. *Summary of EDX data of VS_2 samples. Standard deviation is evaluated based on 12 different points for samples VS_2-Na and VS_2-Li and 8 different points for VS_2-h.*

	VS_2-Na at. %		VS_2-Li at. %		VS_2-h at. %	
Element	V	S	V	S	V	S
Experimental	32.9(11)	67.1(11)	33.2(14)	66.7(14)	33.9(14)	66.1(14)
Theoretical	33.3	66.6	33.3	66.6	33.3	66.6

Since it was not possible to maintain the same morphology while applying different synthetic methods, it was anticipated that discrepancies in electrochemical behaviour would arise. Surprisingly, apart from improvements in overpotential (Table 3-13), no other discrepancies

were observed. Even with improvement in overpotential for nanostructured VS_2-h, −840 mV vs NHE is an extremely high value, rendering the catalyst poor for hydrogen evolution reaction.

Table 3-13. *Summary of potentials needed to achieve −10 mA cm^{-2} on the second LSV run as well as double layer capacitance of all three samples.*

Sample	VS_2-Na	VS_2-Li	VS_2-h
E at −10 mA cm^{-2} vs NHE	−1051	−1071	−840
C_{DL}, mF cm^{-2}	1.85	0.774	5.47

While it was speculated that oxidative deintercalation used to obtain VS_2-Na and -Li might have been the reason behind the reductive curves, the VS_2-h sample expressing the same reductive curve deemed this speculation invalid (Table 3-14). Interestingly, the reductive wave in the VS_2-h sample is narrower than in VS_2-Na and VS_2-Li samples. When the peak area is integrated, the value of the charge passed is obtained. If a reduction wave arises from surface oxides alone it is interesting to see that the hydrothermal sample is supposedly coated by twice as much oxide. However, from ECSA values estimated from double layer capacitance measurements, the active surface area of VS_2-h is at least five times larger than that of its counterparts VS_2-Na and VS_2-Li. With a much larger surface area of VS_2-h sample (as seen from SEM images), and assuming that both morphologies are equally prone to oxidation it is unexpected that the values are only twofold different. With lots of ambiguity surrounding the processes behind the reduction peak there could be a possibility that the reductive wave could be impacted by both – surface oxides and intrinsic electrochemical characteristics of VS_2.

Table 3-14. *Summary of reduction wave characteristics for all three VS_2 samples indicating that reduction wave is not a fault arising from oxidative deintercalation.*

	Reduction wave range, mV vs NHE	Reduction wave $peak_{max}$ position, mV vs NHE	Current density at $peak_{max}$, mA cm^{-2}	Q, mC (by integrating peak area)
VS_2-Na	−414-992	−628	−39.12	−107
VS_2-Li	−414-990	−658	−35.16	−111
VS_2-h	−310-862	−603	−34.88	−206

3.5. Conclusions

In summary, the chapter focused on the synthesis of stoichiometric layered VS_2 that cannot be synthesised by standard solid-state synthesis. The synthetic route *via* alkali metal intercalates ($NaVS_2$ and $LiVS_2$) has been successfully applied in order to produce phase pure VS_2. This allowed for an insight into the intrinsic electrochemical behaviour of this material, where overpotential is not enhanced by synergistic effects with carbon nanostructures or nanostructured morphology of the sample itself. Samples have displayed a reductive wave that is too intense to arise from surface oxides. However, it does disappear after just one cathodic scan. The possibility that the wave arises because of oxidative deintercalation used in sample preparation has been disproved when hydrothermal synthesis was used to synthesise VS_2. While having very similar unit cell and sample stoichiometry and not being subjected to oxidative processes during synthesis, the VS_2-h sample was no different when it came to electrochemical properties, thus confirming, that it is intrinsic electrochemistry of VS_2. Once the reduction wave is removed, the true overpotential of layered VS_2 was revealed and ranged from −840 mV vs NHE for VS_2-h to −1071 mV vs NHE for VS_2-Li, rendering the catalyst extremely inefficient for electrochemical hydrogen evolution reaction.

3.6. References

1. J. C. McGlynn, T. Dankwort, L. Kienle, N. A. G. Bandeira, J. P. Fraser, E. K. Gibson, I. Cascallana-Matías, K. Kamarás, M. D. Symes, H. N. Miras and A. Y. Ganin, The rapid electrochemical activation of $MoTe_2$ for the hydrogen evolution reaction, *Nat. Commun.*, 2019, **10**, 4916.

2. J. C. McGlynn, M. Friskey and A. Y. Ganin, Parameter optimisation for electrochemically activated $MoTe_2$, *Sustain. Energy Fuels*, 2020, **4**, 4473–4477.

3. J. Wang, N. Wang, Y. Guo, J. Yang, J. Wang, F. Wang, J. Sun, H. Xu, Z.-H. Liu and R. Jiang, Metallic-Phase MoS_2 Nanopetals with Enhanced Electrocatalytic Activity for Hydrogen Evolution, *ACS Sustain. Chem. Eng.*, 2018, **6**, 13435–13442.

4. D. Voiry, M. Salehi, R. Silva, T. Fujita, M. Chen, T. Asefa, V. B. Shenoy, G. Eda and M. Chhowalla, Conducting MoS_2 nanosheets as catalysts for hydrogen evolution reaction, *Nano Lett.*, 2013, **13**, 6222–6227.

5. P. M. Pataniya and C. K. Sumesh, Enhanced electrocatalytic hydrogen evolution reaction by injection of photogenerated electrons in Ag/WS_2 nanohybrids, *Appl. Surf. Sci.*, 2021, **563**, 150323.

6.. L. Xie, L. Wang, W. Zhao, S. Liu, W. Huang and Q. Zhao, WS_2 moiré superlattices derived from mechanical flexibility for hydrogen evolution reaction, *Nat. Commun.*, 2021, **12**, 1–9.

7. H. Zhang, L. M. Liu and W. M. Lau, Dimension-dependent phase transition and magnetic properties of VS_2, *J. Mater. Chem. A*, 2013, **1**, 10821–10828.

8. H. Pan, Metal dichalcogenides monolayers: Novel catalysts for electrochemical hydrogen production, *Sci. Rep.*, 2014, **4**, 1–6.

9. C. Tsai, K. Chan, J. K. Nørskov and F. Abild-Pedersen, Theoretical insights into the hydrogen evolution activity of layered transition metal dichalcogenides, *Surf. Sci.*, 2015, **640**, 133–140.

10. Q. He, X. Chen, S. Chen, L. Liu, F. Zhou, X. B. Li and G. Wang, Electrochemical Hydrogen Evolution at the Interface of Monolayer VS_2 and Water from First-Principles Calculations, *ACS Appl. Mater. Interfaces*, 2019, **11**, 2944–2949.

11. N. Ran, B. Sun, W. Qiu, E. Song, T. Chen and J. Liu, Identifying Metallic Transition-Metal Dichalcogenides for Hydrogen Evolution through Multilevel High-Throughput Calculations and Machine Learning, *J. Phys. Chem. Lett.*, 2021, **12**, 2102–2111.

12. Y. Wang, Z. Sofer, J. Luxa and M. Pumera, Lithium Exfoliated Vanadium Dichalcogenides (VS_2, VSe_2, VTe_2) Exhibit Dramatically Different Properties from Their Bulk Counterparts, *Adv. Mater. Interfaces*, 2016, **3**, 1–8.

13. J. Zhang, C. Zhang, Z. Wang, J. Zhu, Z. Wen, X. Zhao, X. Zhang, J. Xu and Z. Lu, Synergistic Interlayer and Defect Engineering in VS_2 Nanosheets toward Efficient Electrocatalytic Hydrogen Evolution Reaction, *Small*, 2018, **14**, 1–10.

14. W. Zhang, X. Chen, J. Zhang, C. Tuo, L. Ji, H. Li, X. Zhang and F. Yang, Exposure of active edge structure for electrochemical H2 evolution from VS_2/MWCNTs hybrid catalysts, *Int. J. Hydrogen Energy*, 2018, **43**, 22949–22954.

15. J. Xu, Y. Zhu, B. Yu, C. Fang and J. Zhang, Metallic 1T-VS_2 nanosheets featuring V^{2+} self-doping and mesopores towards an efficient hydrogen evolution reaction , *Inorg. Chem. Front.*, 2019, **6**, 3510–3517.

16. G. M. Kumar, P. Ilanchezhiyan, H. D. Cho, D. J. Lee, D. Y. Kim and T. W. Kang, Ultrathin VS_2 nanodiscs for highly stable electro catalytic hydrogen evolution reaction, *Int. J. Energy Res.*, 2020, **44**, 811–820.

17. W. He, X. Zheng, J. Peng, H. Dong, J. Wang and W. Zhao, Mo-dopant-strengthened basal-plane activity in VS_2 for accelerating hydrogen evolution reaction, *Chem. Eng. J.*, 2020, **396**, 125227.

18. J. Yuan, J. Wu, W. J. Hardy, P. Loya, M. Lou, Y. Yang, S. Najmaei, M. Jiang, F. Qin, K. Keyshar, H. Ji, W. Gao, J. Bao, J. Kono, D. Natelson, P. M. Ajayan and J. Lou, Facile Synthesis of Single Crystal Vanadium Disulfide Nanosheets by Chemical Vapor Deposition for Efficient Hydrogen Evolution Reaction, *Adv. Mater.*, 2015, **27**, 5605–5609.

19. K. Karthick, T. K. Bijoy, A. Sivakumaran, A. B. Mansoor Basha, P. Murugan and S. Kundu, Enhancing Hydrogen Evolution Reaction Activities of 2H-Phase VS_2 Layers with Palladium Nanoparticles, *Inorg. Chem.*, 2020, **59**, 10197–10207.

20. Y. Qu, M. Shao, Y. Shao, M. Yang, J. Xu, C. T. Kwok, X. Shi, Z. Lu and H. Pan, Ultra-high electrocatalytic activity of VS_2 nanoflowers for efficient hydrogen evolution reaction, *J. Mater. Chem. A*, 2017, **5**, 15080–15086.

21. S. A. Patil, I. Rabani, S. Hussain, Y.-S. Seo, J. Jung, N. K. Shrestha, H. Im and H. Kim, A Facile Design of Solution-Phase Based VS_2 Multifunctional Electrode for Green Energy Harvesting and Storage, *Nanomaterials*, 2022, **12**, 339.

22. P. Mohan, J. Yang, A. Jena and H. Suk Shin, VS_2/rGO hybrid nanosheets prepared by annealing of VS_4/rGO, *J. Solid State Chem.*, 2015, **224**, 82–87.

23. H. Liang, H. Shi, D. Zhang, F. Ming, R. Wang, J. Zhuo and Z. Wang, Solution Growth of Vertical VS_2 Nanoplate Arrays for Electrocatalytic Hydrogen Evolution , *Chem. Mater.*, 2016, **28**, 5587–5591.

24. J. K. Das, A. K. Samantara, A. K. Nayak, D. Pradhan and J. N. Behera, VS_2 an efficient catalyst for an electrochemical hydrogen evolution reaction in an acidic medium, *Dalt. Trans.*, 2018, **47**, 13792–13799.

25. P. Hu, G. Long, A. Chaturvedi, S. Wang, K. Tan, Y. He, L. Zheng, G. Liu, Y. Ke, Y. Zhou, H. Jiang, Z. Liu, M. Zhang and Y. Long, Agent-assisted VSSe ternary alloy single crystals as an efficient stable electrocatalyst for the hydrogen evolution reaction, *J. Mater. Chem. A*, 2019, **7**, 15714–15721.

26. X. Xia, G. Zhao, Z. Hou, C. Yuan, L. Sun and C. Han, High Active and Durable Vanadium Sulfide Multilayer Structure Featuring Rich Hole Defects Constructed for Accelerated Hydrogen Evolution Reaction, *J. Electrochem. Soc.*, 2020, **167**, 116525.

27. R. Bajpai, S. Roy and S. Verma, Microwave-Assisted Solid-State Synthesis of Dichalcogenide Nanostructures for Electrocatalytic Hydrogen Evolution, *ACS Appl. Nano Mater.*, 2022, **5**, 8511–8525.

28. B. Predel, *Pu-Re – Zn-Zr*, Springer-Verlag, Berlin/Heidelberg, 1998, vol. 5 J.

29. F. De Vries, A.B. Jellinek, A structural study of vanadium sulfides, *Rev. Chim. Miner.*, 1974, **11**, 624–636.

30. J. Tudo and G. Tridot, Pyrolyse du tetrasulfure de vanadium: contribution a l'etude du systeme vanadium-soufre, *C. R. Acad. Sci,*1964, **258**, 6437-6440.

31. F. Jellinek, Sulfides of the transition metals of groups IV, V and VI, *Akriv Kemi*, 1962, **20**, 447–480.

32. D. W. Murphy, C. Cros, F. J. Di Salvo and J. V. Waszczak, Preparation and properties of Li_xVS_2 ($0 < x < 1$), *Inorg. Chem.*, 1977, **16**, 3027–3031.

33. J. Feng, X. Sun, C. Wu, L. Peng, C. Lin, S. Hu, J. Yang and Y. Xie, Metallic few-layered VS_2 ultrathin nanosheets: High two-dimensional conductivity for in-plane supercapacitors, *J. Am. Chem. Soc.*, 2011, **133**, 17832–17838.

34. L. Jian-Zhe and G. Peng-Fei, VS_2 Nanosheets: A Potential Anode Materiral for Li-ion Batteriers, *J. Inorg. Mater.*, 2015, **30**, 1339.

35. J. Zhou, L. Wang, M. Yang, J. Wu, F. Chen, W. Huang, N. Han, H. Ye, F. Zhao, Y. Li and Y. Li, Hierarchical VS_2 Nanosheet Assemblies: A Universal Host Material for the Reversible Storage of Alkali Metal Ions, *Adv. Mater.*, 2017, **29**, 1–8.

36. Z. Ding, Q. Zhang, Y. Chen, G. Liu, X. Xin, H. He, B. Cai, J. Wu and X. Yao, PEDOT-PSS coated VS_2 nanosheet anodes for high rate and ultrastable lithium-ion batteries, *New J. Chem.*, 2019, **43**, 1681–1687.

37. L. Cai, Q. Zhang, J. P. Mwizerwa, H. Wan, X. Yang, X. Xu and X. Yao, Highly Crystalline Layered VS_2 Nanosheets for All-Solid-State Lithium Batteries with Enhanced Electrochemical Performances, *ACS Appl. Mater. Interfaces*, 2018, **10**, 10053–10063.

38. J. Chen, Z. Tang, Z. Pan, W. Shi, Y. Wang, Z. Q. Tian and P. K. Shen, Template-free growth of spherical vanadium disulfide nanoflowers as efficient anodes for sodium/potassium ion batteries, *Mater. Des.*, 2020, **192**, 108780.

39. R. Sun, Q. Wei, J. Sheng, C. Shi, Q. An, S. Liu and L. Mai, Novel layer-by-layer stacked VS_2 nanosheets with intercalation pseudocapacitance for high-rate sodium ion charge storage, *Nano Energy*, 2017, **35**, 396–404.

40. J. Wang, N. Luo, J. Wu, S. Huang, L. Yu and M. Wei, Hierarchical spheres constructed by ultrathin VS_2 nanosheets for sodium-ion batteries, *J. Mater. Chem. A*, 2019, **7**, 3691–3696.

41. Q. Ji, C. Li, J. Wang, J. Niu, Y. Gong, Z. Zhang, Q. Fang, Y. Zhang, J. Shi, L. Liao, X. Wu, L. Gu, Z. Liu and Y. Zhang, Metallic vanadium disulfide nanosheets as a platform material for multifunctional electrode applications, *Nano Lett.*, 2017, **17**, 4908–4916.

42. M. Hossain, J. Wu, W. Wen, H. Liu, X. Wang and L. Xie, Chemical Vapor Deposition of 2D Vanadium Disulfide and Diselenide and Raman Characterization of the Phase Transitions, *Adv. Mater. Interfaces*, 2018, **5**, 1–6.

43. P. Gnanasekar, M. K. Eswaran, G. Palanichamy, T. K. Ng, U. Schwingenschlögl, B. S. Ooi and J. Kulandaivel, Sustained Solar-Powered Electrocatalytic H_2 Production by Seawater Splitting Using Two-Dimensional Vanadium Disulfide, *ACS Sustain. Chem. Eng.*, 2021, **9**, 8572–8580.

44. S. Zhang, P. Chang, Y. Zhang, X. Xu, L. Guan and J. Tao, Effect of morphology and stacking on atomic interaction and magnetic characteristics in two-dimensional H-phase VS_2 few layers, *J. Mater. Sci.*, 2022, **57**, 5873–5884.

45. G. A. Wiegers, R. van der Meer, H. van Heiningen, H. J. Kloosterboer and A. J. A. Alberink, The sodium intercalates of vanadium disulfide and their hydrolysis products, *Mater. Res. Bull.*, 1974, **9**, 1261–1265.

46. E. Lee, W. C. Lee, N. M. Asl, D. Kim, M. Slater, C. Johnson and Y. Kim, Reversible $NaVS_2$ (De)Intercalation Cathode for Na-Ion Batteries, *ECS Electrochem. Lett.*, 2012, **1**, A71–A73.

47. G. A. Wiegers, Physical properties of first-row transition metal dichalcogenides and their intercalates, *Phys. B+C*, 1980, **99**, 151–165.

48. H. Moutaabbid, Y. Le Godec, D. Taverna, B. Baptiste, Y. Klein, G. Loupias and A. Gauzzi, High-Pressure Control of Vanadium Self-Intercalation and Enhanced Metallic Properties in 1T-$V_{1+x}S_2$ Single Crystals, *Inorg. Chem.*, 2016, **55**, 6481–6486.

49. M. Nakano-Onoda, S. Yamaoka, K. Yukino, K. Kato and I. Kawada, A trigonal phase $V_{1+x}S_2$ prepared under high pressure, *J. Less Common Met.*, 1976, **44**, 341–344.

50. D. Wu, L. L. Chang and C. R. Knowles, Phase relations in the Cu-V-S system, *J. Less Common Met.*, 1986, **115**, 243–251.

51. A. J. Littlejohn, Z. Li, Z. Lu, X. Sun, P. Nawarat, Y. Wang, Y. Li, T. Wang, Y. Chen, L. Zhang, H. Li, K. Kisslinger, S. Shi, J. Shi, A. Raeliarijaona, W. Shi, H. Terrones, K. M. Lewis, M. Washington, T. Lu and G. Wang, Large Metallic Vanadium Disulfide Ultrathin Flakes for Spintronic Circuits and Quantum Computing Devices, *ACS Appl. Nano Mater.*, 2019, **2**, 3684–3694.

52. G. Wang, Z. Zhang, Y. Wang, E. Gao, X. Jia, Z. Dai, C. Weng, L. Liu, Y. Zhang and Z. Zhang, Out-of-plane deformations determined mechanics of vanadium disulfide (VS_2) sheets, *ACS Appl. Mater. Interfaces*, 2021, **13**, 3040–3050.

53. R. Xu, J. Huang, L. Cao, L. Feng, Y. Feng, L. Kou, Q. Liu, D. Yang and L. Feng, VS_2 Microflowers with In Situ Embedded Few-Layer MoS_2 Nanobelts for Enhanced Hydrogen Evolution Reaction at High Current Density , *J. Electrochem. Soc.*, 2020, **167**, 026508.

54. H. Dong, A. Duan, S. Zhong, Y. Zhang and X. Zhou, Chemical vapor deposition growth of broadband tunable light absorption and anti-reflection properties of VS_2 nanostructure films, *Mater. Lett.*, 2019, **252**, 227–230.

55. R. Sakthivel, S. Kubendhiran, S. M. Chen and J. V. Kumar, Rational design and facile synthesis of binary metal sulfides VS_2-SnS_2 hybrid with functionalized multiwalled carbon nanotube for the selective detection of neurotransmitter dopamine, *Anal. Chim. Acta*, 2019, **1071**, 98–108.

56. L. Wu, R. Sun, F. Xiong, C. Pei, K. Han, C. Peng, Y. Fan, W. Yang, Q. An and L. Mai, A rechargeable aluminum-ion battery based on a VS_2 nanosheet cathode, *Phys. Chem. Chem. Phys.*, 2018, **20**, 22563–22568.

57. W. Li, J. Huang, L. Feng, L. Cao, Y. Liu and L. Pan, Nano-grain dependent 3D hierarchical VS_2 microrods with enhanced intercalation kinetic for sodium storage properties, *J. Power Sources*, 2018, **398**, 91–98.

58. R. Karthik, J. Vinoth Kumar, S. M. Chen, P. Sundaresan, B. Mutharani, Y. Chi Chen and V. Muthuraj, Simple sonochemical synthesis of novel grass-like vanadium disulfide: A viable non-enzymatic electrochemical sensor for the detection of hydrogen peroxide, *Ultrason. Sonochem.*, 2018, **48**, 473–481.

59. Z. Guo, L. Yang, W. Wang, L. Cao and B. Dong, Ultrathin VS_2 nanoplate with in-plane and out-of-plane defects for an electrochemical supercapacitor with ultrahigh specific capacitance, *J. Mater. Chem. A*, 2018, **6**, 14681–14688.

60. W. Li, J. Huang, L. Feng, L. Cao, Y. Feng, H. Wang, J. Li and C. Yao, Facile: In situ synthesis of crystalline VOOH-coated VS_2 microflowers with superior sodium storage performance, *J. Mater. Chem. A*, 2017, **5**, 20217–20227.

61. M. Cao, L. Gao, X. Lv and Y. Shen, TiO_2-B@VS_2 heterogeneous nanowire arrays as superior anodes for lithium-ion batteries, *J. Power Sources*, 2017, **350**, 87–93.

62. L. Pang, L. Li, R. Wang, Q. Zhao, W. Liu, R. Wu and Y. Lv, Vanadium disulfide for ultrafast photonic application, *Nanotechnology*, 2021, **32**, 015202.

63. T. M. Masikhwa, F. Barzegar, J. K. Dangbegnon, A. Bello, M. J. Madito, D. Momodu and N. Manyala, Asymmetric supercapacitor based on VS_2 nanosheets and activated carbon materials, *RSC Adv.*, 2016, **6**, 38990–39000.

64. L. Li, Z. Li, A. Yoshimura, C. Sun, T. Wang, Y. Chen, Z. Chen, A. Littlejohn, Y. Xiang, P. Hundekar, S. F. Bartolucci, J. Shi, S. F. Shi, V. Meunier, G. C. Wang and N. Koratkar, Vanadium disulfide flakes with nanolayered titanium disulfide coating as cathode materials in lithium-ion batteries, *Nat. Commun.*, 2019, **10**, 1–10.

65. P. Shvets, O. Dikaya, K. Maksimova and A. Goikhman, A review of Raman spectroscopy of vanadium oxides, *J. Raman Spectrosc.*, 2019, **50**, 1226–1244.

66. A. T. Ward, Raman spectroscopy of sulfur, sulfur-selenium, and sulfur-arsenic mixtures, *J. Phys. Chem.*, 1968, **72**, 4133–4139.

67. B. van Laar and D. J. W. Ijdo, Preparation, crystal structure, and magnetic structure of $LiCrS_2$ and $LiVS_2$, *J. Solid State Chem.*, 1971, **3**, 590–595.

68. N. M. Asl, J. H. Kim, W. C. Lee, Z. Liu, P. Lu and Y. Kim, A new chemical route for the synthesis of β′-Li xV_2O_5 for use as a high performance cathode, *Electrochim. Acta*, 2013, **105**, 403–411.

69. M. Noel and P. N. Anantharaman, Voltammetric studies on glassy carbon electrodes I: Electrochemical behaviour of glassy carbon electrodes in H_2SO_4, Na_2SO_4 and NaOH media, *Surf. Coatings Technol.*, 1986, **28**, 161–179.

4. MS_2 (M = Ti, V, Cr) for electrochemical water splitting

4.1. Introduction

In the previous chapter, efforts were focused on one metallic TMDC – VS_2. Despite the fallbacks in electrochemical behaviour, VS_2 can be a steppingstone in investigating metallic TMDCs that are more stable in their 1T phase than 2H. VS_2 is isostructural with TiS_2 and CrS_2. If the structure remains the same, the effect of the transition metal on electrochemical performance could be investigated. This would lead to a better understanding of where the intrinsic catalytic activity of the compound arises.

4.1.1. Active sites of TMDCs

Numerous computational and experimental studies have been conducted to study the active sites of TMDCs. One of the most explored systems, MoS_2, has shown that in semiconducting polymorphs the basal planes are inert and only the edge sites – chalcogen and metal – are electrochemically active.[1] This led to research efforts to expose as many edge sites as possible to unveil more HER active sites in semiconducting TMDCs.[2–5]

Over the years, attention has shifted from edge site engineering in semiconducting TMDCs to activating the otherwise inert basal plane. The strategies include metal doping, non-metal doping, defect on the basal plane engineering and phase transitions.[6–9] The strategies have been successful in multiple cases; for example, in the semiconducting polymorph of MoS_2, sulphur vacancies in the inert basal plane were shown to create active sites, improving the overall catalytic activity of the semiconducting MoS_2.[9] The strategy of phase transition is one of the more intriguing ones. MoS_2 was shown to have dramatically improved HER performance when it was synthesised in its metallic polymorph. It was later revealed that metallic polymorphs of other TMDCs that usually appear in their semiconducting state show improved electrocatalytic activity upon phase transition.[10–12]

Once metallic TMDCs were proven superior to their semiconducting counterparts, more attention was focused on investigating the impact of phase transition on HER activity. This led to increased efforts to synthesise otherwise naturally semiconducting TMDCs in their metallic phase. While phase engineering has been proven successful to a degree, it comes with its drawbacks. For example, in MoS_2, the phase transition can be induced if the sample undergoes chemical exfoliation. The procedure usually results in a mixed-phase product.[13,14] Additional challenges are faced as the conditions needed to induce phase transition are usually harsh, or complex apparatus and equipment are required. Not to mention, there is no

one recipe that works for all TMDCs; therefore, procedures are very intricate between different TMDCs.[15,16] Finally, the product of the reaction is metastable, and further efforts are needed to stabilise the phase – whether by using surfactants in dispersions or functionalisation of the edges to prevent them from oxidising.[17–19]

With metallic TMDCs showing the advantage of an active basal plane, attention then turned towards TMDCs that naturally appear in their metallic state or exhibit metallic behaviour in both polymorphs. Many of these studies include computational examination and predictions and will be discussed further in the next section.

4.1.2. Computational studies on MS_2 (M = Ti, V, Cr) activity toward HER

With metallic TMDCs in the spotlight, computational methods were employed to estimate which TMDCs display metallic character in their stable polymorphs. A study by Tsai *et al.* showed that group V TMDCs are metallic in both polymorphs, and group IV TMDCs are metallic in their 1T polymorph, which is also the most thermodynamically stable polymorph for that group.[20] Group VI TMDCs had a clear distinction between 1T polymorphs showing metallic and 2H polymorphs showing semiconducting character. The study also discussed the impact of the transition metal on the activity of metallic TMDCs. Since the basal plane is considered to provide active sites highly contributing to overall activity, the metal active site on the edges would appear to have less impact than it would in semiconducting polymorphs with active edge sites. In their research, it was revealed that even though the metal sites are not the main active sites, the metal chalcogen bonding impacts the binding strength of adsorbed hydrogen, impacting the overall electrochemical activity of the dichalcogenide.

Qu *et al*. conducted a study screening transition metal dichalcogenides in an effort to find plausible candidates for HER.[21] Thirty-three different monolayers were screened in the study, and it was found that the TiS_2 monolayer shows promising characteristics to be a suitable HER catalyst. However, interestingly, it was found that it was 2H and not 1T polymorph that was more promising, as it showed lower overpotentials (estimated from overall free Gibbs energy) than the 1T polymorph at various hydrogen coverages. It was noted in the study that the 2H polymorph was not stable. However, a phase transition back to 1T would occur during the process of HER due to hydrogen coverage on the surface. A later study on TiS_2 by Das *et al*. contradicted the results published by Qu *et al.*, claiming that their research revealed the opposite result.[22] Das *et al*. found metallic 1T polymorph to be

more effective towards HER, and semiconducting 2H polymorph showed more potential as an oxygen evolution reaction (OER) catalyst.

CrS_2 is the most exotic compound of the three in focus in this chapter. While included in most screening studies, CrS_2 is not usually named as the most promising catalyst for HER. This is likely caused by the calculations showing it would not compare or outperform platinum. Despite that, the results point towards CrS_2 showing catalytic activity towards HER. [23] A study by Sun *et al*. was done on the 2H polymorph of CrS_2 and revealed that the compound is not HER active unless defects are introduced into the structure.[24] The results are in line with 2H TMDCs behaviour; however, the study is very narrow, focusing on only one polymorph, therefore, does not allow for better insight into the system.

4.1.3. MS_2 (M = Ti, V, Cr) electrocatalytic activity towards HER

VS_2 electrochemical activity towards HER has been widely reported and was discussed in Chapter 3. Layered disulphides of its neighbouring transition metals, TiS_2 and CrS_2, have not been reported often as catalysts. When it comes to TiS_2, several reports on its catalytic activity have been published (Table 4-1). The highest overpotential was reported by Toh *et al*.; their bulk TiS_2 powder had an overpotential of –1130 mV vs NHE at –10 mA cm^{-2}. It is important to note that the inks they prepared for catalyst characterisation were deionised water based. TiS_2 is well known to oxidise in air and moisture, therefore, chances are their TiS_2 was at least partially oxidised during ink preparation. This claim can be further confirmed by visual representation of their ink dispersions, where TiS_2 ink dispersion was white in colour. Authors also claim to observe peaks in the XPS spectrum that arise from titanium oxide. Zeng *et al.* reported TiS_2 nanosheets synthesised via liquid exfoliation. In their report, the TiS_2 catalyst did not reach benchmark current densities at all in the range of the measurements.

Moreover, the catalyst activity degraded even more with cycling, indicating poor stability. The issues with stability of TiS_2 were also reported by Nguyen et al., where their TiS_2 sheets were reported to show decent catalytic activity; catalyst reached benchmark current density at –300 mV vs NHE, however, the potential increased to around –400 mV after 1000 cycles. It is possible that TiS_2, just as VS_2, also displays a reduction wave at higher overpotentials, and whilst the cycling is carried out without completely crossing the peak of the wave, the catalyst performance seems to be degrading.

Even though TiS_2 has limited stability in 'wet' environments, the oxidation of this compound is not rapid. A study by Long et al. demonstrated that TiS_2 is oxidised more rapidly in deionised water than in an atmospheric oxygen environment.[25] It was noted that the commercial TiS_2 powder already had a 2 nm thick layer of surface oxide prior to treatment with water. After 21 days in deionised water, the thickness of the oxide layer had increased to 80 nm. These findings could explain the poor stability of TiS_2 during HER in acidic media and why this compound would be a poor choice for a catalyst. However, to achieve our goals of investigating trends in catalytic activity, a fresh sample should not have too much impact from possible surface oxides.

Su *et al*. synthesised CrS_2 flakes via CVD. When flakes were studied in an electrochemical setup, it was found that they show a low overpotential of –260 mV vs NHE to reach benchmark current densities. Moreover, the authors have synthesised Cr intercalated CrS_2 and its porous counterpart, which decreased the overpotential to –151 and –89 mV vs NHE, respectively.[26]

Table 4-1. *Literature reports on electrocatalytic activity of TiS_2 toward HER*

Morphology/ composite	Overpotential at –10 mA cm^{-2}, mV vs RHE	Tafel slope, mV dec^{-1}	Ref
TiS_2 Bulk powder	1130	147	[27]
Exfoliated TiS_2 sheets	N/A	102	[28]
TiS_2 sheets (exfoliation via sonication)	Approx. 300	91	[29]
TiS_2 sheets	350	88	[30]
TiS_2 quantum dots	245	77	

4.2. Aims

The main aim of this chapter is to synthesise isostructural MS_2 (M = Ti, V, Cr) and investigate the electrochemical activity trends towards HER. The uniform synthesis method via deintercalation compounds will be employed to maintain the morphology of the samples. Keeping the crystal structure and the morphology of the samples the same allows for insight into the effect varying the transition metal has on the overall electrocatalytic activity of metallic TMDCs towards HER.

4.3. Results and discussion

4.3.1. TiS_2 synthesis and characterisation

4.3.1.1. Synthesis of $LiTiS_2$

To keep the uniformity of the samples, the synthesis method via alkali metal deintercalation was applied first. TiS_2, just like many other layered compounds, is a great host material. Therefore, $LiTiS_2$ forms easily in a solid-state reaction between Li_2S, Ti powder and sulphur. And so, this method was used in this work, and the crystal structure and phase purity of the product was investigated using PXRD. As can be seen in Figure 4-1, the product is not phase pure. Whilst the majority of the product is rhombohedral $LiTiS_2$, the secondary phase that matches $Li_{0.9}TiS_2$ can also be observed. Reannealing was carried out to ensure that the reaction went to completion and to investigate whether it would improve the phase purity of the sample. As can be seen in Figure 4-1, annealing had little effect on the sample. The major change could be seen on the earliest peak at 15°, where annealing resulted in the removal of the shoulder.

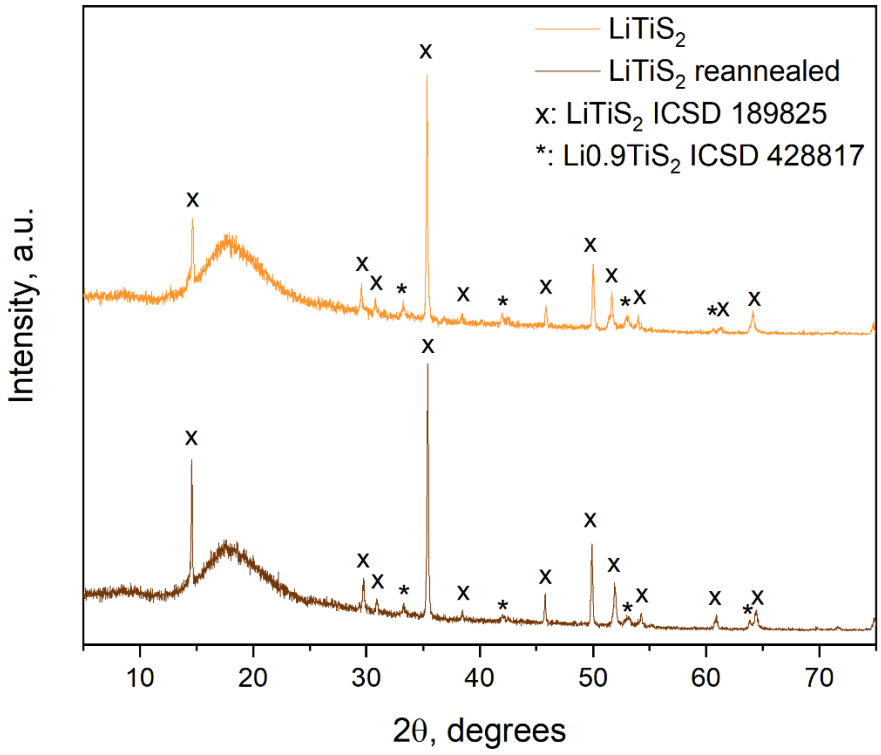

Figure 4-1. *PXRD pattern of the product of reaction between Li_2S, Ti and S powders sealed under vacuum and heated at 600 °C for 72 hours (top, orange). Diffraction pattern of the product after 24 h reannealing step is at the bottom (brown). Broad peak at 15-20 degrees in the experimental patterns comes from an air sensitive holder used in the measurement, $LiTiS_2$ peaks corresponding to ICSD reference pattern no 189825 are noted 'x' and $Li_{0.9}TiS_2$ peaks corresponding to ICSD pattern no 428817 are noted '*'.*

4.3.1.2. $LiTiS_2$ deintercalation attempts

Previous experiments in the VS_2 system have shown that phase mixture usually does not have an impact on the success of deintercalation reaction (Figure A 5). Therefore, the $LiTiS_2$ sample was used for deintercalation without further phase purification. The deintercalation reaction was carried out the same way as it was done for VS_2 samples, and the full procedure can be found in chapter 2. The main difference in this sample was that it was only washed with acetonitrile and ethanol as TiS_2 is not stable in water and forms an oxide. Once the reaction vial was opened, a strong H_2S smell escaped the vial, indicating possible sample degradation. Phase identification of the product was carried out from PXRD data. It was noticed that all major peaks in the diffraction pattern are split (Figure 4-2). This suggests that the deintercalation reaction did not complete, as diffraction peaks of TiS_2 and isostructural Li_xTiS_2 shift according to Li content in the sample. To ensure that the sample could undergo deintercalation fully, the reaction time was extended to 48 hours. The extended reaction time did have an impact on the product; however, the reaction still has not gone to completion, as the peak splitting remained in the pattern (Figure 4-3). The ratio of the TiS_2 and Li_xTiS_2 peaks has improved (TiS_2 peak intensity has increased, whilst Li_xTiS_2 has decreased). However, the prolonged deintercalation times appear to have damaged the sample even more. Not only the strong smell was noticed when the sample vial was opened, there was a clear decrease in the diffraction pattern quality. Knowing that the sample can also be made via direct solid-state synthesis, the efforts to deintercalate $LiTiS_2$ were abandoned.

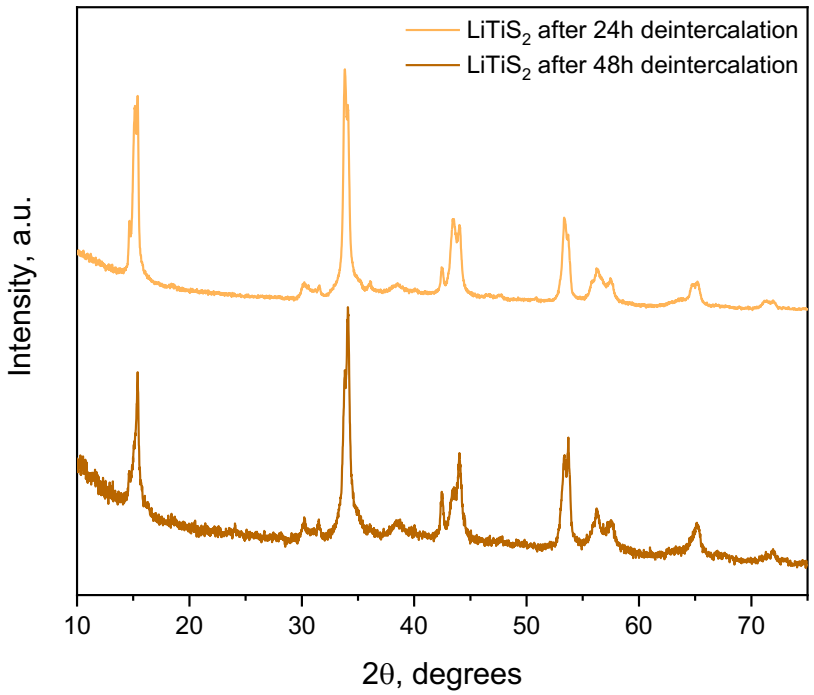

Figure 4-2. *PXRD pattern of deintercalation reaction where $LiTiS_2$ was reacted with I_2 in acetonitrile for 24 h (top, light orange) and 48 h (bottom, light brown) products.*

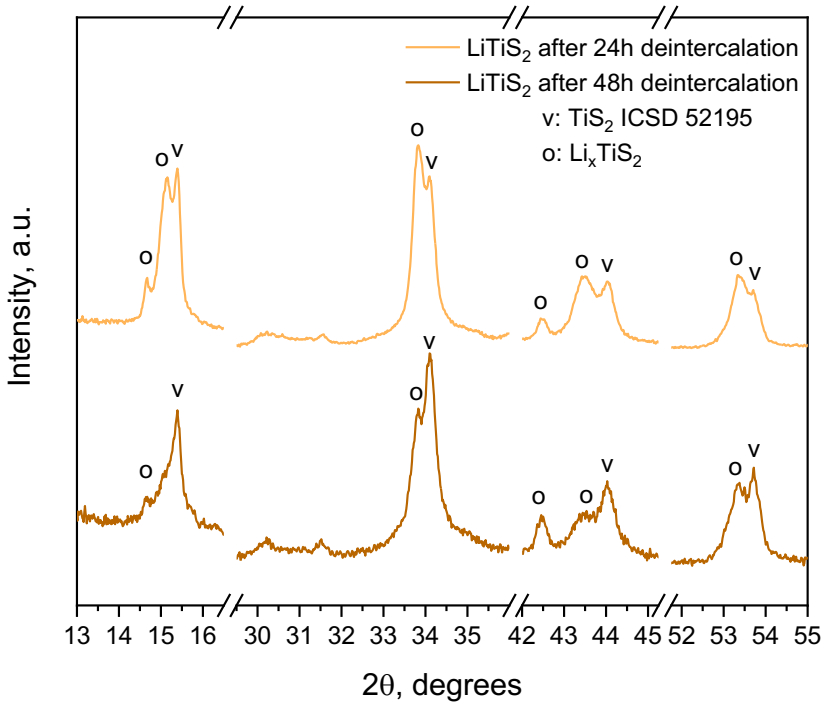

Figure 4-3. *PXRD pattern of deintercalation reaction where $LiTiS_2$ was reacted with I_2 in acetonitrile for 24 h (top, light orange) and 48 h (bottom, light brown) products. Break points have been inserted in x axis to better represent peak splitting in the major peaks of the pattern. Peaks corresponding to reference TiS_2 pattern calculated from ICSD card no 52195 are noted 'v'. Peaks corresponding to the reference patterns of Li_xTiS_2 calculated from ICSD card no 428817 and no 428812 by adjusting Li content are noted 'o'.*

4.3.1.3. TiS_2 solid-state synthesis

Since the deintercalation reaction has failed to obtain TiS_2 from $LiTiS_2$, a conventional solid-state synthesis was employed to synthesise the sample. Opting for solid-state synthesis is a deviation from initial goals; however, it allows us to produce the sample and later on use it for catalytic properties investigation. Ti and S powders were reacted in an evacuated ampoule at 600 °C for 72 hours. The sample was investigated using PXRD, and the pattern matched the reference pattern of TiS_2 well (Figure 4-4). To ensure sample homogeneity and completion of the reaction, the sample was reannealed. Reannealing of the sample has not provided any major improvement, indicating that the reaction goes to completion during an initial heating cycle (Figure 4-4).

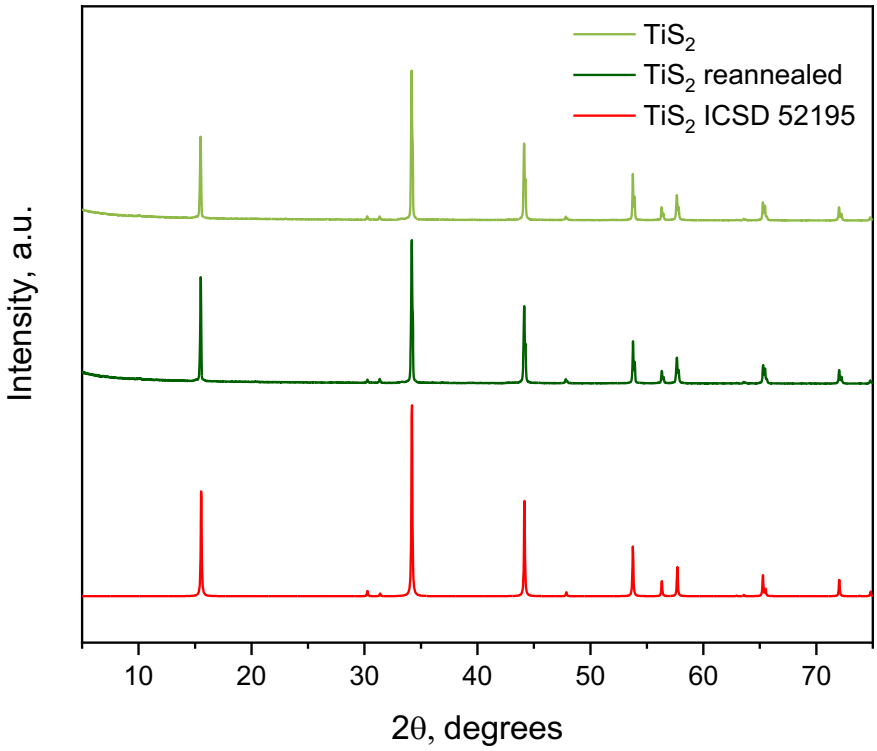

Figure 4-4. *PXRD pattern of TiS_2 synthesised via solid-state reaction between Ti and S at 600 ºC for 72 hours (top, light green) and annealed product pattern (middle, dark green) in comparison with TiS_2 reference pattern calculated from ICSD card no 52195 (bottom, red).*

A Le Bail refinement was performed on the reannealed sample to obtain cell parameters. The refined pattern is in Figure 4-5, and cell parameter values obtained from the refinement can be found in Table 4-2. As can be seen from the data provided in the table, the cell parameters agree well with the values reported in the literature.

***Table 4-2**. Cell parameters of TiS_2 synthesised at 600 °C from elements via solid-state reaction in comparison with values reported in the literature.*

Sample	*a*, Å	*c*, Å	Ref
TiS_2	3.40397(6)	5.6970 (1)	This work
TiS_2	3.4073	5.6953	[31]
TiS_2	3.4097	5.7052	[32]
TiS_2	3.4079	5.6989	[33]
TiS_2	3.402	5.716	[34]
TiS_2	3.407	5.695	[35]

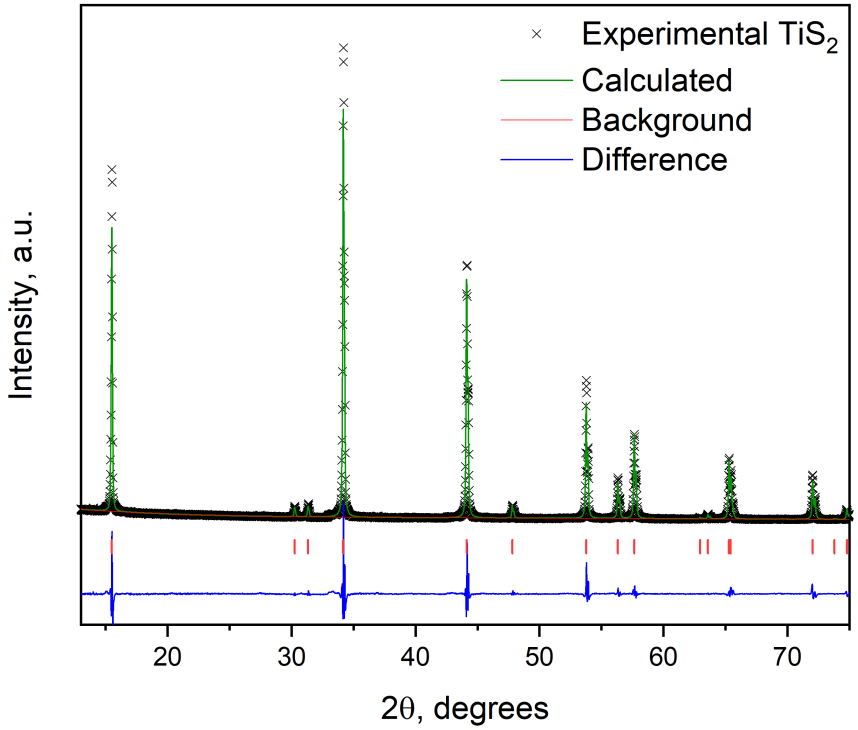

***Figure 4-5.** Le Bail refinement of TiS_2 solid-state sample. Experimental pattern is noted as scatter plot with 'x', calculated pattern is in green, background in red and difference in blue line plots. Refinement was carried out in GSASII software.*

4.3.1.4. Elemental composition and morphology of TiS_2

The morphology of the sample was investigated using SEM imaging. Figure 4-6 depicts the images collected and represents the sample morphology. It can be noticed that the sample is comprised of much smaller crystallites than that of VS_2 samples. While the crystallites are smaller, they still maintain a platelet-like shape. The edges of the platelets are well-defined and sharp. The particle size distribution in the sample is quite large – most crystallites appear

to be below 5 µm in diameter, while some are much bigger, coming in at around 10 µm or more in diameter.

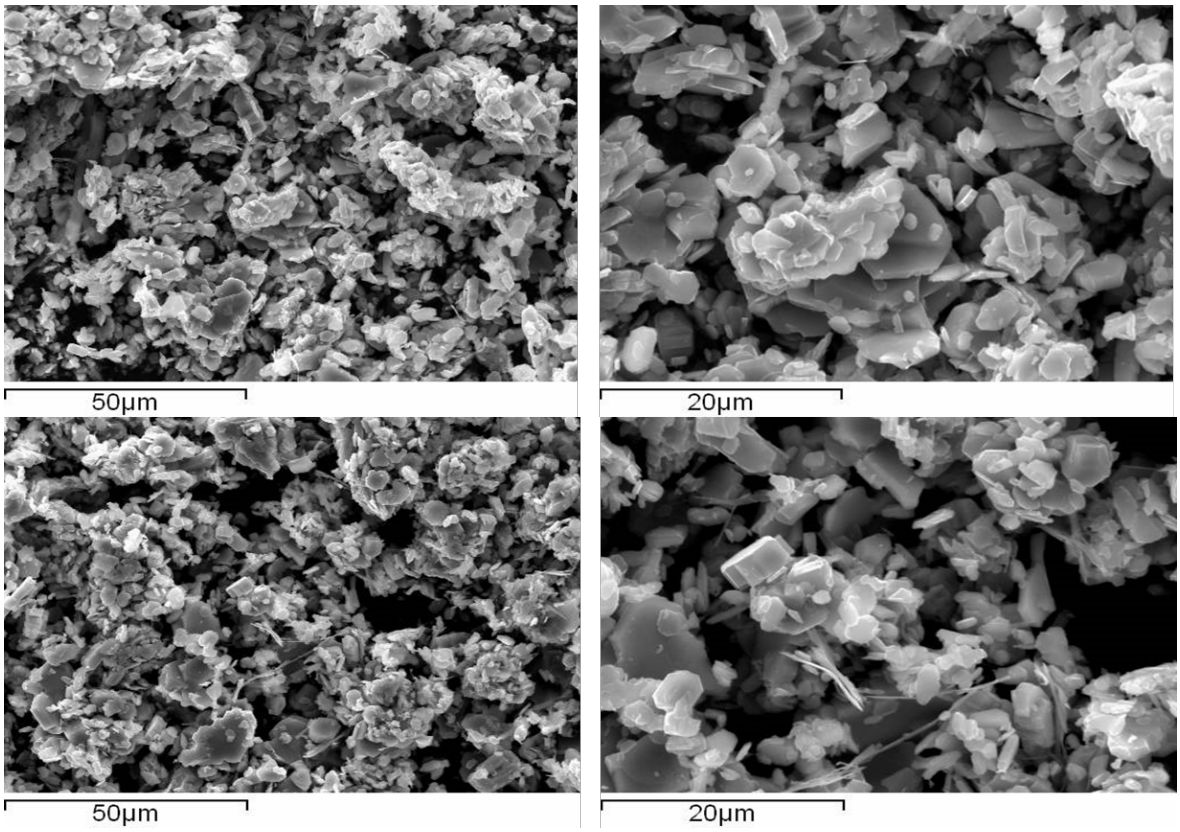

Figure 4-6. *SEM images of two different spots of sample TiS_2 using two different magnification settings.*

The elemental composition of the sample was calculated from collected EDX data. The results of the measurement are displayed in Table 4-3. The sample stoichiometry is calculated to be TiS_2 and is an ideal stoichiometry expected for this sample within the error. The results agree well with the reports that stoichiometric TiS_2 can only be prepared in a temperature range of 450 – 600 °C, as higher synthesis temperature leads to a slight loss of sulphur and samples being slightly metal-rich.[36]

Table 4-3. *EDX data of sample TiS_2. The standard deviation was calculated from 10 independent points*

	TiS_2 at. %	
Element	Ti	S
Experimental	33.3 (16)	66.6 (16)
Theoretical	33.3	66.6

4.3.1.5. Raman spectroscopy of TiS_2

Raman spectroscopy was employed for further phase investigation. Just as VS_2, TiS_2 was found to be easily oxidised during measurement under laser irradiation if the measurement is carried out in ambient conditions. Therefore, the sample was measured in a capillary sealed under an inert Ar atmosphere with the spectrum displayed in Figure 4-7. The sample displays a prominent peak at 329 cm^{-1} with a shoulder at 370 cm^{-1}. There is also a low-intensity peak at around 233 cm^{-1}. These results agree well with previous literature reports on TiS_2.[37–39] Wide range Raman measurements are a great way to investigate the purity of the sample as well, as some impurities may not be picked up by PXRD, however, be Raman active. In this case, unreacted sulphur would show up in the Raman measurements at 80 cm^{-1}, 148 cm^{-1}, 217 cm^{-1}, 473 cm^{-1}. As it can be seen from the pattern – only the TiS_2 peak with the shoulder is present.

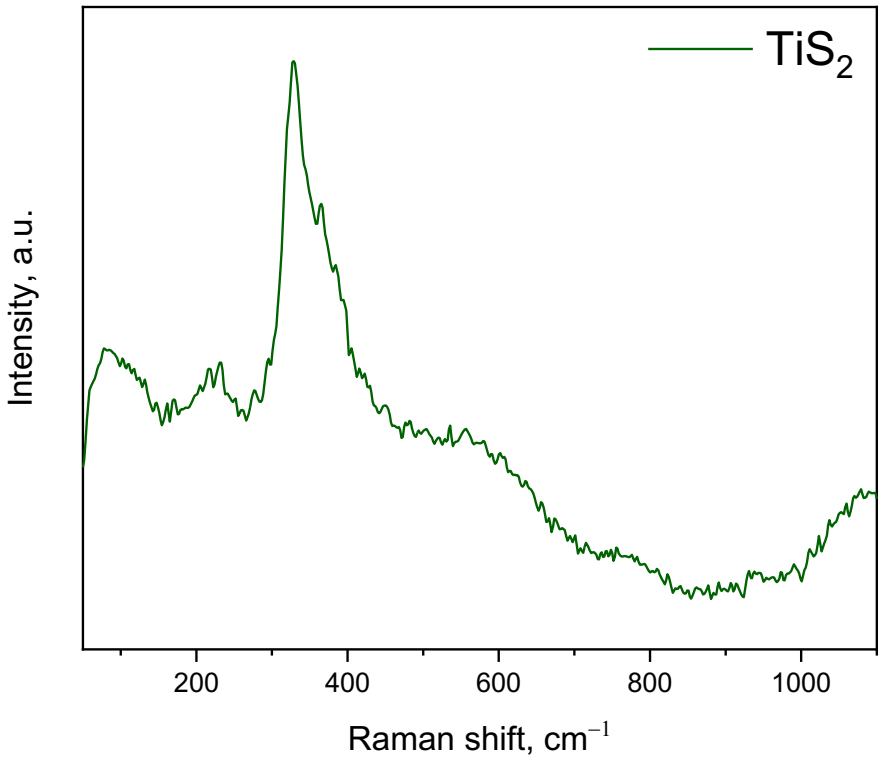

Figure 4-7. *Raman spectrum of TiS_2. Spectrum was collected on a sample sealed in a capillary under an inert Ar atmosphere.*

4.3.1.6. Electrocatalytic activity toward HER

Once the crystal structure and purity of the sample were established, the electrochemical properties of TiS_2 towards HER can be investigated. As usual, an LSV scan was collected first to get the first impression of the catalytic performance of the catalyst and is displayed in Figure *4-8*. The first scan reveals a sharp current increase early on at around –200 mV vs NHE. However, it should not be mistaken with the HER process starting to take place. At these low overpotentials, no hydrogen formation on the electrode could be noticed; moreover, when the scan was continued into higher potentials, the LSV curve started to take the shape of a reduction peak. Interestingly, not one but three major reduction peaks were observed in this sample. The first two waves come early on in a potential window of –200 to –400 mV vs NHE, the third one appearing at between –700-850 mV vs NHE. There is also one minor peak at –400 mV vs NHE. Reduction waves in the LSV scan appeared in VS_2 samples as well; however, there was only one prominent peak. It is highly likely that the peaks originate from surface oxides that form on catalyst film, especially since the position and visual appearance of the peak resembles that observed for rutile form of TiO_2 in work by Diaz-Real.[40] On the second LSV scan run on the same electrode, it can be seen

that the curve is dramatically different from that of the first scan. Assuming that the second scan reveals the actual HER overpotential of the catalyst, it is apparent that TiS_2 does not perform well. The overpotential needed to reach the benchmark current density of –10 mA cm^{-2} is –1185 mV vs NHE. This value is extremely high, rendering the catalyst ineffective towards HER. Furthermore, it is not clear whether all surface oxides were removed in the first scan, therefore it is hard to tell if this performance originates from TiS_2 alone.

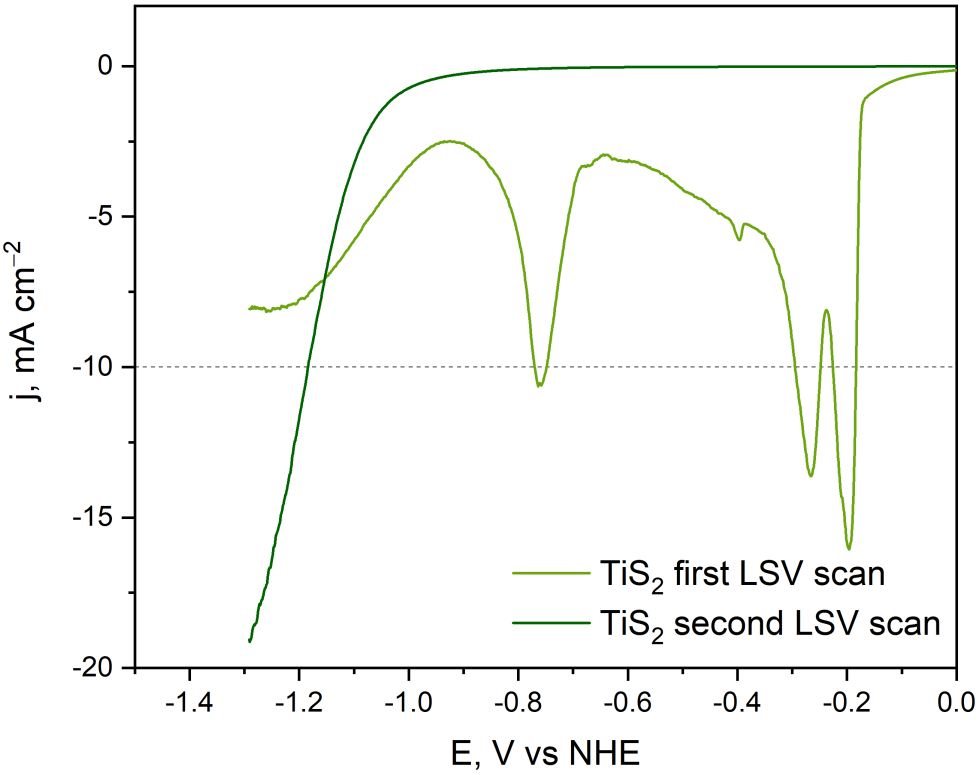

Figure 4-8. *Polarization curves recorded on sample TiS_2. The first scan reveals multiple reduction waves, whereas a second scan shows the actual HER overpotential. Polarization curves were recorded using a sweep rate of 5 mV s^{-1}. Three electrode setup in 1 M H_2SO_4 electrolyte where glassy carbon modified with catalyst was working electrode, carbon felt was used as a counter electrode and 3 M Ag/AgCl electrode as a reference electrode. Current density is calculated using geometric electrode area (0.071 cm^2).*

4.3.2. CrS_2 synthesis and characterisation

4.3.2.1. $LiCrS_2$ synthesis

Similar to VS_2 and TiS_2, the synthesis of CrS_2 was approached via alkali metal deintercalation reactions. With minimal literature on CrS_2 synthesis, the route of VS_2, where it was made through Li and Na intercalated compounds, was chosen. $NaCrS_2$ was

synthesised by heating Na_2S, Cr and S powders in an ampoule sealed under a vacuum for 72 hours. The reaction failed to yield $NaCrS_2$, likely due to temperatures being much lower than the 900 °C reported in previous literature on the synthesis of this compound.[41] Since the means to carry out synthesis at this temperature were unavailable; efforts were focused on $LiCrS_2$. $LiCrS_2$ was synthesised analogous to $NaCrS_2$, using Li_2S, Cr powder and sulphur powder. The mixture was loaded into an ampoule and sealed under a vacuum, followed by heating at 600 °C for 72 hours. The crystal structure of the product was investigated with PXRD. As can be seen in Figure 4-9, the diffraction pattern matched the reference pattern calculated from the ICSD database. The sample was reannealed to ensure the reaction went to completion and equilibrium was reached. The annealed reaction product did not show any major differences in the diffraction pattern, confirming that the single heating step is sufficient for complete synthesis of $LiCrS_2$.

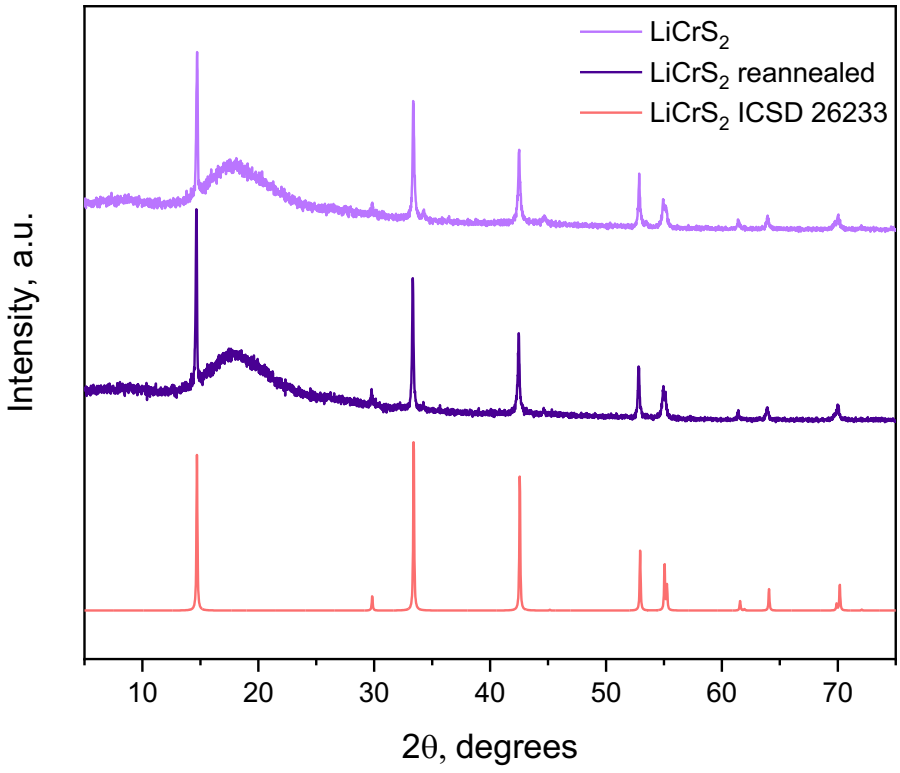

Figure 4-9. *PXRD pattern of the product of reaction between Li_2S, Cr and S powders sealed under vacuum and heated at 600 °C for 72 hours (top, light purple). Diffraction pattern of the product after 24 h reannealing step is in the middle (purple). Reference pattern of $LiCrS_2$ calculated from ICSD card no 26233 is displayed at the bottom (red). Broad peak at 15-20 degrees in the experimental patterns comes from an air sensitive holder used in the measurement.*

4.3.2.2. $LiCrS_2$ deintercalation attempts

Once a successful and reproducible synthesis for $LiCrS_2$ was established, the compound was then used for deintercalation reaction. The usual procedure was first carried out, and the product of the deintercalation was characterised by PXRD. The diffraction pattern of the product of the reaction still resembled the pattern of the initial compound $LiCrS_2$. Some minor changes in the pattern were noticed, such as minor peaks at around 6, 16 and 34 2θ degrees. The main phase in the product of deintercalation was still $LiCrS_2$, however, peak broadening could be observed. After achieving little success in room temperature deintercalation, the deintercalation reaction was carried out at an elevated temperature of 50 °C. This decision was based on literature reports by Kobayashi *et al*. of successful Li deintercalation from $LiCrSe_{0.9}S_{0.1}$.[42] In their research, elevated temperatures were used to achieve successful deintercalation. As it can be seen in Figure *4-10*, the product of deintercalation at 50 °C is still showing the pattern of $LiCrS_2$. However, more changes can be seen this time. It appears that the peaks that had emerged during the room temperature deintercalation have increased intensity. A broad peak at around 6 degrees likely points towards the intercalation of solvent into the structure of the starting material. To add, further broadening of the $LiCrS_2$ peaks could be observed.

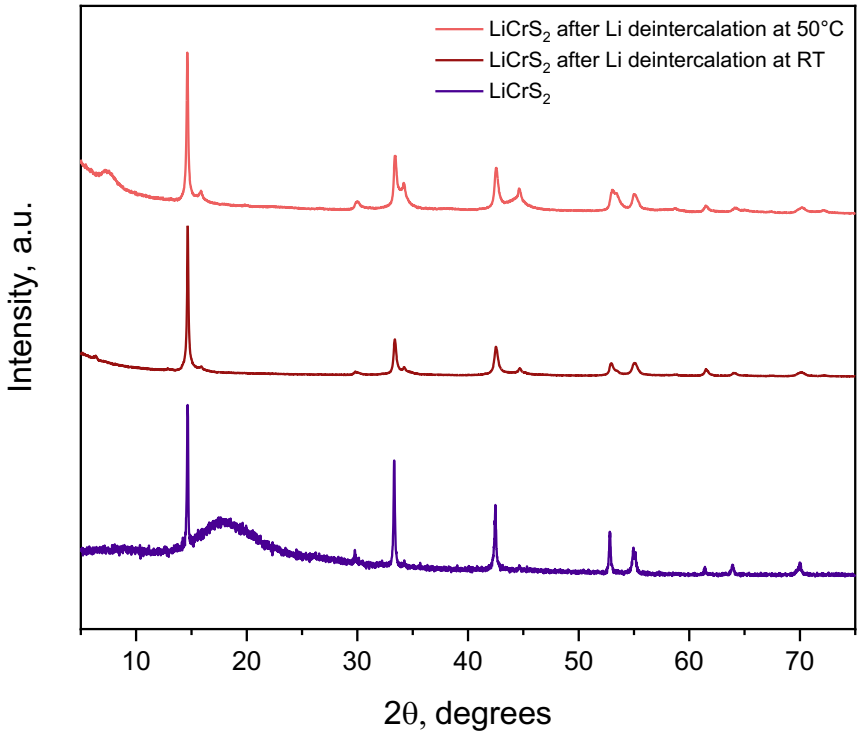

Figure 4-10. *PXRD pattern of the product of deintercalation reaction using I_2 in acetonitrile at room temperature (middle, dark red). Diffraction pattern of the product of deintercalation reaction at elevated temperature (top, coral). PXRD pattern of the starting material $LiCrS_2$ for reference (bottom, purple). Broad peak at 15-20 degrees in the experimental pattern of $LiCrS_2$ comes from air sensitive holder used in the measurement.*

At this point, an alternative synthesis method would be preferable as the deintercalation reaction does not appear to work for this compound. However, no reports of successful synthesis of CrS_2 as a layered compound in this stoichiometry could be found. Therefore, attempts to deintercalate lithium from the structure were continued. After the first two deintercalation attempts, it was noticed that $LiCrS_2$ did not display any signs of being air or moisture sensitive. This characteristic of the compound was an interesting insight. All the other alkali metal intercalated layered transition metal dichalcogenides that were encountered in this work were highly moisture sensitive. They also deintercalated quite easily (except for $LiTiS_2$).

The starting material was set up in a reflux configuration for the following deintercalation attempts. This was a must as $LiCrS_2$ powders were mixed in boiling I_2 in acetonitrile solution for 48 hours. The resulting powders were filtered and washed, and PXRD was run to

characterise the product of the reaction. Not much improvement could be seen in the pattern when compared to the deintercalation carried out in 50 °C. The product was still predominantly $LiCrS_2$. The last attempt to deintercalate was carried out in boiling I_2 in acetonitrile solution for 5 days. The PXRD pattern of the product is in Figure 4-11. This resulted in another failed attempt, however, this time the pattern did show some major changes. While peaks did not appear to shift, the intensities of the peaks have changed. The intensity of a major peak at 14.6 degrees has decreased significantly in respect to other peaks. Moreover, the peaks at around 35 degrees are now displaying equal intensities. The peak at the low 2θ angles further increased implying more solvent was intercalated in the structure. Overall, these changes only point towards degradation of $LiCrS_2$ phase without any solid proof of formation of deintercalated phase of CrS_2. With this, the efforts to achieve CrS_2 were abandoned.

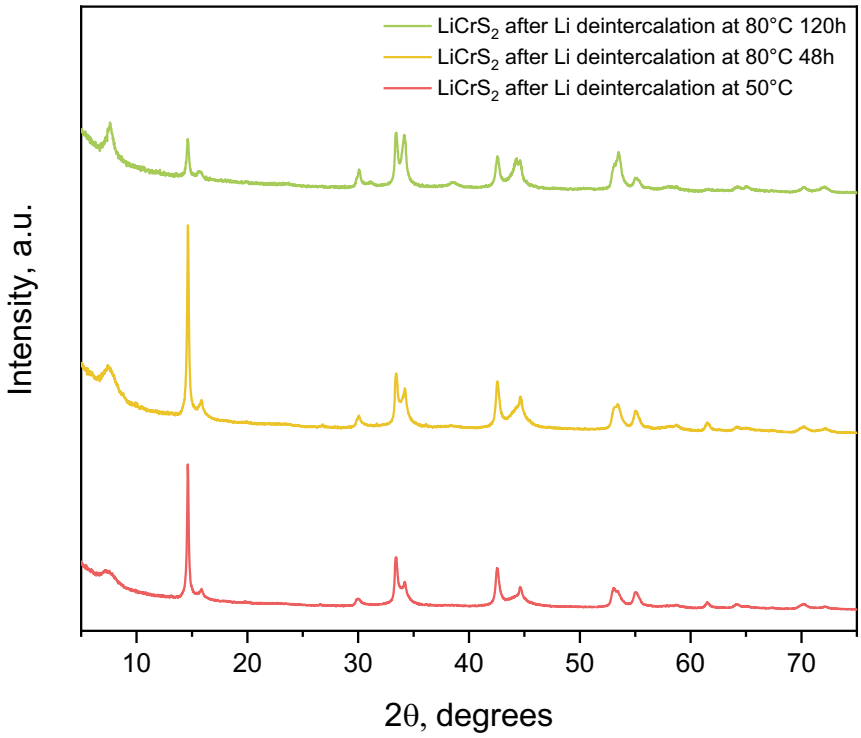

Figure 4-11. *PXRD pattern of the product of deintercalation reaction using I_2 in acetonitrile at elevated temperature (50 ºC, bottom, coral). Diffraction pattern of the product of deintercalation reaction at elevated temperature (80 ºC, middle, yellow). Diffraction pattern of the product of deintercalation reaction at elevated temperature and extended reaction time (80 ºC, top, green).*

4.3.3. Summary and comparison of TiS_2 and VS_2

Despite the failed attempt to synthesise CrS_2, the first two compounds of the isostructural first row sulphides can be compared.

Both samples, TiS_2 and VS_2-Li (from chapter 3), are crystalline and isostructural. Cell parameters were obtained from the Le Bail refinement of the samples. As it can be seen in Table 4-4, the cell parameters of these compounds are similar.

Table 4-4. *Cell parameters of TiS_2 and VS_2-Li as obtained from Le Bail refinement of the PXRD data of the samples.*

Sample	a, Å	c, Å
TiS_2	3.40397(6)	5.6970 (1)
VS_2-Li	3.2180(9)	5.7554(8)

The elemental composition of both samples is close to the ideal 1:2 ratio as indicated by EDX analysis and highlighted in Table 4-5. Keeping the sample stoichiometry this similar provides for a more appropriate comparison of the electrochemical properties as we can be assured none of the samples may be benefiting from unintentional defects in the structure.

Table 4-5. *Results of EDX analysis on samples TiS_2 and VS_2-Li. Standard deviation was calculated from 10 different points for TiS_2 and 12 different points for VS_2-Li.*

	TiS_2 at. %		VS_2-Li at. %	
Element	Ti	S	V	S
Experimental	33.3(16)	66.6(16)	33.2(14)	66.7(14)
Theoretical	33.3	66.6	33.3	66.6

SEM images had revealed that the samples have slightly different morphology, therefore, electrochemically active surface area was estimated and compared. Double layer capacitance measurements, surprisingly, revealed that the electrochemically active surface area is higher for VS_2-Li than it is for TiS_2 (Figure 4-12 and Table 4-6, Figure A 9). It was unexpected, since SEM images had shown that TiS_2 sample is composed of smaller crystallites than VS_2-Li.

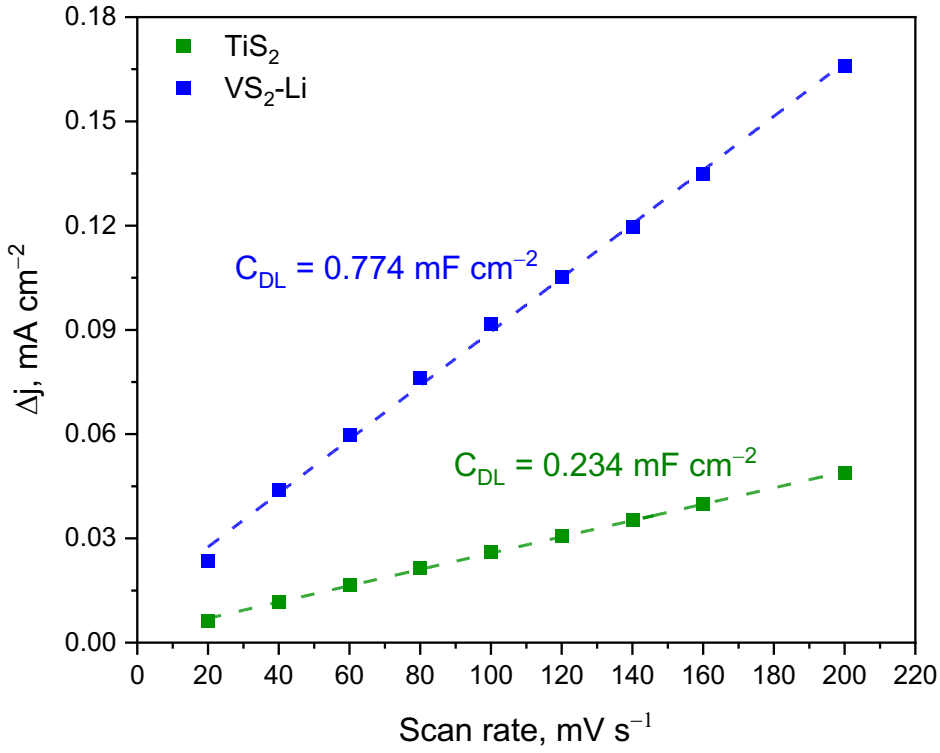

Figure 4-12. *Evaluation of double layer capacitance of TiS_2 and VS_2-Li samples. Current density difference (reading taken at 209 mV vs NHE in 1 M H_2SO_4) is plotted against scan rate.*

The initial assessment of the samples shows potential for a trend of catalytic activity of early transition metal sulphides towards HER that may be linked to a transition metal in the structure. Despite both compounds being poor catalysts, it still provides insight into possible trends in catalytic activity. However, two points are too few to draw a conclusion on the trend confidently.

Table 4-6. *Summary of potentials needed to achieve -10 mA cm^{-2} on the second LSV run for TiS_2 and VS_2-Li samples. Double layer capacitance of both samples is also included.*

Sample	TiS_2	VS_2-Li
E at –10 mA cm^{-2} vs NHE, mV	–1185	–1071
C_{DL}, mF cm^{-2}	0.234	0.774
Q (integrated peak area), mC	–45	–111

4.4. Conclusions

In summary, the chapter focused on synthesis attempts to apply deintercalation reactions from alkali intercalates of TiS_2 and CrS_2. The efforts were unsuccessful in both cases. While TiS_2 showed more promise, full deintercalation could not be achieved, $LiCrS_2$ also could not be deintercalated even under harsh reaction conditions. The idea behind synthesising these compounds was investigation of catalytic activity of isostructural compounds while only changing the transition metal, which leads to essentially adding an electron as we move from left to right along the periodic table. Therefore, to stick to this, TiS_2 was made via solid-state synthesis, as the compound is thermodynamically stable. CrS_2 is not accessible this way, leading to the comparison between two isostructural compounds: TiS_2 and VS_2. Investigation of electrocatalytic properties revealed that the TiS_2 sample, just like VS_2 samples, displayed intense reduction waves during the first scan. The waves could likely be attributed to the formation of surface oxides, however, were not confirmed nor denied in this study. The second LSV scan, on the other hand, provides us with a 'clean' curve, and HER overpotential is revealed to be –1185 mV vs NHE for TiS_2. When compared to VS_2 (overpotential for which was measured to be –1071 mV vs NHE), it shows promise for the trend of increasing electrons leading to better performance to be true. However, two points are insufficient to draw conclusions; therefore, the investigation could be expanded, and hence, selenides, also isostructural with sulphides, could be explored.

4.5. References

1. J. Zhang, J. Wu, H. Guo, W. Chen, J. Yuan, U. Martinez, G. Gupta, A. Mohite, P. M. Ajayan and J. Lou, Unveiling Active Sites for the Hydrogen Evolution Reaction on Monolayer MoS_2, *Adv. Mater.*, 2017, **29**, 1701955.

2. M. Qorbani, A. Sabbah, Y. R. Lai, S. Kholimatussadiah, S. Quadir, C. Y. Huang, I. Shown, Y. F. Huang, M. Hayashi, K. H. Chen and L. C. Chen, Atomistic insights into highly active reconstructed edges of monolayer 2H-WSe_2 photocatalyst, *Nat. Commun.*, 2022, **13**, 1–8.

3. P. V. Sarma, A. Kayal, C. H. Sharma, M. Thalakulam, J. Mitra and M. M. Shaijumon, Electrocatalysis on Edge-Rich Spiral WS_2 for Hydrogen Evolution, *ACS Nano*, 2019, **13**, 10448–10455.

4. H. Zhang, L. Yu, T. Chen, W. Zhou and X. W. (David) Lou, Surface Modulation of Hierarchical MoS_2 Nanosheets by Ni Single Atoms for Enhanced Electrocatalytic Hydrogen Evolution, *Adv. Funct. Mater.*, 2018, **28**, 1807086.

5. L. Zhang, K. Liu, A. B. Wong, J. Kim, X. Hong, C. Liu, T. Cao, S. G. Louie, F. Wang and P. Yang, Three-dimensional spirals of atomic layered MoS_2, *Nano Lett.*, 2014, **14**, 6418–6423.

6. X. Chen, Y. Qiu, G. Liu, W. Zheng, W. Feng, F. Gao, W. Cao, Y. Fu, W. Hu and P. Hu, Tuning electrochemical catalytic activity of defective 2D terrace $MoSe_2$ heterogeneous catalyst: Via cobalt doping, *J. Mater. Chem. A*, 2017, **5**, 11357–11363.

7. Y. Zhou, J. Zhang, E. Song, J. Lin, J. Zhou, K. Suenaga, W. Zhou, Z. Liu, J. Liu, J. Lou and H. J. Fan, Enhanced performance of in-plane transition metal dichalcogenides monolayers by configuring local atomic structures, *Nat. Commun.*, 2020, **11**, 1–8.

8. W. Xiao, P. Liu, J. Zhang, W. Song, Y. P. Feng, D. Gao and J. Ding, Dual-Functional N Dopants in Edges and Basal Plane of MoS_2 Nanosheets Toward Efficient and Durable Hydrogen Evolution, *Adv. Energy Mater.*, 2017, **7**, 1602086.

9. G. Li, D. Zhang, Q. Qiao, Y. Yu, D. Peterson, A. Zafar, R. Kumar, S. Curtarolo, F. Hunte, S. Shannon, Y. Zhu, W. Yang and L. Cao, All the Catalytic Active Sites of MoS_2 for Hydrogen Evolution, *J. Am. Chem. Soc.*, 2016, **138**, 16632–16638.

10. R. J. Toh, Z. Sofer, J. Luxa, D. Sedmidubský and M. Pumera, 3R phase of MoS_2 and WS_2 outperforms the corresponding 2H phase for hydrogen evolution, *Chem. Commun.*, 2017, **53**, 3054–3057.

11. M. A. Lukowski, A. S. Daniel, C. R. English, F. Meng, A. Forticaux, R. J. Hamers and S. Jin, Highly active hydrogen evolution catalysis from metallic WS_2 nanosheets, *Energy Environ. Sci.*, 2014, **7**, 2608–2613.

12. J. C. McGlynn, I. Cascallana-Matías, J. P. Fraser, I. Roger, J. McAllister, H. N. Miras, M. D. Symes and A. Y. Ganin, Molybdenum Ditelluride Rendered into an Efficient and Stable Electrocatalyst for the Hydrogen Evolution Reaction by Polymorphic Control, *Energy Technol.*, 2018, **6**, 345–350.

13. M. J. Park, K. Park and H. Ko, Near-infrared photodetector achieved by chemically-exfoliated multilayered MoS 2 flakes, *Appl. Surf. Sci.*, 2018, **448**, 64–70.

14. L. Wang, Z. Xu, W. Wang and X. Bai, Atomic mechanism of dynamic electrochemical lithiation processes of MoS_2 nanosheets, *J. Am. Chem. Soc.*, 2014, **136**, 6693–6697.

15. K. G. Zhou, N. N. Mao, H. X. Wang, Y. Peng and H. L. Zhang, A mixed-solvent strategy for efficient exfoliation of inorganic graphene analogues, *Angew. Chemie - Int. Ed.*, 2011, **50**, 10839–10842.

16. J. Zhang, T. Ji, H. Jin, Z. Wang, M. Zhao, D. He, G. Luo and B. Mao, Mild Liquid-Phase Exfoliation of Transition Metal Dichalcogenide Nanosheets for Hydrogen Evolution, *ACS Appl. Nano Mater.*, 2022, **5**, 8020–8028.

17. K. Lobo, S. Trivedi and H. S. S. R. Matte, Highly concentrated and stabilizer-free transition-metal dichalcogenide dispersions in low-boiling point solvent for flexible electronics, *Nanoscale*, 2019, **11**, 10746–10755.

18. R. Anbazhagan, H. J. Wang, H. C. Tsai and R. J. Jeng, Highly concentrated MoS_2 nanosheets in water achieved by thioglycolic acid as stabilizer and used as biomarkers, *RSC Adv.*, 2014, **4**, 42936–42941.

19. M. M. Bernal, L. Álvarez, E. Giovanelli, A. Arnáiz, L. Ruiz-González, S. Casado, D. Granados, A. M. Pizarro, A. Castellanos-Gomez and E. M. Pérez, Luminescent transition metal dichalcogenide nanosheets through one-step liquid phase exfoliation, *2D Mater.*, 2016, **3**, 035014.

20. C. Tsai, K. Chan, J. K. Nørskov and F. Abild-Pedersen, Theoretical insights into the hydrogen evolution activity of layered transition metal dichalcogenides, *Surf. Sci.*, 2015, **640**, 133–140.

21. Y. Qu, H. Pan and C. T. Kwok, Hydrogenation-controlled phase transition on two-dimensional transition metal dichalcogenides and their unique physical and catalytic properties, *Sci. Rep.*, 2016, **6**, 1–13.

22. T. Das, S. Chakraborty, R. Ahuja and G. P. Das, TiS_2 Monolayer as an Emerging Ultrathin Bifunctional Catalyst: Influence of Defects and Functionalization, *ChemPhysChem*, 2019, **20**, 608–617.

23. N. Ran, B. Sun, W. Qiu, E. Song, T. Chen and J. Liu, Identifying Metallic Transition-Metal Dichalcogenides for Hydrogen Evolution through Multilevel High-Throughput Calculations and Machine Learning, *J. Phys. Chem. Lett.*, 2021, **12**, 2102–2111.

24. F. Sun, A. Hong, W. Zhou, C. Yuan and W. Zhang, Prediction for structure stability and ultrahigh hydrogen evolution performance of monolayer 2H-CrS_2, *Mater. Today Commun.*, 2020, **25**, 101707.

25. E. Long, S. O'Brien, E. A. Lewis, E. Prestat, C. Downing, C. S. Cucinotta, S. Sanvito, S. J. Haigh and V. Nicolosi, An in situ and ex situ TEM study into the oxidation of titanium (IV) sulphide, *npj 2D Mater. Appl.*, 2017, **1**, 22.

26. M. Su, W. Zhou, Z. Jiang, M. Chen, X. Luo, J. He and C. Yuan, Elimination of Interlayer Potential Barriers of Chromium Sulfide by Self-Intercalation for Enhanced Hydrogen Evolution Reaction, *ACS Appl. Mater. Interfaces*, 2021, **13**, 13055–13062.

27. R. J. Toh, Z. Sofer and M. Pumera, Catalytic properties of group 4 transition metal dichalcogenides (MX_2; M = Ti, Zr, Hf; X = S, Se, Te), *J. Mater. Chem. A*, 2016, **4**, 18322–18334.

28. Z. Zeng, C. Tan, X. Huang, S. Bao and H. Zhang, Growth of noble metal nanoparticles on single-layer TiS_2 and TaS_2 nanosheets for hydrogen evolution reaction, *Energy Environ. Sci.*, 2014, **7**, 797–803.

29. T. P. Nguyen, S. Choi, J. M. Jeon, K. C. Kwon, H. W. Jang and S. Y. Kim, Transition Metal Disulfide Nanosheets Synthesized by Facile Sonication Method for the Hydrogen Evolution Reaction, *J. Phys. Chem. C*, 2016, **120**, 3929–3935.

30. Y. Liu, C. Liang, J. Wu, T. Sharifi, H. Xu, Y. Nakanishi, Y. Yang, C. F. Woellne, A. Aliyan, A. A. Martí, B. Xie, R. Vajtai, W. Yang and P. M. Ajayan, Atomic Layered Titanium Sulfide Quantum Dots as Electrocatalysts for Enhanced Hydrogen Evolution Reaction, *Adv. Mater. Interfaces*, 2018, **5**, 1700895.

31. R. R. Chianelli, J. C. Scanlon and A. H. Thompson, Structure refinement of stoichiometric TiS_2, *Mater. Res. Bull.*, 1975, **10**, 1379–1382.

32. T. Kusawake, Y. Takahashi and K.-I. Ohshima, Structural Analysis of the Layered Compounds Cu_xTiS_2, *Mol. Cryst. Liq. Cryst. Sci. Technol. Sect. A. Mol. Cryst. Liq. Cryst.*, 2000, **341**, 93–98.

33. J. R. Dahn, W. R. McKinnon, R. R. Haering, W. J. L. Buyers and B. M. Powell, Structure determination of Li_xTiS_2 by neutron diffraction, *Can. J. Phys.*, 1980, **58**, 207–213.

34. F. A. S. Al-Alamy, A. A. Balchin and M. White, The expansivities and the thermal degradation of some layer compounds, *J. Mater. Sci.*, 1977, **12**, 2037–2042.

35. M. J. McKelvy and W. S. Glaunsinger, Synthesis and characterization of nearly stoichiometric titanium disulfide, *J. Solid State Chem.*, 1987, **66**, 181–188.

36. S. N. Patel and A. A. Balchin, The preparation of titanium disulphide with different stoichiometries, $Ti_{(1+x)}S_2$, and comparison of lattice parameters, *J. Mater. Sci. Lett.*, 1984, **3**, 942–944.

37. P. C. Sherrell, K. Sharda, C. Grotta, J. Ranalli, M. S. Sokolikova, F. M. Pesci, P. Palczynski, V. L. Bemmer and C. Mattevi, Thickness-Dependent Characterization of Chemically Exfoliated TiS2 Nanosheets, *ACS Omega*, 2018, **3**, 8655–8662.

38. X.-F. Tang, S.-X. Zhu, H. Liu, C. Zhang, Q.-Y. Wu, Z.-T. Liu, J.-J. Song, X. Guo, Y.-S. Wang, H. Ma, Y.-Z. Zhao, F.-Y. Wu, S.-Y. Liu, K.-H. Liu, Y.-H. Yuan, H. Huang, J. He, W. Xu, H.-Y. Liu, Y.-X. Duan and J.-Q. Meng, Growth, characterization, and Raman spectra of the 1T phases of $TiTe_2$, $TiSe_2$, and TiS_2, *Chinese Phys. B*, 2022, **31**, 037103.

39. S. Sharma, S. Singh, R. C. Singh and S. Sharma, Structural transformation and room temperature ammonia sensing properties of TiS_2 nanostructures, *SN Appl. Sci.*, 2020, **2**, 887.

40. J. A. Diaz-Real, P. Elsaesser, T. Holm and W. Mérida, Electrochemical reduction on nanostructured TiO_2 for enhanced photoelectrocatalytic oxidation, *Electrochim. Acta*, 2020, **329**, 135162.

41. Z. Shadike, Y. N. Zhou, L. L. Chen, Q. Wu, J. L. Yue, N. Zhang, X. Q. Yang, L. Gu, X. S. Liu, S. Q. Shi and Z. W. Fu, Antisite occupation induced single anionic redox chemistry and structural stabilization of layered sodium chromium sulfide, *Nat. Commun.*, 2017, **8**, 1–9.

42. S. Kobayashi, N. Katayama, T. Manjo, H. Ueda, C. Michioka, J. Sugiyama, Y. Sassa, O. K. Forslund, M. Månsson, K. Yoshimura and H. Sawa, Linear Trimer Formation with Antiferromagnetic Ordering in 1T-$CrSe_2$ Originating from Peierls-like Instabilities and Interlayer Se–Se Interactions, *Inorg. Chem.*, 2019, **58**, 14304–14315.

5. MSe_2 (M = Ti, V, Cr) for electrochemical water splitting

5.1. Introduction

In the previous chapter, the aim to investigate trends of HER activity for the isostructural compounds TiS_2, VS_2 and CrS_2 was limited by the synthetic challenge of obtaining CrS_2. Despite that, an intriguing/promising trend could be noticed by comparing TiS_2 and VS_2. For this reason, the investigation was expanded to selenides of the same metals. $TiSe_2$, VSe_2 and $CrSe_2$ are all isostructural with their respective sulphides and between each other. Moreover, there are literature reports on the successful synthesis of $CrSe_2$. Even though that synthesis calls for a deintercalation reaction, the previous chapters proved that no adverse behaviours result from this synthesis method. This way, all three isostructural selenides can be compared and trends in their catalytic activity towards HER explored.

5.1.1. Synthesis of MSe_2 (M = Ti, V, Cr)

Most of the research done on $TiSe_2$ is done on either single crystal samples or bulk solid-state samples. Therefore, the literature reports on synthesising this dichalcogenide are overwhelmingly dominated by chemical vapour transport reactions or solid-state sample preparation.[1–6] Crystals can easily grow in a wide temperature range from 600 to 950 °C. The rare reports on other methods include 'wet' synthesis, ball milling, and CVD methods being employed in attempts to synthesise $TiSe_2$.[7–10] Nanostructuring of this compound appears to be approached solely via liquid exfoliation.

Synthetic approaches of VSe_2 vary more than those of $TiSe_2$. Whilst solid-state remains a popular method for single crystal and bulk samples just like for $TiSe_2$, there are methods such as hydrothermal/solvothermal, CVD, and molecular beam epitaxy reported for the synthesis of nanostructures of VSe_2.[11–17]

According to the literature, bulk layered $CrSe_2$ can only be accessed through the deintercalation reaction of K_xCrSe_2.[18,19] Attempts to apply other synthetic methods to obtain bulk samples have so far been unsuccessful due to Cr^{3+} being a preferred oxidation state for Cr. This is illustrated by chromium forming Cr_2S_3 and Cr_2Se_3 in solid-state reactions in a wide temperature range.[20,21] Recently, Li *et al.* achieved success in the epitaxial growth of $CrSe_2$ nanosheets.[22] The published results are promising, and other synthetic routes might finally be tuned to produce layered $CrSe_2$.

5.1.2. The catalytic activity of MSe_2 (M=Ti, V, Cr)

The catalytic activity of VSe_2 is widely reported compared to the other two dichalcogenides. While not as many reports can be found on VSe_2 as there were for VS_2, different morphologies from bulk to nanostructured and doped VSe_2 samples have been investigated as possible catalysts for HER in acidic media. Reported overpotentials for a benchmark current density range from –126 mV vs RHE (nanosheet morphology) to nearly –1000mV vs RHE (bulk powders) for pristine VSe_2 samples (Table 5-1). The range of –500-550 mV vs RHE is the range that reported activities fall into most often. Efforts have also been made to improve the electrochemical performance via various sample modifications such as oxygen plasma treatment, cobalt doping, and defect engineering.

Literature on the HER activity of $TiSe_2$ and $CrSe_2$ is incredibly scarce. While no reports of electrochemical studies on HER of $CrSe_2$ were found, a study was published on group IV dichalcogenides and their catalytic activity. $TiSe_2$ was investigated in that study and was found to be a poor catalyst, reaching a current density of –10 mA cm^{-2} at –1050 mV vs NHE.[23]

Despite a lack of experimental reports, $CrSe_2$ has been named as a promising catalyst in a computational study by Ran *et al*.[24] The study was focused on monolayers, perfect and defect containing and so, imperfect monolayers of $CrSe_2$ have been identified as a promising catalyst. This must be considered, as it is well known that mono to a few layered materials and their bulk counterparts exhibit differences in properties. Unfortunately, no studies on bulk $CrSe_2$ or any experimental reports could be found.

Table 5-1. *Literature reports on the catalytic activity of VSe_2 and its composites*

Morphology/ composite	Overpotential at –10 mA cm^{-2}, mV vs RHE	Tafel slope, mV dec^{-1}	C_{DL}, mF cm^{-2}	Ref
VSe_2 flakes	543	160	N/A	[25]
Co-decorated VSe_2	349	102	N/A	
Pt-decorated VSe_2	294	106	N/A	
O_2 plasma treated VSe_2	304	171	N/A	[26]
VSe_2 quantum dots	400	80	5.5	[27]
VSe_2 nanosheets	530	96	N/A	
VSe_2	247	108	8.74	[28]
$VSe_{1.8}$	160	85	18.1	
$VSe_{1.6}$	189	98	8.95	
Liquid exfoliated VSe_2 sheets	540	121	N/A	[29]
$V_{0.8}Fe_{0.2}Se_2$	390	112	5.7	
VSe_2 nanosheets	414	142	0.24	[13]
Co-doped VSe_2 nanosheets	230	63	1.38	
VSe_2 flakes	126	70	N/A	[30]
VSe_2 bulk	950-1000	N/A	N/A	[23]
Liquid exfoliated VSe_2	940-980	N/A	N/A	
VSe_2 pristine nanosheets	547	101	N/A	[15]
O_2 plasma treated VSe_2 nanosheets	206	88	N/A	

5.2. Aims

The main aim of this chapter is to synthesise isostructural selenides $TiSe_2$, VSe_2 and $CrSe_2$ with comparable morphology and stoichiometry. Then, the electrochemical characterisation of all three samples will be carried out, and trends in catalytic activity will be explored. It will provide an insight into the origins of the catalytic activity of these materials, as the only difference between the structures is the transition metal in the centre of octahedra, and the metals all differ by one electron from each other.

5.3. Results and discussion

5.3.1. $TiSe_2$ synthesis and characterisation

5.3.1.1. $TiSe_2$ solid-state synthesis

A direct solid-state reaction between the elements at a temperature of 600 °C has been carried out to synthesise $TiSe_2$. Excess Se crystallised on the inner walls of the reaction tube after the initial heating. The product of the reaction was taken out of the ampoule to be ground using mortar and pestle, and a PXRD measurement was done to investigate the phase purity. Even though the sample appeared pure from the initial PXRD assessment (Figure 5-1), due to the Se residue on the reaction tube walls, it was decided to reanneal the sample. The sample was reannealed at 600 °C for 24 hours, and after this reaction, no Se residue could be noticed on the reaction tube walls. PXRD was rerun on the sample, and the pattern strongly agreed with the reference pattern from ICSD (Figure 5-1).

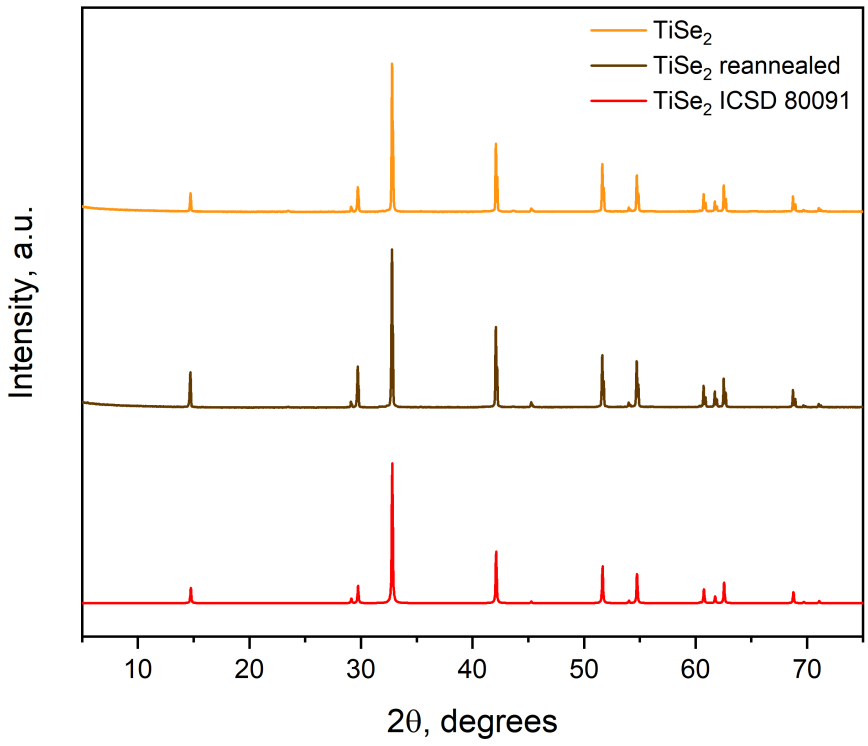

Figure 5-1. *PXRD pattern of the reaction product between Ti powder and Se shots sealed under vacuum and heated at 600 °C for 72 hours (top, orange) compared with PXRD pattern of the same sample after annealing it at 600 °C for another 24 hours (middle, brown). Pattern calculated from ICSD card no 80091 for reference (red, bottom)*

Le Bail refinement was carried out to obtain cell parameters of the sample, and the results are in Table 5-2 below. The refinement results agreed well with the published data for $TiSe_2$.

The cell parameters match well within two significant numbers of reported values. Refined PXRD data is in Figure 5-2.

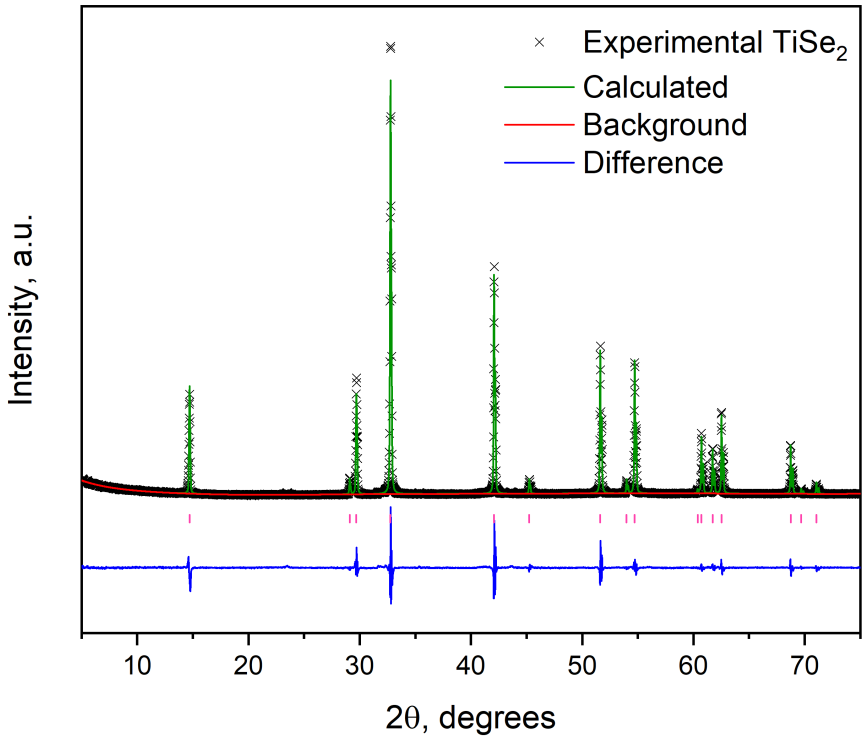

Figure 5-2. *Le Bail refinement plot of sample $TiSe_2$. Experimental pattern is noted as scatter plot with 'x', calculated pattern is in green, background in red and difference in blue line plots. Refinement was carried out in GSASII software.*

Table 5-2. *Cell parameters of $TiSe_2$ synthesised at 600 °C from elements via solid-state reaction in comparison with values reported in the literature.*

Sample	*a*, Å	*c*, Å	Ref
$TiSe_2$	3.53553(7)	6.00305(6)	This work
$TiSe_2$	3.5395	6.0082	[31]
$TiSe_2$	3.533	5.995	[32]
$TiSe_2$	3.537	6.005	[2]
$TiSe_2$	3.53825	6.00923	[33]
$TiSe_2$	3.537	6.00	[34]

5.3.1.2. Raman spectroscopy of $TiSe_2$

Raman measurements were carried out for further phase identification. Raman spectra were recorded on a sample at ambient conditions as well as a sample sealed in a capillary under

an inert atmosphere and are displayed in Figure 5-3. The reasoning behind this is, similar to the case in VS_2, conflicting literature reports. While most reports agree that there are only two active modes of $TiSe_2$ at room temperature at 137 cm^{-1} and 200 cm^{-1}, other reports claim there are also peaks in a range of 230-260 cm^{-1} visible in the Raman spectrum.[35–41] While reports on the position of usually broad peaks at 230-260 cm^{-1} agree, the reasoning behind where the peaks originate from differs. Some claim that the broad peak at 250 cm^{-1} arises from a high concentration of selenium vacancies in the sample, others argue that the peak arises due to migration and aggregation of selenium on the surface of the sample.[37,40] The peak sometimes even splits into two distinct peaks and they can be attributed to two different selenium allotropes.[38] This migration of selenium to the surface of the sample could simply be due to sample decomposition. However, no titanium oxide peaks emerge as the selenium peaks appear, leading to the assumption that the selenium migration to the surface is a legitimate explanation for the emerging peaks. In our study, the broad peak at 250 cm^{-1} can only be seen in the Raman spectrum of the sample measured under ambient conditions. A Raman study conducted by Duong *et al.* revealed that the mode at 233 cm^{-1} is only present when the measurement is done on the sample after prolonged storage and exposure to ambient conditions and is absent in the measurements carried out on freshly cleaved crystal surface.[42] In our study, this peak is not present in the Raman spectrum of the same sample sealed in a capillary under an inert atmosphere and agrees well with observations by Duong *et al*. Only two Raman modes are present in our measured Raman spectrum – 133 cm^{-1} and 196 cm^{-1}. They agree well with literature reports, although are slightly shifted.

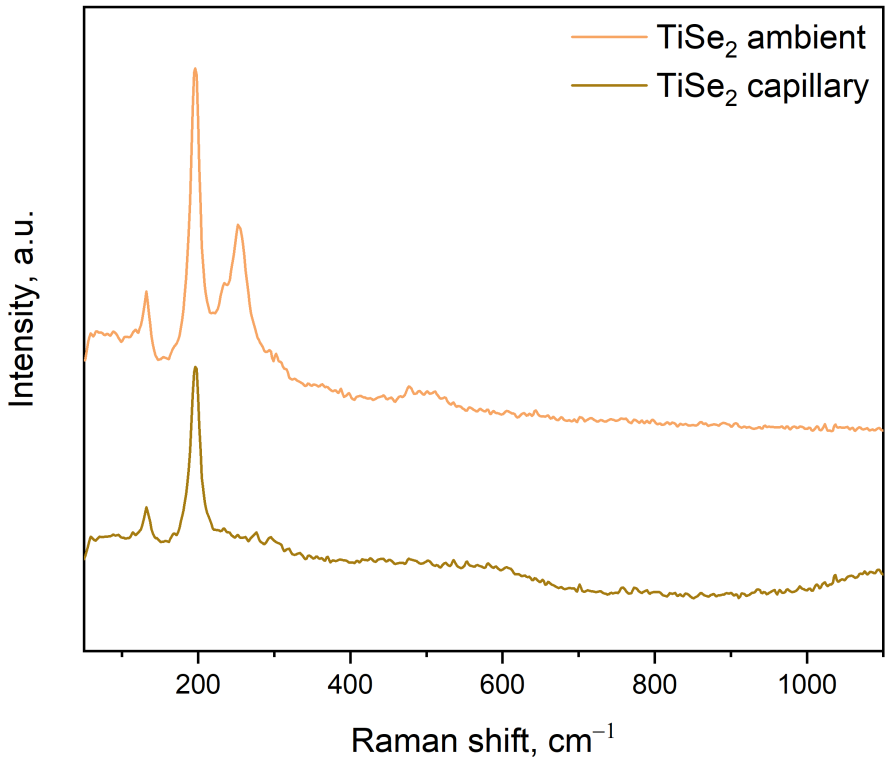

Figure 5-3. *Raman spectrum of sample $TiSe_2$. The top spectrum (orange) was collected on sample at ambient conditions. Bottom spectrum (brown) was collected on sample sealed in a capillary under an inert atmosphere. The same laser intensity and spectrum acquisition time was used to collect both spectra.*

5.3.1.3. Elemental composition and morphology of $TiSe_2$

The elemental composition of the sample was investigated using EDX measurements. The results revealed that the sample has a slight excess of selenium (Table 5-3). The final composition of the sample was calculated to be $TiSe_{2.07}$. This agrees with other literature reports as the temperature used in synthesis was considerably low. For example, Levy *et al.* remarked that $TiSe_2$ crystals grown at temperatures of 500 °C resulted in stoichiometric compounds, usually with a slight selenium excess.[43] Whereas $TiSe_2$ crystals grown at higher temperatures (above 740 °C) are usually found to be slightly selenium deficient with a stoichiometry of $TiSe_{1.94(2)}$.[44] Moreover, Rimmington *et al.* carried out a careful investigation of lattice parameters with the change of stoichiometry and found, that the lattice shrinks (both *a* and *c* parameters) with increasing Se deficiency in the samples. Therefore, EDX data combined with the lattice parameters obtained from PXRD point towards $TiSe_2$ with higher Se contents being made in this work.

Table 5-3. *EDX data of $TiSe_2$ sample prepared via solid-state reaction between elemental Ti and Se. The standard deviations are evaluated based on 8 independent points.*

	$TiSe_2$ at. %	
Element	Ti	Se
Experimental	32.6(22)	67.4(22)
Theoretical	33.3	66.6

Sample morphology was observed via SEM imaging, shown in Figure 5-4. The crystallite size varies quite a bit, with some crystallites being around 10 µm in diameter, and others have grown up to 50 µm in diameter. Despite wide distribution in size, they all adopt a similar shape. The crystals resemble hexagonal platelets; however, the edges are quite rounded, giving the platelets more of a button-like appearance.

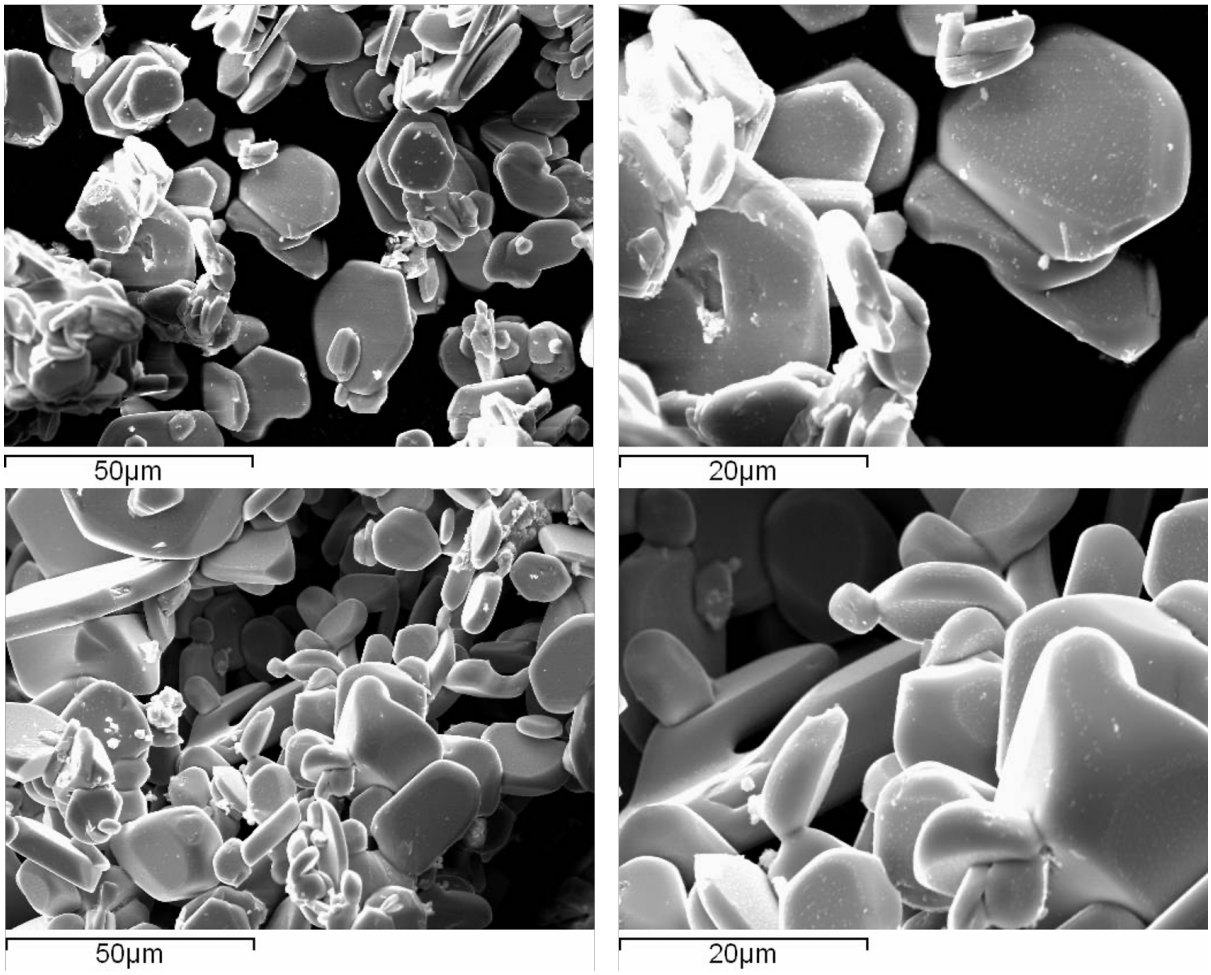

Figure 5-4. *SEM images of $TiSe_2$ sample. Two different magnifications of two different spots are displayed.*

5.3.1.4. Electrocatalytic activity towards HER

Having confirmed the crystal structure of the sample, phase purity and elemental composition, electrochemical studies have been carried out. An initial assessment of the sample revealed a behaviour very similar to that of VS_2 (Figure 5-5). Quite an intense reduction wave was observed on an initial LSV scan at around –700 mV vs NHE, moreover, a couple of smaller reduction waves appeared between –500 and –600 mV vs NHE. The LSV profile is similar to that of TiS_2. All these waves would be removed during the initial scan and the second LSV run would result in the polarization curve of the expected shape. The overpotential needed to achieve benchmark current densities is at an extremely high value of –1091 mV *vs* NHE. Potential this high truly limits the investigation of the material as this region is way beyond the inert region for the glassy carbon electrode. Even with material completely covering the surface of the electrode, the possible breakage of catalyst film on the electrode and exposure of bare glassy carbon to the highly acidic environment would influence the measurements. Due to this, stability testing could not be carried out. Nevertheless, even if the catalyst would display great stability, the overpotential alone deems this catalyst ineffective towards the hydrogen evolution reaction.

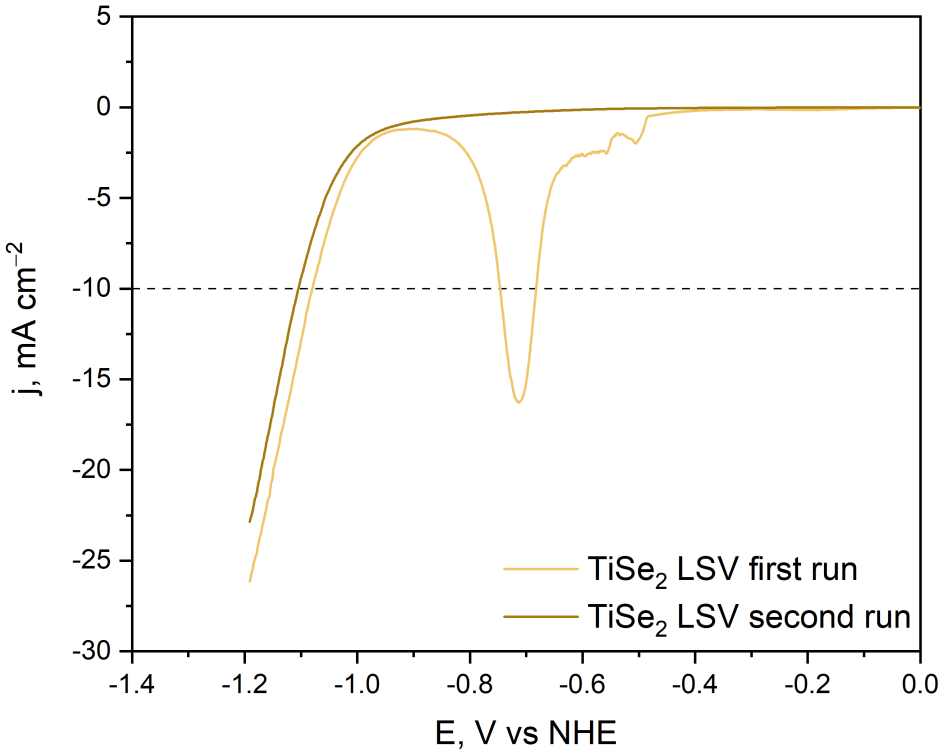

Figure 5-5. *Polarization curves recorded on $TiSe_2$. The first scan reveals a reduction wave, whereas a second scan shows the actual HER overpotential. Polarization curves were recorded using a sweep rate of 5 mV s^{-1}. Three electrode setup in 1 M H_2SO_4 electrolyte where glassy carbon modified with catalyst was working electrode, carbon felt was used as a counter electrode and 3 M Ag/AgCl electrode as a reference electrode. Current density is calculated using geometric electrode area (0.071 cm^2).*

5.3.2. VSe_2 Synthesis and characterisation

5.3.2.1. VSe_2 solid-state synthesis

As well as $TiSe_2$, VSe_2 was synthesised via a solid-state reaction between the elements at 600 °C. Similar to $TiSe_2$, excess Se could be seen on the inner walls of the reaction tube after the initial heating step. PXRD revealed that the main product of the reaction was formed after the first heating (Figure 5-6). The experimental pattern agreed well with the reference pattern calculated from ICSD. However, to ensure that the reaction went to completion the product was reannealed at 600 °C. No Selenium could be seen on the walls of the tube this time. When PXRD patterns of the sample after the initial heating step and re-annealing were compared, no major differences could be noticed, meaning, that the final product forms within the timeframe of the first heating.

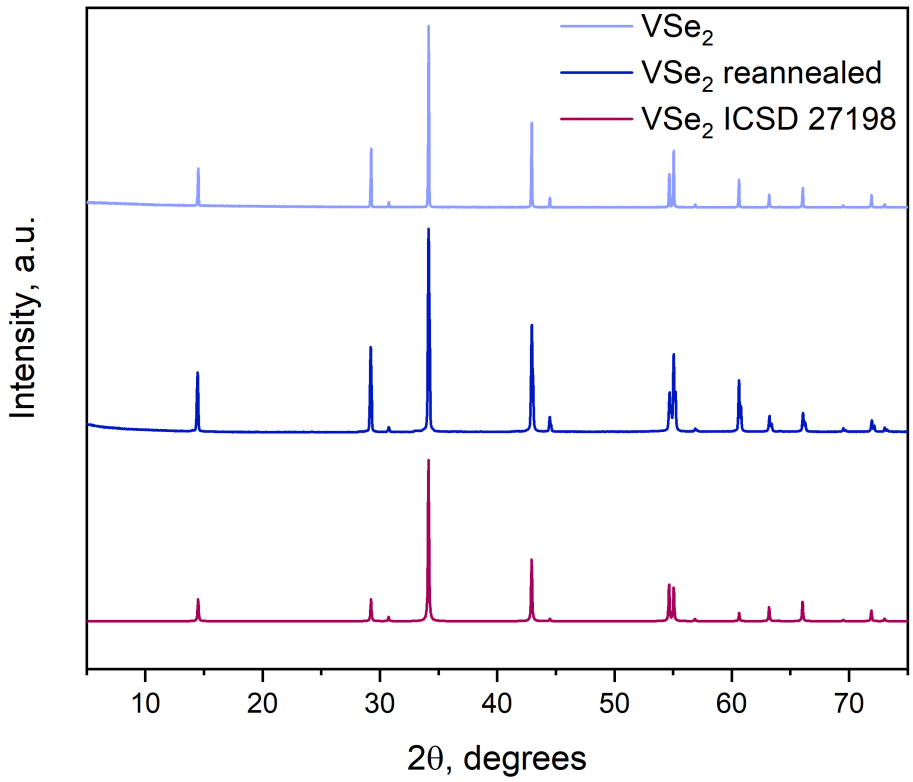

Figure 5-6. *PXRD pattern of the product of reaction between V powder and Se shot sealed under vacuum and heated at 600 °C for 72 hours (top, light blue) in comparison with PXRD pattern of the same sample after annealing it at 600 °C for another 24 hours (middle, navy blue). Pattern calculated from ICSD card no 27198 for reference (bottom, dark plum).*

Le Bail refinement was carried out to obtain cell parameters of the sample and the refined diffraction pattern, as well as refinement results, are in Figure 5-7 and Table 5-4 below. While *a* parameter of the unit cell varies very little throughout literature reports, parameter *c* seems to deviate. Nakahira *et al.* have investigated the trends of cell parameters with the change of vanadium content in the sample.[45] The research revealed, that as vanadium content increases, parameter *a* expands and parameter *c* shrinks. Considering this, cell parameters obtained for the sample in this research point towards the product being stoichiometric VSe_2.

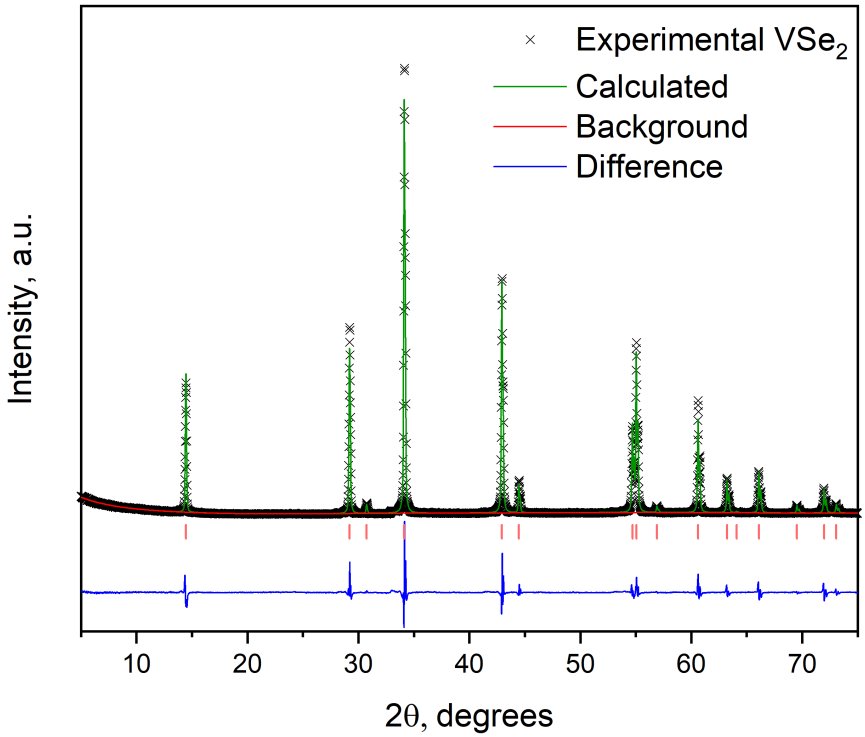

Figure 5-7. *Le Bail refinement plot of sample VSe_2. Experimental pattern is noted as scatter plot with 'x', calculated pattern is in green, background in red and difference in blue line plots. Refinement was carried out in GSASII software.*

Table 5-4. *Cell parameters (from Le Bail refinement of PXRD data) of VSe_2 synthesised at 600 °C from elements via solid-state reaction in comparison with values reported in literature.*

Sample	*a*, Å	*c*, Å	Ref
VSe_2	3.35059(7)	6.10069(6)	This work
$V_{1.02}Se_2$	3.348	6.122	[46]
VSe_2	3.3587	6.1075	[47]
VSe_2	3.345	6.048	[48]
VSe_2	3.356	6.150	[49]
$V_{1.005}Se_2$	3.356	6.104	[50]
$V_{1.04}Se_2$	3.363	6.0946	[45]
$V_{1.13}Se_2$	3.4227	5.9659	
$V_{1.156}Se_2$	3.4314	5.9729	

5.3.2.2. Elemental composition and morphology of VSe_2

EDX measurements revealed the sample composition to be $VSe_{2.05}$ (Table 5-5). It indicates that the sample is selenium-rich. The result is similar to that of $TiSe_2$, where a selenium excess was detected during EDX measurements as well.

Table 5-5*. EDX data of VSe_2 sample prepared via solid-state reaction between elemental V and Se. The standard deviations are evaluated based on 8 independent points.*

	VSe_2 at. %	
Element	V	Se
Experimental	32.8(23)	67.2(23)
Theoretical	33.3	66.6

The sample morphology was investigated as well. SEM images displayed in Figure 5-8 revealed that the sample consists of platelet-like crystallites. The distribution in size is comparable to that of the $TiSe_2$ sample. Moreover, the overall morphology of the two samples is extremely similar. This, in turn, would allow for an adequate comparison of the electrochemical properties of the two samples, as any discrepancy regarding morphology will be avoided.

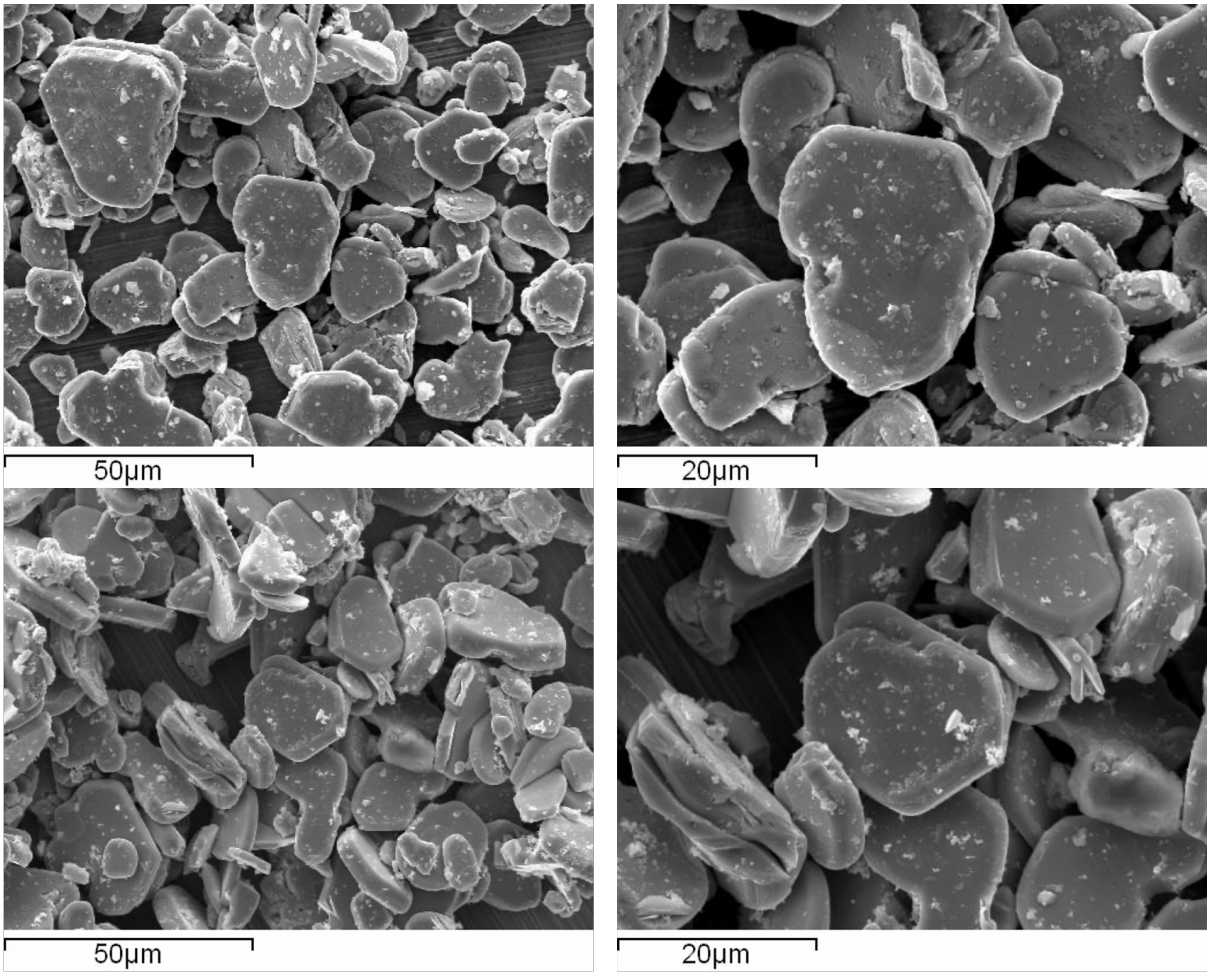

Figure 5-8. *SEM images of VSe_2 sample. Two different magnifications of two different spots are displayed.*

5.3.2.3. Raman spectroscopy of VSe_2

Raman measurements were carried out for further characterisation and phase confirmation. Just like VS_2, when measured under ambient conditions, VSe_2 oxidises. Therefore, the measurements were also carried out on a sample sealed in a capillary. The Raman spectrum obtained from these measurements is in Figure 5-9. The spectrum is not very high in quality, as very fine tuning of the laser power and measurement conditions is needed to avoid burning the sample. However, as the figure shows, only one peak at 204 cm^{-1} is observed for this sample. It agrees well with the literature reports for VSe_2.[51–53] Wide range Raman measurements in a capillary also show that there are no unreacted Se or other impurities, such as oxides, present in the sample.

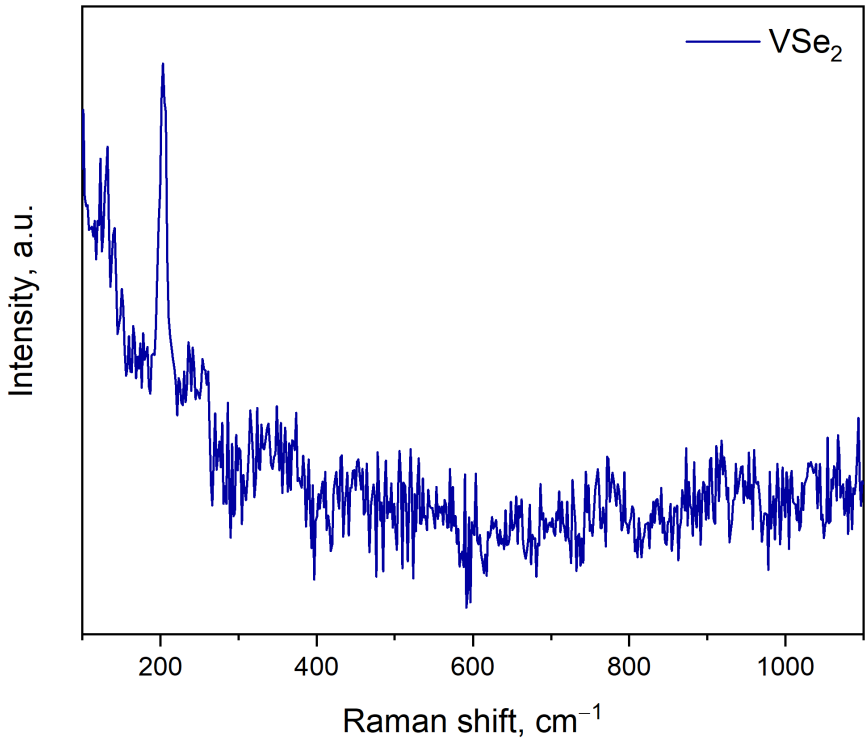

Figure 5-9. *Raman spectrum of sample VSe_2. Spectrum was collected on sample sealed in a capillary under inert atmosphere.*

5.3.2.4. Electrocatalytic activity of VSe_2 towards HER

Following the sample synthesis and characterisation, electrochemical performance towards hydrogen evolution has been investigated. Initial assessment revealed that just like VS_2 and now $TiSe_2$, VSe_2 displays the reduction wave when the first LSV scan is run (Figure 5-10). The reduction wave appears to be positioned at the same potential values as in the case for VS_2, however, in this sample, the peak appears sharper. In addition, the peak achieves high current densities and considerably surpasses the benchmark. This creates an opportunity to mistakenly claim the HER overpotential to be much lower, although, the value of –561 mV vs NHE falls right into the range of the most reported values within the literature. However, in the second LSV scan, the peak is no longer visible. Once the reduction peak is removed, the overpotential required to achieve the benchmark current density of –10 mA cm^{-2} is revealed. VSe_2 reaches this benchmark at –882 mV vs NHE.

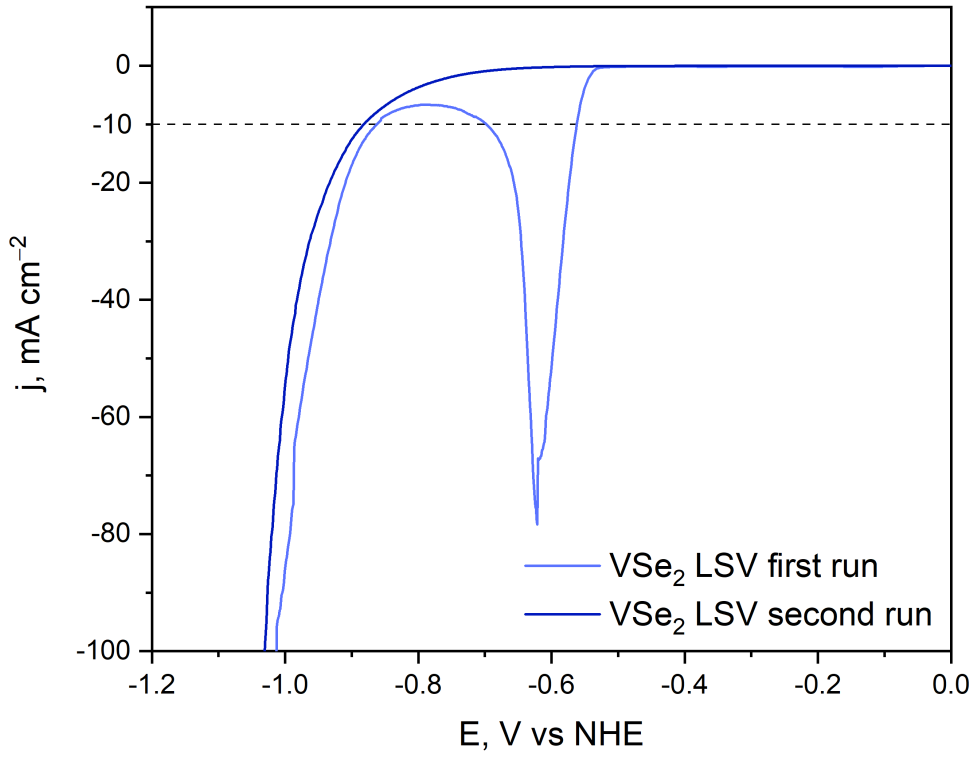

Figure 5-10. *Polarization curves recorded on sample VSe_2. The first scan reveals a reduction wave, whereas a second scan shows the actual HER overpotential. Polarization curves were recorded using a sweep rate of 5 mV s^{-1}. Three electrode setup in 1 M H_2SO_4 electrolyte where glassy carbon modified with catalyst was working electrode, carbon felt was used as a counter electrode and 3 M Ag/AgCl electrode as a reference electrode. Current density is calculated using geometric electrode area (0.071 cm^2).*

5.3.3. Synthesis and characterisation of $CrSe_2$

5.3.3.1. K_xCrSe_2 synthesis

$CrSe_2$ in the form of layered dichalcogenide is only accessible via the deintercalation route. It also can only be made from $KCrSe_2$ as other alkali metals cannot be deintercalated using iodine. Therefore, $KCrSe_2$ synthesis was attempted first. Even though the literature reports call for the synthesis between the elements at 850 °C, in this work the synthesis was attempted at 600 °C with the intention that keeping the same temperature will help with keeping the morphology similar to the other selenide samples.[19,54] Another deviation from the reported synthesis was the content of potassium which was kept at 0.7 for the initial reaction. It was reported that $KCrSe_2$ is isostructural with $NaCrSe_2$ and $KCrS_2$ adapting a crystal structure with a space group *R–3m*, which would also make it isostructural with $NaVS_2$. This led to the assumption that the lower content of K used in synthesis would lead

to the single-phase sample that would then be easier to identify. PXRD was run on the sample and the resulting pattern did not match to the one reported in the literature (Figure 5-11).[54] Considering the lower temperature used for the synthesis, the sample was reannealed at an increasingly higher temperature. Nevertheless, the sample's PXRD pattern never matched that reported in the literature. The assumption that lower potassium content will lead to a pure phase sample was further disproven by Song *et al.* in their publication of the kinetics of deintercalation reaction. It became apparent that this system is more complex than that of $NaVS_2$.

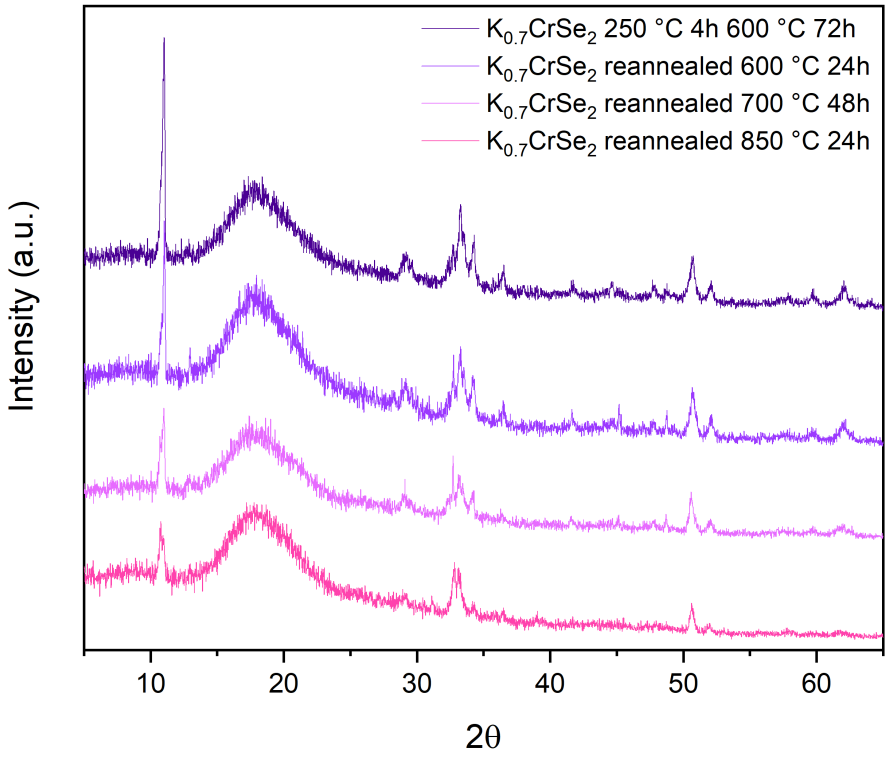

Figure 5-11. *PXRD pattern of the product of reaction between elemental K, Cr powder and Se shots sealed under vacuum and heated at 600 °C for 72 hours (top, dark purple) in comparison with PXRD pattern of the same sample after annealing it at various temperatures. The bottom pattern (bright pink) is the pattern of the last reannealing and final product.*

To begin with, while using the same previously reported strategy, the authors have found that their polycrystalline $KCrSe_2$ sample has a different crystal structure and could be identified using *C2/m* space group. Although it is important to note that the synthesis was carried out at lower temperatures (700 °C), there is a possibility that a different crystal structure is a result of lower temperature. Moreover, it was reported that some of their samples had a mixture of $KCrSe_2$ and another potassium deficient phase. However, the crystal structure of this deficient phase was never reported as the phase could not be isolated.

The deintercalation studies of the phase-pure sample revealed that multiple potassium deficient phases form as potassium is removed from the structure.

Multiple phases that form at lower potassium content would explain why the sample when 0.7 equivalents of potassium was used for synthesis could not fit with the pattern of a stoichiometric compound. Therefore, stoichiometric amounts were used in the following syntheses. Unfortunately, stoichiometric amounts did not lead to a single-phase sample. After the initial heating step, PXRD of the resulting powders showed that together with possible K_xCrSe_2 phases, the K_2Se_2 phase has also formed (Figure 5-12). This led to another sample annealing after homogenising it using a mortar and pestle in the glove box. As the PXRD pattern collected after reannealing revealed, the K_2Se_2 phase was no longer present in the product. Also, there was still a mixture of potassium deficient phases instead of the expected single-phase product. This time, however, the pattern could be examined using the nonstoichiometric phases identified by Song *et al.* (Figure 5-12).

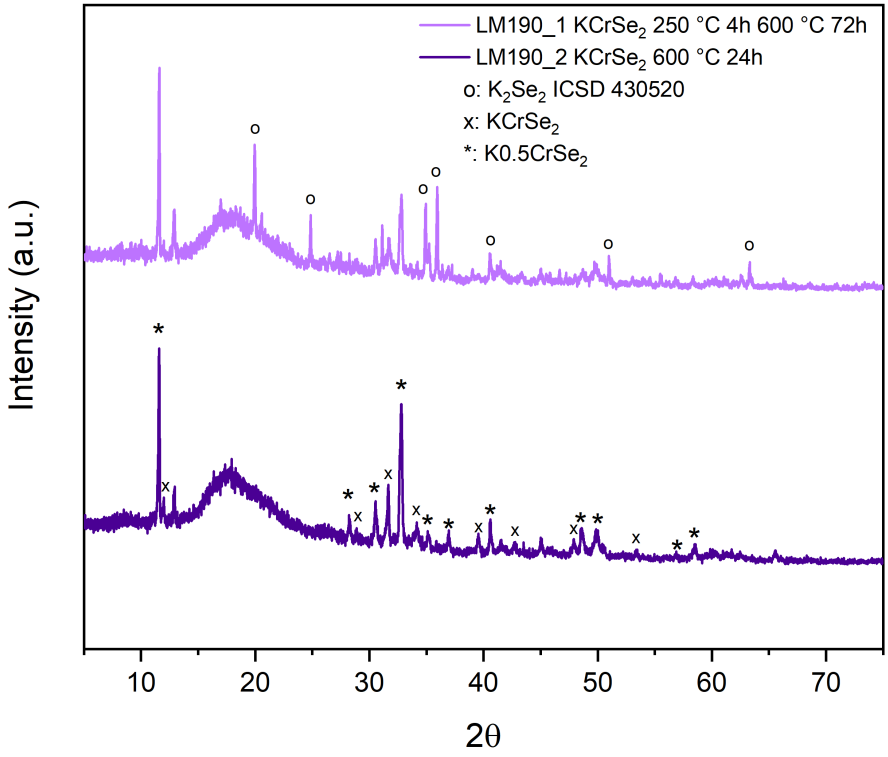

Figure 5-12. *PXRD pattern of the product of reaction between elemental K, Cr powder and Se shots in respective molar ratio of 1:1:2 sealed under vacuum and heated at 600 °C for 72 hours (top, violet) in comparison with PXRD pattern of the same sample after annealing it at 600 °C for 24 hours (bottom, dark purple). The K_2Se_2 phase peaks are denoted as 'o', $K_{0.5}CrSe_2$ peaks as '*' and $KCrSe_2$ peaks as 'x'*

5.3.3.2. Synthesis of $CrSe_2$

Even though a single phase of this sample could not be achieved, having confirmed that the sample is a mixture of intercalated phases, the sample was then used in a deintercalation reaction. The product of the deintercalation reaction was first characterised using PXRD. The pattern (Figure 5-13) collected at ambient conditions revealed that the sample is single phase $CrSe_2$ as it visually matched the reference pattern well. There is a broad peak at ca. 10º, which could be attributed to the possible intercalation of solvent during the deintercalation reaction. Moreover, the peaks are broad, hinting at lower crystallinity and smaller crystallite size of the sample than its solid-state titanium and vanadium counterparts. The peak shape is closer to that of nanostructured VS_2 described in chapter 3. No rapid degradation of the sample under ambient conditions was noticed.

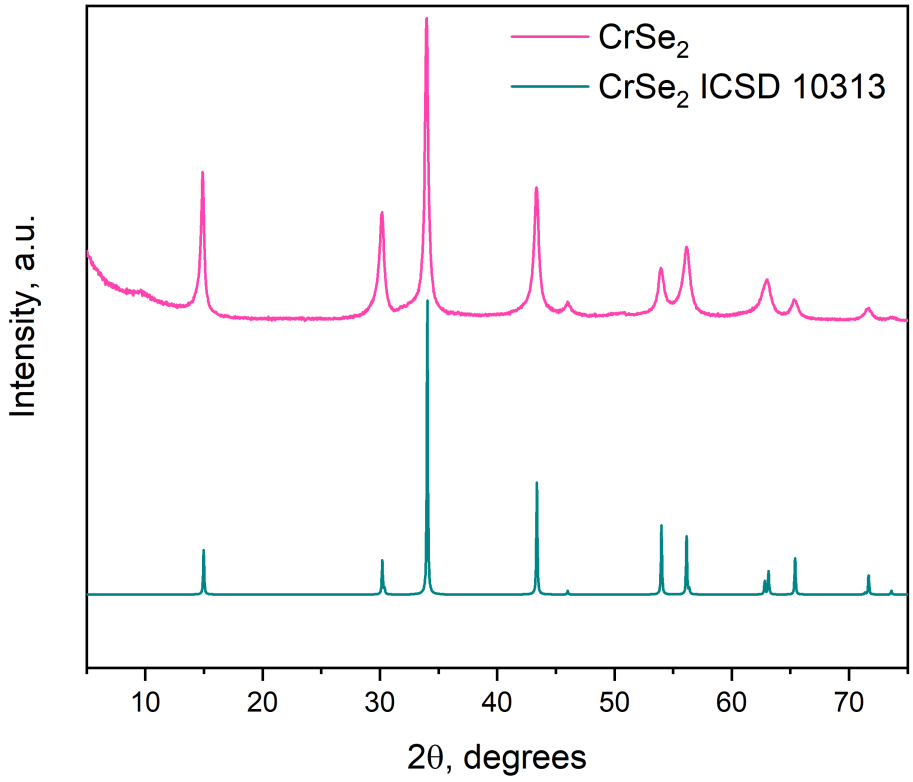

Figure 5-13. *PXRD pattern of potassium deintercalation reaction product $CrSe_2$ (top, pink) in comparison with $CrSe_2$ pattern calculated from ICSD (card no. 10313) at the bottom (green).*

Cell parameters obtained from Le Bail refinement (Figure 5-14) agree well with cell parameters reported in the literature (Table *5-6*). It also hints toward the sample being stoichiometric, as the chromium-rich phase would display expansion in parameter *a* and decrease in parameter *c*.

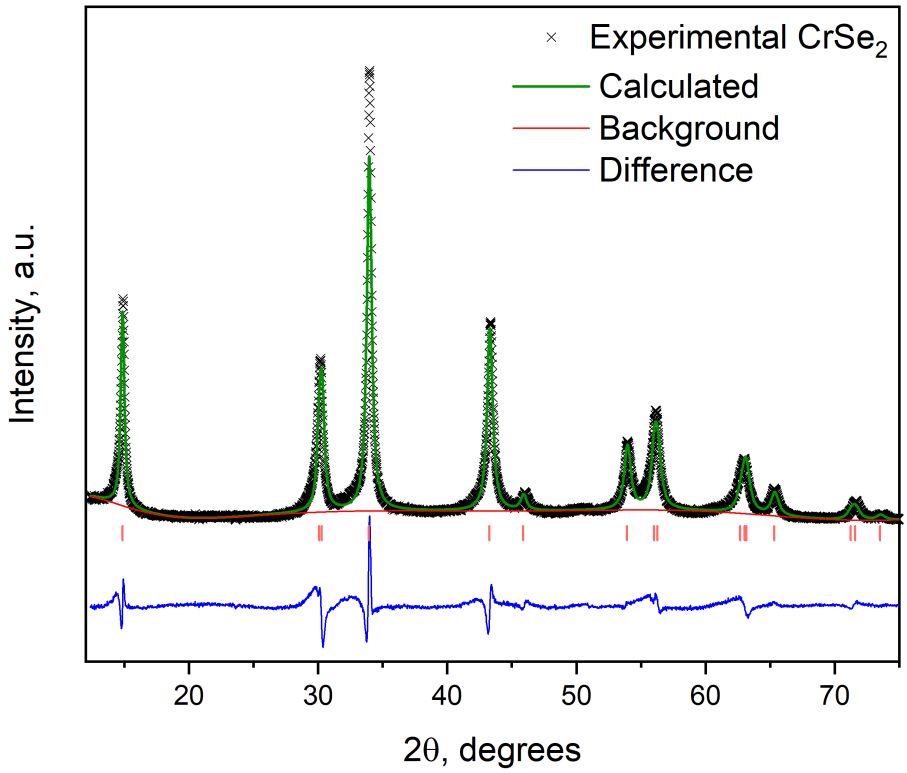

Figure 5-14. *Le Bail refinement plot of sample $CrSe_2$. Experimental pattern is noted as scatter plot with 'x', calculated pattern is in green, background in red and difference in blue line plots. The refinement was done using GSASII software.*

Table 5-6. *Cell parameters (from Le Bail refinement of PXRD data) of $CrSe_2$ synthesised via deintercalation reaction in comparison with values reported in literature.*

Sample	*a*, Å	*c*, Å	Ref
$CrSe_2$	3.3907(3)	5.9084(4)	This work
$CrSe_2$	3.39307(4)	5.91301(7)	[55]
$CrSe_2$	3.399	5.915	[18]
$Cr_{1.36}Se_2$	3.609(1)	5.767(1)	[56]

5.3.3.3. Elemental composition and morphology of $CrSe_2$

The stoichiometry of the sample was confirmed by EDX measurements. As it can be seen from Table 5-7, the sample has an ideal stoichiometry of $CrSe_2$. Nearly perfect stoichiometry was also present for VS_2 prepared via the deintercalation method, which points toward this method being superior to the direct reaction between the elements for the synthesis of stoichiometric dichalcogenides. Moreover, it is important to remember that other selenides

discussed in this chapter have a slight selenium excess and this can also impact catalytic performance.

Table 5-7. *EDX data of $CrSe_2$ sample prepared via deintercalation reaction. The standard deviations are evaluated based on 8 independent points.*

	$CrSe_2$ at. %	
Element	Cr	Se
Experimental	33.35(10)	66.65(10)
Theoretical	33.3	66.6

The morphology of this sample differs from other selenides discussed in this chapter. It was expected that the crystallites were going to be much smaller than those of $TiSe_2$ and VSe_2 as the PXRD pattern showed broader peaks. SEM images (Figure 5-15) show that the sample is composed of small crystallites that do not seem to adopt any distinct shape. Despite that, they are quite thin and platelet-like, which goes hand in hand with the material being layered. The sample's crystallite size can impact its catalytic performance; therefore, it must be taken into consideration that the particles are much smaller than those of the other selenides.

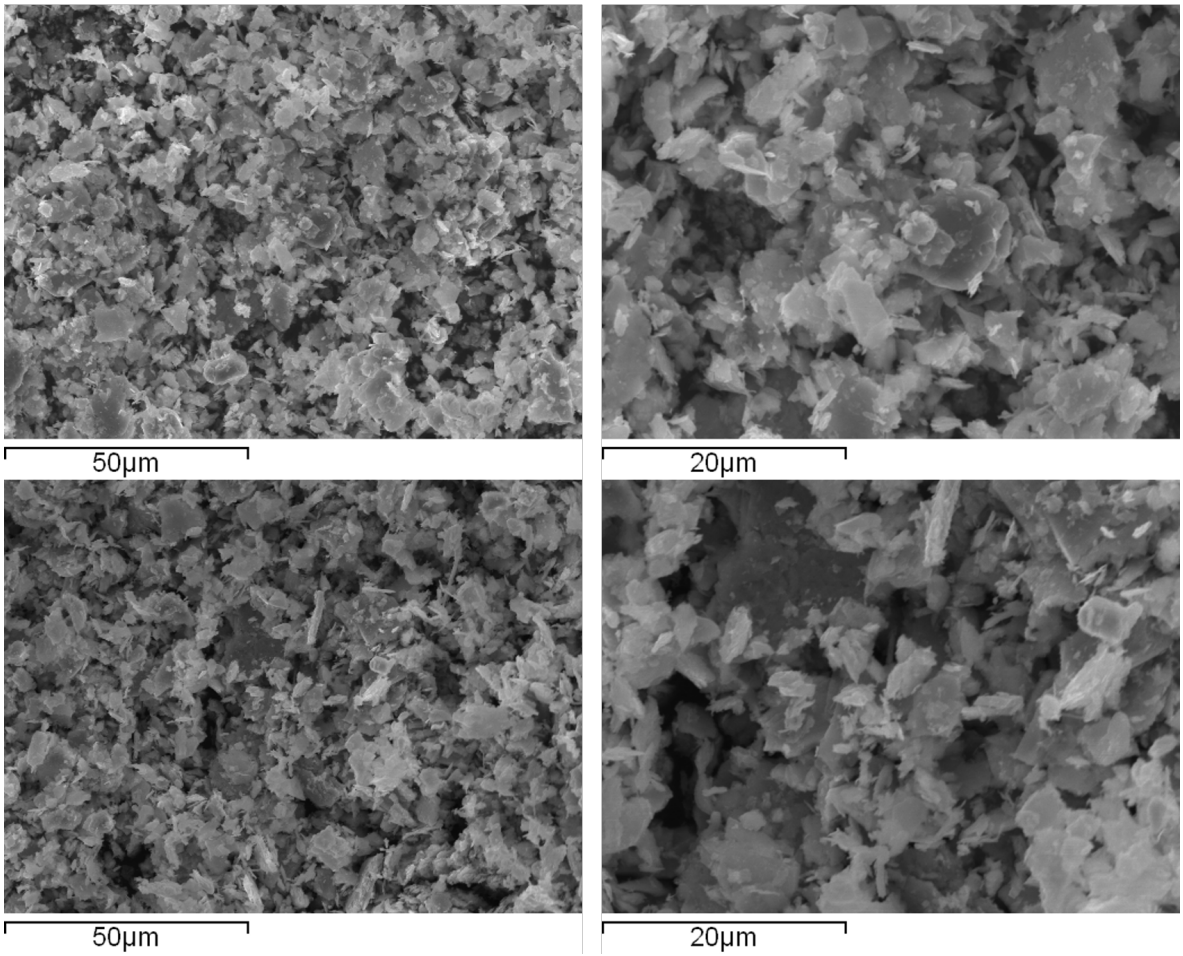

Figure 5-15. SEM images of $CrSe_2$ sample. Two different magnifications of two different spots are displayed.

5.3.3.4. Electrocatalytic activity of $CrSe_2$ towards HER

Having confirmed the sample's crystal structure, stoichiometry and morphology, electrochemical performance was evaluated. As per other selenides, an LSV scan was run for the initial assessment. Just as with other selenides, the first LSV scan of $CrSe_2$ displays a reductive wave as depicted in Figure 5-16. However, this reductive wave shows up quite early into the scan, appearing at ~200 mV vs NHE. What is different in the case of $CrSe_2$ is that the reductive wave is still present at the second LSV scan, whereas in $TiSe_2$ and VSe_2 this wave would disappear after the first scan. Despite this, the overpotentials needed to reach current densities of –10 mA cm^{-2} are the highest out of all selenides discussed in this chapter. A staggering –1271 mV vs NHE is needed for this material to reach benchmark current densities. This deems the catalyst inefficient as well as hinders the possibility of conducting stability tests.

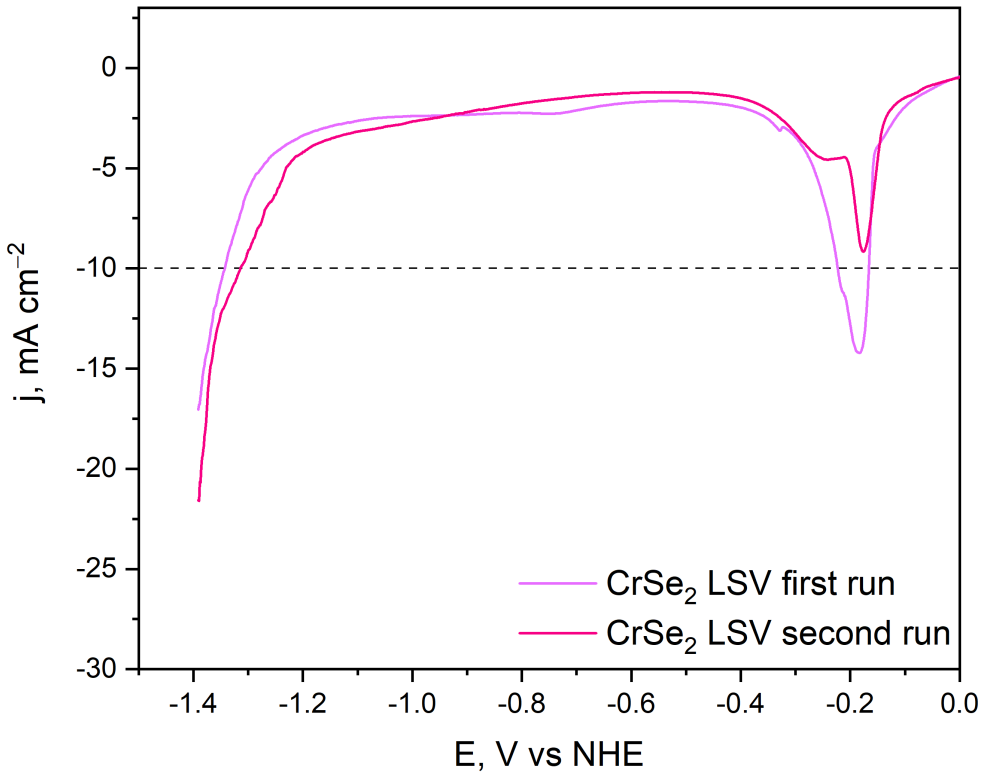

Figure 5-16. *Polarization curves recorded on sample $CrSe_2$. The first scan reveals a reduction wave. A second scan shows that the reductive wave stays present. The actual HER overpotential seems to only shift marginally between the two scans. Polarization curves were recorded using a sweep rate of 5 mV s^{-1}. Three electrode setup in 1 M H_2SO_4 electrolyte where glassy carbon modified with catalyst was working electrode, carbon felt was used as a counter electrode and 3 M Ag/AgCl electrode as a reference electrode. Current density is calculated using geometric electrode area (0.071 cm^2).*

5.3.4. Summary and comparison

Now that all three samples have been characterised, we can compare them. Firstly, the crystal structure was kept the same throughout the samples and synthesis conditions, where possible, were also similar. The summary of cell parameters of selenide samples from this chapter is in Table 5-8. No trends could be noticed in this data, as the vanadium selenide sample, being in the middle of the other two samples, has the smallest *a* parameter and the largest *c* parameter. It also leads to the sample having the highest c/a ratio.

Table 5-8. *Comparison of all three samples' cell parameters obtained from Le Bail refinement of PXRD patterns.*

Sample	*a*, Å	*c*, Å	*c/a*
$TiSe_2$	3.53553(7)	6.00305(6)	1.698
VSe_2	3.35059(7)	6.10069(6)	1.820
$CrSe_2$	3.3907(3)	5.9084(4)	1.742

The elemental composition of samples is summarised in Table 5-9. Although all samples are close to the ideal metal:chalcogen ratio of 1:2, the sample closest to this ideal composition is $CrSe_2$. The other selenides, $TiSe_2$ and VSe_2, were found to have an excess of selenium.

Table 5-9. *Comparison of EDX data of all selenide samples discussed in this chapter.*

	$TiSe_2$, at. %		VSe_2, at. %		$CrSe_2$, at. %	
Element	Ti	Se	V	Se	Cr	Se
Experimental	32.6(22)	67.4(22)	32.8(23)	67.2(23)	33.35(10)	66.65(10)
Theoretical	33.3	66.6	33.3	66.6	33.3	66.6

Despite the efforts to keep morphology uniform through the samples, $CrSe_2$ was shown to have different morphology. The crystallites of $TiSe_2$ and VSe_2 were similar in size and appearance. Unfortunately, crystallites of $CrSe_2$ were much smaller and thinner, although they arguably had a similar shape. Due to these differences, it was important to estimate electrochemically active surface area; therefore double layer capacitance measurements were carried out (Figure A 10, Figure A 11, Figure A 12). As it can be seen from Figure 5-17, double layer capacitance measurements reflect the difference in morphology well. $CrSe_2$ sample displays almost two times larger value than $TiSe_2$ and VSe_2. A nearly identical double layer capacitance value for $TiSe_2$ and VSe_2 was to be expected based on similarity in crystallite size observed in SEM images and was confirmed in this measurement. A higher double layer capacitance value of $CrSe_2$ would imply this sample has an advantage in electrocatalytic measurements. Higher estimated surface area leads to more active sites in contact with the electrolyte, hence, enhancing the catalyst performance.

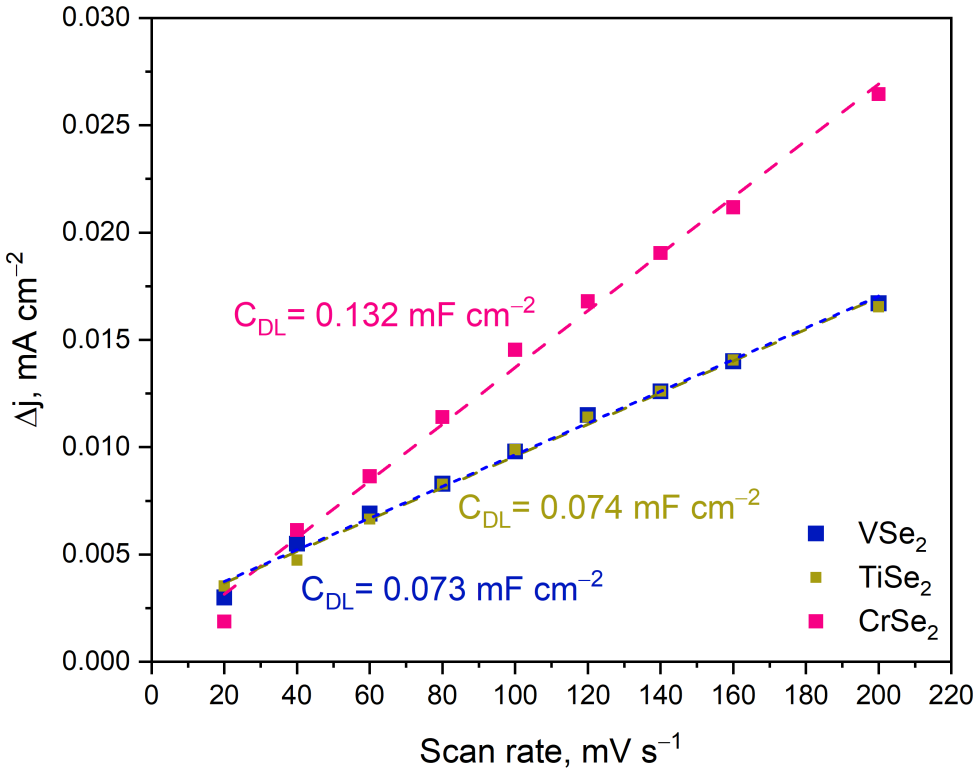

Figure 5-17. *Evaluation of double layer capacitance of three selenide samples. Current density difference (reading taken at 209 mV vs NHE in 1M H_2SO_4) is plotted against scan rate.*

Similar to cell parameters, no linear trend could be observed in the catalytic activity of selenides (Table 5-10). The lowest overpotential needed to achieve benchmark current densities was observed for VSe_2. The highest overpotential was observed for $CrSe_2$. It was expected to show the best performance out of all three samples for multiple reasons: more electrons in the structure, and different sample morphology (more exposed active sites). However, all these assumed advantages did not lead to the sample performing the best.

Table 5-10. *Comparison of electrochemical performance and parameters of all three selenide samples.*

Sample	$TiSe_2$	VSe_2	$CrSe_2$
E at –10 mA cm^{-2} , mV vs NHE	–1091	–882	–1271
C_{DL}, mF cm^{-2}	0.074	0.073	0.132
Q (integrated reduction peak), mC	–35	–71	N/A

Reduction peaks were observed in all three samples. The peaks were present only in the first LSV scan for samples $TiSe_2$ and VSe_2. In chapter 3, the values of charge passed in reduction wave were hard to correlate directly to the observed morphology of the sample and surface oxide layer. This remains an issue, as the charge values obtained for VSe_2 would point to 36% lower amount of oxide layer when compared to VS_2. However, double layer capacitance values are at least 10 times smaller for VSe_2. This would imply that a reduction wave could arise not only from surface oxides but also from the inherent electrochemistry of the samples.

5.4. Conclusions

All three selenides ($TiSe_2$, VSe_2, $CrSe_2$) have been successfully synthesised. PXRD measurements confirmed the samples to be isostructural, and cell parameters were obtained by refining the structures. Unfortunately, no trends in cell parameters could be observed for these samples. The morphology of the samples could not be kept the same, as the $CrSe_2$ sample showed vastly different morphology. The crystallites of this sample were much smaller than $TiSe_2$ and VSe_2. This was well reflected in double layer capacitance measurements, where the $CrSe_2$ sample showed values nearly twice as big as the other two selenides in this work. The electrochemical performance of selenides was investigated and LSV curves were compared. All three samples display high overpotentials needed to reach the benchmark current density of -10 mA cm^{-2}. With VSe_2 showing the lowest overpotential at –882 mV vs NHE, $TiSe_2$ coming in next with an overpotential of –1091 mV vs NHE and $CrSe_2$ coming in last with –1271 mV vs NHE. $CrSe_2$ was expected to be the best performing catalyst in this study, as it has a higher number of electrons in the transition metal, the sample morphology showed the crystallites to be the smallest which gives it an advantage in contact with the electrolyte and exposed active sites. However, with this catalyst performing the worst, there appears to be no linear relationship between the number of electrons in the transition metal and the catalytic performance of isostructural compounds.

5.5. References

1. Y. I. Joe, X. M. Chen, P. Ghaemi, K. D. Finkelstein, G. A. de la Peña, Y. Gan, J. C. T. Lee, S. Yuan, J. Geck, G. J. MacDougall, T. C. Chiang, S. L. Cooper, E. Fradkin and P. Abbamonte, Emergence of charge density wave domain walls above the superconducting dome in 1T-$TiSe_2$, *Nat. Phys.*, 2014, **10**, 421–425.

2. F. Grønvold, F. J. Langmyhr and N. E. Stjernström, X-Ray Study of Titanium Selenides., *Acta Chem. Scand.*, 1961, **15**, 1949–1962.

3. Z. Sofer, D. Sedmidubský, J. Luxa, D. Bouša, Š. Huber, P. Lazar, M. Veselý and M. Pumera, Universal Method for Large-Scale Synthesis of Layered Transition Metal Dichalcogenides, *Chem. - A Eur. J.*, 2017, **23**, 10177–10186.

4. F. Gascoin, N. Raghavendra, E. Guilmeau and Y. Bréard, CdI_2 structure type as potential thermoelectric materials: Synthesis and high temperature thermoelectric properties of the solid solution TiS_xSe_{2-x}, *J. Alloys Compd.*, 2012, **521**, 121–125.

5. A. Kogar, M. S. Rak, S. Vig, A. A. Husain, F. Flicker, Y. Il Joe, L. Venema, G. J. MacDougall, T. C. Chiang, E. Fradkin, J. van Wezel and P. Abbamonte, Signatures of exciton condensation in a transition metal dichalcogenide, *Science*, 2017, **358**, 1314–1317.

6. A. Saini, K. Kumar, M. M. Sharma, R. P. Aloysius and V. P. S. Awana, Growth, Structure, Micro-structure and Magneto-transport of an Easy Route Synthesized Bulk Polycrystalline $TiSe_2$, *J. Supercond. Nov. Magn.*, 2022, **35**, 1383–1387.

7. L. Zhang, C. Chen, J. Zhou, G. Yang, J. Wang, D. Liu, Z. Chen and W. Lei, Solid Phase Exfoliation for Producing Dispersible Transition Metal Dichalcogenides Nanosheets, *Adv. Funct. Mater.*, 2020, **30**, 2004139.

8. D. Zhang, G. Zhao, P. Li, Y. Zhang, W. Qiu, J. Shu, Y. Jiang, S. X. Dou and W. Sun, Readily Exfoliated $TiSe_2$ Nanosheets for High-Performance Sodium Storage, *Chem. – A Eur. J.*, 2018, **24**, 1193–1197.

9. W. Ge, S. Jiao, M. Xu, J. Shi and Z. Chang, Trioctylphosphine (TOP)-free synthesis of $TiSe_2$ plates for enhanced photocatalytic degradation performance of Rhodamine B dyes, *Solid State Sci.*, 2020, **103**, 106189.

10. S. Jeong, D. Yoo, J. Jang, M. Kim and J. Cheon, Well-Defined Colloidal 2-D Layered Transition-Metal Chalcogenide Nanocrystals via Generalized Synthetic Protocols, *J. Am. Chem. Soc.*, 2012, **134**, 18233–18236.

11. D. Song, Y. Zhou, M. Zhang, X. He and X. Li, Structural and Transport Properties of 1T-VSe_2 Single Crystal Under High Pressures, *Front. Mater.*, 2021, **8**, 710849

12. C. F. van Bruggen and C. Haas, Magnetic susceptibility and electrical properties of VSe_2 single crystals, *Solid State Commun.*, 1976, **20**, 251–254.

13. Q. Zhu, M. Shao, S. H. Yu, X. Wang, Z. Tang, B. Chen, H. Cheng, Z. Lu, D. Chua and H. Pan, One-Pot Synthesis of Co-Doped VSe_2 Nanosheets for Enhanced Hydrogen Evolution Reaction, *ACS Appl. Energy Mater.*, 2019, **2**, 644–653.

14. F. Ming, H. Liang, Y. Lei, W. Zhang and H. N. Alshareef, Solution synthesis of VSe_2 nanosheets and their alkali metal ion storage performance, *Nano Energy*, 2018, **53**, 11–16.

15. W. Zhao, B. Dong, Z. Guo, G. Su, R. Gao, W. Wang and L. Cao, Colloidal synthesis of VSe_2 single-layer nanosheets as novel electrocatalysts for the hydrogen evolution reaction, *Chem. Commun.*, 2016, **52**, 9228–9231.

16. Y. Xue, Y. Zhang, H. Wang, S. Lin, Y. Li, J.-Y. Dai and S. P. Lau, Thickness-dependent magnetotransport properties in 1T-VSe_2 single crystals prepared by chemical vapor deposition, *Nanotechnology*, 2020, **31**, 145712.

17. C. Wang, X. Wu, Y. Ma, G. Mu, Y. Li, C. Luo, H. Xu, Y. Zhang, J. Yang, X. Tang, J. Zhang, W. Bao and C. Duan, Metallic few-layered VSe_2 nanosheets: high two-dimensional conductivity for flexible in-plane solid-state supercapacitors, *J. Mater. Chem. A*, 2018, **6**, 8299–8306.

18. C. F. van Bruggen, R. J. Haange, G. A. Wiegers and D. K. G. de Boer, $CrSe_2$, a new layered dichalcogenide, *Phys. B+C*, 1980, **99**, 166–172.

19. C. M. Fang, P. R. Tolsma, C. F. van Bruggen, R. A. de Groot, G. A. Wiegers and C. Haas, Electronic structure and magnetic properties of $KCrSe_2$, *J. Phys. Condens. Matter*, 1996, **8**, 4381–4388.

20. D. J. Young, W. W. Smeltzer and J. S. Kirkaldy, Nonstoichiometry and Thermodynamics of Chromium Sulfides, *J. Electrochem. Soc.*, 1973, **120**, 1221.

21. F. H. Wehmeier, E. T. Keve and S. C. Abrahams, Preparation, structure, and properties of some chromium selenides. Crystal growth with selenium vapor as a novel transport agent, *Inorg. Chem.*, 1970, **9**, 2125–2131.

22. B. Li, Z. Wan, C. Wang, P. Chen, B. Huang, X. Cheng, Q. Qian, J. Li, Z. Zhang, G. Sun, B. Zhao, H. Ma, R. Wu, Z. Wei, Y. Liu, L. Liao, Y. Ye, Y. Huang, X. Xu, X. Duan, W. Ji and X. Duan, Van der Waals epitaxial growth of air-stable $CrSe_2$ nanosheets with thickness-tunable magnetic order, *Nat. Mater.*, 2021, **20**, 818–825.

23. R. J. Toh, Z. Sofer and M. Pumera, Catalytic properties of group 4 transition metal dichalcogenides (MX_2; M = Ti, Zr, Hf; X = S, Se, Te), *J. Mater. Chem. A*, 2016, **4**, 18322–18334.

24. N. Ran, B. Sun, W. Qiu, E. Song, T. Chen and J. Liu, Identifying Metallic Transition-Metal Dichalcogenides for Hydrogen Evolution through Multilevel High-Throughput Calculations and Machine Learning, *J. Phys. Chem. Lett.*, 2021, **12**, 2102–2111.

25. X. Zhang, J. Li, P. Xiao, Y. Wu, Y. Liu, Y. Jiang, X. Wang, X. Xiong, T. Song, J. Han and W. Xiao, Morphology-Controlled Electrocatalytic Performance of Two-Dimensional VSe_2 Nanoflakes for Hydrogen Evolution Reactions, *ACS Appl. Nano Mater.*, 2022, **5**, 2087–2093.

26. L. Najafi, R. Oropesa-Nuñez, S. Bellani, B. Martín-García, L. Pasquale, M. Serri, F. Drago, J. Luxa, Z. Sofer, D. Sedmidubský, R. Brescia, S. Lauciello, M. I. Zappia, D. V. Shinde, L. Manna and F. Bonaccorso, Topochemical Transformation of Two-Dimensional VSe_2 into Metallic Nonlayered VO_2 for Water Splitting Reactions in Acidic and Alkaline Media, *ACS Nano*, 2022, **16**, 351–367.

27. C. Wang, M. Jin, D. Liu, F. Liang, C. Luo, P. Li, C. Cai, H. Bi, X. Wu and Z. Di, VSe_2 quantum dots with high-density active edges for flexible efficient hydrogen evolution reaction, *J. Phys. D. Appl. Phys.*, 2021, **54**, 214006.

28. J. Fu, R. Ali, C. Mu, Y. Liu, N. Mahmood, W.-M. Lau and X. Jian, Large-scale preparation of 2D VSe_2 through a defect-engineering approach for efficient hydrogen evolution reaction, *Chem. Eng. J.*, 2021, **411**, 128494.

29. C. Wang, X. Wu, X. Zhang, G. Mu, P. Li, C. Luo, H. Xu and Z. Di, Iron-doped VSe_2 nanosheets for enhanced hydrogen evolution reaction, *Appl. Phys. Lett.*, 2020, **116**, 223901.

30. M. Yan, X. Pan, P. Wang, F. Chen, L. He, G. Jiang, J. Wang, J. Z. Liu, X. Xu, X. Liao, J. Yang and L. Mai, Field-Effect Tuned Adsorption Dynamics of VSe_2 Nanosheets for Enhanced Hydrogen Evolution Reaction, *Nano Lett.*, 2017, **17**, 4109–4115.

31. S. Kitou, A. Nakano, S. Kobayashi, K. Sugawara, N. Katayama, N. Maejima, A. Machida, T. Watanuki, K. Ichimura, S. Tanda, T. Nakamura and H. Sawa, Effect of Cu intercalation and pressure on excitonic interaction in 1T−$TiSe_2$, *Phys. Rev. B*, 2019, **99**, 104109.

32. I. Oftedal, Röntgenographische Untersuchungen von SnS_2, TiS_2, $TiSe_2$, $TiTe_2$, *Zeitschrift für Phys. Chemie*, 1928, **134U**, 301–310.

33. R. Zheng, H. Yu, X. Zhang, Y. Ding, M. Xia, K. Cao, J. Shu, A. Vlad and B. Su, A $TiSe_2$ -Graphite Dual Ion Battery: Fast Na-Ion Insertion and Excellent Stability, *Angew. Chemie Int. Ed.*, 2021, **60**, 18430–18437.

34. D. L. Greenaway and R. Nitsche, Preparation and optical properties of group IV–VI_2 chalcogenides having the CdI_2 structure, *J. Phys. Chem. Solids*, 1965, **26**, 1445–1458.

35. S. Sugai, K. Murase, S. Uchida and S. Tanaka, Raman studies of lattice dynamics in 1T-$TiSe_2$, *Solid State Commun.*, 1980, **35**, 433–436.

36. X.-F. Tang, S.-X. Zhu, H. Liu, C. Zhang, Q.-Y. Wu, Z.-T. Liu, J.-J. Song, X. Guo, Y.-S. Wang, H. Ma, Y.-Z. Zhao, F.-Y. Wu, S.-Y. Liu, K.-H. Liu, Y.-H. Yuan, H. Huang, J. He, W. Xu, H.-Y. Liu, Y.-X. Duan and J.-Q. Meng, Growth, characterization, and Raman spectra of the 1T phases of $TiTe_2$, $TiSe_2$, and TiS_2, *Chinese Phys. B*, 2022, **31**, 037103.

37. P. Goli, J. Khan, D. Wickramaratne, R. K. Lake and A. A. Balandin, Charge Density Waves in Exfoliated Films of van der Waals Materials: Evolution of Raman Spectrum in $TiSe_2$, *Nano Lett.*, 2012, **12**, 5941–5945.

38. U. P. Sahoo, A. Mukherjee and P. K. Sahoo, Short-Range Charge Density Wave and Bandgap Modulation by Au-Implanted Defects in $TiSe_2$, *ACS Appl. Electron. Mater.*, 2022, **4**, 3428–3434.

39. L. Cui, R. He, G. Li, Y. Zhang, Y. You and M. Huang, Raman spectroscopy of optical phonon and charge density wave modes in 1T-$TiSe_2$ exfoliated flakes, *Solid State Commun.*, 2017, **266**, 21–25.

40. D. B. Lioi, D. J. Gosztola, G. P. Wiederrecht and G. Karapetrov, Photon-induced selenium migration in $TiSe_2$, *Appl. Phys. Lett.*, 2017, **110**, 081901.

41. H. Hedayat, C. J. Sayers, D. Bugini, C. Dallera, D. Wolverson, T. Batten, S. Karbassi, S. Friedemann, G. Cerullo, J. van Wezel, S. R. Clark, E. Carpene and E. Da Como, Excitonic and lattice contributions to the charge density wave in 1T−TiS_2 revealed by a phonon bottleneck, *Phys. Rev. Res.*, 2019, **1**, 023029.

42. D. L. Duong, G. Ryu, A. Hoyer, C. Lin, M. Burghard and K. Kern, Raman Characterization of the Charge Density Wave Phase of 1T-$TiSe_2$: From Bulk to Atomically Thin Layers, *ACS Nano*, 2017, **11**, 1034–1040.

43. F. Levy, Electrical resistivity and Hall effect in $TiSe_2$ containing vanadium impurities, *J. Phys. C Solid State Phys.*, 1979, **12**, 3725–3732.

44. H. P. B. Rimmington and A. A. Balchin, The growth by iodine vapour transport techniques and the crystal structures of layer compounds in the series TiS_xSe_{2-x}, TiS_xTe_{2-x}, $TiSe_xTe_{2-x}$, *J. Cryst. Growth*, 1974, **21**, 171–181.

45. M. Nakahira and K. Hayashi, Characterization of the layered transition-metal dichalcogenides with octahedral coordination, *Mater. Res. Bull.*, 1978, **13**, 1403–1408.

46. E. Hoschek and W. Klemm, Vanadinselenide, *Zeitschrift fur Anorg. und Allg. Chemie*, 1939, **242**, 49–62.

47. G. A. Wiegers, Physical properties of first-row transition metal dichalcogenides and their intercalates, *Phys. B+C*, 1980, **99**, 151–165.

48. F. Levy and Y. Froidevaux, Structural and electrical properties of layered transition metal selenides $V_xTi_{1-x}Se_2$ and $Ta_xTi_{1-x}Se_2$, *J. Phys. C Solid State Phys.*, 1979, **12**, 473–487.

49. K. Hayashi and M. Nakahira, Stability and the equilibrium selenium vapor pressure of the VSe_2 phase, *J. Solid State Chem.*, 1978, **24**, 153–161.

50. J. Rigoult, C. Guidi-Morosini, A. Tomas and P. Molinie, An accurate refinement of 1 T-VSe_2 at room temperature, *Acta Crystallogr. Sect. B Struct. Crystallogr. Cryst. Chem.*, 1982, **38**, 1557–1559.

51. J. Pandey and A. Soni, Electron-phonon interactions and two-phonon modes associated with charge density wave in single crystalline 1T−VSe_2, *Phys. Rev. Res.*, 2020, **2**, 033118.

52. D. Li, X. Wang, C. Kan, D. He, Z. Li, Q. Hao, H. Zhao, C. Wu, C. Jin and X. Cui, Structural Phase Transition of Multilayer VSe_2, *ACS Appl. Mater. Interfaces*, 2020, **12**, 25143–25149.

53. J. Zhou, Strong charge-density-wave order of large-area 2D metallic VSe_2 nanosheets discovered by temperature-dependent Raman spectra, *Appl. Phys. Lett.*, 2020, **116**, 033102.

54. X. Song, S. N. Schneider, G. Cheng, J. F. Khoury, M. Jovanovic, N. Yao and L. M. Schoop, Kinetics and Evolution of Magnetism in Soft-Chemical Synthesis of $CrSe_2$ from $KCrSe_2$, *Chem. Mater.*, 2021, **33**, 8070–8078.

55. S. Kobayashi, N. Katayama, T. Manjo, H. Ueda, C. Michioka, J. Sugiyama, Y. Sassa, O. K. Forslund, M. Månsson, K. Yoshimura and H. Sawa, Linear Trimer Formation with Antiferromagnetic Ordering in 1T-$CrSe_2$ Originating from Peierls-like Instabilities and Interlayer Se–Se Interactions, *Inorg. Chem.*, 2019, **58**, 14304–14315.

56. R. Blachnik, P. G. Gunia, M. Fischer and H. D. Lutz, Das system chrom-selen, *J. Less Common Met.*, 1987, **134**, 169–177.

6. Sulphur-rich vanadium sulphides

6.1. Introduction

After the investigation of isostructural layered sulphides and selenides of titanium, vanadium, and chromium, we once again return to the V-S system. Vanadium compounds were found to perform the best in previous chapters; therefore, an exploratory investigation of the thermodynamically stable phases in the system was approached in this chapter.

6.1.1. Revisiting V – S phase diagram

Looking back at the phase diagram briefly presented in chapter 3, we can see that there are multiple well-established phases in this system (Figure 6-1). For example, VS_4, a well-known sulphide occurring naturally in the form of mineral Patronite. It is also the most sulphur-rich compound known in the system. The other two quite well structurally characterised and established sulphides are V_3S_4 and V_5S_8. The latter is closest in stoichiometry to the layered VS_2. Right on the boundary between sulphur-rich and vanadium-rich compounds in the system is VS. This compound was the third one that was investigated in this work. The vanadium rich part of the phase diagram shows two more well-established sulphides; however, they are not within the scope of this work and will not be discussed in detail.

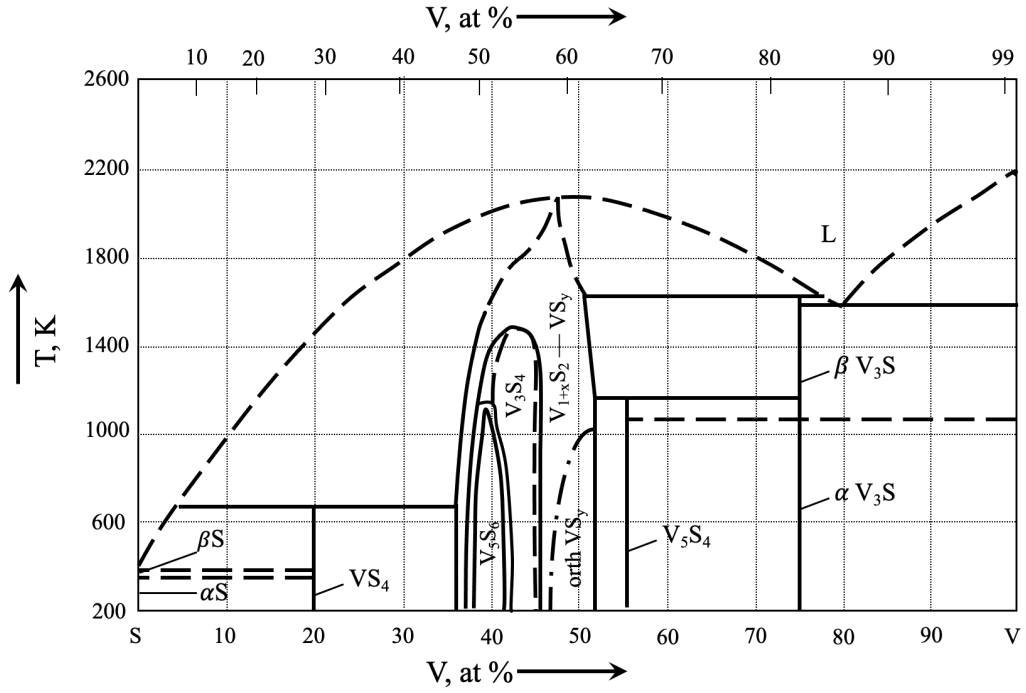

Figure 6-1. *Vanadium-sulphur binary phase diagram. Adopted from B. Predel.*[1]

6.1.2. Structure and synthesis of VS_4

As mentioned in the previous section, VS_4 occurs naturally as a mineral called Patronite. It is the most sulphur-rich vanadium sulphide. It appears as a compound with a monoclinic unit cell, *C2/c* (12) space group. As seen in Figure 6-2, the crystal structure of this compound consists of vanadium metal chains that are held together by weak van der Waals forces. Each vanadium atom is coordinated by eight sulphur atoms which exist as a bis(persulfide) anion, that is, $(S_2^{2-})_2$. Two S_2^{2-} moieties between the V^{4+} centres form a chain-like structure. This chain-like structure is why this material is often referred to as quasi-1D material.

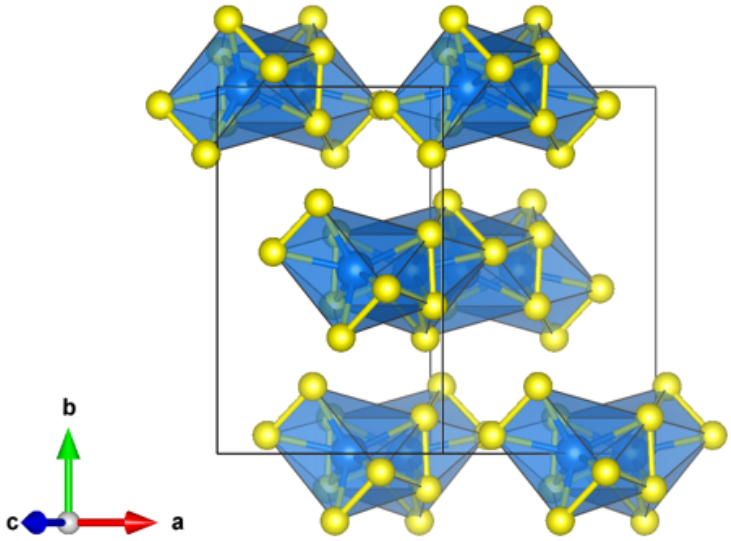

Figure 6-2. *Crystal structure of VS_4, showing chain-like structure.*

The solid-state synthesis of this compound calls for elemental powders to be heated at 400 °C for as long as four months. The reports by B. Pedersen claimed that even when the sample was heated for months, the excess sulphur would be visible in the reaction tube, indicating that it never fully reacted.[2] Kozlova *et al.* report that pure phase VS_4 was synthesised at 400 °C in 10 days.[3] An alternative solid-state synthesis for VS_4 was recently reported by Qin *et al.*[4] The synthesis temperature is lowered from 400 °C to 200 °C, and reaction times are as short as five hours. Such a dramatic decrease in reaction time and duration is made possible by swapping elemental sulphur for thiourea and elemental vanadium for vanadium orthovanadate. This synthesis, however, produces interlayer engineered VS_4, with $[NCN]^{2-}$ anion, produced during synthesis, inserted into the interchains of the product. To remove the $[NCN]^{2-}$ anion, further calcination of the sample is needed at a temperature of 320 °C.

The hydrothermal synthesis method was successfully applied in the synthesis of composite materials with carbon nanostructures.[5,6] Thin films of VS_4 were successfully grown by atomic layer deposition.[7]

6.1.3. Structure and synthesis of V_5S_8

V_5S_8 is reported to have a monoclinic unit cell. The reported space group is often a non-standard *F2/m*, allowing a more straightforward comparison with the NiAs structure type. The *F2/m* space group can be reduced to a more common monoclinic *C2/m*. The structure consists of alternating metal full and metal deficient layers, which is depicted in Figure 6-3. Six sulphur atoms octahedrally coordinate each vanadium atom. The structure is usually viewed as a layered VS_2 with interlayer vanadium between the layers.

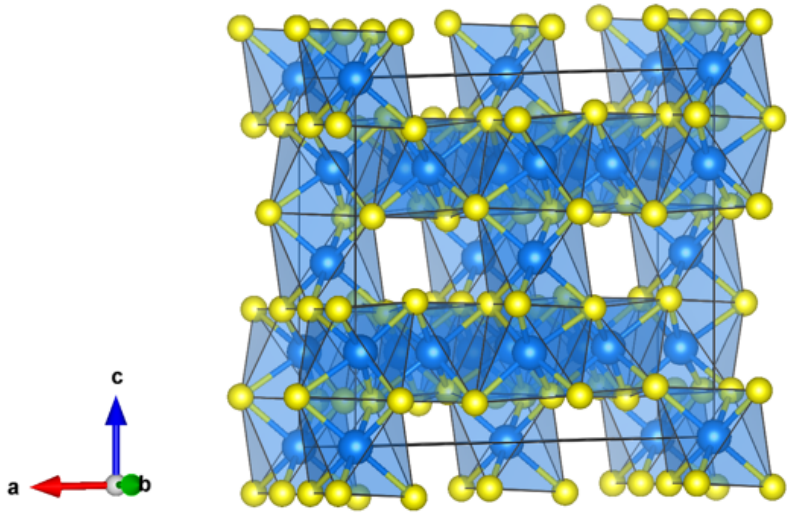

Figure 6-3. *Crystal structure of V_5S_8.*

As reported by Oka *et al.*, the V_5S_8 phase exists in a composition range from $VS_{1.57}$ to $VS_{1.68}$.[8] This vanadium sulphide undergoes a metal vacancy order-disorder transition at around 800 °C. The high-temperature phase of this sulphide is believed to be stable up to 1000 °C. Solid state synthesis is the most reported synthesis method for this sulphide. Elemental powders of vanadium and sulphur are used with reaction temperatures ranging from 700 °C to 900 °C and reaction times varying from days to weeks.[9–11] Hydrothermal synthesis methods coupled with calcination or template synthesis have also been reported to result in the V_5S_8 phase successfully.[12–14]

6.1.4. Structure and synthesis of VS

VS can adopt two different crystal structures – orthorhombic MnP-type and hexagonal NiAs-type.[15] The orthorhombic structure is observed in samples with stoichiometries of $VS_{0.92}$-

$VS_{1.06,}$ and the hexagonal structure is observed in samples with stoichiometries of $VS_{1.06}$-$VS_{1.16}$. Interestingly, no two-phase region is observed between the two phases. The hexagonal VS structure (space group *P63/mmc*) is depicted in Figure 6-4. It is composed of hexagonal close-packed layers that alternate metal and non-metal atoms. Six sulphur atoms octahedrally coordinate the metal atom.

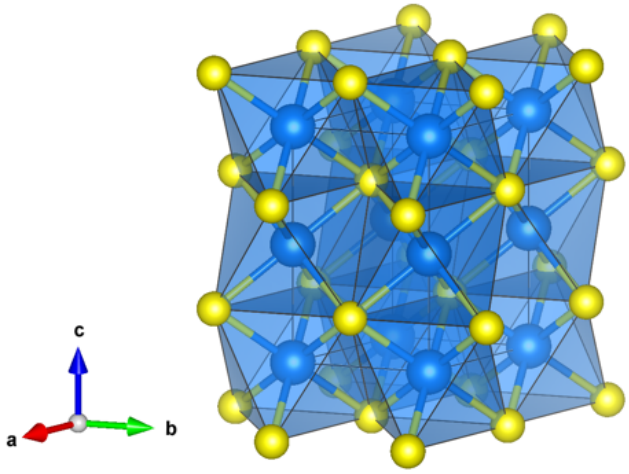

Figure 6-4. *Crystal structure of VS.*

Vanadium monosulphide is only synthesised via solid-state synthesis between the elements. The temperature ranges from 800 ºC to 1300 ºC, and the reaction time varies from several days to weeks, as in the case of other vanadium sulphides.[9,16,17]

6.1.5. The catalytic activity of vanadium sulphides

Multiple issues hinder the collection of reports on vanadium sulphides for the hydrogen evolution reaction. The first one is the nonstoichiometry of the samples; therefore, there are issues trying to sort them by phase. Moreover, sometimes V_5S_8 is reported as VS_2, causing difficulties distinguishing the catalytic performance. There was no success in trying to find any reports on VS. The reports on VS_4 are also not plentiful. However, Xu *et al.* reported that oxygen-doped VS_4 microspheres had a low overpotential of –50 mV vs RHE and even outperformed the VS_2 samples prepared by the same researchers.[18]

With so little information on catalytic activity, it is interesting and necessary to investigate these materials with a well-characterised structure to get an insight into the system and determine their activity towards the HER.

6.2. Aims

In this chapter, the V – S system will be explored. Thermodynamically stable vanadium sulphides – VS_4, V_5S_8 and VS – will be synthesised, and their electrochemical performance toward HER will be evaluated. Starting with VS_4, the most sulphur-rich vanadium sulphide, and ending with VS, the full spectrum of sulphur-rich vanadium sulphides will be investigated. This will also allow insight into where metastable VS_2 falls within the thermodynamically stable vanadium sulphides and how metastable phases compare with the thermodynamically stable ones.

6.3. Results and discussion

6.3.1. Synthesis and characterisation of VS_4

6.3.1.1. Synthesis of VS_4

VS_4 was synthesised *via* a solid state reaction between the elements at 400 °C, with the procedure adapted from the publication by Kozlova *et al.*[3] The reported synthesis procedure uses one ten-day long heating step. However, we have split it into multiple shorter heating periods with sample homogenisation using mortar and pestle between each step. The initial heating step duration was 48 hours. The product was a dark grey lump with sulphur within the lump and on the walls of the reaction ampoule (Figure 6-5).

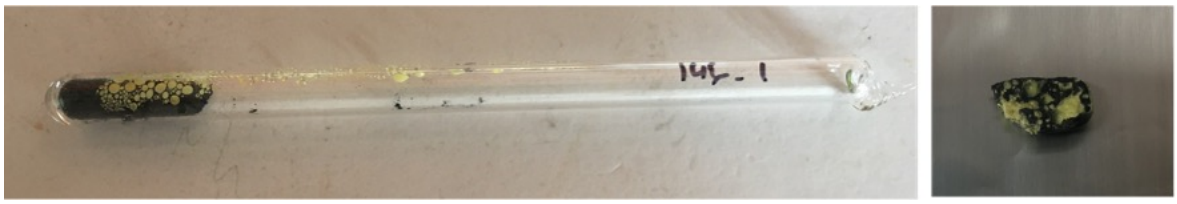

Figure 6-5. *Reaction ampoule after the first heating step (left). Unreacted sulphur had deposited on the walls of the ampoule. The product of the first heating step (right) cracked open for homogenisation showing unreacted sulphur within the product.*

X-ray diffraction was run, and the results revealed that the target phase of VS_4 had formed. As can be seen in Figure 6-6, there is unreacted sulphur and unreacted vanadium also present in the diffraction pattern. It was expected since the heating duration was shorter than the literature procedure.

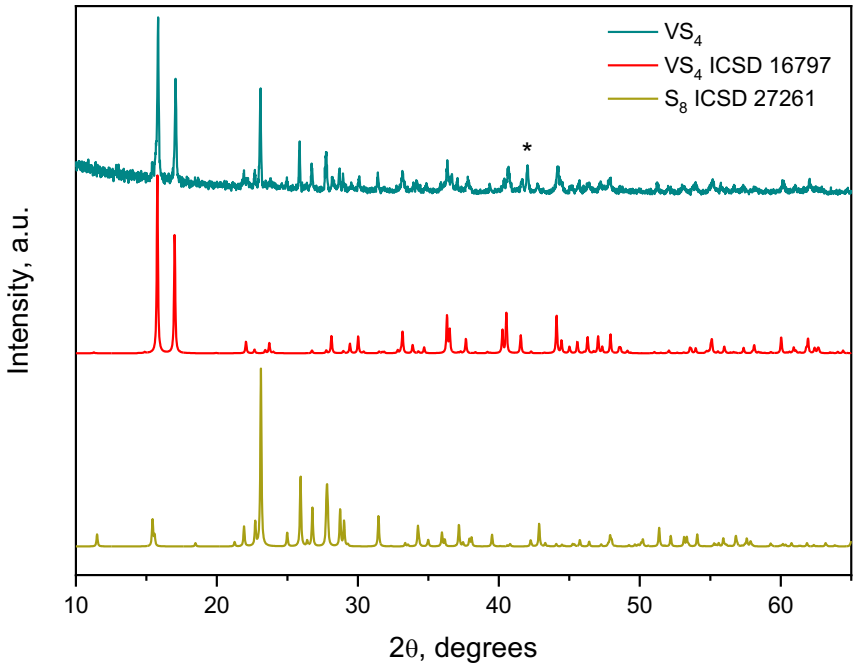

Figure 6-6. *PXRD pattern of the reaction product between V and S powders sealed under vacuum and heated at 400 °C for 48 hours (top, dark teal). The calculated reference pattern of VS_4 from ICSD (card no 16797) is displayed in the middle (red), and the sulphur reference pattern calculated from ICSD (card no 27261) is displayed at the bottom (mustard). Vanadium impurity is noted as '*'.*

The product was ground using mortar and pestle, the sulphur powder was added to the sample, and the sample was reannealed at 400 °C for 24 hours. It was noticed that there was less sulphur on the ampoule walls this time. The X-ray diffraction pattern of the annealed product (Figure 6-7) shows that there is unreacted sulphur in the sample still. However, the vanadium metal peak has reduced intensity compared to the 1st heating cycle of this sample. The second anneal was carried out to ensure that vanadium reacts fully. As can be seen from X-ray diffraction (Figure 6-7), there is no vanadium peak present in the pattern after the second annealing step. There is still excess sulphur, which could be expected as an excess of sulphur was added to ensure all vanadium reacts (full detail of synthesis can be found in chapter 2).

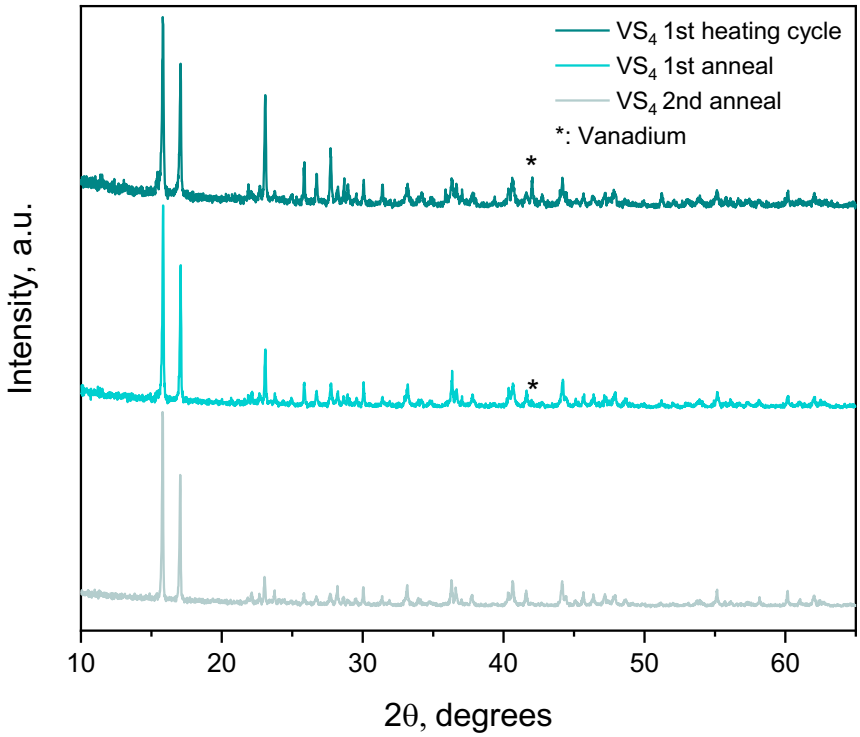

Figure 6-7. *PXRD pattern of reannealed VS_4 (middle, teal; bottom, grey) compared with the pattern obtained after the initial heating cycle (top, dark teal). Vanadium impurity is noted as '*' and is no longer present after the second annealing of the sample.*

The excess sulphur was evaporated from the sample by annealing it under a dynamic vacuum for 30 minutes, and the final product diffraction pattern was used for Le Bail refinement (Figure 6-8). Cell parameters obtained from the refinement are in Table 6-1 and agree well with other literature reports.

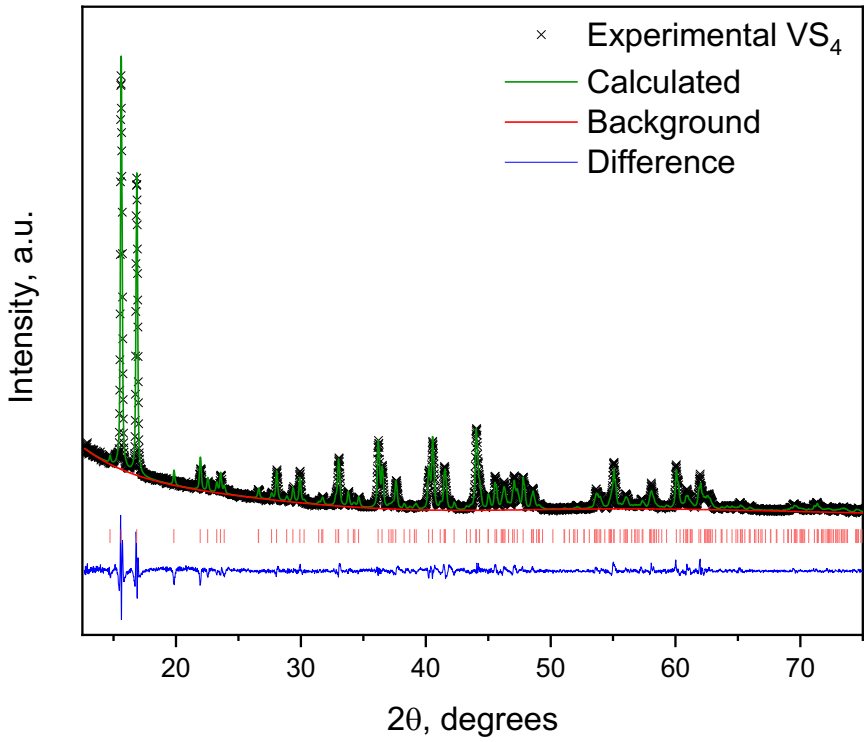

Figure 6-8. *Le Bail refinement of VS_4 solid-state sample after evaporation of excess sulphur. The experimental pattern is noted as a scatter plot with 'x'; the calculated pattern is in green, the background in red and the difference in blue line plots. Refinement was carried out in GSASII software.*

Table 6-1. *Cell parameters of VS_4 synthesised at 400 °C from elements via solid-state reaction compared with values reported in the literature.*

Sample	*a*, Å	*b*, Å	*c*, Å	Ref
VS_4	6.7571(4)	10.3804(3)	12.0616(9)	This work
VS_4	6.7494	10.3532	12.7131	[3]
VS_4	6.780	10.42	12.11	[19]
VS_4	6.775	10.42	12.11	[20]

Splitting the reaction into multiple heating steps was proven to speed up the synthesis procedure for the VS_4 sample. It is likely that once VS_4 starts to form, vanadium particles form a core-shell structure with a vanadium core and a vanadium sulphide shell making the diffusion rate to the middle of the vanadium particles relatively slow. The homogenisation of the sample increases the reaction rate by breaking up the structures and exposing vanadium cores for further reaction with sulphur.

6.3.1.2. Morphology and elemental composition of VS_4

The morphology of the sample was investigated using SEM imaging. As seen in Figure 6-9, VS_4 crystallites grow in rod-like structures. The homogeneity of the sample is not perfect as crystallites of different shapes can be noticed, as well as rod-like structures greatly varying in dimensions. However, the rod-like structure is expected for VS_4, considering its quasi-one-dimensional crystal structure.

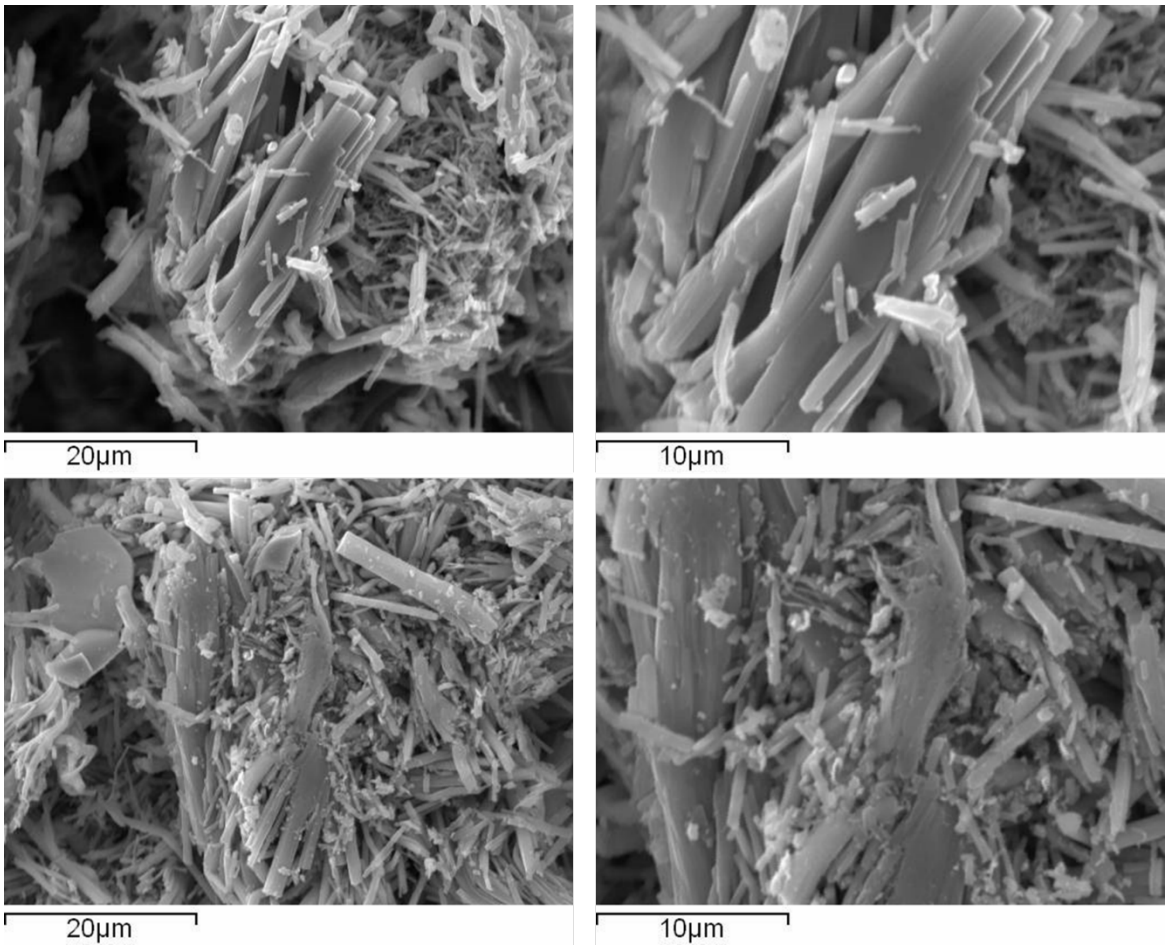

Figure 6-9. *SEM images of two different spots of sample VS_4 using two magnification settings.*

EDX analysis was performed to obtain the elemental composition of the sample. The results in Table 6-2 show that the sample is sulphur deficient, with the sample stoichiometry being $VS_{3.74}$. The result could be expected because of the wide range of non-stoichiometry in the V – S system. Moreover, the last step of excess sulphur evaporation could have had a slight impact, and more than just excess sulphur could have been removed from the sample. However, this is unlikely, as dynamic vacuum anneal is an alternative to excess chalcogen removal via chemical transport reaction and is a standard procedure in removing excess chalcogenide from products of solid-state reactions where slight excess of chalcogenide was used in the synthesis.

Table 6-2. *EDX data of sample VS_4. The standard deviation was calculated from 4 independent points.*

	VS_4 at. %	
Element	V	S
Experimental	21.1(17)	78.9 (17)
Theoretical	20.0	80.0

6.3.1.3. Raman Spectroscopy of VS_4

A Raman spectrum was collected from the sample for further phase characterisation and possible impurity determination. Like VS_2, the VS_4 sample oxidised under laser irradiation in ambient conditions. The peaks at 93 cm^{-1}, 137 cm^{-1}, 280 cm^{-1}, 403 cm^{-1}, 520 cm^{-1}, 689 cm^{-1} and 989 cm^{-1} observed in the spectrum displayed in Figure 6-10 can be attributed to V_6O_{13} and peaks at 157 cm^{-1}, 295 cm^{-1}, 833 cm^{-1} and 871 cm^{-1} which can be attributed to V_3O_7.[21] Once the sample was remeasured in a capillary sealed under an inert atmosphere, a very different Raman spectrum was recorded. The peaks in this spectrum at 190 cm^{-1}, 223 cm^{-1}, 272 cm^{-1}, 287 cm^{-1}, 350 cm^{-1} and 557 cm^{-1} were observed. The peak positions match those reported by Weimer *et al.* and match the calculated spectrum for VS_4 reported by the same authors.[7] Interestingly, unlike VS_2, VS_4 does not decompose, and this sample's Raman spectrum could be obtained. Moreover, the wide range Raman measurements confirmed that there are no impurities such as oxides or sulphur in the sample.

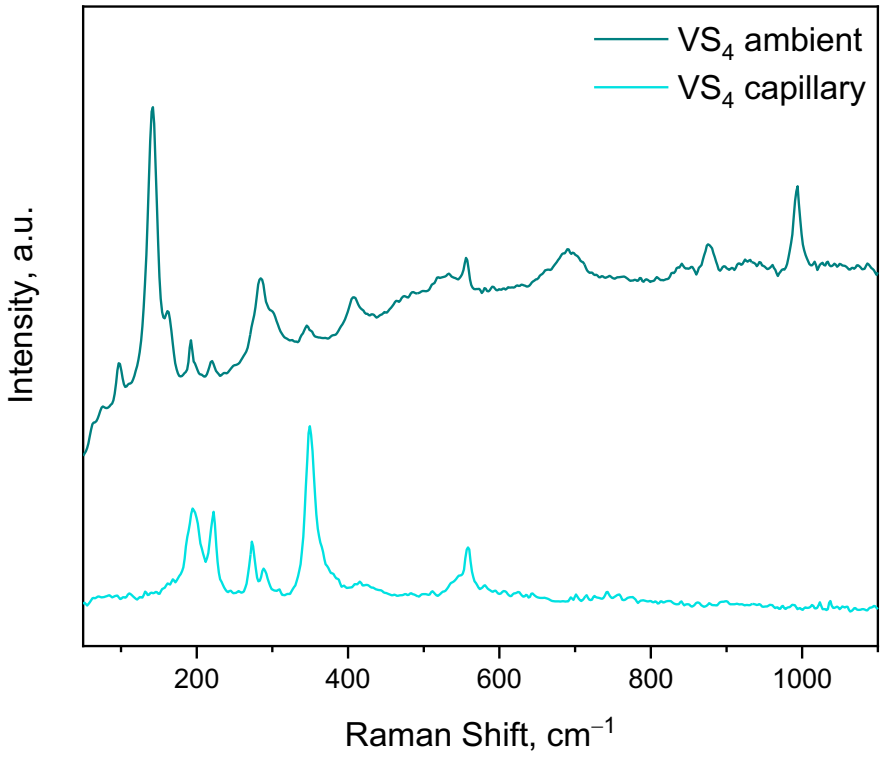

Figure 6-10. *Raman spectrum of VS_4 collected in ambient conditions (top, dark teal) and on the sample sealed in a capillary under inert Ar atmosphere (bottom, light teal). The measurement conditions were the same in both measurements.*

6.3.1.4. Electrocatalytic performance of VS_4 toward HER

Once the sample was identified as pure phase VS_4, the electrochemical performance of the sample towards HER was evaluated. The initial LSV scan shown in Figure 6-11 revealed that the catalyst is not active towards HER, reaching the benchmark current density of 10 mA cm^{-2} at potentials of −971 mV vs NHE. There are no reduction waves, as was the case in VS_2. The second LSV scan shows that the overpotential needed to reach benchmark current densities improves and is almost 100 mV lower than in the initial scan (−862 mV vs NHE).

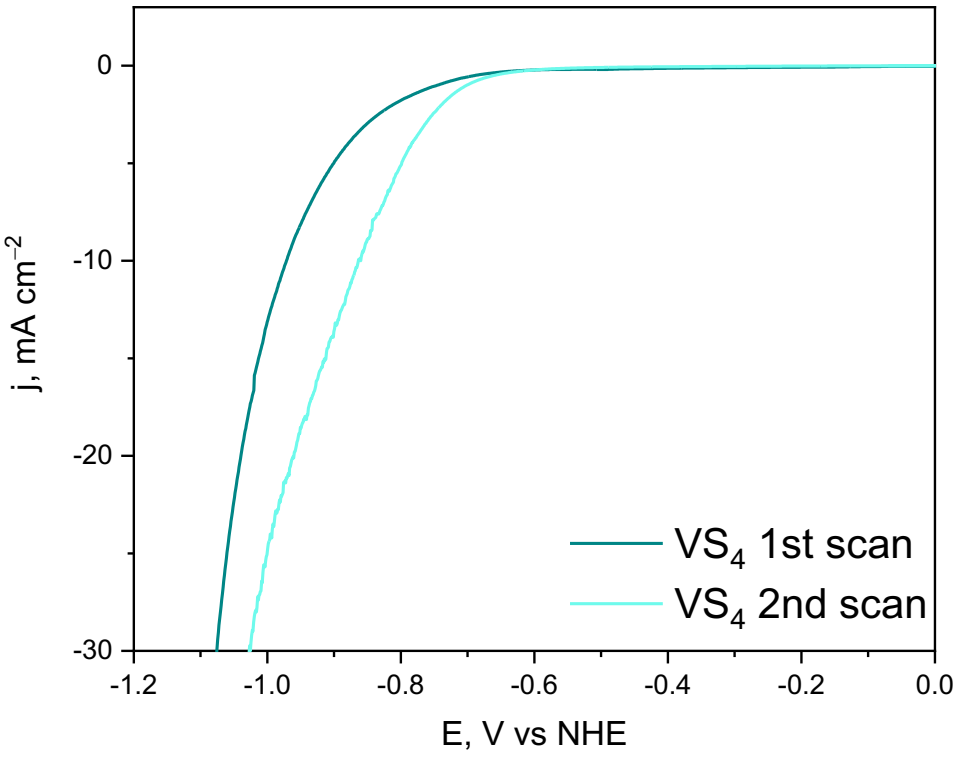

Figure 6-11. *Polarization curves recorded on sample VS_4. The second scan shows improvement in the performance with the overpotential lowered by more than 100 mV. Polarization curves were recorded using a sweep rate of 5 mV s^{-1}. Three electrode setup in 1 M H_2SO_4 electrolyte where glassy carbon modified with catalyst was working electrode, carbon felt was used as a counter electrode and 3 M Ag/AgCl electrode as a reference electrode. Current density is calculated using geometric electrode area (0.071 cm^2).*

Intrigued by these results, the sample was subjected to continuous cycling for 150 cycles. The overpotential was gradually improving with each scan. However, the improvement in the overpotential was getting smaller as the cycle number increased. Figure 6-12 depicts CV scans (cathodic sweep shown) every 50 cycles. The improvement within the first fifty cycles was the biggest, with overpotential lowering to −897 mV vs NHE. A further fifty cycles decreased it to −834 mV vs NHE, and finally, at the 150th cycle, the overpotential dropped to −805 mV vs NHE. That is almost a 200 mV improvement in performance with only 150 CV cycles.

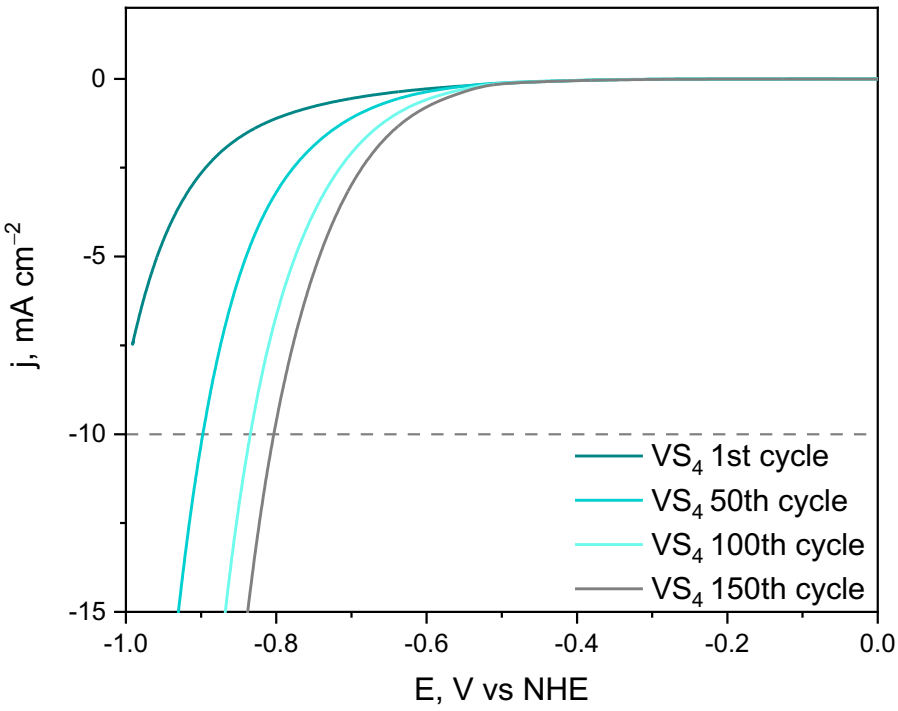

Figure 6-12. *Cathodic CV scan sweep of sample VS_4. The overpotential is improving with each CV cycle, and every 50th sweep is depicted in the figure. Cyclic voltammetry was recorded using a sweep rate of 100 mV s^{-1}. Three electrode setup in 1 M H_2SO_4 electrolyte where glassy carbon modified with catalyst was working electrode, carbon felt was used as counter electrode and 3 M Ag/AgCl electrode as a reference electrode. Current density is calculated using geometric electrode area (0.071 cm^2).*

The improvement of catalyst performance under continuous cycling has been reported in the literature for other transition metal dichalcogenides such as TaS_2, NbS_2 and $MoTe_2$, as well as carbon-based electrocatalysts. [22–25]

One of the earlier reports by Dong *et al*. claimed that the electrochemical activation of carbon cathodes resulted from platinum counter electrode dissolving into the electrolyte and depositing on the surface of the working electrode. The activation did not take place once the counter electrode was swapped for the graphite rod.[25] However, later reports on electrochemical activation ensure that the platinum counter electrode does not impact the activation process by using a graphite rod as a counter electrode and still noticing the catalyst activation.

A study by Liu *et al.* unveiled that TaS_2 and NbS_2 catalysts show significant improvement in their HER activity by continuous cycling.[22] The overpotential improved from over –500 mV needed to achieve benchmark current density to only –50-60 mV after 5000 cycles. The authors checked for platinum contamination and confirmed that no platinum was contaminating the working electrodes. Extensive catalyst characterisation before and after activation revealed that the increased catalytic activity could be attributed to morphology changes and a higher number of exposed active sites. Non-reversible catalyst activation was also reported for N-doped carbon catalyst by Liang *et al*.[26] They also attributed the increased catalytic activity to the changes in the morphology of the surface, resulting in enhanced surface hydrophilicity. This, in turn, makes active sites more accessible to the protons. Morphological changes at the surface were also named as the main reason for electrochemical catalyst activation in a study by Shao *et al*. on Fe-based alloys.[24]

Another study on rapid catalyst activation published by McGlynn *et al*. reported on $MoTe_2$ catalyst showing a reversible catalyst activation.[23] The catalytic performance of $MoTe_2$ increased by more than 100 mV in just 100 CV cycles. The authors showed that the improvement does not arise from structural or morphological changes. The process reversibility points towards electron doping during the process and subsequent adsorption of protons onto the surface of the catalyst. Once the reductive bias is interrupted, the catalyst reverts to the initial performance.

The reversible activation of the catalyst was ruled out in the case of VS_4 as the electrocatalytic performance did not revert once the reductive bias was interrupted and measurement restarted. With that in mind, it is highly likely, that VS_4 just undergoes morphological or structural changes on the surface while being cycled.

Another possibility is that silver ions are leaching out of the reference electrode, and subsequently deposits on the surface of the catalyst coated electrode. This has been reported by *Roger et al.*[27] In their study, the GC electrode was found to be covered in particles containing significant amounts of silver. The particles could be observed using SEM imaging. Silver particles have been reported to be HER active, therefore, deposition of these particles on the catalyst surface could be the reason causing the improvement in catalytic activity with cycling.

The PXRD patterns were collected on the catalyst deposited on the GC electrode before and after measurement to check if any structural changes were happening to the catalyst while

cycling. As can be seen from Figure 6-13, only the most intense VS_4 peaks are present in the pattern. There is no peak position or shape change after the catalyst was cycled. The only difference is the peak intensity, as it has slightly decreased. Nevertheless, structural changes were not observed. It is important to note that if any changes occurred at the catalyst's surface, it would not be detected by PXRD alone.

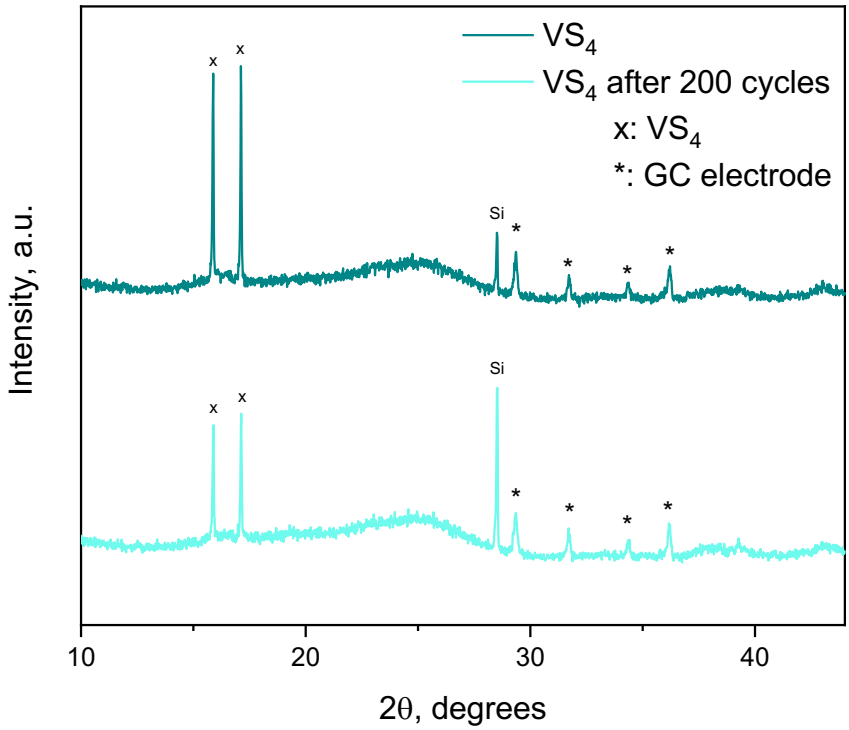

Figure 6-13. *PXRD patterns of VS_4 before (top, dark teal) and post (bottom, light teal) CV cycling. The patterns have been recorded directly on a glassy carbon electrode. VS_4 peaks are marked with an 'x'.*

6.3.2. Synthesis and characterisation of V_5S_8

6.3.2.1. Synthesis of V_5S_8

Most literature reports on this compound focus on the growth of single crystals. The reported single crystal growth temperature ranges from 700 °C to 800 °C. Since our focus was on obtaining a bulk sample, the lower end of the temperature range was chosen, and reactions to obtain V_5S_8 were carried out at 700 °C. The PXRD pattern of the product is displayed in Figure 6-14 and shows that the sample, while closely resembling the reference pattern of V_5S_8, has an impurity. Since reannealing of the sample at the same temperature did not improve the phase purity, it was decided to increase the synthesis temperature. The

temperature was increased to 800 °C, and the product of this reaction was pure phase V_5S_8, as shown by PXRD (Figure 6-15). Preferred orientation in the direction of *00l* planes can be observed in the pattern. It is much more expressed in this sample than in the one prepared at 700 °C. It is important to note that, unlike in VS_4, no excess sulphur was observed on the walls of the reaction ampoule at both temperatures, which points towards much quicker reaction kinetics between the elements at elevated temperatures.

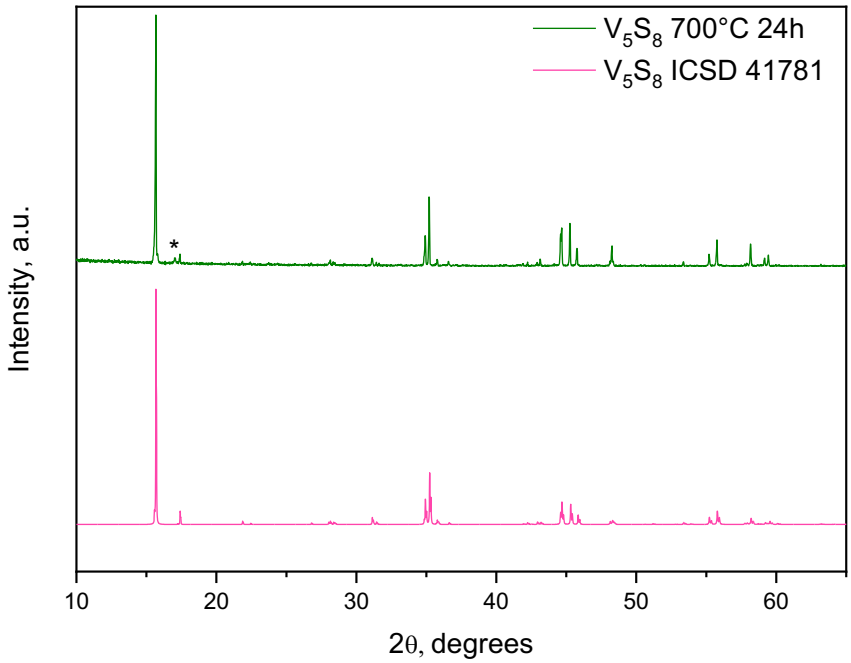

Figure 6-14. *PXRD pattern of the product of the reaction between elemental vanadium and sulphur at 700 °C for 24 hours (top, green). For comparison, the calculated diffraction pattern of V_5S_8 from the ICSD (card number 41781) is displayed at the bottom (pink). Impurity is noted as '*'*

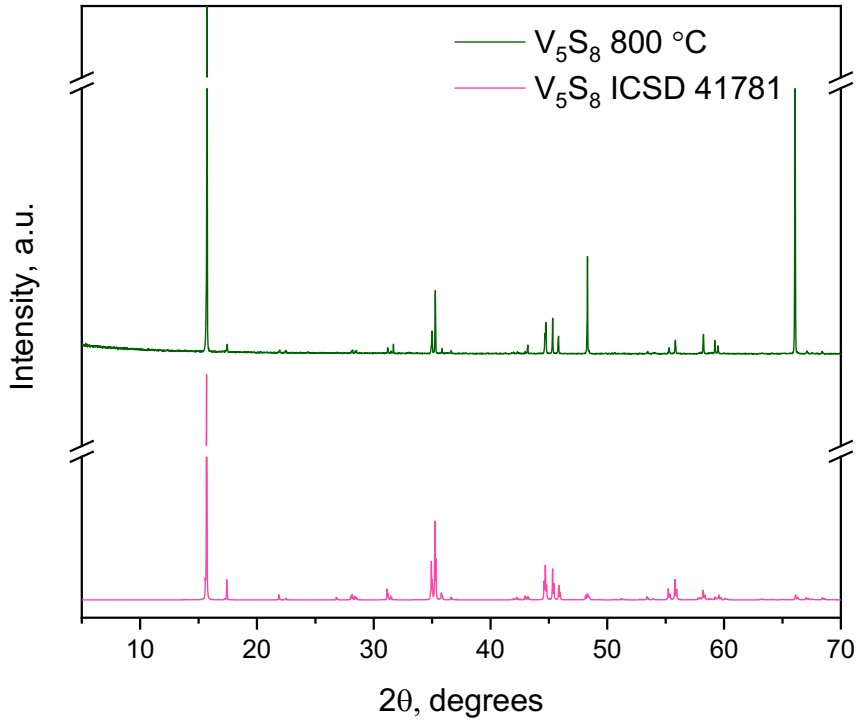

Figure 6-15. *PXRD pattern of the product of the reaction between elemental vanadium and sulphur at 800 °C for 24 hours (top, green). The calculated diffraction pattern of V_5S_8 from the ICSD (card number 41781) is displayed at the bottom (pink). The sample shows preferred orientation in the direction of the 00l plane. Axis breaks were included so that other peaks with less intensity could be seen clearly in the graph.*

Le Bail refinement was done using the collected pattern to obtain cell parameters of the sample. The resulting cell parameters obtained from the refinement are in Table 6-3, where it is compared with values reported in the literature. The refined pattern is displayed in Figure 6-16; the first peak was cut out, as the extreme preferred orientation of the sample was overcomplicating the refinement of the pattern. This does not impact the refinement in the sense of obtaining cell parameters, as peak intensity is not related to it. What matters in cell parameters is the peak position. As seen in Table 6-3, the unit cell of the sample prepared in this work matches well with the values reported in the literature previously.

Table 6-3. *Cell parameters of V_5S_8 synthesised at 800 °C from elements via solid-state reaction compared with values reported in the literature.*

Sample	*a*, Å	*b*, Å	*c*, Å	Ref
V_5S_8	11.3795(7)	6.6462(4)	11.3130(2)	This work
V_5S_8	11.396	6.645	11.293	[10]
V_5S_8	11.399	6.668	11.311	[28]
V_5S_8	11.375	6.648	11.299	[9]

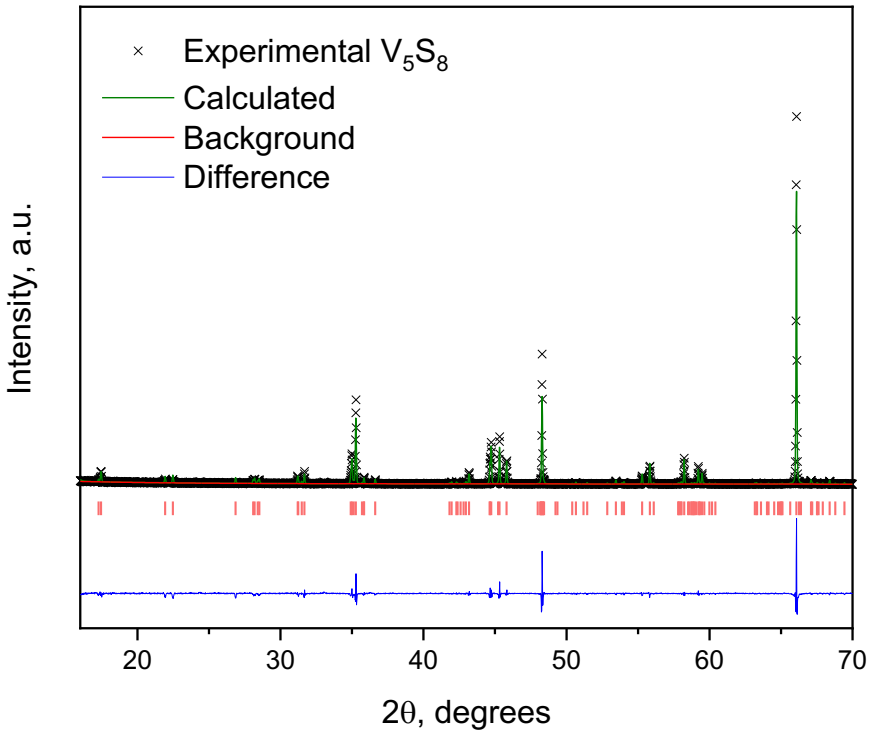

Figure 6-16. *Le Bail refinement of V_5S_8 solid-state sample. The experimental pattern is noted as a scatter plot with 'x'; the calculated pattern is in green, the background in red and the difference in blue line plots. Refinement was carried out in GSASII software. The first peak is removed from refinement due to the strong anisotropy of the shape.*

6.3.2.2. Morphology and elemental composition of V_5S_8

The morphology of the V_5S_8 sample differs dramatically from that of VS_4. V_5S_8 forms platelike crystallites that are larger in size (10-20 μm). The sample morphology is very similar to the layered compound morphology and resembles VS_2 samples prepared via the alkali metal deintercalation route in chapter 3.

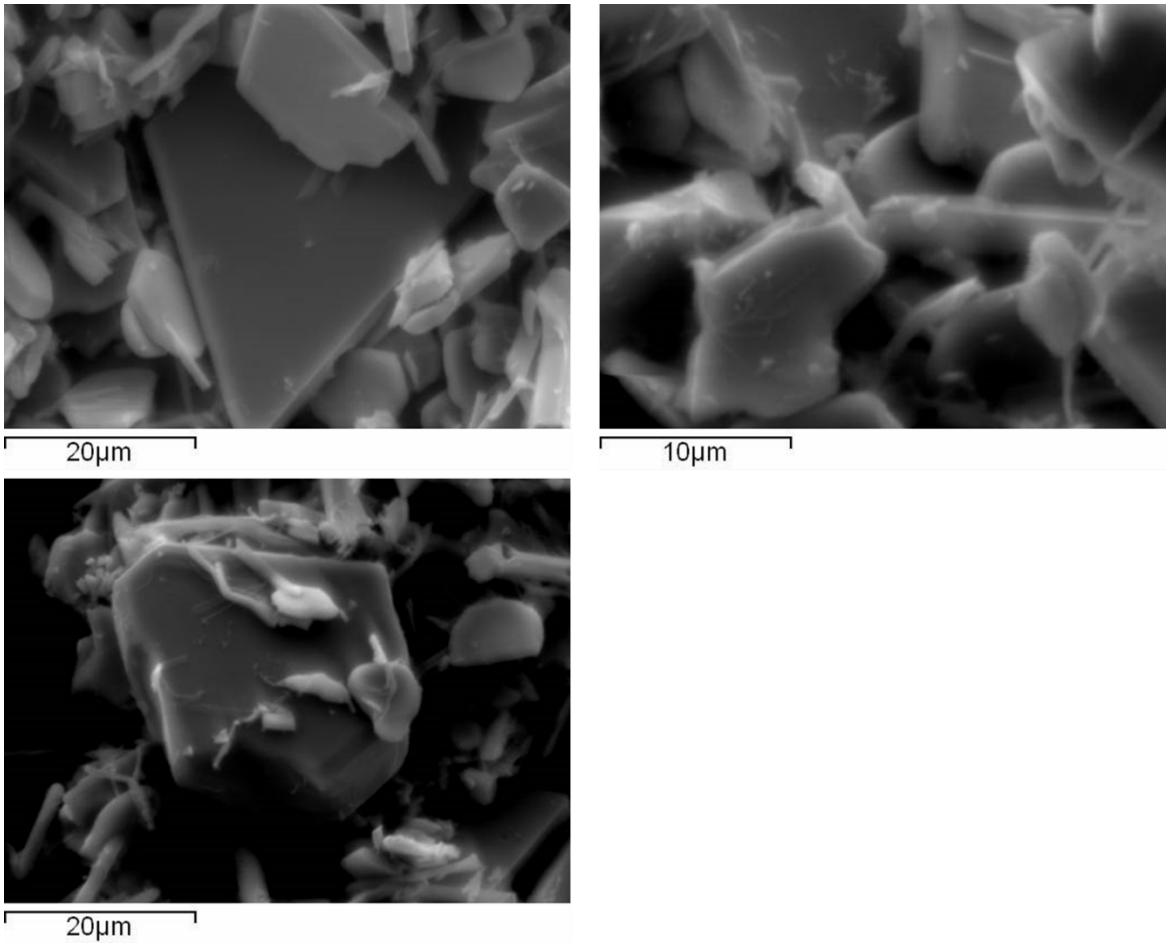

Figure 6-17. *SEM images of three different spots of sample V_5S_8 showing the sample morphology.*

The elemental composition of the sample was determined by EDX analysis. According to the obtained data (displayed in Table 6-4), the sample stoichiometry is $VS_{1.68}$, which deviates from the ideal $VS_{1.6}$ stoichiometry; however, it agrees well with it within the error. Non-stoichiometry is characteristic of the V-S system, with the V_5S_8 structure having a homogeneity range of $VS_{1.54}$ to $VS_{1.68}$.[9,16,29]

Table 6-4. *EDX data of sample V_5S_8. The standard deviation was calculated from 4 independent points.*

	V_5S_8 at. %	
Element	V	S
Experimental	37.2(24)	62.8(24)
Theoretical	38.5	61.5

6.3.2.3. Raman Spectroscopy of V_5S_8

Raman spectroscopy of V_5S_8 suffers from the same issues as VS_2 did. While literature reports, in this case, do not contradict each other, many claim that V_5S_8 is just a defective VS_2. Therefore, the Raman spectrum should be the same, only slightly shifted. However, the reports on the V_5S_8 Raman spectrum completely overlook the spectrum resemblance to that of Vanadium oxides. The major giveaway that the spectrum is that of the oxide usually contains a sharp peak at 990-1000 cm^{-1}.[21] With this in mind, the Raman spectrum recorded on the V_5S_8 sample under ambient conditions agreed well with the literature (Figure 6-18).[30,31] However, the spectrum also resembled every other Raman spectrum of V_xS_y collected under ambient conditions. Moreover, the peaks at 93 cm^{-1}, 137 cm^{-1}, 280 cm^{-1}, 403 cm^{-1}, 520 cm^{-1}, 689 cm^{-1} and 989 cm^{-1} match the reported Raman spectrum of V_6O_{13} and the shoulder at 157 cm^{-1}, 295 cm^{-1} and peaks at 833 cm^{-1} and 871 cm^{-1} match V_3O_7.[21]

When the Raman measurements were done on a sample sealed in a capillary under an inert atmosphere, the Raman spectrum was dramatically different as it was in the case of other vanadium sulphides in this study. The Raman spectrum of V_5S_8 sealed under inert atmosphere show peaks at 222 cm^{-1}, 273 cm^{-1}, 349 cm^{-1} and 560 cm^{-1}. While it is significantly lower quality than the spectrum recorded at ambient conditions, this spectrum resembles the one of VS_4. Moreover, the Raman peaks in our measurements closely match the ones reported by Huan *et al.* for their V_5S_8 sample.[32]

Such difficulties in recording the Raman spectrum without oxidising the sample point towards low thermal stability of this sample. Local heat generated by a laser used in Raman measurement is enough to provoke oxidation of the measured spot.

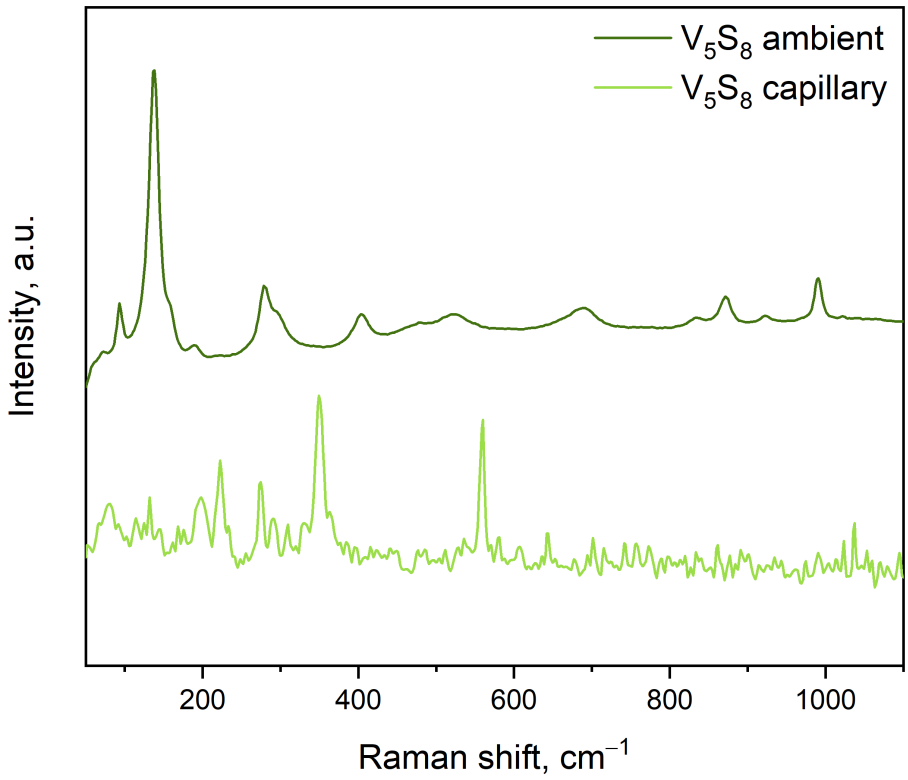

Figure 6-18. *Raman spectrum of V_5S_8 collected in ambient conditions (top, dark green) and on the sample sealed in a capillary under inert Ar atmosphere (bottom, light green). The measurement conditions were the same in both measurements.*

6.3.2.4. Electrocatalytic activity of V_5S_8 toward HER

Once phase identification and characterisation confirmed sample phase and purity, the electrochemical measurements were carried out. An initial scan of V_5S_8 shows a shoulder in the LSV curve and is shown in Figure 6-19. This shoulder, which appears at around –400 mV vs NHE, usually is caused by surface oxides, and the initial cycle is enough to remove the oxide layer. The second LSV run on the same electrode revealed that the overpotential increases dramatically, the opposite of what we saw in VS_4. In V_5S_8, the overpotential to achieve a benchmark current density of –10 mA cm^{-2} was recorded at –610 mV vs NHE and did not reach the same current density on the second scan within the measured potential window. The extended potential window could not be employed in the measurements as the bubbles would blast the catalyst off the electrode surface due to gas evolution.

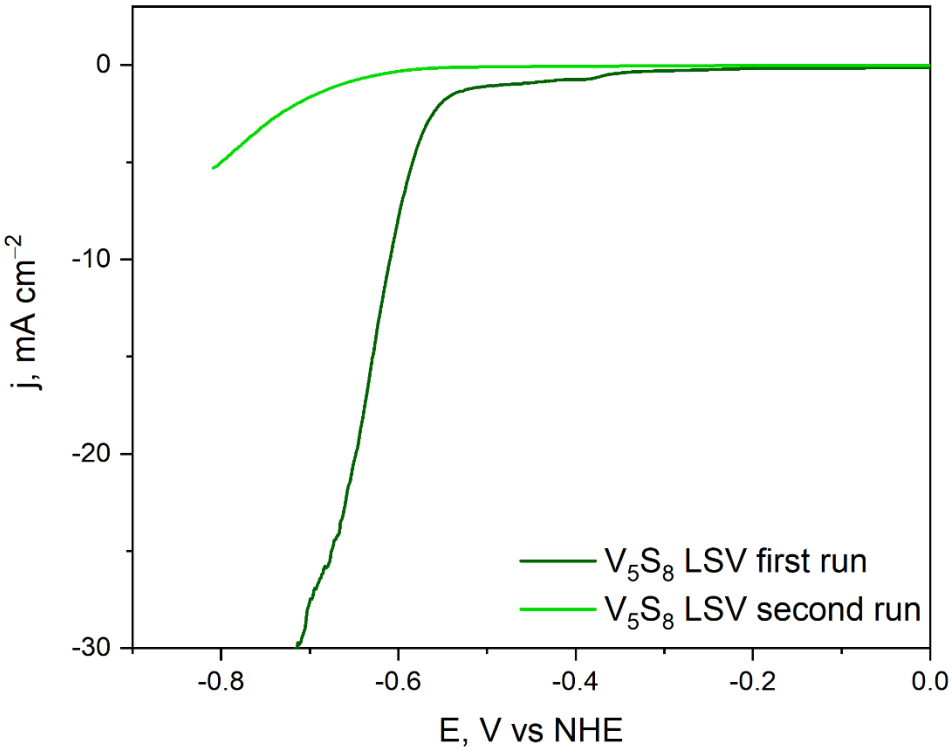

Figure 6-19. *Polarization curves recorded on sample V_5S_8. The second scan shows a shift toward higher overpotentials. Polarization curves were recorded using a sweep rate of 5 mV s^{-1}. Three electrode setup in 1 M H_2SO_4 electrolyte where glassy carbon modified with catalyst was working electrode, carbon felt was used as counter electrode and 3 M Ag/AgCl electrode as a reference electrode. Current density is calculated using geometric electrode area (0.071 cm^2).*

The catalyst was cycled in acidic media for 100 cycles to investigate this behaviour further. As seen in Figure 6-20, when cycled continuously, the V_5S_8 catalyst appears to be passivated, as the overpotential to reach –10 mA cm^{-2} increases from –651 mV vs NHE to –739 mV vs NHE within the first 50 cycles. However, as the catalyst is cycled further, the overpotential appears to stay around that value and does not increase or reduce further. The eventual stabilisation of overpotential shows that catalyst exhibits short-term stability. More studies need to be done to evaluate its long-term stability. This overpotential is high compared to other state-of-the-art catalysts and incredibly high compared to the performance of platinum. So far, the electrocatalytic performance of V_5S_8 has been the best out of the three investigated sulphides: VS_4, VS_2 and V_5S_8.

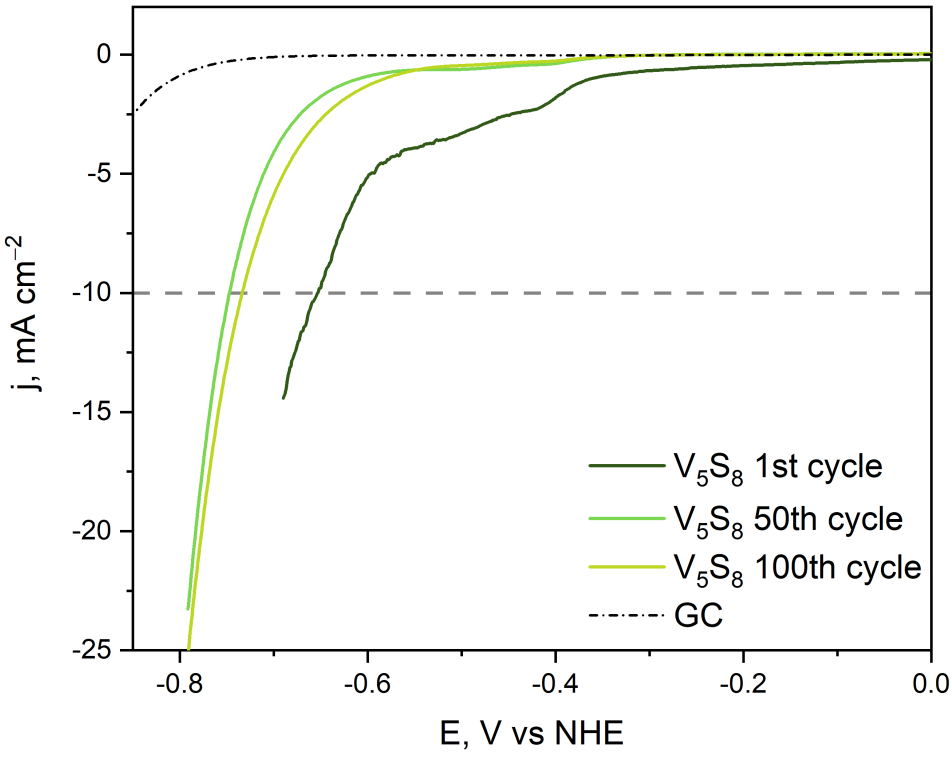

Figure 6-20. *Cathodic CV scan sweep of sample V_5S_8. Cyclic voltammetry was recorded using a sweep rate of 100 mV s^{-1}. Three electrode setup in 1 M H_2SO_4 electrolyte where glassy carbon modified with catalyst was working electrode, carbon felt was used as counter electrode and 3 M Ag/AgCl electrode as a reference electrode. Bare glassy carbon (GC) electrode data inserted for reference. Current density is calculated using geometric electrode area (0.071 cm^2).*

6.3.3. Synthesis and characterisation of VS

6.3.3.1. Synthesis of VS

Solid state synthesis between vanadium and sulphur was employed to obtain this compound. As the sulphur content in vanadium sulphides is getting smaller, the reported synthesis temperatures are getting higher. The typical temperature range for the synthesis of VS is reported to be 1000-1300 °C. In our work, a considerably lower temperature of 700 °C was employed. The reaction appears to have reached completion during the initial 24-hour heating step. There were no traces of excess sulphur on the inner walls of the synthesis ampoule. As seen in Figure 6-21, the PXRD pattern of the product after the first heating step visually matches the calculated pattern from the ICSD. The sample agrees well with NiAs structure type VS, and this pattern was used for Le Bail refinement and unit cell parameters.

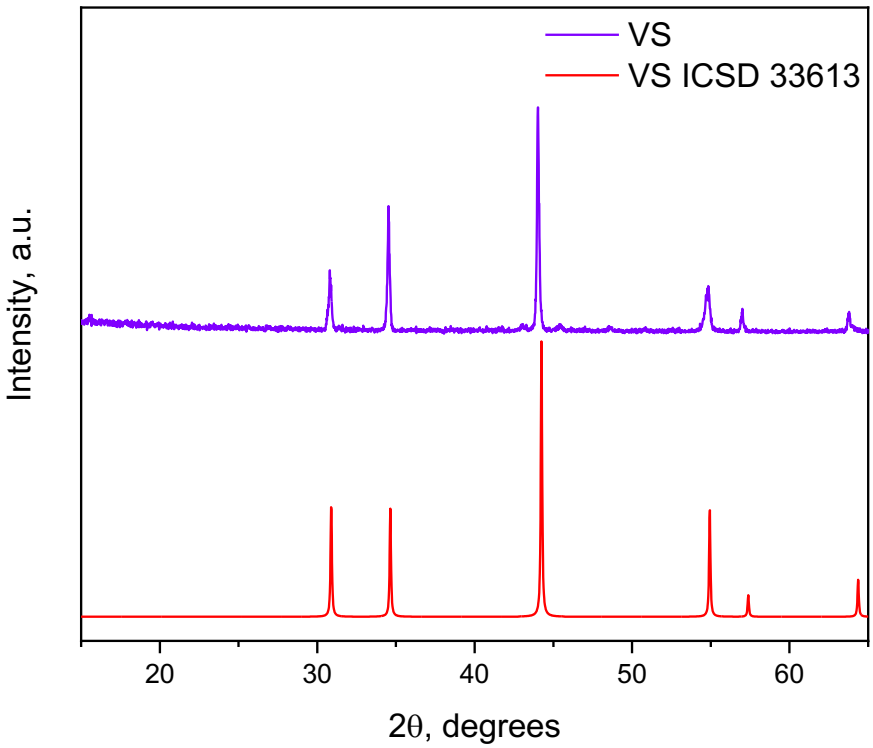

Figure 6-21. *PXRD pattern of the product of the reaction between elemental vanadium and sulphur at 700 °C for 24 hours (top, purple). For comparison, the calculated diffraction pattern of VS from the ICSD (card number 33613) is displayed at the bottom (red).*

A refined structure can be seen in Figure 6-22. Like V_5S_8, obtaining the excellent agreement of calculated and experimental data in the refinement was difficult. There were difficulties in matching peak intensity. However, this parameter does not impact the cell parameters obtained. Therefore, the fit was deemed sufficient.

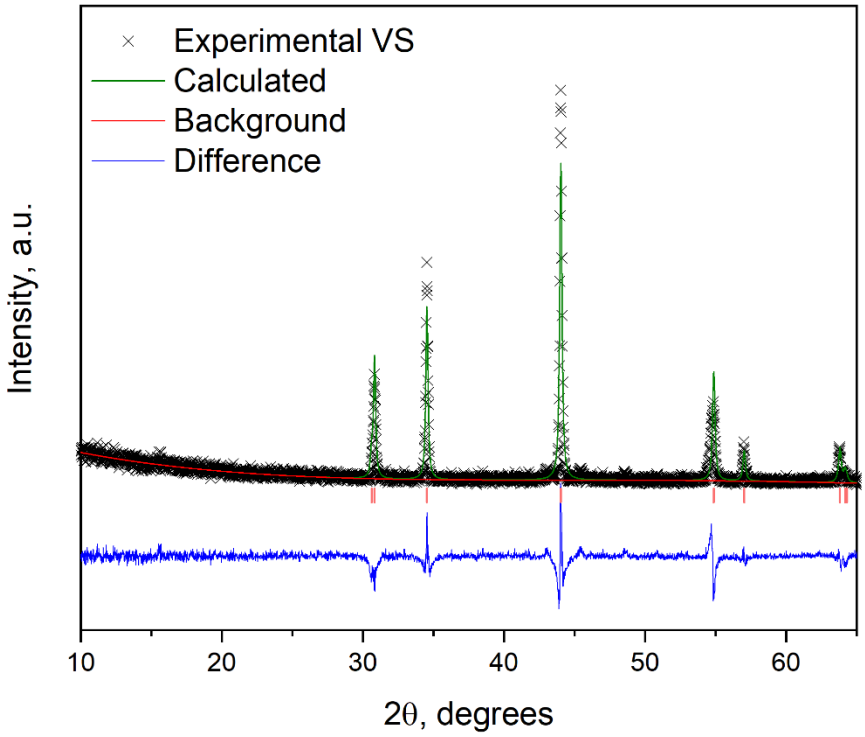

Figure 6-22. *Le Bail refinement of VS solid-state sample. The experimental pattern is noted as a scatter plot with 'x'; the calculated pattern is in green, the background in red and the difference in blue line plots. Refinement was carried out in GSASII software.*

As can be seen from Table 6-5, cell parameters are in good agreement with values reported in the literature. With our VS sample falling in the middle of reported *c* parameter values and a parameter matching the smaller end of literature reports.

Table 6-5. *Cell parameters of VS as obtained from Le Bail refinement in comparison with values reported in the literature.*

Sample	*a*, Å	*c*, Å	Ref
VS	3.340(1)	5.8258(8)	This work
VS	3.34	5.785	[33]
VS	3.34	5.845	[17]
VS	3.36	5.81	[34]
$V_{0.98}S$	3.36	5.813	[35]

6.3.3.2. Morphology and elemental composition of VS

SEM imaging was done to investigate the sample morphology. As seen in Figure 6-23, the crystallites are much smaller than other vanadium sulphides prepared in this work. The crystallites appear to be very thin platelets, which agrees well with the sample having a hexagonal structure.

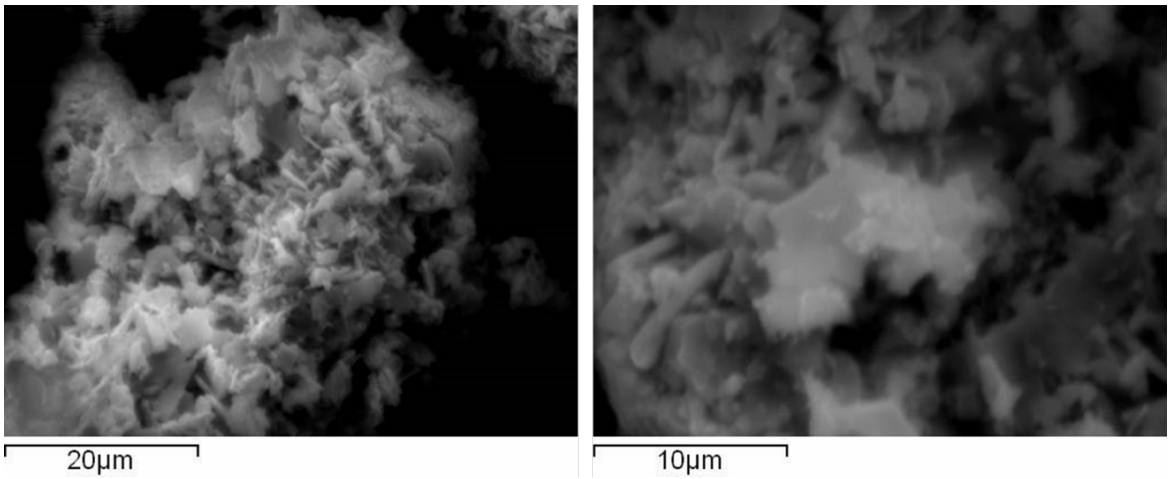

Figure 6-23. *SEM images of two different spots of sample V_5S_8 showing the sample morphology.*

EDX analysis (data displayed in Table 6-6) revealed the sample composition to be $VS_{1.06}$. This agrees well with the sample having NiAs structure. According to research conducted by Franzen *et al*., VS starts to adopt NiAs structure at a stoichiometry of $VS_{1.06}$, with samples closer to the ideal VS stoichiometry adopting an MnP type structure.[17]

Table 6-6. *EDX data of sample VS. The standard deviation was calculated from 4 independent points.*

	VS at. %	
Element	V	S
Experimental	48.5(1)	51.5(1)
Theoretical	50	50

6.3.3.3. Raman Spectroscopy of VS

VS was no different from other vanadium sulphides in terms of Raman measurements. The spectrum collected under ambient conditions presented a very familiar shape. The peaks could be observed at 93 cm^{-1}, 137 cm^{-1}, 190cm^{-1}, 280 cm^{-1}, 298 cm^{-1}, 403 cm^{-1}, 520 cm^{-1}, 689 cm^{-1} and 989 cm^{-1}. All of these peak positions match V_6O_{13} Raman spectrum peaks reported by Shvets *et al*.[21] Once the sample was remeasured in a capillary sealed under an inert atmosphere, the Raman spectrum changed dramatically. The most prominent peak is observed at 484 cm^{-1}, and two minor peaks are observed at 132 cm^{-1} and 234 cm^{-1}. The peak at 498 cm^{-1} was also observed in the Raman spectrum of VS films prepared and discussed by A. Hardy in their doctoral thesis.[36] While shifted, our Raman spectrum appears to confirm that the peak represents VS. The different forms of the samples can explain the shift; in our research, the spectrum was collected on bulk powders, where Hardy was working with films.

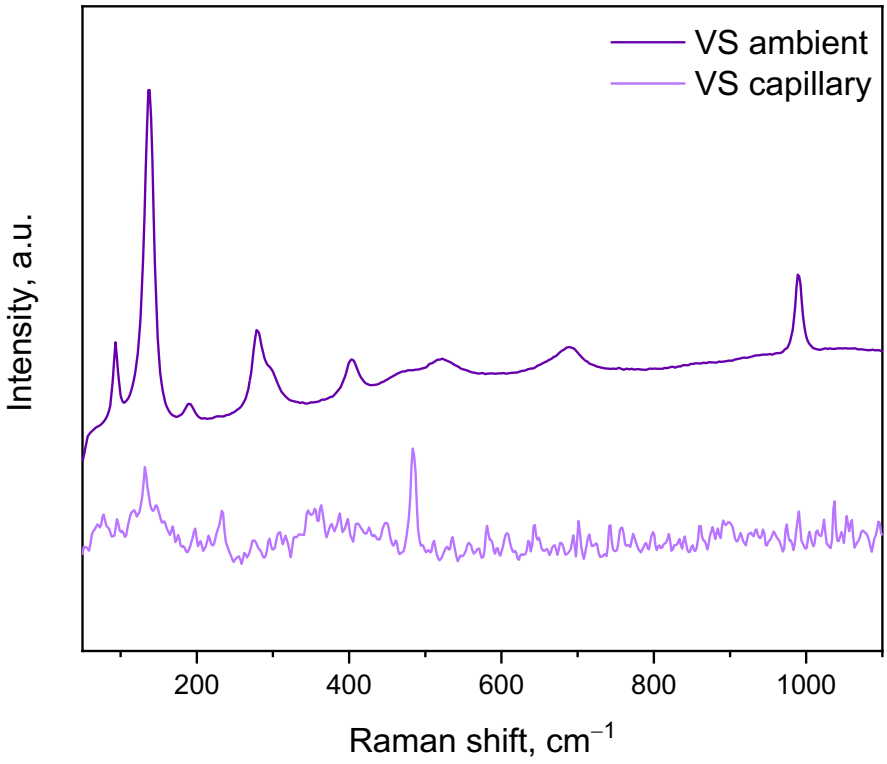

Figure 6-24. *Raman spectrum of VS collected in ambient conditions (top, dark purple) and on the sample sealed in a capillary under inert Ar atmosphere (bottom, light purple). The measurement conditions were the same in both measurements.*

6.3.3.4. Electrocatalytic activity of VS toward HER

The electrochemical performance of VS was assessed by running an LSV scan (Figure 6-25). Unlike other sulphides investigated in this work, VS did not show any change in overpotential in the second LSV scan. There also were no reductive waves in the LSV curve, and the catalyst appears to have the lowest overpotential out of all vanadium sulphides in this study, reaching –10mA cm^{-2} at –640 mV vs NHE.

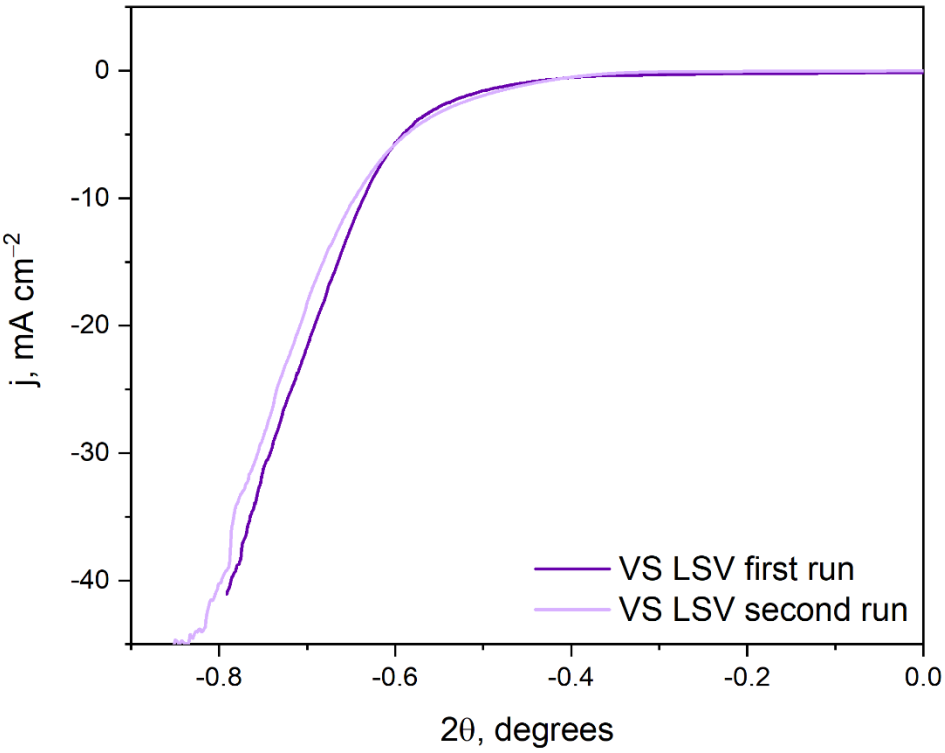

Figure 6-25. *Polarisation curves recorded on sample VS. The second scan shows that the potential remains stable. Polarisation curves were recorded using a sweep rate of 5 mV s^{-1}. Three electrode setup in 1 M H_2SO_4 electrolyte where glassy carbon modified with catalyst was working electrode, carbon felt was used as counter electrode and 3 M Ag/AgCl electrode as a reference electrode. Current density is calculated using geometric electrode area (0.071 cm^2).*

When cycled, VS shows a negligible variation in overpotential. As shown in Figure 6-26, the electrocatalytic behaviour remains almost constant in the initial 50 cycles, only starting to improve afterwards. The improvement in the overpotential is slight, around 20 mV, and is accompanied by the improvement in current densities achieved at the cut-off potentials.

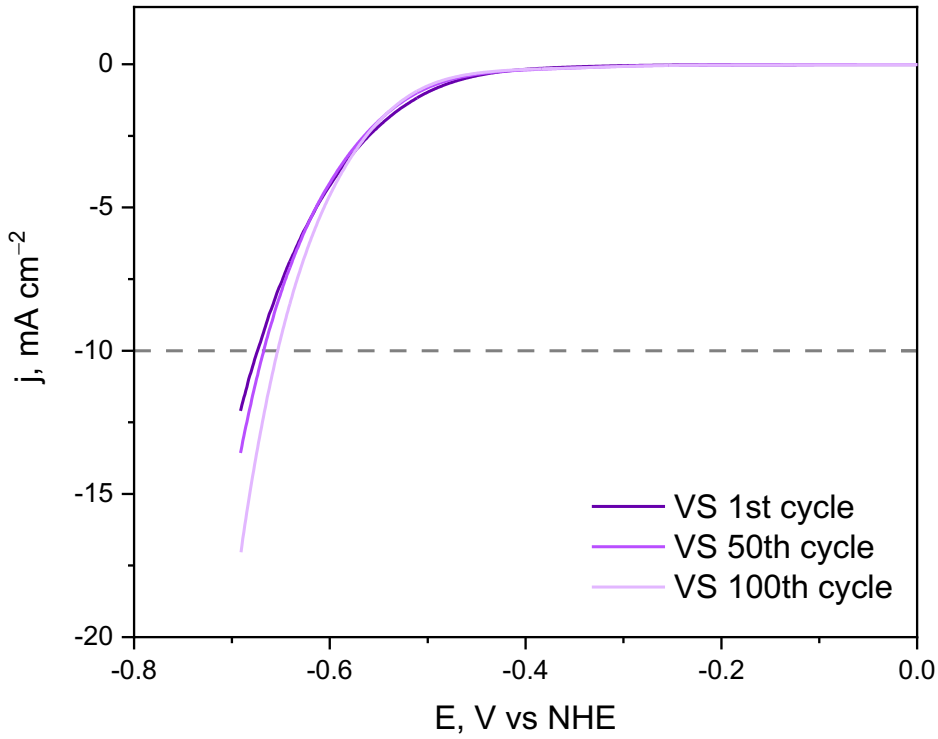

Figure 6-26. *Cathodic CV scan sweep of sample VS. Cyclic voltammetry was recorded using a sweep rate of 100 mV s^{-1}. Three electrode setup in 1 M H_2SO_4 electrolyte where glassy carbon modified with catalyst was working electrode, carbon felt was used as counter electrode and 3 M Ag/AgCl electrode as a reference electrode. Current density is calculated using geometric electrode area (0.071 cm^2).*

6.4. Summary and conclusions

Thermodynamically stable vanadium sulphides – VS_4, V_5S_8 and VS – were explored. All of the compounds were synthesised via a solid-state route between the elements. VS_4, as the most sulphur-rich vanadium sulphide, needed multiple homogenisation and annealing steps to achieve a single-phase product, indicating sluggish reaction kinetics. Synthesis of V_5S_8 and VS was attempted at 700 ºC and worked nicely to obtain pure phase VS. However, V_5S_8 had impurities at this temperature and had to be synthesised at 800 ºC to achieve a single-phase sample.

All samples display different morphology. VS_4 grows in rod-like crystallites, V_5S_8 grows in big (up to 20 µm) thin platelet-like crystallites, and VS grows in small thin platelet-like crystallites under the conditions used in synthesis. None of the samples achieves ideal stoichiometry, with VS_4 being sulphur deficient at a composition of $VS_{3.74}$, V_5S_8 slightly

sulphur rich at $VS_{1.68}$ and VS showing a sulphur rich composition of $VS_{1.06}$ as well. This illustrates the non-stoichiometry of the V – S system well.

It was found that the Raman spectrum recorded under ambient conditions matched between all three samples. This was due to all sulphides quickly oxidising during the laser irradiation of the measurement. The Raman spectrum matched the spectra of mixed vanadium oxides. Once measured in capillaries – Raman spectra were different between the samples. With the exception of VS_4 and V_5S_8 displaying very similar peak positions. It highlights the careful considerations needed to reliably record the Raman spectrum of vanadium sulphides.

Electrochemical performance toward HER reaction was investigated for all three vanadium sulphides. VS_4 showed the highest overpotential of the three; however, still smaller than that of VS_2 discussed in chapter 3. With continuous cycling, the overpotential of –971 mV vs NHE shifted to –805 mV vs NHE to achieve benchmark current density. This electrochemical activation of the catalyst was non-reversible, implying that the morphological or structural changes occur at the surface. No structural changes could be observed via PXRD in the bulk of the catalyst. However, that does not rule out the processes taking place at the surface.

V_5S_8 revealed the overpotential of –610 mV vs NHE on the first LSV scan, and there was also an indication of reductive waves in the polarisation curve. With this overpotential, it outperformed VS_4 by 200 mV. However, the catalyst shows an increase in overpotential in subsequent scans, with overpotential settling at –740 mV vs NHE. While this overpotential is still lower than that of VS_4, it is high compared to the state of art catalysts, especially platinum. V_5S_8 appears to have a stable overpotential after 50 reductive CV cycles.

VS showed the best electrochemical performance towards HER. The overpotential recorded from the LSV curve was –640 mV vs NHE and appeared to remain the same with continuous cycling. While a slight improvement in achieved current density was noticed, the overpotential shift was negligible after 100 cycles. The catalyst appears to show the best stability out of the three sulphides.

Even though the morphology and surface area is different for each compound, there appears to be a trend in catalytic activity. As sulphur content in the compound decreases, the electrochemical activity towards HER increases. Less sulphur within the structure goes hand in hand with vanadium atoms having a lower oxidation state. This implies that a lower

oxidation state of the metal is preferred for stable performance. Additionally, all the thermodynamically stable vanadium sulphides outperformed the metastable VS_2 phase, indicating that metastable phases might not be optimal for electrocatalysts.

6.5. References

1. B. Predel, *Pu-Re – Zn-Zr*, Springer-Verlag, Berlin/Heidelberg, 1998, vol. 5 J.

2. B. Pedersen, A. Sundholm, A. Magnéli, B. Högberg, P. Kneip and H. Palmstierna, Unit Cell and Space Group of VS_4., *Acta Chem. Scand.*, 1959, **13**, 1050–1050.

3. M. N. Kozlova, Y. V Mironov, E. D. Grayfer, A. I. Smolentsev, V. I. Zaikovskii, N. A. Nebogatikova, T. Y. Podlipskaya and V. E. Fedorov, Synthesis, Crystal Structure, and Colloidal Dispersions of Vanadium Tetrasulfide (VS_4), *Chem. - A Eur. J.*, 2015, **21**, 4639–4645.

4. Z. Qin, Y. Hu, C. Lv, S. Yao and G. Chen, Low-temperature solid-state synthesis of interlayer engineered VS_4 for high-capacity and ultrafast sodium-ion storage, *Chem. Eng. J.*, 2022, **433**, 133765.

5. M. Ramu, J. R. Chellan, N. Goli, P. Joaquim, V. Cristobal and B. C. Kim, A Self-Branched Lamination of Hierarchical Patronite Nanoarchitectures on Carbon Fiber Cloth as Novel Electrode for Ionic Liquid Electrolyte-Based High Energy Density Supercapacitors, *Adv. Funct. Mater.*, 2020, **30**, 1–13.

6. P. Mohan, J. Yang, A. Jena and H. Suk Shin, VS_2/rGO hybrid nanosheets prepared by annealing of VS_4/rGO, *J. Solid State Chem.*, 2015, **224**, 82–87.

7. M. S. Weimer, R. F. McCarthy, J. D. Emery, M. J. Bedzyk, F. G. Sen, A. Kinaci, M. K. Y. Chan, A. S. Hock and A. B. F. Martinson, Template-Free Vapor-Phase Growth of Patrónite by Atomic Layer Deposition, *Chem. Mater.*, 2017, **29**, 2864–2873.

8. Y. Oka, K. Kosuge and S. Kachi, Order-disorder transition of the metal vacancies in the vanadium-sulfur system. I. An experimental study, *J. Solid State Chem.*, 1978, **23**, 11–18.

9. F. De Vries, A.B. Jellinek, A structural study of vanadium sulfides, *Rev. Chim. Miner.*, 1974, **11**, 624–636.

10. I. Kawada, M. Nakano-Onoda, M. Ishii, M. Saeki and M. Nakahira, Crystal structures of V_3S_4 and V_5S_8, *J. Solid State Chem.*, 1975, **15**, 246–252.

11. H. Nozaki, Y. Ishizawa, M. Saeki and M. Nakahira, Electrical properties of V_5S_8 single crystals, *Phys. Lett. A*, 1975, **54**, 29–30.

12. J. Lu, H. Tong, S. Chen, C. Wang, X. Zeng, J. Tu and Q. Chen, One-Step Construction of V_5S_8 Nanoparticles Embedded in Amorphous Carbon Nanorods for High-Capacity and Long-Life Potassium Ion Half/Full Batteries, *ACS Appl. Mater. Interfaces*, 2021, **13**, 54308–54314.

13. Z. Ren, Y. Sun, Y. Yin, J. Zhang, X. Ren, Y. Zhao, Z. Liang, P. Huai, F. Song, Z. Jiang, W. Wen, X. Li, R. Tai and D. Zhu, Metallic V_5S_8 microparticles with tunnel-like structure for high-rate and stable zinc-ion energy storage, *Energy Storage Mater.*, 2021, **42**, 786–793.

14. J. Li, S. Zhang, S. Zhang, C. An and L. Cao, Templated constructing honeycomb-like V_5S_8@C anode with multi-scale interfacial coactions and high pseudocapacitive contribution for enhanced potassium storage capability, *J. Alloys Compd.*, 2021, **851**, 156920.

15. H. F. Franzen and G. A. Wiegers, The NiAsMnP phase transition in VS, *J. Solid State Chem.*, 1975, **13**, 114–117.

16. T. Uchida, H. Hinode, M. Wakihara and M. Taniguchi, Phase equilibria of the VS-V_5S_8 system from 923 to 1323 K, *Metall. Trans. B*, 1981, **12**, 71–75.

17. H. F. Franzen and T. J. Burger, Second-Order Phase Transition in the VS One-Phase Region, *J. Chem. Phys.*, 1968, **49**, 2268–2272.

18. J. Xu, B. Yu, H. Zhao, S. Cao, L. Song, K. Xing, R. Zhou and X. Lu, Oxygen-Doped VS_4 Microspheres with Abundant Sulfur Vacancies as a Superior Electrocatalyst for the Hydrogen Evolution Reaction, *ACS Sustain. Chem. Eng.*, 2020, **8**, 15055–15064.

19. R. Allmann, I. Baumann, A. Kutoglu, H. R□sch and E. Hellner, Die Kristallstruktur des Patronits $V(S_2)_2$, *Naturwissenschaften*, 1964, **51**, 263–264.

20. R. Kutoglu, A. Allmann, Strukturverfeinerung des Patronits, $V(S_2)_2$, *Neues Jahrb. für Mineral.*, 1972, 339–345.

21. P. Shvets, O. Dikaya, K. Maksimova and A. Goikhman, A review of Raman spectroscopy of vanadium oxides, *J. Raman Spectrosc.*, 2019, **50**, 1226–1244.

22. Y. Liu, J. Wu, K. P. Hackenberg, J. Zhang, Y. M. Wang, Y. Yang, K. Keyshar, J. Gu, T. Ogitsu, R. Vajtai, J. Lou, P. M. Ajayan, B. C. Wood and B. I. Yakobson, Self-optimizing, highly surface-active layered metal dichalcogenide catalysts for hydrogen evolution, *Nat. Energy*, 2017, **2**, 1–7.

23. J. C. McGlynn, T. Dankwort, L. Kienle, N. A. G. Bandeira, J. P. Fraser, E. K. Gibson, I. Cascallana-Matías, K. Kamarás, M. D. Symes, H. N. Miras and A. Y. Ganin, The rapid electrochemical activation of $MoTe_2$ for the hydrogen evolution reaction, *Nat. Commun.*, 2019, **10**, 4916.

24. G. Shao, Q. Wang, F. Miao, J. Li, Y. Li and B. Shen, Improved catalytic efficiency and stability by surface activation in Fe-based amorphous alloys for hydrogen evolution reaction in acidic electrolyte, *Electrochim. Acta*, 2021, **390**, 138815.

25. G. Dong, M. Fang, H. Wang, S. Yip, H. Y. Cheung, F. Wang, C. Y. Wong, S. T. Chu and J. C. Ho, Insight into the electrochemical activation of carbon-based cathodes for hydrogen evolution reaction, *J. Mater. Chem. A*, 2015, **3**, 13080–13086.

26. C. lu Liang, N. ni Ye, J. li Li, X. qiu Li, S. Lei, Y. peng Huang, J. jie Wu, Y. Liu and W. Yang, Electrochemical Activated Nitrogen-doped Carbon as Highly Efficient Electrocatalysts for Hydrogen Evolution Reactions, *ChemNanoMat*, 2022, **8**, 0–7.

27. I. Roger and M. D. Symes, Silver Leakage from Ag/AgCl Reference Electrodes as a Potential Cause of Interference in the Electrocatalytic Hydrogen Evolution Reaction, *ACS Appl. Mater. Interfaces*, 2017, **9**, 472–478.

28. W. Bensch and J. Koy, The single crystal structure of V_5S_8 determined at two different temperatures: anisotropic changes of the metal atom network, *Inorganica Chim. Acta*, 1993, **206**, 221–223.

29. M. Saeki, M. Nakano and M. Nakahira, Crystal growth of nonstoichiometric V_5S_8 by chemical transport, *J. Cryst. Growth*, 1974, **24**–**25**, 154–157.

30. L. Xu, X. Chen, W. Guo, L. Zeng, T. Yang, P. Xiong, Q. Chen, J. Zhang, M. Wei and Q. Qian, Co-construction of sulfur vacancies and carbon confinement in V_5S_8/CNFs to induce an ultra-stable performance for half/full sodium-ion and potassium-ion batteries, *Nanoscale*, 2021, **13**, 5033–5044.

31. Q. Ji, C. Li, J. Wang, J. Niu, Y. Gong, Z. Zhang, Q. Fang, Y. Zhang, J. Shi, L. Liao, X. Wu, L. Gu, Z. Liu and Y. Zhang, Metallic vanadium disulfide nanosheets as a platform material for multifunctional electrode applications, *Nano Lett.*, 2017, **17**, 4908–4916.

32. Y. Huan, J. Shi, X. Zou, Y. Gong, C. Xie, Z. Yang, Z. Zhang, Y. Gao, Y. Shi, M. Li, P. Yang, S. Jiang, M. Hong, L. Gu, Q. Zhang, X. Yan and Y. Zhang, Scalable Production of Two-Dimensional Metallic Transition Metal Dichalcogenide Nanosheet Powders Using NaCl Templates toward Electrocatalytic Applications, *J. Am. Chem. Soc.*, 2019, **141**, 18694–18703.

33. W. Biltz and A. Köcher, Beiträge zur systematischen Verwandtschaftslehre. 88. Über das System Vanadium/Schwefel, *Zeitschrift für Anorg. und Allg. Chemie*, 1939, **241**, 324–337.

34. N. Schönberg, The tungsten carbide and nickel arsenide structures, *Acta Metall.*, 1954, **2**, 427–432.

35. E. Hoschek and W. Klemm, Vanadinselenide, *Zeitschrift fur Anorg. und Allg. Chemie*, 1939, **242**, 49–62.

36. A. Hardy, University College London, 2002.

7. Conclusions and outlook

The work described in this thesis provided an insight into the electrocatalytic activity of layered compounds VS_2, VSe_2, TiS_2, $TiSe_2$ and $CrSe_2$. All mentioned chalcogenides can be successfully synthesised as phase-pure and adventitious impurities-free 1T-phases according to powder X-ray diffraction. Raman studies revealed that care must be taken during an investigation of chalcogenides. This was because all samples oxidised easily under laser irradiation when measured in ambient conditions. Moreover, even after taking appropriate measures, recording Raman spectra required very delicate control of the laser power and protection under an inert atmosphere. It could be concluded that the chalcogenides generally displayed limited chemical stability.

The isolation of VS_2 as a pure phase stand-alone product allowed for an insight into the intrinsic electrochemical behaviour of this material. The main conclusion was that since the electrochemical performance was poor (even on a sample with nanostructured morphology), VS_2 is an intrinsically poor electrocatalyst. This conclusion contradicts the previous literature reports that often claimed Pt-like catalytic performance on VS_2. It is unclear whether impurities, synergistic effects from carbon nanostructures or other factors made the authors demonstrate exceptional results. However, as electrochemical testing revealed a reductive wave, one can speculate that it could be erroneously attributed to "electrocatalytic" behaviour (especially on high surface area samples) if the authors did not venture to explore broader voltage ranges in their LSV studies.

Following these findings, the attention is shifted toward sulphides isostructural with VS_2 – TiS_2 and CrS_2. It was concluded that standard solid-state methods (rather than deintercalation from the alkali metal intercalation compound) were a superior synthetic technique for the synthesis of TiS_2. It was impossible to deintercalate $LiCrS_2$ fully to yield a phase pure sample. Electrochemically TiS_2 behaved similarly to VS_2 – with a reduction wave present in initial scans. In addition, the results in electrocatalytic activity pointed toward a possible trend of increasing activity when moving from left to right through transition metals. However, differences in activity were subtle, and ECSA estimated from double layer capacitance measurements showed a vast difference between TiS_2 and VS_2. It was therefore deemed that the data was insufficient to draw conclusions.

Subsequently, the investigation was expanded to $TiSe_2$, VSe_2 and $CrSe_2$. The former two compounds were synthesised *via* solid-state synthesis between the elements. $CrSe_2$ could only be accessed through alkali metal intercalated compounds. While $TiSe_2$ and VSe_2

samples were composed of large platelike crystallites, the $CrSe_2$ consisted of much smaller particles. This was well reflected in double layer capacitance, with $CrSe_2$ having an estimated ECSA nearly twice the size of $TiSe_2$ and VSe_2. While VSe_2 outperformed $TiSe_2$ (and thus, confirmed the trend observed for sulphide analogues), CrS_2, despite smaller particle sizes and higher ECSA, showed the highest overpotential at the benchmark current density. Therefore, it was not possible to confirm the initial hypothesis that electrocatalytic performance in isostructural dichalcogenides depends on the atomic number of the transition metal (i.e. the number of *d*-electrons). Overall, vanadium compounds showed the best performance suggesting that a further trend may be observed by investigation of the vanadium sulphur system in more detail.

The synthesis and investigation of the electrocatalytic performance of thermodynamically stable vanadium sulphides revealed that rod-like crystallites of VS_4 showed high overpotentials and were deemed to be a poor electrocatalyst. Remarkably, the overpotential could be improved with continuous cyclic under a reductive environment, a phenomenon characteristic of some transition metal dichalcogenides. Phase-pure V_5S_8 showed improved electrocatalytic performance compared to VS_4, thus setting a trend that suggested reducing S content may lead to improved catalytic behaviour. Finally, phase pure VS showed the lowest overpotential and reasonable current densities accompanied by good stability. Therefore, it was concluded that high S content limits the catalytic performance. In addition, as no reduction waves were observed for these sulphides (and further confirming that the reduction wave is an intrinsic electrochemical characteristic of metastable VS_2) it was concluded that thermodynamic stability might be a key to electrochemical stability.

Overall, by comparing with literature benchmarks (such as MoS_2), the results pointed out that early transition metals display very high overpotentials making them unattractive for industry applications. However, as they can be reliably prepared as single-phase 1T phases, they are exciting materials from a fundamental science point of view. $TiSe_2$ and VSe_2 formed large crystallites with vast basal planes, which could then be tested directly as microelectrodes. Therefore, they could serve as a perfect system for correlating the results of computer simulations for the HER with the experiments. Unlike other 2D chalcogenides, they seem underexplored, and their poor performance for HER makes them interesting targets for the electroreduction of CO_2, where HER is often a competitive reaction and should be suppressed. The highly defined surfaces of these chalcogenides then should allow for finding direct correlations between computational methods (such as DFT) and experimental results without obscuring the effects of myriad crystal-faces often found in non-2D

materials. Finally, as demonstrated by the examples of thermodynamically stable V-S system it seems that low non-metal content is beneficial for electrocatalytic performance. This suggests that future research efforts in electrocatalytic chalcogenides for HER should be targeted toward low valent thermodynamically stable compounds.

8. Appendix

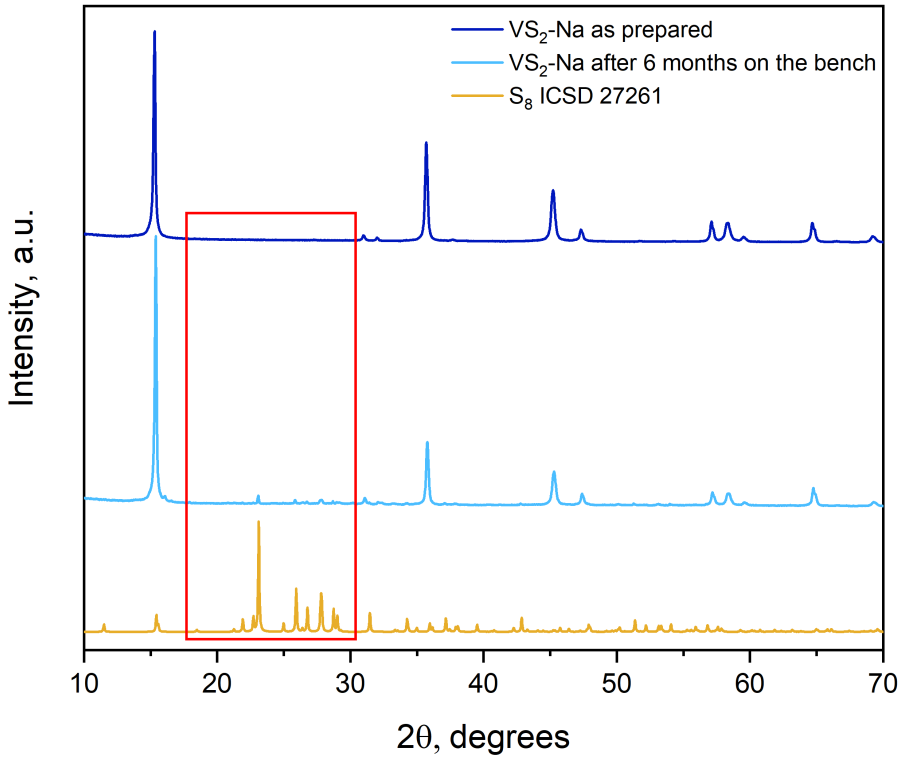

Figure A 1. *PXRD patterns of $NaVS_2$ sample collected on fresh sample after deintercalation (top, dark blue) and the same sample after exposure to ambient conditions by keeping the sample vial on the bench for 6 months (middle, light blue). It can be noted that there are impurities in the sample after 6 months, and they match well with reference pattern of sulphur ICSD 27261 (bottom, mustard).*

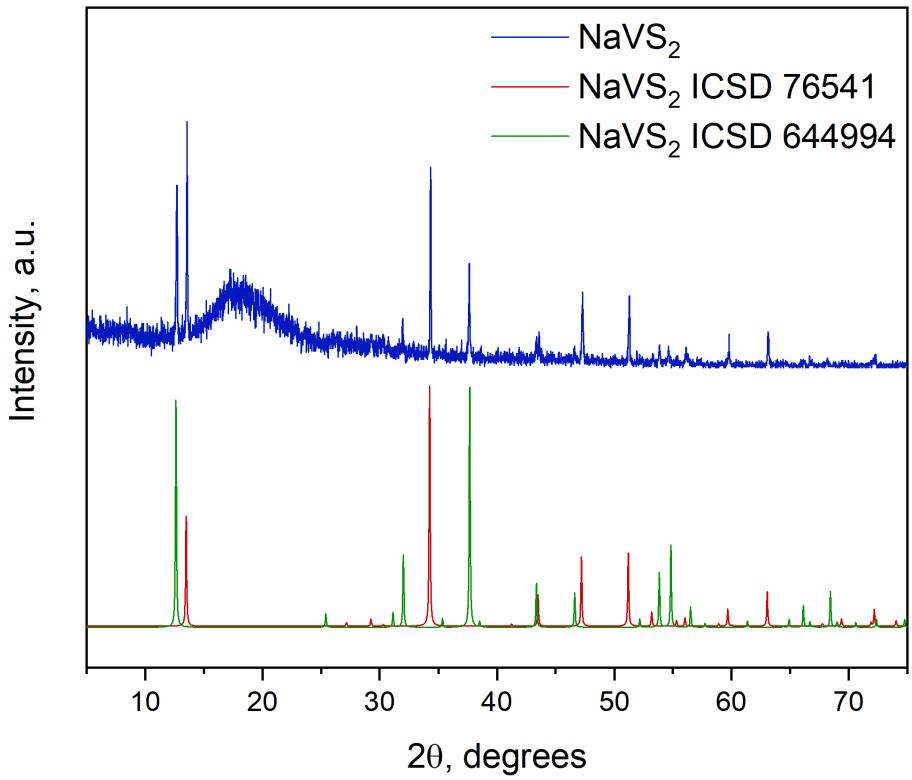

Figure A 2. *PXRD pattern of the product of reaction between Na_2S, V and S powders sealed under vacuum and heated at 600 °C for 72 hours (top, dark blue) when stoichiometry is kept at Na:V:S = 1:1:2. The two rhombohedral phases calculated from ICSD (card no 76541 and 644994) are in red and green for comparison. Wide 'bump' at 15-20 degrees in the experimental pattern (top, blue) comes from air sensitive holder used in the measurement.*

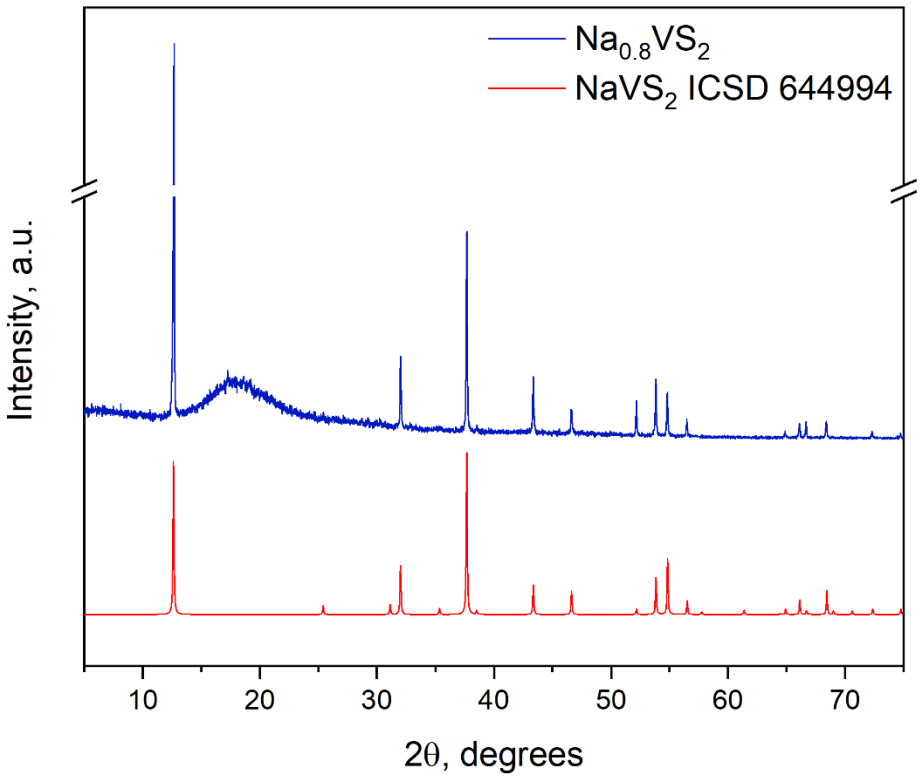

Figure A 3. *PXRD pattern of the product of reaction between Na_2S, V and S powders sealed under vacuum and heated at 600 °C for 72 hours (top, dark blue) when stoichiometry is kept at Na:V:S = 0.8:1:2. The product is single phase and reference pattern calculated from ICSD (card no 644994) is displayed in red. Wide 'bump' at 15-20 degrees in the experimental pattern (top, blue) comes from air sensitive holder used in the measurement.*

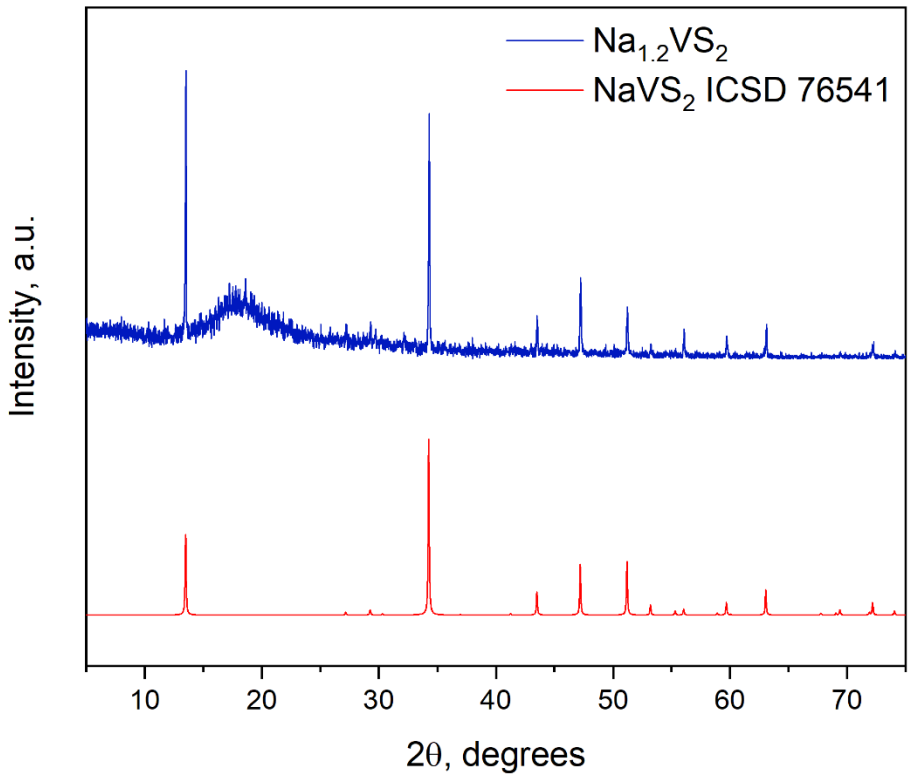

Figure A 4. *PXRD pattern of the product of reaction between Na_2S, V and S powders sealed under vacuum and heated at 600 °C for 72 hours (top, dark blue) when stoichiometry is kept at Na:V:S = 1.2:1:2. The product is single phase and reference pattern calculated from ICSD (card no 76541) is displayed in red. Wide 'bump' at 15-20 degrees in the experimental pattern (top, blue) comes from air sensitive holder used in the measurement.*

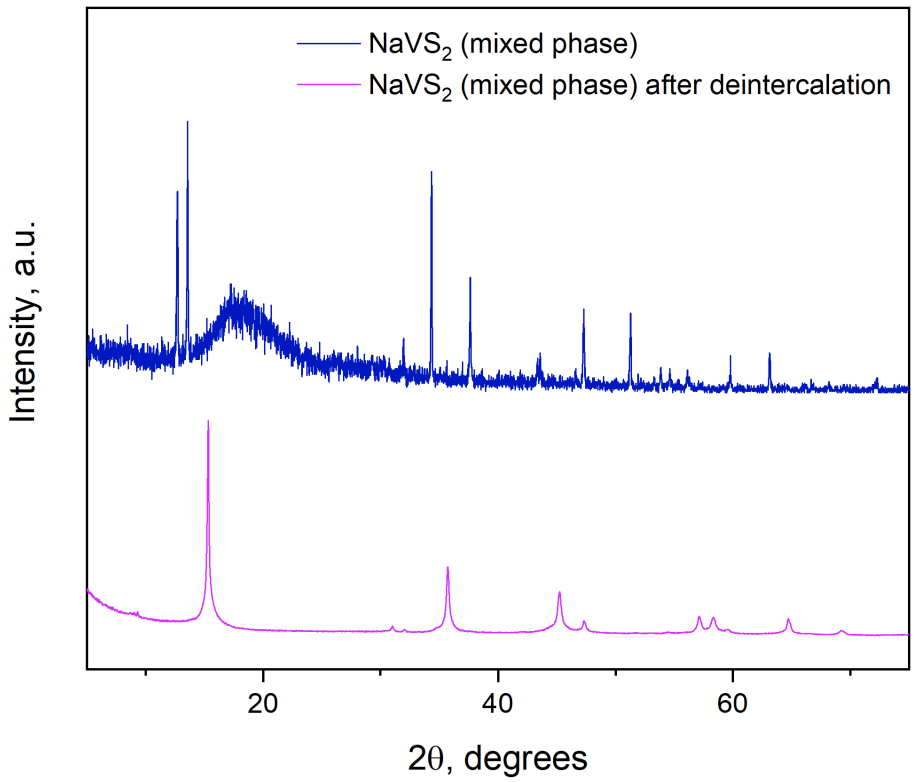

Figure A 5. *PXRD pattern of mixed phase $NaVS_2$ that was used for deintercalation (top, blue), a wide bump at around 15-20 degrees comes from air sensitive holder. PXRD pattern of the product of deintercalation reaction where mixed phase $NaVS_2$ was reacted with I_2 solution in acetonitrile for 48 hours at room temperature under continuous stirring (bottom, pink).*

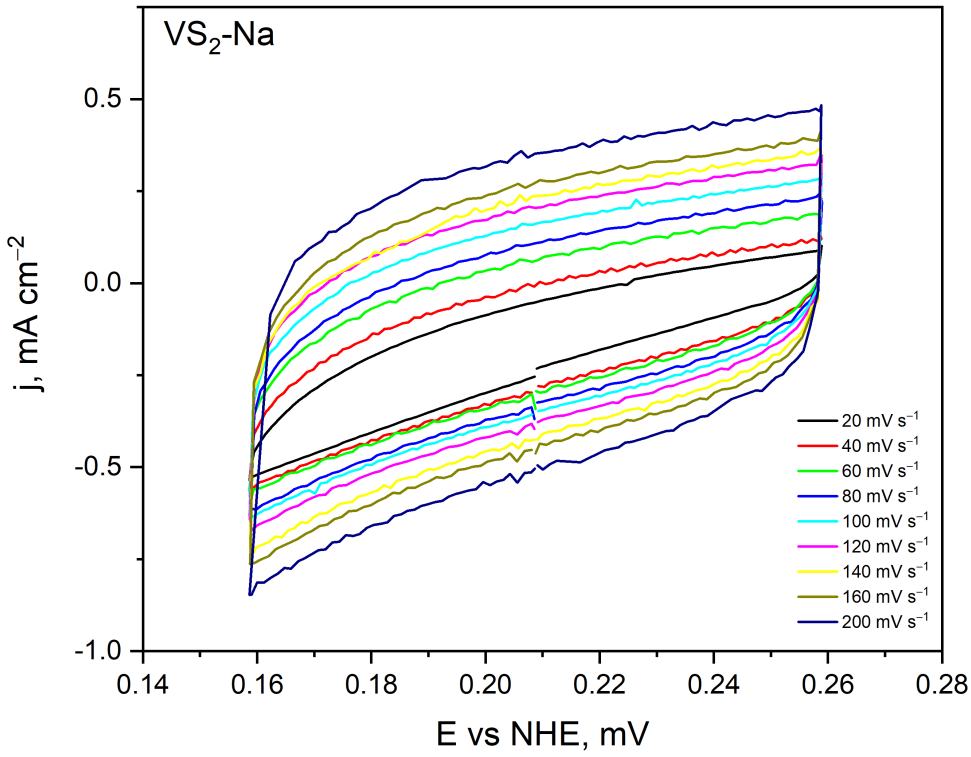

Figure A 6. *CV scans at different scan speeds (from 20 mV s^{-1} to 200 mV s^{-1}) of sample VS_2-Na that were used for double layer capacitance plot. Three electrode setup in 1 M H_2SO_4 electrolyte where glassy carbon modified with catalyst was working electrode, carbon felt was used as counter electrode and 3 M Ag/AgCl electrode as a reference electrode. Current density is calculated using geometric electrode area (0.071 cm^2).*

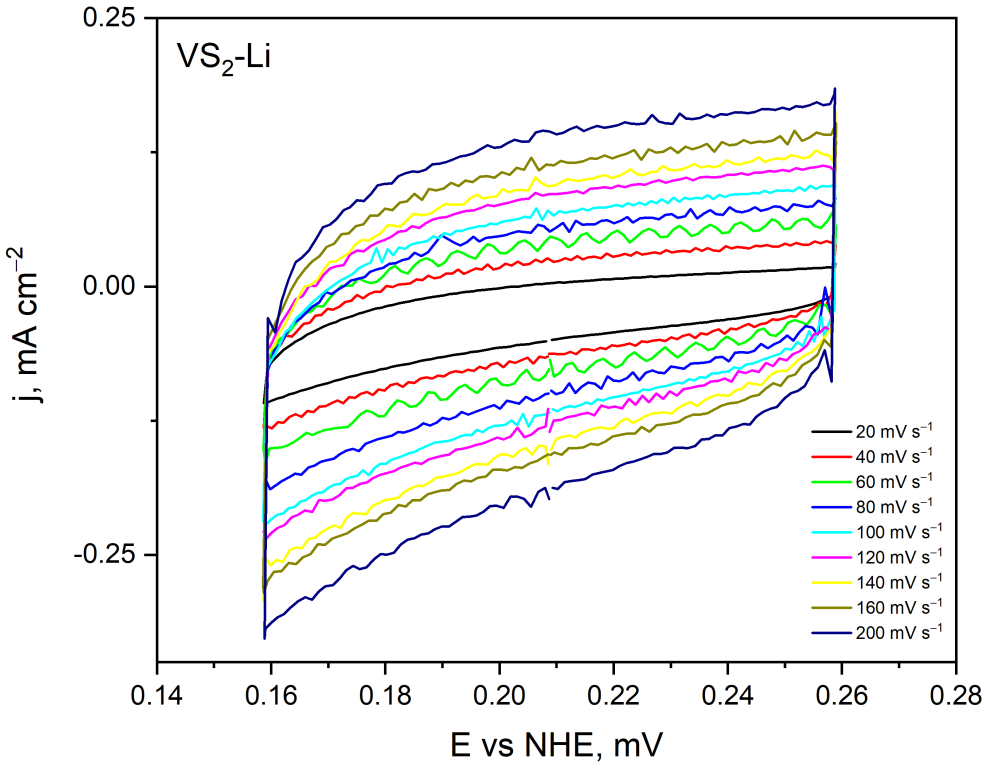

Figure A 7. *CV scans at different scan speeds (from 20 mV s^{-1} to 200 mV s^{-1}) of sample VS_2-Li that were used for double layer capacitance plot. Three electrode setup in 1 M H_2SO_4 electrolyte where glassy carbon modified with catalyst was working electrode, carbon felt was used as counter electrode and 3 M Ag/AgCl electrode as a reference electrode. Current density is calculated using geometric electrode area (0.071 cm^2).*

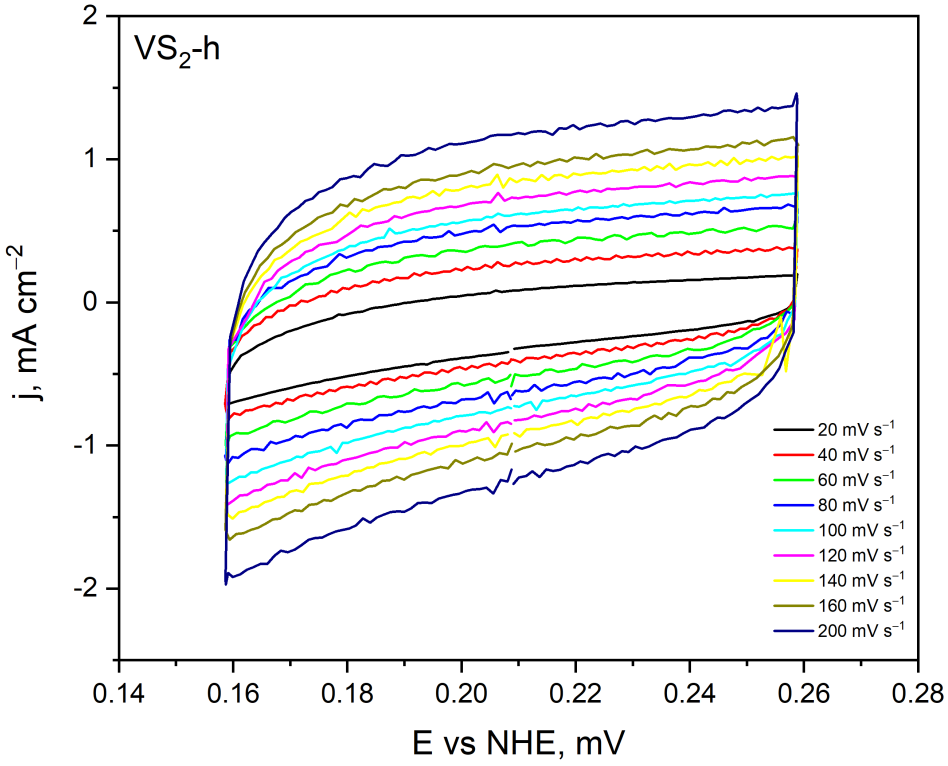

Figure A 8. *CV scans at different scan speeds (from 20 mV s^{-1} to 200 mV s^{-1}) of sample VS_2-h that were used for double layer capacitance plot. Three electrode setup in 1 M H_2SO_4 electrolyte where glassy carbon modified with catalyst was working electrode, carbon felt was used as counter electrode and 3 M Ag/AgCl electrode as a reference electrode. Current density is calculated using geometric electrode area (0.071 cm^2).*

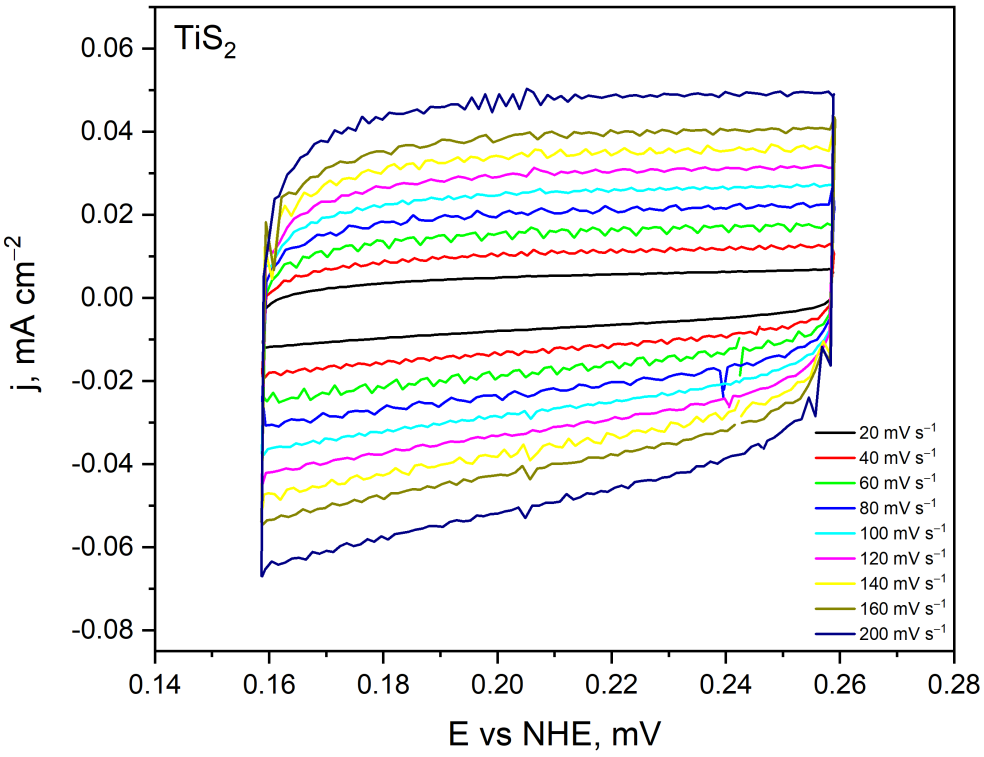

Figure A 9. *CV scans at different scan speeds (from 20 mV s^{-1} to 200 mV s^{-1}) of sample TiS_2 that were used for double layer capacitance plot. Three electrode setup in 1 M H_2SO_4 electrolyte where glassy carbon modified with catalyst was working electrode, carbon felt was used as counter electrode and 3 M Ag/AgCl electrode as a reference electrode. Current density is calculated using geometric electrode area (0.071 cm^2).*

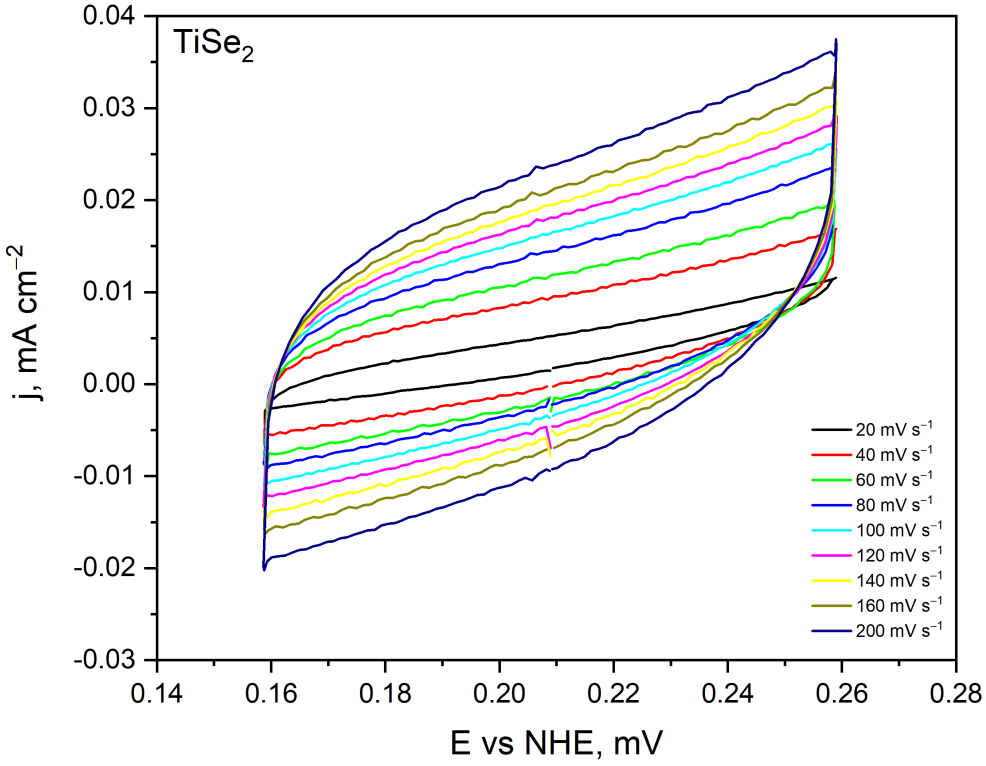

Figure A 10. *CV scans at different scan speeds (from 20 mV s^{-1} to 200 mV s^{-1}) of sample $TiSe_2$ that were used for double layer capacitance plot. Three electrode setup in 1 M H_2SO_4 electrolyte where glassy carbon modified with catalyst was working electrode, carbon felt was used as counter electrode and 3 M Ag/AgCl electrode as a reference electrode. Current density is calculated using geometric electrode area (0.071 cm^2).*

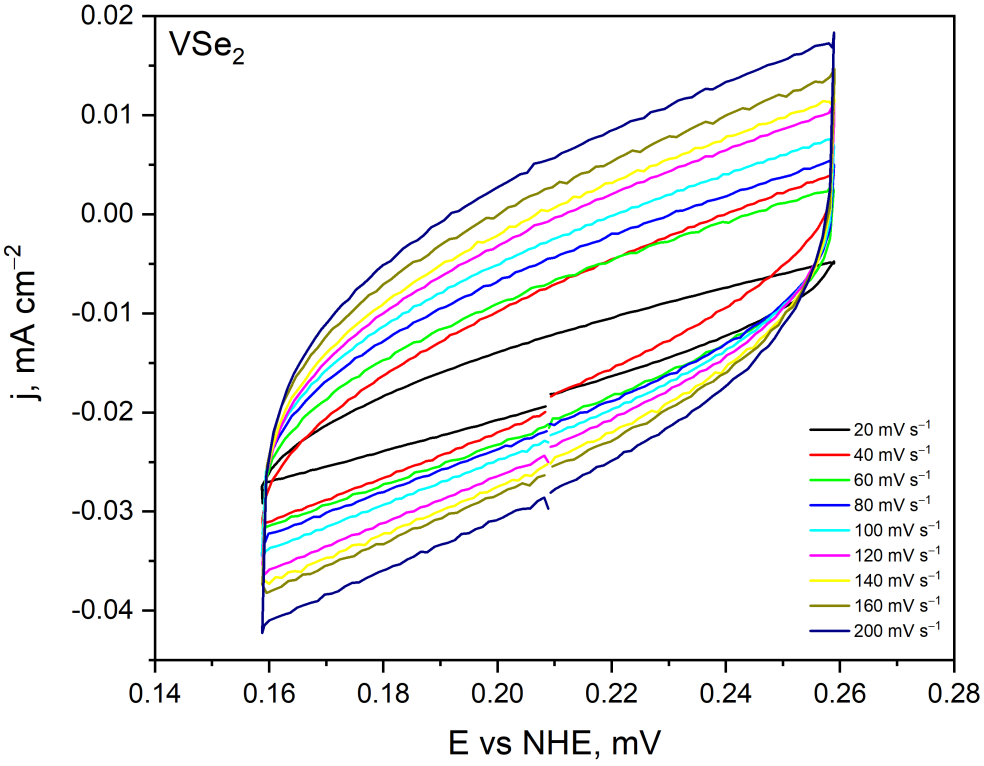

Figure A 11. *CV scans at different scan speeds (from 20 mV s^{-1} to 200 mV s^{-1}) of sample VSe_2 that were used for double layer capacitance plot. Three electrode setup in 1 M H_2SO_4 electrolyte where glassy carbon modified with catalyst was working electrode, carbon felt was used as counter electrode and 3 M Ag/AgCl electrode as a reference electrode. Current density is calculated using geometric electrode area (0.071 cm^2).*

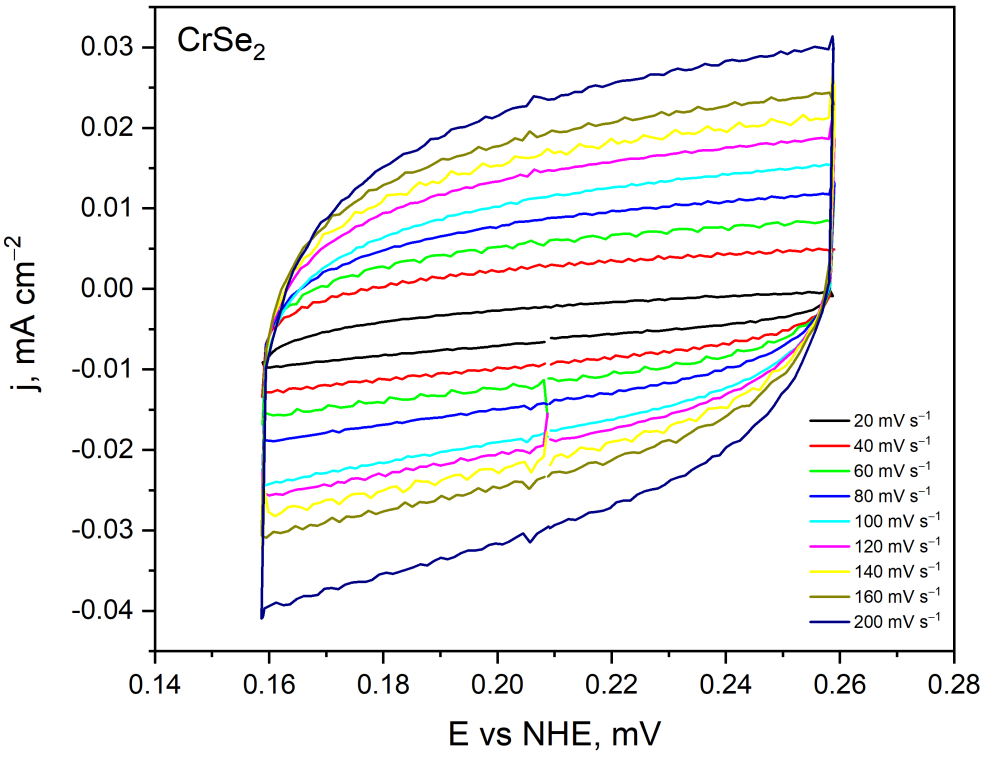

Figure A 12. *CV scans at different scan speeds (from 20 mV s^{-1} to 200 mV s^{-1}) of sample $CrSe_2$ that were used for double layer capacitance plot. Three electrode setup in 1 M H_2SO_4 electrolyte where glassy carbon modified with catalyst was working electrode, carbon felt was used as counter electrode and 3 M Ag/AgCl electrode as a reference electrode. Current density is calculated using geometric electrode area (0.071 cm^2).*